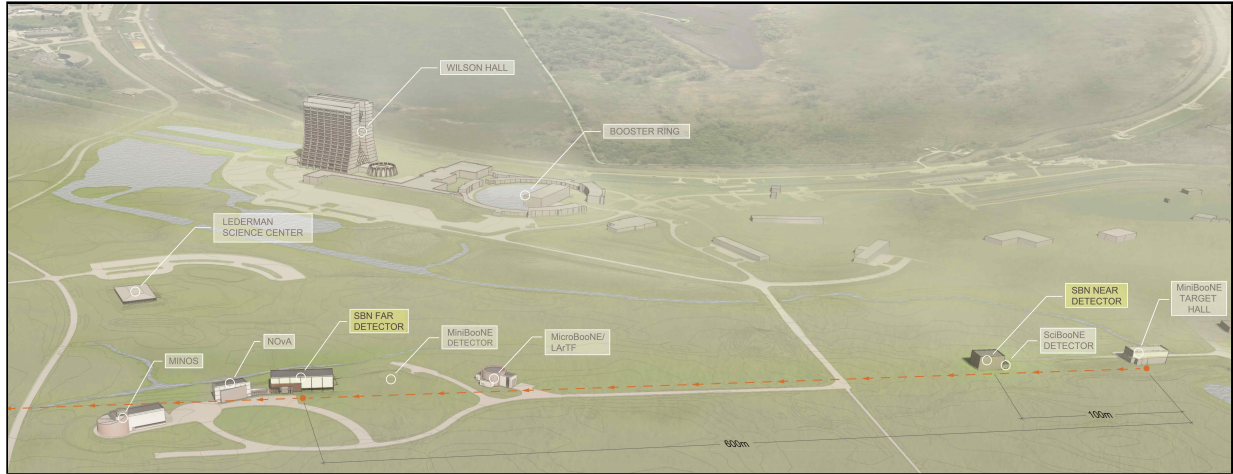


# A Proposal for a Three Detector Short-Baseline Neutrino Oscillation Program in the Fermilab Booster Neutrino Beam



## The ICARUS-WA104 Collaboration

M. Antonello<sup>16</sup>, B. Baibussinov<sup>31</sup>, V. Bellini<sup>5</sup>, P. Benetti<sup>32</sup>, S. Bertolucci<sup>6</sup>, H. Bilokon<sup>15</sup>, F. Boffelli<sup>32</sup>, M. Bonesini<sup>17</sup>, J. Bremer<sup>6</sup>, E. Calligarich<sup>32</sup>, S. Centro<sup>31</sup>, A.G. Cocco<sup>19</sup>, A. Dermenev<sup>20</sup>, A. Falcone<sup>32</sup>, C. Farnese<sup>31</sup>, A. Fava<sup>31</sup>, A. Ferrari<sup>6</sup>, D. Gibin<sup>31</sup>, S. Gninenko<sup>20</sup>, N. Golubev<sup>20</sup>, A. Guglielmi<sup>31</sup>, A. Ivashkin<sup>20</sup>, M. Kirsanov<sup>20</sup>, J. Kisiel<sup>38</sup>, U. Kose<sup>6</sup>, F. Mammoliti<sup>5</sup>, G. Mannocchi<sup>15</sup>, A. Menegolli<sup>32</sup>, G. Meng<sup>31</sup>, D. Mladenov<sup>6</sup>, C. Montanari<sup>32</sup>, M. Nessi<sup>6</sup>, M. Nicoletto<sup>31</sup>, F. Noto<sup>6</sup>, P. Picchi<sup>15</sup>, F. Pietropaolo<sup>31</sup>, P. Płoński<sup>42</sup>, R. Potenza<sup>5</sup>, A. Rappoldi<sup>32</sup>, G.L. Raselli<sup>32</sup>, M. Rossella<sup>32</sup>, C. Rubbia<sup>\*,6,11,16</sup>, P. Sala<sup>18</sup>, A. Scaramelli<sup>18</sup>, J. Sobczyk<sup>44</sup>, M. Spanu<sup>32</sup>, D. Stefan<sup>18</sup>, R. Sulej<sup>43</sup>, C.M. Sutura<sup>5</sup>, M. Torti<sup>32</sup>, F. Tortorici<sup>5</sup>, F. Varanini<sup>31</sup>, S. Ventura<sup>31</sup>, C. Vignoli<sup>16</sup>, T. Wachala<sup>12</sup>, and A. Zani<sup>32</sup>

## The LAr1-ND Collaboration

C. Adams<sup>45</sup>, C. Andreopoulos<sup>23</sup>, A.M. Ankowski<sup>41</sup>, J. Asaadi<sup>40</sup>, L. Bagby<sup>10</sup>, B. Baller<sup>10</sup>, N. Barros<sup>33</sup>, M. Bass<sup>30</sup>, S. Bertolucci<sup>6</sup>, M. Bishai<sup>3</sup>, A. Bitadze<sup>25</sup>, J. Bremer<sup>6</sup>, L. Bugel<sup>26</sup>, L. Camilleri<sup>9</sup>, F. Cavanna<sup>10,a</sup>, H. Chen<sup>3</sup>, C. Chi<sup>9</sup>, E. Church<sup>10,45</sup>, D. Cianci<sup>7</sup>, G.H. Collin<sup>26</sup>, J.M. Conrad<sup>26</sup>, G. De Geronimo<sup>3</sup>, R. Dharmapalan<sup>1</sup>, Z. Djurcic<sup>1</sup>, A. Ereditato<sup>2</sup>, J. Esquivel<sup>40</sup>, J. Evans<sup>25</sup>, B.T. Fleming<sup>45</sup>, W.M. Foreman<sup>7</sup>, J. Freestone<sup>25</sup>, T. Gamble<sup>37</sup>, G. Garvey<sup>24</sup>, V. Genty<sup>9</sup>, D. Göldi<sup>2</sup>, E. Gramellini<sup>45</sup>, H. Greenlee<sup>10</sup>, R. Guenette<sup>30</sup>, A. Hackenburg<sup>45</sup>, R. Hänni<sup>2</sup>, J. Ho<sup>7</sup>, J. Howell<sup>10</sup>, C. James<sup>10</sup>, C.M. Jen<sup>41</sup>, B.J.P. Jones<sup>26</sup>, L.N. Kalousis<sup>41</sup>, G. Karagiorgi<sup>25</sup>, W. Ketchum<sup>24</sup>, J. Klein<sup>33</sup>, J. Klinger<sup>37</sup>, U. Kose<sup>6</sup>, I. Kreslo<sup>2</sup>, V.A. Kudryavtsev<sup>37</sup>, D. Lissauer<sup>3</sup>, P. Livesly<sup>22</sup>, W.C. Louis<sup>24</sup>, M. Lüthi<sup>2</sup>, C. Mariani<sup>41</sup>, K. Mavrokoridis<sup>23</sup>, N. McCauley<sup>23</sup>, N. McConkey<sup>37</sup>, I. Mercer<sup>22</sup>, T. Miao<sup>10</sup>, G.B. Mills<sup>24</sup>, D. Mladenov<sup>6</sup>, D. Montanari<sup>10</sup>, J. Moon<sup>26</sup>, Z. Moss<sup>26</sup>, S. Mufson<sup>14</sup>, M. Nessi<sup>6</sup>, B. Norris<sup>10</sup>, F. Noto<sup>6</sup>, J. Nowak<sup>22</sup>, S. Pal<sup>37</sup>, O. Palamara<sup>\*,10,b</sup>, J. Pater<sup>25</sup>, Z. Pavlovic<sup>10</sup>, J. Perkin<sup>37</sup>, G. Pulliam<sup>40</sup>, X. Qian<sup>3</sup>, L. Qiuguang<sup>24</sup>, V. Radeka<sup>3</sup>, R. Rameika<sup>10</sup>, P.N. Ratoff<sup>22</sup>, M. Richardson<sup>37</sup>, C. Rudolf von Rohr<sup>2</sup>, B. Russell<sup>45</sup>, D.W. Schmitz<sup>\*,7</sup>, M.H. Shaevitz<sup>9</sup>, B. Sippach<sup>9</sup>, M. Soderberg<sup>40</sup>, S. Söldner-Rembold<sup>25</sup>, J. Spitz<sup>26</sup>, N. Spooner<sup>37</sup>, T. Strauss<sup>2</sup>, A.M. Szec<sup>45</sup>, C.E. Taylor<sup>24</sup>, K. Terao<sup>9</sup>, M. Thiesse<sup>37</sup>, L. Thompson<sup>37</sup>, M. Thomson<sup>4</sup>, C. Thorn<sup>3</sup>, M. Touns<sup>26</sup>, C. Touramanis<sup>23</sup>, R.G. Van de Water<sup>24</sup>, M. Weber<sup>2</sup>, D. Whittington<sup>14</sup>, T. Wongjirad<sup>26</sup>, B. Yu<sup>3</sup>, G.P. Zeller<sup>10</sup>, and J. Zennamo<sup>7</sup>

## The MicroBooNE Collaboration

R. Acciarri<sup>10</sup>, C. Adams<sup>45</sup>, R. An<sup>13</sup>, A.M. Ankowski<sup>41</sup>, J. Asaadi<sup>40</sup>, L. Bagby<sup>10</sup>, B. Baller<sup>10</sup>, G. Barr<sup>30</sup>, M. Bass<sup>30</sup>, M. Bishai<sup>3</sup>, A. Blake<sup>4</sup>, T. Bolton<sup>21</sup>, C. Bromberg<sup>27</sup>, L. Bugel<sup>26</sup>, L. Camilleri<sup>9</sup>, D. Caratelli<sup>9</sup>, B. Carls<sup>10</sup>, F. Cavanna<sup>10,a</sup>, H. Chen<sup>3</sup>, E. Church<sup>10,45</sup>, G.H. Collin<sup>26</sup>, J.M. Conrad<sup>26</sup>, M. Convery<sup>39</sup>, S. Dytman<sup>34</sup>, B. Eberly<sup>39</sup>, A. Ereditato<sup>2</sup>, J. Esquivel<sup>40</sup>, B.T. Fleming<sup>\*,45</sup>, W.M. Foreman<sup>7</sup>, V. Genty<sup>9</sup>, D. Göldi<sup>2</sup>, S. Gollapinni<sup>21</sup>, M. Graham<sup>39</sup>, E. Gramellini<sup>45</sup>, H. Greenlee<sup>10</sup>, R. Grosso<sup>8</sup>, R. Guenette<sup>30</sup>, A. Hackenburg<sup>45</sup>, O. Hen<sup>26</sup>, J. Hewes<sup>25</sup>, J. Ho<sup>7</sup>, G. Horton-Smith<sup>21</sup>, C. James<sup>10</sup>, C.M. Jen<sup>41</sup>, R.A. Johnson<sup>8</sup>, B.J.P. Jones<sup>26</sup>, J. Joshi<sup>3</sup>, H. Jostlein<sup>10</sup>, D. Kaleko<sup>9</sup>, L.N. Kalousis<sup>41</sup>, G. Karagiorgi<sup>25</sup>, W. Ketchum<sup>24</sup>, B. Kirby<sup>3</sup>, M. Kirby<sup>10</sup>, T. Kobilarcik<sup>10</sup>, I. Kreslo<sup>2</sup>, Y. Li<sup>3</sup>, B. Littlejohn<sup>13</sup>, D. Lissauer<sup>3</sup>, S. Lockwitz<sup>10</sup>, W.C. Louis<sup>24</sup>, M. Lüthi<sup>2</sup>, B. Lundberg<sup>10</sup>, A. Marchionni<sup>10</sup>, C. Mariani<sup>41</sup>, J. Marshall<sup>4</sup>, K. McDonald<sup>35</sup>, V. Meddage<sup>21</sup>, T. Miceli<sup>28</sup>, G.B. Mills<sup>24</sup>, J. Moon<sup>26</sup>, M. Mooney<sup>3</sup>, M.H. Moulai<sup>26</sup>, R. Murrells<sup>25</sup>, D. Naples<sup>34</sup>, P. Nienaber<sup>36</sup>, O. Palamara<sup>10,b</sup>, V. Paolone<sup>34</sup>, V. Papavassiliou<sup>28</sup>, S. Pate<sup>28</sup>, Z. Pavlovic<sup>10</sup>, S. Pordes<sup>10</sup>, G. Pulliam<sup>40</sup>, X. Qian<sup>3</sup>, J.L. Raaf<sup>10</sup>, V. Radeka<sup>3</sup>, R. Rameika<sup>10</sup>, B. Rebel<sup>10</sup>, L. Rochester<sup>39</sup>, C. Rudolf von Rohr<sup>2</sup>, B. Russell<sup>45</sup>, D.W. Schmitz<sup>7</sup>, A. Schukraft<sup>10</sup>, W. Seligman<sup>9</sup>, M.H. Shaevitz<sup>9</sup>, M. Soderberg<sup>40</sup>, S. Söldner-Rembold<sup>25</sup>, J. Spitz<sup>26</sup>, J. St. John<sup>8</sup>, T. Strauss<sup>2</sup>, A.M. Szec<sup>45</sup>, N. Tagg<sup>29</sup>, K. Terao<sup>9</sup>, M. Thomson<sup>4</sup>, C. Thorn<sup>3</sup>, M. Touns<sup>26</sup>, Y. Tsai<sup>39</sup>, T. Usher<sup>39</sup>, R. Van de Water<sup>24</sup>, M. Weber<sup>2</sup>, S. Wolbers<sup>10</sup>, T. Wongjirad<sup>26</sup>, K. Woodruff<sup>28</sup>, M. Xu<sup>13</sup>, T. Yang<sup>10</sup>, B. Yu<sup>3</sup>, G.P. Zeller<sup>\*,10</sup>, J. Zennamo<sup>7</sup>, and C. Zhang<sup>3</sup>

## Additional Fermilab Contributors

W. Badgett<sup>10</sup>, K. Biery<sup>10</sup>, S.J. Brice<sup>10</sup>, S. Dixon<sup>10</sup>, M. Geynisman<sup>10</sup>, C. Moore<sup>10</sup>, E. Snider<sup>10</sup>, and P. Wilson<sup>10</sup>

- <sup>1</sup> Argonne National Laboratory, Lemont, IL, USA
- <sup>2</sup> Laboratory for High Energy Physics, Universität Bern, Bern, Switzerland
- <sup>3</sup> Brookhaven National Laboratory, Upton, NY, USA
- <sup>4</sup> University of Cambridge, Cambridge, UK
- <sup>5</sup> Department of Physics, Catania University, and INFN, Catania, Italy
- <sup>6</sup> CERN, Geneva, Switzerland
- <sup>7</sup> Enrico Fermi Institute, University of Chicago, Chicago, IL, USA
- <sup>8</sup> University of Cincinnati, Cincinnati, OH, USA
- <sup>9</sup> Nevis Labs, Columbia University, Irvington, NY, USA
- <sup>10</sup> Fermi National Accelerator Laboratory, Batavia, IL, USA
- <sup>11</sup> GSSI, Gran Sasso Science Institute, L'Aquila, Italy
- <sup>12</sup> Henryk Niewodniczanski Institute of Nuclear Physics, Polish Academy of Science, Kraków, Poland
- <sup>13</sup> Illinois Institute of Technology, Chicago, IL, USA
- <sup>14</sup> Indiana University, Bloomington, IN, USA
- <sup>15</sup> INFN LNF, Frascati (Roma), Italy
- <sup>16</sup> INFN LNGS, Assergi (AQ), Italy
- <sup>17</sup> INFN Milano Bicocca, Milano, Italy
- <sup>18</sup> INFN Milano, Milano, Italy
- <sup>19</sup> INFN Napoli, Napoli, Italy
- <sup>20</sup> Institute for Nuclear Research of the Russian Academy of Sciences, Moscow, Russia
- <sup>21</sup> Kansas State University, Manhattan, KS, USA
- <sup>22</sup> Lancaster University, Lancaster, UK
- <sup>23</sup> University of Liverpool, Liverpool, UK
- <sup>24</sup> Los Alamos National Laboratory, Los Alamos, NM, USA
- <sup>25</sup> University of Manchester, Manchester, UK
- <sup>26</sup> Massachusetts Institute of Technology, Cambridge, MA, USA
- <sup>27</sup> Michigan State University, East Lansing, MI, USA
- <sup>28</sup> New Mexico State University, Las Cruces, NM, USA
- <sup>29</sup> Otterbein University, Westerville, OH, USA
- <sup>30</sup> University of Oxford, Oxford, UK
- <sup>31</sup> Department of Physics and Astronomy, Padova University, and INFN, Padova, Italy
- <sup>32</sup> Department of Physics, Pavia University, and INFN, Pavia, Italy
- <sup>33</sup> University of Pennsylvania, Philadelphia, PA, USA
- <sup>34</sup> University of Pittsburgh, Pittsburgh, PA, USA
- <sup>35</sup> Princeton University, Princeton, NJ, USA
- <sup>36</sup> Saint Mary's University of Minnesota, Winona, MN, USA
- <sup>37</sup> University of Sheffield, Sheffield, UK
- <sup>38</sup> Institute of Physics, University of Silesia, Katowice, Poland
- <sup>39</sup> SLAC National Accelerator Laboratory, Menlo Park, CA, USA
- <sup>40</sup> Syracuse University, Syracuse, NY, USA
- <sup>41</sup> Center for Neutrino Physics, Virginia Tech, Blacksburg, VA, USA
- <sup>42</sup> Institute for Radioelectronics, Warsaw University of Technology, Warsaw, Poland
- <sup>43</sup> National Centre for Nuclear Research, Warsaw, Poland
- <sup>44</sup> Institute of Theoretical Physics, Wroclaw University, Wroclaw, Poland
- <sup>45</sup> Yale University, New Haven, CT, USA

\*Spokespeople

<sup>a</sup>on leave of absence from University of L'Aquila and INFN, L'Aquila, Italy

<sup>b</sup>on leave of absence from INFN Gran Sasso Laboratories, Assergi (AQ), Italy

# Contents

Introduction . . . . .	1
------------------------	---

## Part 1 Physics Program

I. Overview of the SBN Experimental Program . . . . .	6
A. The Booster Neutrino Beam . . . . .	7
B. The Detector Systems: MicroBooNE, LAr1-ND, ICARUS-T600 . . . . .	9
C. SBL Neutrino Anomalies and the Physics of Sterile Neutrinos . . . . .	12
D. The Current Experimental Landscape . . . . .	14
II. SBN Oscillation Searches . . . . .	17
A. Analysis Methods . . . . .	17
B. $\nu_e$ and $\nu_\mu$ Signal Selection . . . . .	20
C. Neutrino Flux Uncertainties . . . . .	22
D. Neutrino Interaction Uncertainties . . . . .	24
E. Detector Systematics . . . . .	26
F. Beam-Induced “Dirt” Events . . . . .	28
G. Cosmogenic Backgrounds . . . . .	32
H. $\nu_\mu \rightarrow \nu_e$ Appearance Sensitivity . . . . .	41
I. $\nu_\mu \rightarrow \nu_x$ Disappearance Sensitivity . . . . .	47
III. Other SBN Physics . . . . .	49
A. Neutrino-Argon Interactions . . . . .	49
B. Additional Searches . . . . .	49

## Part 2 LAr1-ND Conceptual Design

I. Introduction . . . . .	52
II. Physics of LAr1-ND . . . . .	52
A. MiniBooNE Low Energy Excess . . . . .	52
B. Neutrino Cross Section Measurements . . . . .	54
III. Overview of the LAr1-ND Detector . . . . .	54
A. Detector Dimensions . . . . .	56
IV. TPC Design . . . . .	56
A. The Anode Plane Assembly . . . . .	58
B. The Cathode Plane Assembly . . . . .	61
C. The High Voltage Feedthrough . . . . .	62
D. The Field Cage . . . . .	63
E. Installation Procedure . . . . .	63
F. Quality Control and Quality Assurance . . . . .	64
G. Risks . . . . .	64

V. TPC Electronics, DAQ and Trigger . . . . .	65
A. Introduction . . . . .	65
B. The Front End Electronics . . . . .	65
C. The TPC readout . . . . .	71
D. The Trigger Board . . . . .	74
E. An Alternative Scheme . . . . .	75
VI. UV Laser-Based Field Calibration System. . . . .	76
A. Calibration of Drift Field by UV Laser Beam . . . . .	76
B. Laser Beam Arrangement and Beam Optics . . . . .	78
C. Rotating Feed-Through . . . . .	78
D. Expected Performance . . . . .	79
VII. Light Detection System . . . . .	82
A. Introduction and Motivation . . . . .	82
B. A Light Collection System for LAr1-ND . . . . .	84
VIII. Cosmic Ray Tagging System. . . . .	89
A. Scintillating Tracker Design and Operation. . . . .	90
B. Electronic Readout System. . . . .	90
C. Expected Performance . . . . .	91
IX. The LAr1-ND Detector: A Development Toward LBNF. . . . .	94

### **Part 3 T600 Design and Refurbishing**

I. Introduction . . . . .	98
II. Physics of Far Detector . . . . .	100
A. The SBN experimental program . . . . .	100
B. T600 Physics with the NuMI beam . . . . .	100
III. Requirements for Detector Performance . . . . .	101
IV. The T600 Detector: present configuration. . . . .	102
A. TPC design . . . . .	103
B. Light Collection system . . . . .	112
C. Electronics, DAQ and Trigger . . . . .	115
D. Cryogenics and Purification systems. . . . .	116
V. Overhauling of the T600 Detector: WA104. . . . .	120
A. TPC modifications . . . . .	122
B. New Light Collection System Layout and Implementation . . . . .	125
C. New Electronics, DAQ and Trigger . . . . .	129
D. New Cryogenic and Purification systems . . . . .	134
VI. Cosmic Ray Tagging System . . . . .	139
A. CRTS efficiency . . . . .	140
B. CRTS layout. . . . .	141

## **Part 4 Infrastructure and Civil Construction**

I. Introduction . . . . .	144
II. Cryostats . . . . .	145
A. Near Detector Cryostat . . . . .	145
B. Far Detector Cryostat . . . . .	154
III. Cryogenic Systems . . . . .	156
IV. Requirements for Near and Far Detector Buildings . . . . .	160
V. Near Detector Siting and Construction . . . . .	160
VI. Far Detector Siting and Construction . . . . .	162
VII. Computing Infrastructure and Software . . . . .	164
A. Data Acquisition and Data Quality Monitoring . . . . .	164
B. Data Storage and Processing . . . . .	167
C. Data Analysis Framework and Tools. . . . .	168
D. Toward an Automated Reconstruction. . . . .	170

## **Part 5 Booster Neutrino Beam**

I. Overview . . . . .	176
II. A Re-optimized Horn Configuration . . . . .	177
III. Making Space for the New Horn Configuration . . . . .	179
IV. Secondary Beamline Instrumentation. . . . .	180
V. Request . . . . .	182

## **Part 6 Coordination and Schedule**

I. Introduction . . . . .	184
II. Schedule . . . . .	185
A. Near Detector Schedule . . . . .	186
B. Far Detector Schedule. . . . .	188
C. Infrastructure Schedule . . . . .	188
A. Detector Volumes and Masses . . . . .	195
. References . . . . .	196

## Introduction

We propose a Short-Baseline Neutrino (SBN) physics program of three LAr-TPC detectors located along the Booster Neutrino Beam (BNB) at Fermilab. This new SBN Program will deliver a rich and compelling physics opportunity, including the ability to resolve a class of experimental anomalies in neutrino physics and to perform the most sensitive search to date for sterile neutrinos at the eV mass-scale through both appearance and disappearance oscillation channels. Additional physics of the SBN Program includes the study of neutrino-argon cross sections with millions of interactions using the well characterized neutrino fluxes of the BNB. The SBN detectors will also record events from the off-axis flux of the NuMI neutrino beam with its higher electron neutrino content and different energy spectrum. Finally, the SBN Program is an excellent opportunity to further develop this important technology for the future long-baseline neutrino program while utilizing its remarkable capabilities to explore one of the exciting open questions in neutrino physics today.

The recent report of the Particle Physics Prioritization Panel (P5) specifically recommended a near-term, world-leading short-baseline experimental neutrino program with strong participation by the domestic and international neutrino physics communities working toward LBNF:

- P5 Recommendation #12: In collaboration with international partners, develop a coherent short- and long-baseline neutrino program hosted at Fermilab.
- P5 Recommendation #15: Select and perform in the short term a set of small-scale short-baseline experiments that can conclusively address experimental hints of physics beyond the three-neutrino paradigm. Some of these experiments should use liquid argon to advance the technology and build the international community for LBNF at Fermilab.

This proposal outlines exactly such a program. The SBN program brings together three LAr-TPC detectors built and operated by leading teams of scientists and engineers from Europe and the U.S. The ICARUS-T600 detector is the first successful large-scale LAr-TPC to be exposed to a neutrino beam and to this point the largest LAr-TPC for neutrino physics. The MicroBooNE detector is the largest LAr-TPC built in the U.S. and will have been operational for several years at the start of the three detector program. The new near detector, LAr1-ND, is being developed by an international team with experience from ArgoNeuT, MicroBooNE, and LBNE prototypes. The combination of these three detectors and associated collaborations represents a tremendous R&D opportunity toward the future LBN program.

At the January 2014 meeting of the Fermilab PAC, presentations were made by two collaborations to significantly enhance the physics capabilities of the Booster Neutrino Beam (BNB) with additional LAr-TPC detectors. Both proposals were targeted at providing definitive measurements of the LSND and MiniBooNE anomalies. The ICARUS collaboration proposed [1] a two detector experiment incorporating the existing T600 LAr-TPC located 700 m from the BNB as a far detector and a new T150 LAr-TPC located  $150 \pm 50$  m from the target as a near detector. The primary physics goal of the ICARUS proposal was the search for light sterile neutrinos. The idea to utilize multiple LAr-TPC detectors for a comprehensive test of neutrino anomalies was first put forth by the ICARUS collaboration at CERN as early as 2009 [2–4] and later extended to include the addition of magnetized spectrometer detectors [5] by the NESSIE collaboration. The ICARUS-NESSIE proposal [6] required the construction of a new neutrino beam (CENF) from the 100 GeV proton SPS in the CERN north area, which has not since been realized.

Also at the January 2014 Fermilab PAC meeting, the LAr1-ND collaboration proposed [7] to install a new LAr-TPC based on LBNE-type technology 100 m from the BNB target in an existing enclosure that was constructed for the SciBooNE experiment. The proposed LAr1-ND detector, in concert with the MicroBooNE experiment, would address the MiniBooNE neutrino mode anomaly and enable improved searches for oscillations. LAr1-ND was seen as the next step in a phased short-baseline neutrino program at Fermilab. The full LAr1 detector, a 1 kton LAr-TPC previously presented in an LOI in 2012 [8], could then, together with LAr1-ND, definitively address the question of neutrino oscillations in the  $\Delta m^2 \approx 1 \text{ eV}^2$  region. LAr1 was not encouraged by P5, however, due to the high cost of a new detector of this scale.

Following the recommendation of the PAC, the MicroBooNE, LAr1-ND, and ICARUS collaborations were asked by the Fermilab Director to propose a combined Short-Baseline Neutrino (SBN) program to address the short-baseline anomalies and search for sterile neutrinos. The SBN Task Force was created to steer the activities of the collaborations required to create this proposal including a conceptual design for the program components. The task force was charged jointly by the directorates of CERN, Fermilab, and INFN. The task force consists of five members, one representing each of the three collaborations (LAr1-ND, MicroBooNE, ICARUS), one representing CERN, and the Fermilab SBN Program Coordinator. This proposal is the result of this joint effort over a period of about nine months. The proposal is organized into six parts that are briefly summarized below.

Part 1 describes the primary physics case for the SBN program: the search for sterile neutrinos and exploration of the LSND and MiniBooNE anomalies. This chapter describes the physics motivations including the current landscape of oscillation anomalies at the  $\Delta m^2 \sim 1 \text{ eV}^2$  scale. The physics sensitivity for  $\nu_\mu$  disappearance and  $\nu_e$  appearance are evaluated for the proposed three detector configuration. The extensive evaluation of systematics includes the impact of neutrino interaction uncertainties and differences in the neutrino flux at the different detectors. The primary backgrounds to the  $\nu_e$  signal have been carefully considered in the sensitivities:

- Intrinsic  $\nu_e$  content of the beam,
- Neutral current  $\gamma$  production,
- $\nu_\mu$  charged current  $\gamma$  production,
- Neutrino interactions in material surrounding the detectors,
- Cosmogenic photons.

Using data sets of  $6.6 \times 10^{20}$  protons on target (P.O.T.) in the LAr1-ND and T600 detectors plus  $13.2 \times 10^{20}$  P.O.T. in the MicroBooNE detector, we conservatively estimate that a search for  $\nu_\mu \rightarrow \nu_e$  appearance can be performed covering with  $\sim 5\sigma$  sensitivity the LSND allowed (99% C.L.) region. This level of sensitivity is achieved using relatively simple event selection criteria that have undergone only a preliminary optimization. A more detailed analysis will likely yield even better results. However, achieving this level of sensitivity will require careful control over cosmogenic backgrounds. The external muon tagging/veto systems proposed in Parts 2 & 3 of this proposal will be essential in ensuring an efficient independent method of identifying tracks in the TPCs associated with cosmogenic muons. Further, requiring precision timing of the already planned light detection systems will play an important role in rejecting cosmogenic photons. Since the measurement is statistically limited, an increase in the number of  $\nu$  interactions provided by more protons on target and/or greater efficiency of the target/horn



system will be highly desirable. Part 5 of this proposal outlines a possible reconfiguration of the BNB with a two horn system.

Part 2 describes the conceptual design of the SBN near detector (LAr1-ND) which will be located 110 m from the BNB target. The detector design draws extensively on the design of the LBNF far detector including cryostat technology, TPC design, and electronics. Also described are the synergies between LAr1-ND and the LBNF development. Potential benefits include expanded experience in construction of membrane cryostats, development of standardized cryogenic system modules, wire plane assembly techniques, testing of next generation cold electronics, and the development of scintillation light collection systems for LAr-TPCs. A system of scintillators external to the cryostat are proposed to provide a system for identifying tracks from cosmic rays. The near detector has been approved by Fermilab as a test experiment (T-1053).

Part 3 describes the SBN far detector (ICARUS-T600), presently the largest physics oriented operational LAr-TPC detector [9], and its very successful performance during operations in the Gran Sasso laboratory (LNGS) on the CNGS beam. The T600 will be located 600 m from the BNB target. In preparation for a thorough refurbishing, the T600 was transported from LNGS to CERN at the end of 2014. The light detection system will be improved with many additional photo-multipliers to provide better timing resolution and spatial segmentation of the light signals. These improvements are essential to handling the much higher flux of cosmic rays through the detector with operation near the surface on the BNB. Like the near detector, counters surrounding the sensitive LAr-TPC volume are proposed to provide a system for identifying tracks from cosmic rays. These cosmic tagger systems provide a clear opportunity for shared development within the SBN program.

Part 4 describes the conceptual design of infrastructure needed for the LAr1-ND and T600 detectors. This includes construction of two new detector enclosures on the beamline at 110 m and 600 m from the BNB target for the near and far detectors, respectively. Each of the detectors will be located on axis with the BNB. The design of the new detector cryostats and cryogenic systems are also described. The new cryogenics infrastructure is being developed by a joint team of engineers at CERN, Fermilab, and INFN taking advantage of opportunities for common solutions for the two detectors. While a completely new LAr filtration and circulation system is needed for the near detector, the LAr systems used at LNGS for the T600 will be reused. A possible model for a common DAQ software platform for the detectors is described. Similarly, a model is described for common reconstruction and analysis tool development based on the presently working algorithms from the ICARUS-T600 experience and the LArSoft platform currently in use by ArgoNeuT, MicroBooNE, and the LBNE 35 ton prototype.

Part 5 describes potential improvements to the Booster Neutrino Beamline. A modest reconfiguration of the beamline leading up to target and horn could provide sufficient space to convert the beamline from a single horn to a two horn system. An optimization based on a fast simulation demonstrates that the  $\nu_\mu$  rate can be approximately doubled relative to the existing MiniBooNE horn. A more detailed study is required to take this pre-conceptual design to a conceptual design that could be used to estimate cost and schedule to create a two horn configuration. Such an improvement would be an extremely valuable addition to the program providing headroom on the statistical power of the measurements. We propose that a detailed study of the cost and schedule for conversion to a two horn system be initiated immediately. This should include the cost of new horns, new or refurbished power supplies capable of 20 Hz operation, and necessary work for reconfiguration of the incoming beamline and of the collimator.

Part 6 describes the organization of the SBN program and the schedule for completion of

---

the detectors. A set of high level milestones is shown that has installation of both the near and far detectors during 2017 culminating in the three detector configuration ready for beam data-taking in the spring of 2018. Funding for the program is expected from a combination of US DOE, US NSF, and international in-kind contributions. The overhauling, improvements, and transport of the ICARUS-T600 is a major contribution of INFN and of CERN in terms of equipment and of associated funding to the realization of the present program. Commitments are already in place for funding from CERN, INFN, and UK-STFC. Funding is being sought from CH-NSF and discussions are in progress with other international partners. Organization of the program draws upon the very successful model of the LHC experiments at CERN. Under the proposed structure, the program will be monitored by an oversight committee organized by Fermilab on behalf of the international partners.

**A Proposal for a Three Detector  
Short-Baseline Neutrino Oscillation Program  
in the Fermilab Booster Neutrino Beam**

---

*Part 1: Physics Program*

---

## I. Overview of the SBN Experimental Program

The future short-baseline experimental configuration is proposed to include three Liquid Argon Time Projection Chamber detectors (LAr-TPCs) located on-axis in the Booster Neutrino Beam (BNB) as summarized in Table I. The near detector (LAr1-ND) will be located in a new building directly downstream of the existing SciBooNE enclosure 110 m from the BNB target. The MicroBooNE detector, which is currently in the final stages of installation, is located in the Liquid Argon Test Facility (LArTF) at 470 m. The far detector (the improved ICARUS-T600) will be located in a new building 600 m from the BNB target and between MiniBooNE and the NOvA near detector surface building. The detector locations were chosen to optimize sensitivity to neutrino oscillations and minimize the impact of flux systematic uncertainties as reported in [10].

Figure 1 shows the locations of the detectors superimposed on an aerial view of the Fermilab neutrino experimental area. The following Sections briefly describe the attributes of the three detectors; more detailed descriptions are provided in dedicated Design Reports submitted with this proposal (see Part II and Part III). Initial physics studies are based on current BNB fluxes, however, studies are on-going to determine what changes could be made to the target and horn systems to re-optimize for LAr-TPC detectors and increase event rates per proton on target (see Part V).

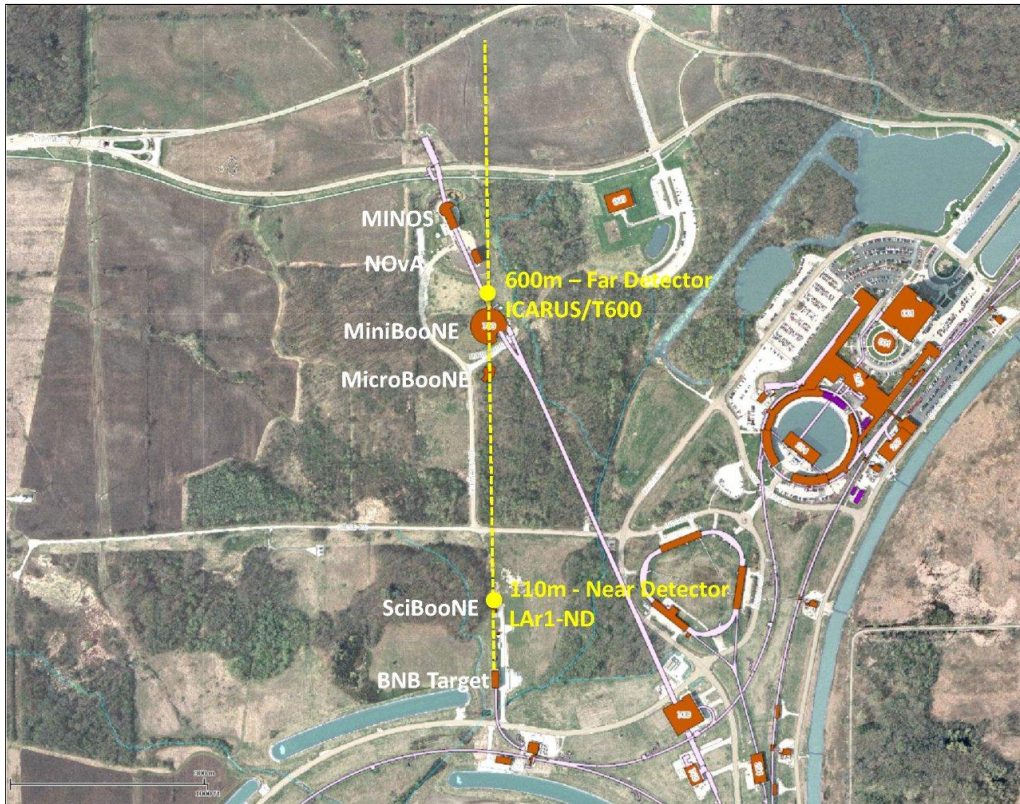


**FIG. 1:** Map of the Fermilab neutrino beamline area showing the axis of the BNB (yellow dashed line) and approximate locations of the SBN detectors at 110 m, 470 m, and 600 m. The pink line indicates the axis of the NuMI neutrino beam for reference.

Detector	Distance from BNB Target	LAr Total Mass	LAr Active Mass
LAr1-ND	110 m	220 t	112 t
MicroBooNE	470 m	170 t	89 t
ICARUS-T600	600 m	760 t	476 t

**TABLE I:** Summary of the SBN detector locations and masses.

### A. The Booster Neutrino Beam

The Booster Neutrino Beam is created by extracting protons from the Booster accelerator at 8 GeV kinetic energy (8.89 GeV/ $c$  momentum) and impacting them on a  $1.7\lambda$  beryllium (Be) target to produce a secondary beam of hadrons, mainly pions. Charged secondaries are focused by a single toroidal aluminum alloy focusing horn that surrounds the target. The horn is supplied with 174 kA in 143  $\mu$ s pulses coincident with proton delivery. The horn can be pulsed with either polarity, thus focusing either positives or negatives and de-focusing the other. Focused mesons are allowed to propagate down a 50 m long, 0.91 m radius air-filled tunnel where the majority will decay to produce muon and electron neutrinos. The remainder are absorbed into a concrete and steel absorber at the end of the 50 m decay region. Suspended above the decay region at 25 m are concrete and steel plates which can be deployed to reduce the available decay length, thus systematically altering the neutrino fluxes. A schematic of the BNB target station and decay region is shown in Figure 2. See Refs. [11, 12] for technical design reports on the 8 GeV extraction line and the Booster Neutrino Beam.

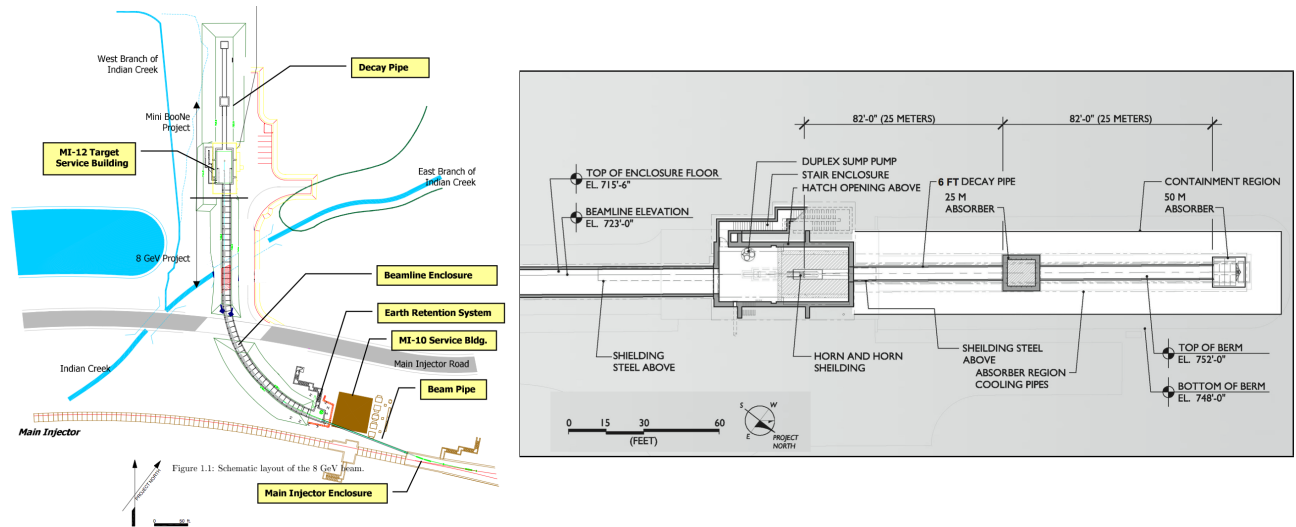


**FIG. 2:** Schematic drawings of the Booster Neutrino Beamline including the 8 GeV extraction line, target hall and decay region.

The timing structure of the delivered proton beam is an important aspect for the physics program. The Booster spill length is 1.6  $\mu$ s with nominally  $\sim 5 \times 10^{12}$  protons per spill delivered to the beryllium target. The main Booster RF is operated at 52.8 MHz, with some 81 buckets filled out of 84. The beam is extracted into the BNB using a fast-rising kicker that extracts all of the particles in a single turn. The resulting structure is a series of 81 bunches of protons each  $\sim 2$  ns wide and 19 ns apart. While the operating rate of the Booster is 15 Hz, the maximum

allowable average spill delivery rate to the BNB is 5 Hz, set by the design of the horn and its power supply.

The BNB has already successfully and stably operated for 12 years in both neutrino and anti-neutrino modes. The fluxes are well understood thanks to a detailed simulation [13] developed by the MiniBooNE Collaboration and the availability of dedicated hadron production data for 8.9 GeV/c  $p$ +Be interactions collected at the HARP experiment at CERN [14, 15]. Systematic uncertainties associated with the beam have also been characterized in a detailed way as seen in Refs. [13, 16] with a total error of  $\sim 9\%$  at the peak of the  $\nu_\mu$  flux and larger in the low and high energy regions.

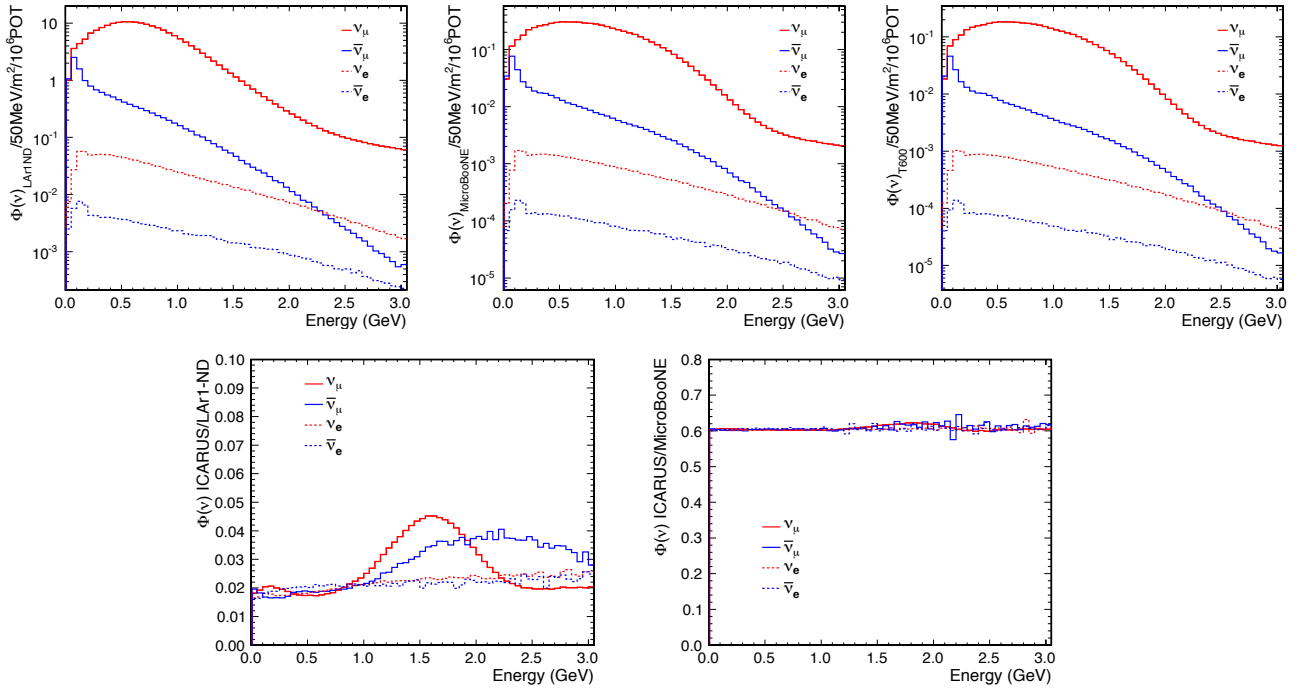


**FIG. 3:** (Top) The Booster Neutrino Beam flux at the three SBN detectors: (left) LAr1-ND, (center) MicroBooNE, and (right) ICARUS-T600. (Bottom) Ratio of the fluxes for each neutrino species between ICARUS and LAr1-ND (left) and between ICARUS and MicroBooNE (right). Fluxes at the far detectors fall off faster than  $1/r^2$  when compared to the 110 m location and the  $\nu_\mu/\bar{\nu}_\mu$  spectra are harder due to the restricted solid angle at the far locations. These effects and associated systematic uncertainties are fully considered in the analysis. The far detector locations are clearly in the  $1/r^2$  regime with  $470^2/600^2 = 0.61$ .

The neutrino fluxes observed at the three SBN detector locations are shown in Figure 3. Note the rate in the near detector is 20-30 times higher than at the MicroBooNE and ICARUS locations. Also, one sees the  $\nu_\mu$  spectrum is slightly harder at the far locations as a result of the narrower solid angle viewed by the far detector. We'll see later, however, that this does not introduce a significant systematic in oscillation searches. The shapes of the  $\nu_e/\bar{\nu}_e$  fluxes are more similar. The composition of the flux in neutrino mode (focusing positive hadrons) is energy dependent, but is dominated by  $\nu_\mu$  ( $\sim 93.6\%$ ), followed by  $\bar{\nu}_\mu$  ( $\sim 5.9\%$ ), with an intrinsic  $\nu_e/\bar{\nu}_e$  contamination at the level of 0.5% at energies below 1.5 GeV. The majority of the  $\nu_\mu$  flux originates from pion decay in flight ( $\pi^+ \rightarrow \mu^+ + \nu_\mu$ ) except above  $\sim 2$  GeV where charged kaon decay is the largest contributor. A substantial portion of the intrinsic  $\nu_e$  flux, 51%, originates

from the pion  $\rightarrow$  muon decay chain ( $\pi^+ \rightarrow \mu^+ \rightarrow e^+ + \nu_e + \nu_\mu$ ) with the remaining portion from  $K^+$  and  $K^0$  decays.

## B. The Detector Systems: MicroBooNE, LAr1-ND, ICARUS-T600

### *MicroBooNE*

MicroBooNE is currently in the final stages of construction and will be commissioned at the end of 2014. The experiment will measure neutrino interactions in argon for multiple reaction channels and investigate the source of the currently unexplained excess of low energy electromagnetic events observed by MiniBooNE. MicroBooNE also incorporates several important R&D features: the use of a non-evacuated cryostat, passive insulation of the cryostat and cryogenics, cold (in liquid) electronics, a long 2.56 meter drift distance, and a novel UV laser calibration system [17]. To accomplish these goals, the MicroBooNE detector is a 170 ton total mass (89 ton active mass) liquid argon TPC contained within a conventional cryostat [18]. The active region of the TPC is a rectangular volume of dimensions 2.33 m  $\times$  2.56 m  $\times$  10.37 m. The TPC cathode plane forms the vertical boundary of the active volume on the left side of the detector when viewed along the neutrino beam direction (beam left). The MicroBooNE TPC design allows ionization electrons from charged particle tracks in the active liquid argon volume to drift up to 2.56 meters to a three-plane wire chamber. Three readout planes, spaced by 3 mm, form the beam-right side of the detector, with 3,456 Y wires arrayed vertically and 2,400 U and 2,400 V wires oriented at  $\pm 60$  degrees with respect to vertical. An array of 32 PMTs are mounted behind the wire planes on the beam right side of the detector to collect prompt scintillation light produced in the argon [19].

MicroBooNE is approved to receive an exposure of  $6.6 \times 10^{20}$  protons on target in neutrino running mode from the BNB. It will also record interactions from an off-axis component of the NuMI neutrino beam. During MicroBooNE running, the BNB will be operated in the same configuration that successfully delivered neutrino and anti-neutrino beam to MiniBooNE for more than a decade, thereby significantly reducing systematic uncertainties in the comparison of MicroBooNE data with that from MiniBooNE.

As of the writing of this document, construction of the MicroBooNE TPC has been completed and on June 23, 2014, the MicroBooNE vessel was moved to the LArTF, a new Fermilab enclosure just upstream of the MiniBooNE detector hall. Final installation and detector commissioning has begun. MicroBooNE is on schedule to begin taking neutrino data in early 2015.

### *LAr1-ND*

The design of the Liquid Argon Near Detector, or LAr1-ND [7], builds on many years of LAr-TPC detector R&D and experience from design and construction of the ICARUS-T600, ArgoNeuT, MicroBooNE, and LBNF detectors. The basic concept is to construct a membrane-style cryostat in a new on-axis enclosure adjacent to and directly downstream of the existing SciBooNE hall. The membrane cryostat will house a CPA (Cathode Plane Assembly) and four APAs (Anode Plane Assemblies) to read out ionization electron signals. The active TPC volume is 4.0 m (width)  $\times$  4.0 m (height)  $\times$  5.0 m (length, beam direction), containing 112 tons of liquid argon. Figure 4 shows the state of the conceptual design for the Near Detector building and the LAr1-ND TPC.

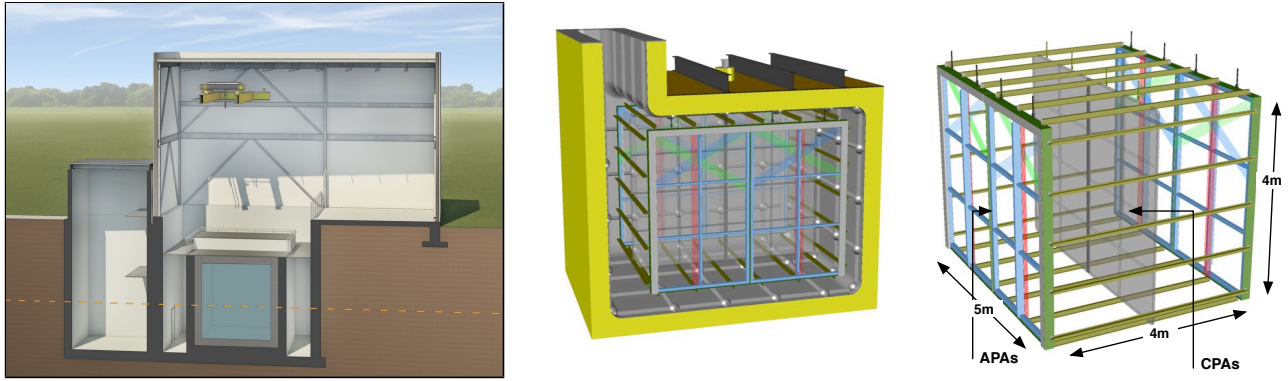


**FIG. 4:** (Left) The LAr1-ND detector building concept. The neutrino beam center is indicated by the orange dashed line and enters from the left. (Right) The LAr1-ND TPC conceptual design.

The two APAs located near the beam-left and beam-right walls of the cryostat will each hold 3 planes of wires with 3 mm wire spacing. The APAs use the same wire bonding method developed for the LBNF APAs, but without the continuous helical wrapping to avoid ambiguity in track reconstruction. Along the common edge of neighboring APAs, the U & V wires are electrically “jumped”. TPC signals are then read out with banks of cold electronics boards at the top and two outer vertical sides of each detector half. The total number of readout channels is 2,816 per APA (11,264 in the entire detector). The CPA has the same dimensions as the APAs and is centered between them. It is made of a stainless-steel framework, with an array of stainless-steel sheets mounted over the frame openings. Each pair of facing CPA and APA hence forms an electron-drift region. The open sides between each APA and the CPA are surrounded by 4 FCAs (Field Cage Assemblies), constructed from FR4 printed circuit panels with parallel copper strips, to create a uniform drift field. The drift distance between each APA and the CPA is 2 m such that the cathode plane will need to be biased at -100 kV for a nominal 500 V/cm field. The LAr1-ND design will additionally include a light collection system for detecting scintillation light produced in the argon volume.

Overall, the design philosophy of the LAr1-ND detector is to serve as a prototype for LBNF that functions as a physics experiment. While the present conceptual design described here is an excellent test of LBNF detector systems sited in a neutrino beam, the LAr1-ND Collaboration is exploring innovations in this design and the opportunity to further test them in a running experiment.

### ICARUS-T600

The ICARUS-T600 detector previously installed in the underground INFN-LNGS Gran Sasso Laboratory has been the first large-mass LAr-TPC operating as a continuously sensitive general purpose observatory. The successful operation of the ICARUS-T600 LAr-TPC demonstrates the enormous potential of this detection technique, addressing a wide physics program with the simultaneous exposure to the CNGS neutrino beam and cosmic-rays [9].

The ICARUS-T600 detector consists of two large identical modules with internal dimensions  $3.6 \times 3.9 \times 19.6 \text{ m}^3$  filled with  $\sim 760$  tons of ultra-pure liquid argon, surrounded by a common thermal insulation [9, 20]. Each module houses two TPCs separated by a common central cathode for an active volume of  $3.2 \times 2.96 \times 18.0 \text{ m}^3$ . A uniform electric field ( $E_D = 500$



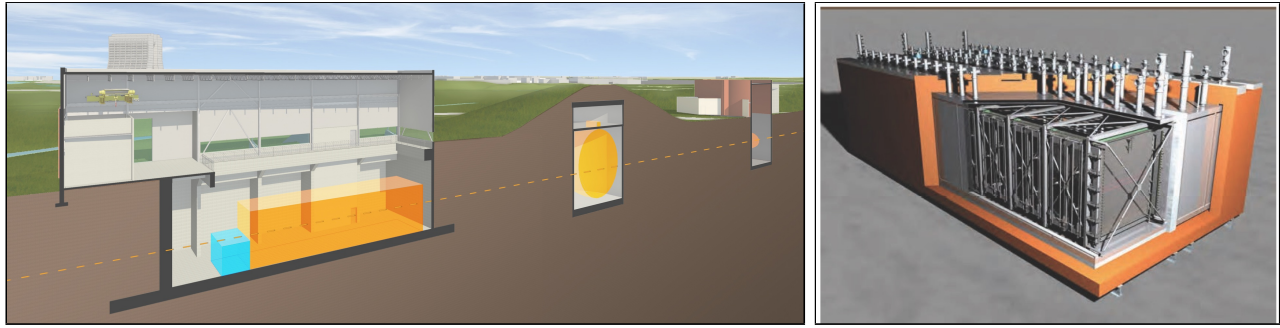


**FIG. 5:** (Left) The ICARUS-T600 detector building concept. The neutrino beam center is indicated by the orange dashed line and enters from the right. The existing MiniBooNE and MicroBooNE buildings are also shown. (Right) ICARUS-T600 detector schematic showing both modules and the common insulation surrounding the detector.

V/cm) is applied to the drift volume. The reliable operation of the high-voltage system has been extensively tested in the ICARUS-T600 up to about twice the operating voltage (150 kV, corresponding to  $E_D = 1$  kV/cm). Each TPC is made of three parallel wire planes, 3 mm apart, with 3 mm pitch, facing the drift path (1.5 m) and with wires oriented at  $0^\circ$ ,  $\pm 60^\circ$  with respect to the horizontal direction, respectively. Globally, 53,248 wires with length up to 9 m are installed in the detector. A three-dimensional image of the ionizing event is reconstructed combining the wire coordinate on each plane at a given drift time with  $\sim 1$  mm<sup>3</sup> resolution over the whole active volume (340 m<sup>3</sup> corresponding to 476 tons).

The ICARUS-T600 detector has been moved to CERN for an overhauling preserving most of the existing operational equipment, while upgrading some components with up-to-date technology in view of its future near surface operation. The refurbishing program, described in detail in Part 3 and Part 4, has been endorsed by a dedicated MoU between INFN and CERN. This mainly includes:

- realization of new vessels for LAr containment and new thermal insulation;
- implementation of an improved light collection system, to allow a more precise event localization and the disentangling of the background induced by cosmic rays;
- although the present electronics would be perfectly adequate for the SBN program, several reasons exist for its substitution with a more modern version that preserves the general architecture with more updated components. A possible solution already at prototype level is described in Part 3. The final solution is under evaluation and cost sharing and responsibilities will be object of a special addendum of the MoU.

Moreover an anti-coincidence system, common to the SBN detectors, will be constructed to automatically tag cosmic rays crossing the LAr active volume.

For what concerns the maintenance and the adaptation of the cryogenic systems to the new experimental layout at FNAL, this activity will be carried-out under the supervision of the ICARUS Collaboration with a major involvement of CERN.

The detector is expected to be transported to FNAL at the beginning of 2017. Installation and operation at Fermilab will require significant involvement of Fermilab technical personnel. All of the above mentioned activities will also bring considerable value as R&D for a future long-baseline neutrino facility based on LAr.

### C. SBL Neutrino Anomalies and the Physics of Sterile Neutrinos

Experimental observations of neutrino oscillations have established a picture consistent with the mixing of three neutrino flavors ( $\nu_e, \nu_\mu, \nu_\tau$ ) with three mass eigenstates ( $\nu_1, \nu_2, \nu_3$ ) whose mass differences turn out to be relatively small, with  $\Delta m_{31}^2 \simeq 2.4 \times 10^{-3} \text{ eV}^2$  and  $\Delta m_{21} \simeq 7.5 \times 10^{-5} \text{ eV}^2$  [21]. However, in recent years, several experimental “anomalies” have been reported which, if experimentally confirmed, could be hinting at the presence of additional neutrino states with larger mass-squared differences participating in the mixing [22].

Two distinct classes of anomalies pointing at additional physics beyond the Standard Model in the neutrino sector have been reported, namely *a*) the apparent disappearance signal in low energy electron anti-neutrinos from nuclear reactors beyond the expected  $\theta_{13}$  effect [23] (the “reactor anomaly”) and from Mega-Curie radioactive electron neutrino sources in the Gallium experiments [24, 25] originally designed to detect solar neutrinos (the “Gallium anomaly”), and *b*) evidence for an electron-like excess in interactions coming from muon neutrinos and anti-neutrinos from particle accelerators [26–29] (the “LSND and MiniBooNE anomalies”). None of these results can be described by oscillations between the three Standard Model neutrinos and, therefore, could be suggesting important new physics with the possible existence of at least one fourth non-standard neutrino state, driving neutrino oscillations at a small distance, with typically  $\Delta m_{new}^2 \geq 0.1 \text{ eV}^2$ .

The “reactor anomaly” refers to the deficit of electron anti-neutrinos observed in numerous detectors a few meters away from nuclear reactors compared to the predicted rates, with  $R_{\text{avg}} = N_{\text{obs}}/N_{\text{pred}} = 0.927 \pm 0.023$  [23]. The reference spectra take advantage of an evaluation of inverse beta decay cross sections impacting the neutron lifetime and account for long-lived radioisotopes accumulating in reactors [30, 31]. Recent updates have changed the predictions slightly giving a ratio  $R_{\text{avg}} = 0.938 \pm 0.023$ , a  $2.7\sigma$  deviations from unity [32]. Moreover, some lack of knowledge of the reactor neutrino fluxes is still remaining and a detailed treatment of forbidden transitions in the reactor spectra computation may result in a few percent increase of systematic uncertainties [33]. A similar indication for electron neutrino disappearance has been recorded by the SAGE and GALLEX solar neutrino experiments measuring the calibration signal produced by intense k-capture sources of  $^{51}\text{Cr}$  and  $^{37}\text{Ar}$ . The combined ratio between the detected and the predicted neutrino rates from the sources is  $R = 0.86 \pm 0.05$ , again about  $2.7$  standard deviations from  $R = 1$  [24, 25]. Both of these deficits of low energy electron neutrinos over very short baselines could be explained through  $\nu_e$  disappearance due to oscillations at  $\Delta m^2 \geq 1 \text{ eV}^2$ .

The LSND experiment [26] at Los Alamos National Laboratory used a decay-at-rest pion beam to produce muon anti-neutrinos between 20-53 MeV about 30 m from a liquid scintillator-based detector where  $\bar{\nu}_e$  could be detected through inverse beta decay (IBD) on carbon,  $\bar{\nu}_e p \rightarrow e^+ n$ . After 5 years of data taking  $89.7 \pm 22.4 \pm 6.0$   $\bar{\nu}_e$  candidate events were observed above backgrounds, corresponding to  $3.8\sigma$  evidence for  $\bar{\nu}_\mu \rightarrow \bar{\nu}_e$  oscillations [26] occurring at a  $\Delta m^2$  in the  $1 \text{ eV}^2$  region. This signal, therefore, cannot be accommodated with the three Standard Model neutrinos, and like the other short-baseline hints for oscillations at  $L/E_\nu \sim 1 \text{ m/MeV}$ , implies new physics.

The MiniBooNE experiment at Fermilab measured neutrino interactions 540 m from the target of the Booster Neutrino Beam (BNB), a predominantly muon neutrino beam peaking at 700 MeV. Muon and electron neutrinos are identified in charged-current interactions by the characteristic signatures of Cherenkov rings for muons and electrons. In a ten year data set including both neutrino and anti-neutrino running [27–29, 34], MiniBooNE has observed a  $3.4\sigma$  signal excess of  $\nu_e$  candidates in neutrino mode ( $162.0 \pm 47.8$  electromagnetic events) and a  $2.8\sigma$

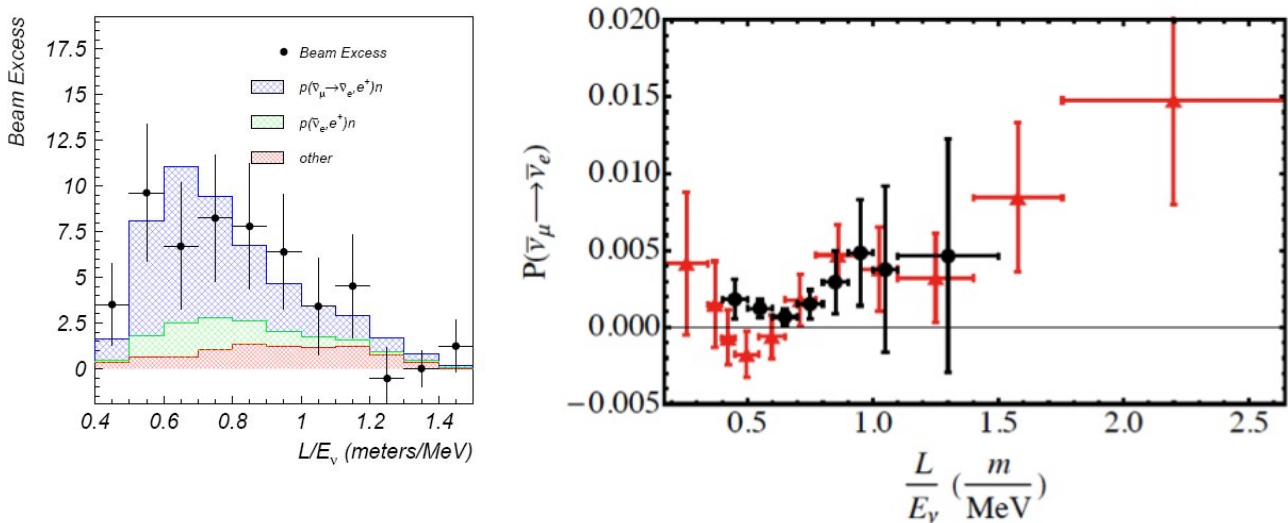


**FIG. 6:** Left: Excess of electron neutrino candidate events observed by the LSND experiment [26]. Right: Oscillation probability as a function of  $L/E_\nu$  if the excess candidate events are assumed to be due to  $\bar{\nu}_\mu \rightarrow \bar{\nu}_e$  transitions using MiniBooNE (red) and LSND (black) data.

excess of  $\bar{\nu}_e$  candidates in anti-neutrino mode ( $78.4 \pm 28.5$  electromagnetic events) as shown in Figure 7. Figure 6 compares the  $L/E_\nu$  dependence of the MiniBooNE anti-neutrino events to the excess observed at LSND. The excess events can be electrons or single photons since these are indistinguishable in MiniBooNE’s Cherenkov imaging detector. MicroBooNE will address this question at the same baseline as MiniBooNE by utilizing the added capability to separately identify electrons and photons.

The most common interpretation of this collection of data is evidence for the existence of one or more additional, mostly “sterile” neutrino states with masses at or below the few eV range. The minimal model consists of a hierarchical 3+1 neutrino mixing, acting as a perturbation of the standard three-neutrino model dominated by the three  $\nu_e$ ,  $\nu_\mu$  and  $\nu_\tau$  active neutrinos with only small contributions from sterile flavors. The new sterile neutrino would mainly be composed of a heavy neutrino  $\nu_4$  with mass  $m_4$  such that the new  $\Delta m^2 = \Delta m_{41}^2$  and  $m_1, m_2, m_3 \ll m_4$  with  $\Delta m_{41}^2 \approx [0.1 - 10] \text{ eV}^2$ .

In the 3+1 minimal extension to the Standard Model, the effective  $\nu_e$  appearance and  $\nu_\mu$  disappearance probabilities are described by:

$$P_{\nu_\alpha \rightarrow \nu_\beta}^{3+1} = \delta_{\alpha\beta} - 4 |U_{\alpha 4}|^2 (\delta_{\alpha\beta} - |U_{\beta 4}|^2) \sin^2 \left( \frac{\Delta m_{41}^2 L}{4E_\nu} \right) \quad (1)$$

where  $U_{ij}$  are elements of the now  $4 \times 4$  mixing matrix and  $L$  is the travel distance of the neutrino of energy  $E_\nu$ . The interpretation of both the LSND and MiniBooNE anomalies in terms of light sterile neutrino oscillations requires mixing of the sterile neutrino with both electron and muon neutrinos. Constraints on sterile neutrino mixing from  $\nu_\mu$  and neutral-current disappearance data are also available [42–46]. An explanation of all the available observations in terms of oscillations suffers from significant tension between appearance and disappearance data, particularly due to the absence of  $\nu_\mu$  disappearance in the  $\Delta m^2 \sim 1 \text{ eV}^2$  region. Many global analyses of experimental results have been performed fitting to models including one or more sterile neutrinos. Figure 8 shows two recent examples [40, 41] of fits to a 3+1 model which indicate similar allowed parameter regions in the  $\Delta m_{41}^2 \approx [0.2 - 2] \text{ eV}^2$  range

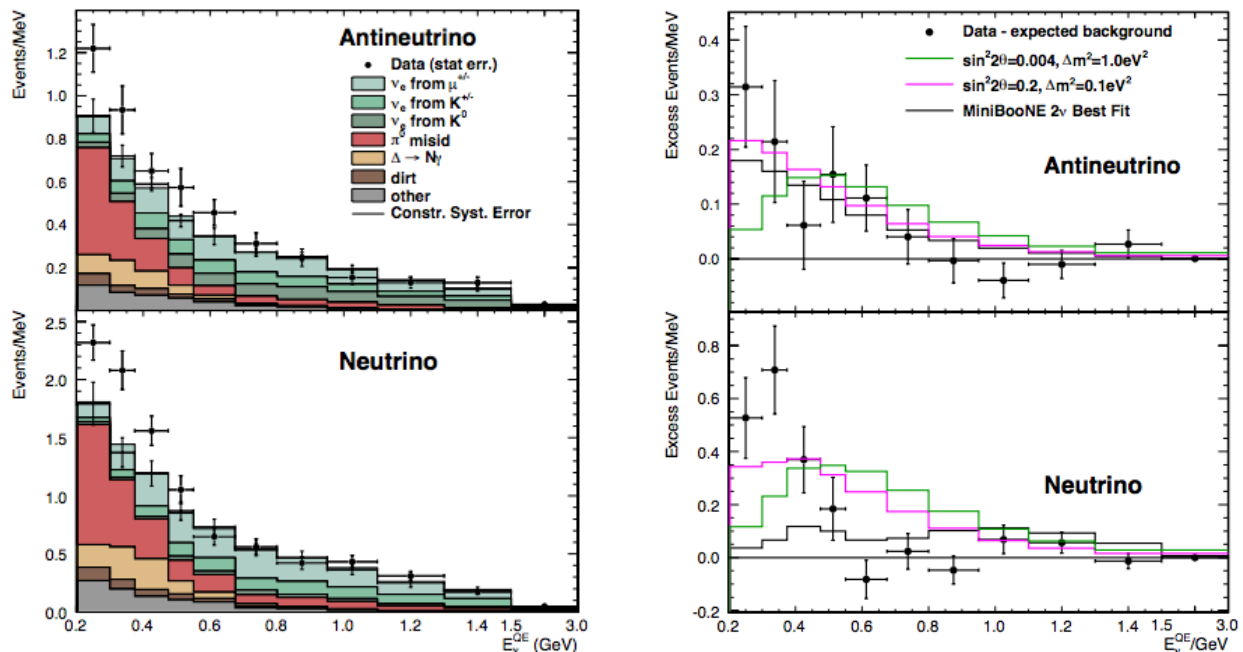


**FIG. 7:** Left:  $\bar{\nu}_e$  (top) and  $\nu_e$  (bottom) candidate events and predicted backgrounds showing the observed excesses in the MiniBooNE data. Right: background subtracted event rates in the MiniBooNE anti-neutrino (top) and neutrino (bottom) data [29].  $E_\nu^{QE}$  refers to the reconstructed neutrino event energy, where a quasi-elastic interaction is assumed in the reconstruction.

when considering available  $\nu_e/\bar{\nu}_e$  appearance data. Later, in Section II A, we will compare SBN sensitivity predictions to the original LSND allowed region and the allowed parameter space in the global data fit from Kopp et al. [41] (the red combined region from Figure 8, right) and Giunti et al. [40] (the green combined region from Figure 8, center).

An important contribution to the sterile neutrino search has already been made using the ICARUS-T600 detector running in the underground INFN-LNGS Gran Sasso Laboratory and exposed to the CERN to Gran Sasso (CNGS) neutrino beam [9]. Although not testing fully the relevant space of oscillation parameters, ICARUS results, corroborated by the OPERA experiment [47], limit the window for the LSND anomaly to a narrow region around  $\Delta m^2 \sim 0.5 \text{eV}^2$  and  $\sin^2 2\theta \sim 0.005$  [39, 48]. In this region, there is overall agreement between the present ICARUS limit, the limit from the KARMEN experiment [35], and the positive signals of LSND and MiniBooNE.

#### D. The Current Experimental Landscape

Given the importance of a sterile neutrino discovery, it is clear that the existing anomalies must be explored further by repeating the existing measurements in an effective way capable of addressing the oscillation hypothesis and many experiments are setting out to explore it [49].

New reactor experiments searching for oscillations with  $L/E_\nu \sim 1 \text{m/MeV}$  are in preparation aiming to detect an oscillation pattern imprinted in the energy distribution of events. Experimentally the detection technique relies on the IBD reaction,  $\bar{\nu}_e p \rightarrow e^+ n$ , where the positron carries out the  $\bar{\nu}_e$  energy and tagging the neutron provides a discriminant signature against

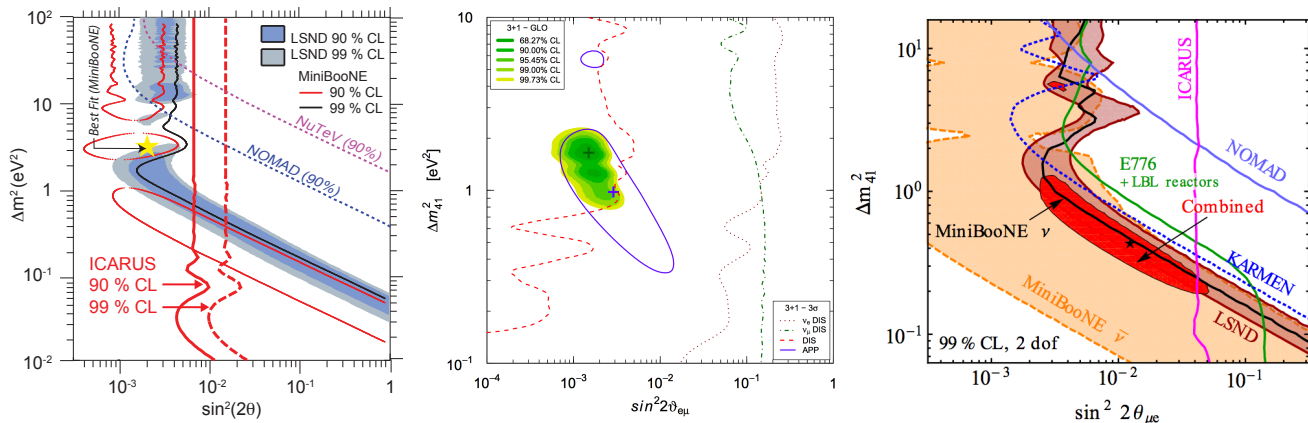


**FIG. 8:** (Left) The main published experimental results sensitive to  $\nu_\mu \rightarrow \nu_e$  at large  $\Delta m^2$  [26–29, 35–38] including the present ICARUS limit [39] from the run in Gran Sasso. Global analysis of short-baseline neutrino results from Giunti et al. [40] (center) and Kopp et al. [41] (right). The blue closed contour on the left and the red solid area on the right are the allowed parameter regions for  $\nu_\mu^{(-)} \rightarrow \nu_e^{(-)}$  appearance data and both indicate preferred  $\Delta m_{41}^2$  values in the  $\sim [0.2\text{--}2]$  eV<sup>2</sup> range.

backgrounds. The backgrounds from radioactive contaminants or induced by the reactor core and by cosmic rays can partially be suppressed through passive shielding while the remaining contribution can be measured in-situ at the analysis stage. The Nucifer experiment [50] at the Osiris nuclear reactor in Saclay could provide first new constraints by 2015. The Stereo experiment [51] will be constructed next to the ILL reactor in Grenoble, France. The DANSS [52] and Neutrino4 [53] experiments are under construction in Russia and should provide first data in 2015. Finally, comprehensive projects for searching for sterile neutrinos at reactors in China [54] and the US [55] are currently under study. All these experiments are designed to test the space of oscillation parameters deduced from the interpretation of the reactor anti-neutrino deficits.

New projects aiming to search for evidence of oscillations using neutrinos from intense radioactive sources have also been proposed. The SOX experiment [56] will perform such a measurement with a 10 MCi <sup>51</sup>Cr source deployed at 8.25 m from the center of the Borexino detector in 2017. At Baksan a 3 MCi <sup>51</sup>Cr source could be placed at the center of a target, containing 50 tons of liquid metallic gallium divided into two areas, an inner 8 ton zone and an outer 42 ton zone. The ratio of the two measured capture rates to its expectation could signify an oscillation. This is a well-proven technique free of backgrounds, developed for the SAGE solar neutrino experiment. The CeLAND and CeSOX projects plan to use 100 kCi of <sup>144</sup>Ce in KamLAND [57, 58] and Borexino [56, 57] to produce an intense anti-neutrino flux which can be detected through the inverse beta decay process. The goal is to deploy the <sup>144</sup>Ce radioisotope about 10 m away from the detector center and to search for an oscillating pattern in both event spatial and energy distributions that would determine neutrino mass differences and mixing angles unambiguously. The CeSOX experiment could take data as early as the end of 2015 at LNGS with Borexino.

A new neutrino,  $\nu_4$ , heavier than the three active neutrinos should be detected in the KATRIN experiment [59]. The detector aims at measuring precisely the high energy tail of the tritium  $\beta$ -decay spectrum by combining an intense molecular tritium source with an integrating high-resolution spectrometer reaching a 200 meV sensitivity on the effective electron neutrino

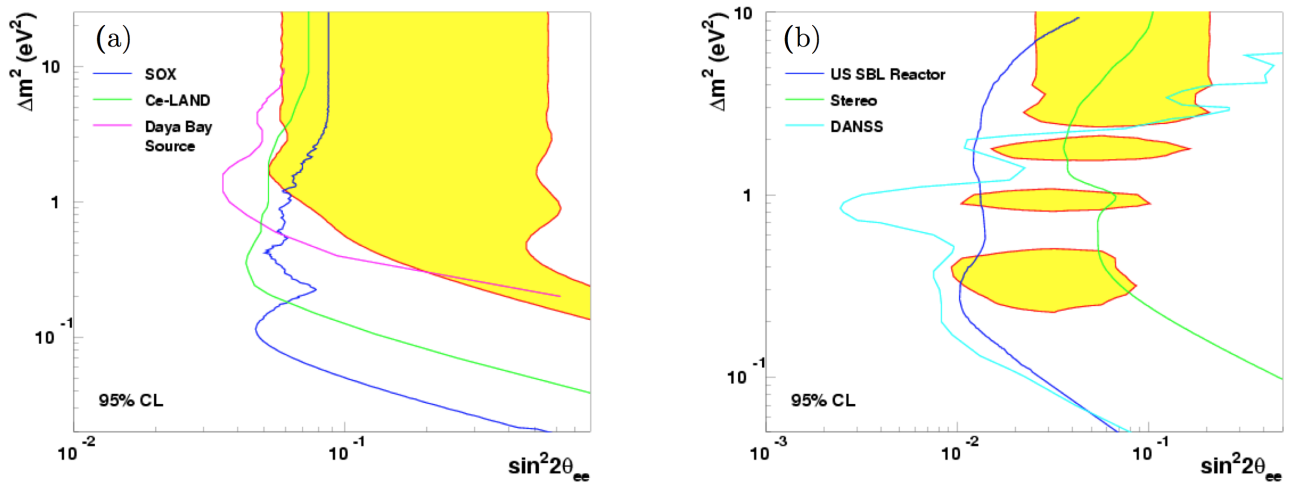


**FIG. 9:** Expected sensitivity curves at 95% C.L. for proposed neutrino experiments with radioactive sources (a) and reactors (b) with the global fits to the existing gallium and reactor data (yellow regions) [64].

mass at 90% C.L. The detection principle for a new sterile neutrino state is to search for a distortion at the high energy endpoint of the electron spectrum of tritium  $\beta$ -decay, since its shape is *a priori* very precisely understood. The KATRIN experiment can probe part of the current allowed region of the reactor anti-neutrino anomaly, especially for  $\Delta m_{new}^2 > 1 \text{ eV}^2$ , with 3 years of data-taking [60, 61]. First results are expected in 2016.

As a long term project, a huge statistics of  $\bar{\nu}_e \rightarrow \bar{\nu}_\mu$  from the  $\beta$ -decay of  $^8\text{Li}$  could be obtained through the development of a high-power low energy cyclotron. The IsoDAR project [62] proposes to place such a device underground in the Kamioka mine to search for an oscillation pattern in the KamLAND detector. This would be a disappearance experiment directly testing both the reactor and the gallium anomalies starting from a well known  $\bar{\nu}_\mu$  spectrum.

The OscSNS project [63] proposes to locate an 800-ton gadolinium-doped scintillator detector 60 m away from the Spallation Neutron Source (SNS) at the Oak Ridge National Laboratory in order to directly test the LSND results. This kind of facility has the advantage of producing a well-understood source of electron and muon neutrinos from  $\pi^+$  and  $\mu^+$  decays-at-rest. The main search channel would be the appearance of  $\bar{\nu}_e$ , taking advantage of the low duty factor of SNS to reduce cosmic induced backgrounds.

A precision sterile neutrino search has been proposed with a clean and well-understood beam of  $\nu_e$  and  $\bar{\nu}_\mu$  produced in a low energy neutrino factory by the decay of stored muons both at CERN [65] and Fermilab [66] by the nuSTORM project. Such a neutrino beam could be used to probe both appearance and disappearance processes including the golden channel of  $\nu_\mu$  appearance in a muon-free electron neutrino beam, which is not possible in a meson decay-in-flight beam.

However, considering the present experimental scenario, an accelerator-based neutrino beam facility provides the best opportunity for a rich oscillation research program with a single experiment, where the existence of an oscillation signal in  $\nu_e$  appearance and disappearance modes as well as  $\nu_\mu$  disappearance can be simultaneously investigated. Neutrino or anti-neutrino beams can be produced in the same experiment and, at accelerator beam energies, both charged-current and neutral-current channels can be explored. This is the approach of the short-baseline neutrino oscillation program on the FNAL Booster Neutrino Beam proposed here. MicroBooNE

is blazing the trail on the BNB with liquid argon technology now, but the challenge of predicting absolute neutrino fluxes in accelerator beam experiments and the large uncertainties associated with neutrino-nucleus interactions, strongly motivate the use of multiple detectors at different baselines to reduce systematic uncertainties in the search for oscillations. The anomalous short-baseline results discussed in Section IC may be hinting at neutrinos oscillating with an amplitude 10 to 100 times *smaller* than the  $\theta_{13}$  signals in experiments like Daya Bay, T2K, or MINOS, all multiple detector experiments. The Fermilab SBN Program, using detectors at different distances from the BNB source, will cover at high confidence level the entirety of the sterile neutrino parameter space suggested by the anomalies.

Finally, the observed set of anomalous results in neutrino physics call for conclusive new experiments capable of exploring the indicated parameter regions in a definitive way and to clarify the possible existence of eV-scale sterile neutrinos. The accelerator-based short-baseline program presented in this proposal is the only means of testing the sterile neutrino picture through multiple channels in a single beam.

## II. SBN Oscillation Searches

Multiple LAr-TPC detectors at different baselines along the BNB will allow a very sensitive search for high- $\Delta m^2$  neutrino oscillations in multiple channels. These searches constitute the flagship measurements of the SBN program, and so we dedicate this section to a careful and detailed description of the sensitivity analysis for  $\nu_\mu \rightarrow \nu_e$  appearance and  $\nu_\mu \rightarrow \nu_x$  disappearance.

This section is organized into subsections as follows. In Section IIA we provide a mathematical description of the analysis methods used to calculate the sensitivities. In Section IIB we describe the procedures for selecting events for the  $\nu_\mu$  and  $\nu_e$  analyses and characterize in-detector intrinsic beam-related backgrounds to each. In Sections IIC and IID we present the systematic uncertainties impacting these predictions related to the neutrino fluxes and neutrino interaction model, with particular emphasis on the correlations between different detector locations that enable the increased sensitivity of a multi-detector experiment. Section IIE discusses detector related systematic uncertainties. Section IIF deals with out-of-detector but beam-induced backgrounds; these include neutrino interactions in the earth surrounding each detector building, hence we often refer to this category as “dirt” events, though interactions in the the building, cryostat, and inactive argon surrounding the TPC which deposit energy in the detector are all included. In IIG we discuss cosmogenic backgrounds and the strategies to mitigate them. Both the dirt and cosmogenic backgrounds only affect the  $\nu_e$  analysis. Finally, we bring it all together and present the oscillation sensitivities of the SBN program to  $\nu_\mu \rightarrow \nu_e$  appearance and  $\nu_\mu \rightarrow \nu_x$  disappearance in Sections IIH and III, respectively.

### A. Analysis Methods

The sensitivity of the SBN program will be demonstrated using the commonly assumed framework of three active and one sterile neutrino, or a “3+1 model”, as our baseline for evaluation. Of course, other models could be assumed, such as those with multiple sterile states, but this choice provides a straight-forward way to compare to previous experimental

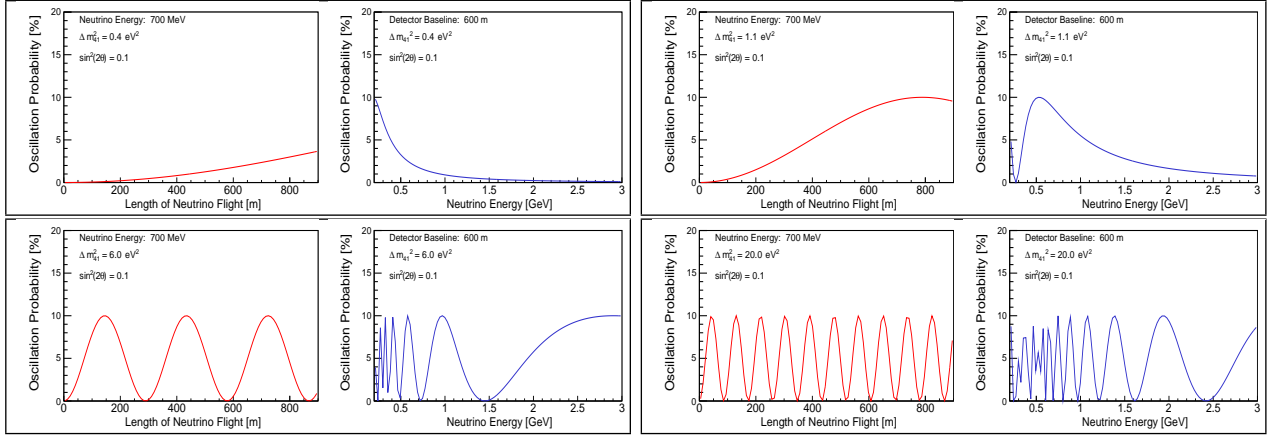


**FIG. 10:** Illustrations of the oscillation probability at SBN for four different values of  $\Delta m^2$  and  $\sin^2 2\theta = 0.1$  in a 3+1 sterile neutrino model:  $\Delta m^2 = 0.4 \text{ eV}^2$  (upper left),  $1.1 \text{ eV}^2$  (upper right),  $6 \text{ eV}^2$  (lower left), and  $20 \text{ eV}^2$  (lower right). In each panel, the left red curve shows the evolution of the probability with distance at a fixed energy ( $E_\nu = 700 \text{ MeV}$ ). The right blue curve shows the probability versus energy at a fixed location (600 m, the ICARUS-T600 location).

results as well as to global data fits that were analyzed using the 3+1 model<sup>1</sup>. In the 3+1 model, the effective oscillation probabilities are described by Eq. 1, reproduced here explicitly for  $\nu_e$  appearance ( $\nu_\mu \rightarrow \nu_e$ ) and  $\nu_\mu$  disappearance ( $\nu_\mu \rightarrow \nu_\mu$ ):

$$P_{\nu_\mu \rightarrow \nu_e}^{3+1} = \sin^2 2\theta_{\mu e} \sin^2 \left( \frac{\Delta m^2 L}{4E_\nu} \right) \quad P_{\nu_\mu \rightarrow \nu_\mu}^{3+1} = 1 - \sin^2 2\theta_{\mu\mu} \sin^2 \left( \frac{\Delta m^2 L}{4E_\nu} \right)$$

with  $L$  the propagation length of the neutrino and  $E_\nu$  the neutrino energy,  $\sin^2 2\theta_{\mu e} \equiv 4|U_{\mu 4}U_{e 4}|^2$  is an effective mixing amplitude that depends on the amount of mixing of both  $\nu_\mu$  and  $\nu_e$  with mass state  $\nu_4$ , and  $\sin^2 2\theta_{\mu\mu} \equiv 4|U_{\mu 4}|^2(1 - |U_{\mu 4}|^2)$  only depends on the amount of  $\nu_\mu - \nu_4$  mixing. In our standard picture, any observation of  $\nu_e$  appearance due to oscillations must be accompanied by some amount of  $\nu_\mu$  disappearance as well as for the similar  $\nu_e$  disappearance.

Figure 10 illustrates the shape of the oscillation probability in the SBN experiments for four different possible values of  $\Delta m^2$  ( $\sin^2 2\theta = 0.1$ ). The red curves show the evolution of the oscillation probability with distance for a fixed neutrino energy,  $E_\nu = 700 \text{ MeV}$ , while the blue curves demonstrate the oscillation probability across the full BNB neutrino energy range at the far detector location, 600 m. From the top row ( $0.4 \text{ eV}^2$  and  $1.1 \text{ eV}^2$ ), one can clearly see why the sensitivity increases with  $\Delta m^2$  up to and a little beyond  $1 \text{ eV}^2$  as the oscillation probability at 600 m increases but also shifts toward the peak of the BNB flux. Also, note that the level of signal at the near detector location (110 m) is very small, making the near detector measurement an excellent constraint on the intrinsic beam content. For  $\Delta m^2$  much larger than  $1 \text{ eV}^2$ , as we see in the bottom row ( $6 \text{ eV}^2$  and  $20 \text{ eV}^2$ ), the oscillation wavelength becomes short compared to the 600 m baseline. As a function of energy in *all* detectors, the oscillations are rapid in neutrino energy and one observes an overall excess (or deficit) at all energies equal to half the

<sup>1</sup>Of course, what we would like to know is the general ability of the experiment to observe either an excess or a deficit relative to the expectation in the absence of any oscillation. In a sense, the 3+1 sensitivity contains this information, but for many different possible distributions of the signal events across the observed energy spectrum.



value of  $\sin^2 2\theta$ . Therefore, at high  $\Delta m^2$ , the near detector is also contaminated with signal and absolute normalization uncertainties become important in determining the sensitivity.

The sensitivity is calculated by computing a  $\chi^2$  surface in the  $(\Delta m_{41}^2, \sin^2 2\theta)$  oscillation parameter plane according to:

$$\chi^2(\Delta m_{41}^2, \sin^2 2\theta) = \sum_{i,j} [N_i^{null} - N_i^{osc}(\Delta m_{41}^2, \sin^2 2\theta)] (E_{ij})^{-1} [N_j^{null} - N_j^{osc}(\Delta m_{41}^2, \sin^2 2\theta)] \quad (2)$$

where  $N_i^{null}$  is the expected event distribution in the absence of oscillations and  $N_i^{osc}(\Delta m_{41}^2, \sin^2 2\theta)$  is the event prediction for an oscillation signal determined by Eq. 1 with mass splitting  $\Delta m_{41}^2$  and amplitude  $\sin^2 2\theta$ . The labels  $i$  and  $j$  indicate bins of reconstructed neutrino energy. Uncertainties, both statistical and systematic, are encoded in the covariance matrix,  $E_{ij}$ . From this surface, sensitivity contours at different confidence levels (C.L.)<sup>2</sup> can be identified based on the  $\chi^2$  values relative to the overall minimum value. We devote the next five Sections to describing how we estimate the background event vectors  $N_i^{null}$  and the covariance matrices  $E_{ij}$  for the  $\nu_e$  appearance and  $\nu_\mu$  disappearance analyses.

The total systematic covariance matrix is a combination of independent matrices constructed for each of the systematic uncertainties considered:

$$E^{syst} = E^{flux} + E^{cross\ section} + E^{cosmic\ bkgd} + E^{dirt\ bkgd} + E^{detector} \quad (3)$$

and  $E^{total} = E^{stat} + E^{syst}$  where  $E^{stat}$  is the completely uncorrelated statistical error matrix,  $E_{ii}^{stat} = N_{ii}^{null}$ . The flux and neutrino cross section covariance matrices are calculated using detailed Monte Carlo simulations based on GEANT4 and the GENIE neutrino event generator, respectively. Reweighting techniques are used to construct possible variations on the event distributions due to uncertainties on the underlying parameters in the models.  $\mathcal{N}$  such ‘‘universes’’ can be combined to construct the covariance matrix:

$$E_{ij} = \frac{1}{\mathcal{N}} \sum_{m=1}^{\mathcal{N}} [N_{CV}^i - N_m^i] \times [N_{CV}^j - N_m^j], \quad (4)$$

where  $i$  and  $j$  correspond to neutrino energy bins *across all three detectors*,  $N_{CV}$  is the number of entries in each energy bin of the nominal event distribution, and  $N_m$  is the number of entries in the  $m^{th}$  ‘‘universe’’.  $E_{ij}$  is the total covariance matrix, sometimes called the total error matrix, with matrix element units of (events)<sup>2</sup>. The fractional covariance matrix is generally a more useful result and is defined as

$$F_{ij} = \frac{E_{ij}}{N_{CV}^i N_{CV}^j}. \quad (5)$$

From  $E_{ij}$  can also be extracted the correlation matrix,

$$\rho_{ij} = \frac{E_{ij}}{\sqrt{E_{ii}} \sqrt{E_{jj}}} \quad [-1 \leq \rho \leq 1], \quad (6)$$

where  $\rho_{ij}$  describes the level of correlation between bins  $i$  and  $j$  of the neutrino energy distributions.

<sup>2</sup> $\Delta\chi_{90}^2 = 1.64$ ,  $\Delta\chi_{3\sigma}^2 = 7.74$ , and  $\Delta\chi_{5\sigma}^2 = 23.40$  corresponding to a one-sided, one degree of freedom  $\Delta\chi^2$  cut.

The flux and cross section error matrices have been constructed according to Eq. 4, while the cosmic background and dirt background error matrices are constructed differently as will be explained in the relevant Sections below.

### B. $\nu_e$ and $\nu_\mu$ Signal Selection

We begin with a discussion of beam-induced neutrino interactions within the TPC active volumes that are selected when isolating  $\nu_e$  and  $\nu_\mu$  charged-current events samples for analysis.

#### *Electron Neutrino Charged-Current Candidates*

Electron neutrino event candidates include intrinsic  $\nu_e$  charged-current (CC) interactions as well as other beam-related (mostly  $\nu_\mu$ -induced) mis-identification backgrounds. The event selection algorithms are given below and are applied identically to all three detectors in the analysis. A full GEANT simulation of GENIE produced neutrino interactions in argon is used and selections are made based on predicted event kinematics. As a cross-check, neutrino interactions in the ICARUS-T600 detector have been also independently simulated using FLUKA[67–69], and consistent results were found. The efficiencies applied to different event types are based on inputs from other simulation results, hand-scanning studies of both simulated and real events in different detectors, and analysis results from LAr-TPC experiments (e.g. ICARUS, ArgoNeuT).

1. **Intrinsic/Signal  $\nu_e$  CC** :  $\nu_e$  charged-current interactions producing an electron with  $E_e > 200$  MeV are accepted with an assumed 80% identification efficiency (after fiducial volume selection) in our baseline sensitivity analysis. The 200 MeV shower threshold is applied to ensure good event reconstruction and identification. The simulation estimates this requirement sacrifices  $\sim 30\%$  of the events in the 200-350 MeV reconstructed neutrino energy bin and less than 5% above 350 MeV. It must be noted, however, that the threshold for analysis of events in LAr should be well below this and lower energy events will be studied in the SBN experiments. The 80% efficiency is informed by hand-scanning exercises of simulated events in LAr-TPCs and significant effort is currently on-going to verify this performance with automated reconstruction algorithms. Stricter requirements on  $\nu_e$  CC event selection have been discussed in the context of rejecting cosmogenic backgrounds (such as requiring hadronic activity at the vertex, a clear indicator of a  $\nu + N$  interaction), but other handles on cosmogenic event rejection will likely deem this unnecessary (see Section II G). Also, selection efficiencies can depend on specific detector performance parameters. For instance, scanning exercises in the ICARUS detector indicate that the efficiency for recognizing isolated electron showers after the vertex is reduced by  $\sim 12\%$  if only one 2-D view (collection) out of three is available for a complete event reconstruction (e.g. due to low signal-to-noise in the induction views). It will be important to carefully monitor such effects. Selected intrinsic  $\nu_e$  CC candidates are shown in the green histograms in Figure 11.
2. **NC  $\gamma$  production** : Photons creating a shower above the 200 MeV selection threshold can fake the  $\nu_e$  CC signature described above. For example, neutral-current interactions with any number of  $\pi^0$  in the final state or radiative resonance decays are sources of such  $\gamma$ 's. These events are analyzed according to the following criteria:

- Second photon cut: If the second photon from a  $\pi^0$  decay (with  $E_\gamma > 100$  MeV as an observation threshold) converts within the TPC active volume, the event is rejected.
- Conversion gap cut: If the neutrino interaction is inside the active volume and produces more than 50 MeV of charged hadronic activity at the vertex, then the vertex is deemed visible. With a visible vertex, if all photon showers convert more than 3 cm from that vertex, the event is rejected.
- $dE/dx$  cut: For events passing the previous two cuts, a 94% photon rejection rate is applied, corresponding to the expected power of separating  $e/\gamma$  showers in the LAr-TPC using the energy deposited in the first few centimeters of an electromagnetic shower.

Beam-related photon backgrounds are shown as the orange histograms in Figure 11 labeled “NC Single  $\gamma$ ”.

3.  $\nu_\mu$  **CC** :  $\nu_\mu$  charged-current interactions with an identified primary electromagnetic (e.m.) shower within the fiducial volume could also be mis-identified as  $\nu_e$  interactions if the muon is not identified. Minimum ionizing tracks longer than 1 m in BNB events are essentially all muons, so events with  $L_\mu \geq 1$  m are rejected. Events with  $L_\mu < 1$  m and a single e.m. shower attached to the CC event vertex could be identified as a  $\mu + \gamma$  ( $\nu_\mu$  CC) or  $\pi + e$  ( $\nu_e$  CC) final state. We, therefore, check for the presence of candidate e.m. showers in  $\nu_\mu$  CC interactions following the same criteria as for NC  $\gamma$  events described above, and if not rejected we retain the event as a background for the  $\nu_e$  CC sample. These are represented by the blue histograms in Figure 11.
4. **Neutrino Electron Scattering** : Neutrinos can scatter off an orbiting electron in an atom, ejecting the electron at high energy. Experimentally, the signature is a very forward going electron and nothing else in the event, which mimics a  $\nu_e$  charged current interaction and will be selected with the same efficiency. However, the  $\nu + e$  cross section is very low and so forms a secondary background. These are too small to be seen in Figure 11 but are included in the analysis.

For estimating these background rates, the full GEANT simulation of events is of fundamental importance. By analyzing the conversion points of photons instead of just the true neutrino interaction vertex, we accurately account for acceptance effects in the differently shaped detectors. Because the  $e/\gamma$  separation is performed entirely with the first few centimeters of a shower, differences in total shower containment do not affect the assumption that the photon identification efficiency should be the same in each detector.

To simulate calorimetric energy reconstruction, the incoming neutrino energy in each Monte Carlo event is estimated by summing the energy of the lepton (or the  $\gamma$  faking an electron) and all charged hadrons above observation thresholds present in the final state. This approach is used in the analysis of both  $\nu_e$  and  $\nu_\mu$  charged-current events described next. It should be noted that this method is one possible approach to estimating the neutrino energy. The liquid argon TPC technology enables a full calorimetric reconstruction, but other methods can be used as well, such as isolating charged-current quasi-elastic (CCQE) events and assuming QE kinematics. The ability to apply complementary approaches to event identification and energy reconstruction will provide valuable cross checks of the measurements performed. The stacked beam-related backgrounds to the  $\nu_e$  analysis are summarized in Figure 11 as a function of the calorimetric reconstructed energy for each of the SBN detectors. Event totals for each background class are tabulated later in Section II H in Table IX.

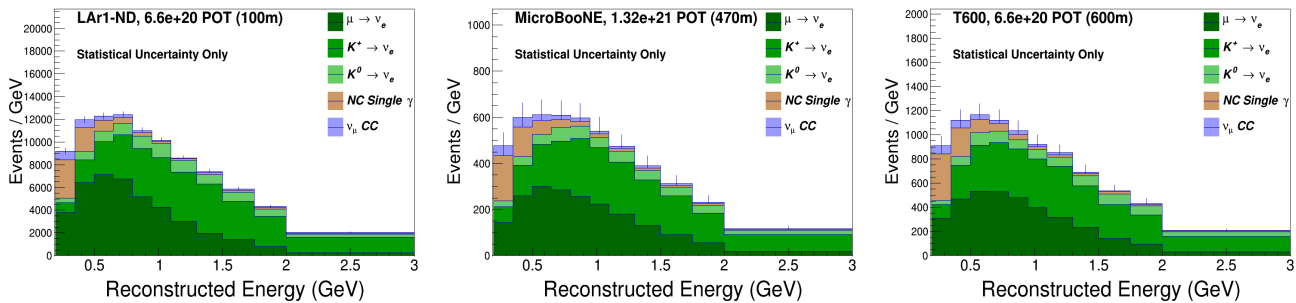


**FIG. 11:** Beam-related electron neutrino charged-current candidate events in LAr1-ND (left), MicroBooNE (center), and ICARUS-T600 (right). Statistical uncertainties only are shown. Data exposures are indicated on the plots and assume inclusion of the full MicroBooNE data set.

### Muon Neutrino Charged-Current Candidates

Muon neutrino charged-current events are selected assuming an 80% reconstruction and identification efficiency (after fiducial volume selection). The only background contribution considered comes from neutral-current charged pion production, where the  $\pi^\pm$  can be mistaken for a  $\mu^\pm$ . Simulations show pion tracks produced in the BNB are short with most charged pions traveling less than half a meter in the liquid argon. We therefore apply a simple cut requiring muon candidates that stop in the TPC active volume to be longer than 50 cm which minimizes the NC contamination in the  $\nu_\mu$  CC selection. The resulting contamination from NC events is shown in Figure 12 and has a negligible impact on the oscillation sensitivity. More sophisticated methods to separate pions and muons stopping in LAr are being explored, but this selection is sufficient for the current analysis.

Measurement resolutions have been introduced for this analysis by smearing both the reconstructed muon energy and hadron energy in the event and  $E_\nu = E_\mu + E_{\text{had-visible}}$ . The smearing of the muon energy changes depending on if the muon is fully contained within the active volume or if it exits the active volume and the energy must be estimated via the multiple scattering of the track. We require, therefore, all exiting tracks to have a minimum track length of 1 m in the active volume to enable this multiple scattering measurement with sufficient resolution. The distributions of selected muon neutrino charged-current events in each detector are shown in Figure 12.

### C. Neutrino Flux Uncertainties

BNB neutrino flux predictions and related systematic uncertainties are assessed using a detailed Monte Carlo program developed by the MiniBooNE Collaboration [13]. In the simulation, charged pion production is constrained using dedicated 8 GeV  $p$ +Be hadron production data from the HARP experiment [14] at CERN. Neutral kaon production has been constrained by BNL E910 data [70] and a measurement made at KEK by Abe et al. [71].  $K^+$  production uncertainties are set by measurements made with the SciBooNE [72] detector when it ran in the BNB. In total, the BNB Monte Carlo treats systematic uncertainties related to the following sources:

- Primary production of  $\pi^+$ ,  $\pi^-$ ,  $K^+$ ,  $K^-$ , and  $K_L^0$  in  $p$ +Be collisions at 8 GeV;

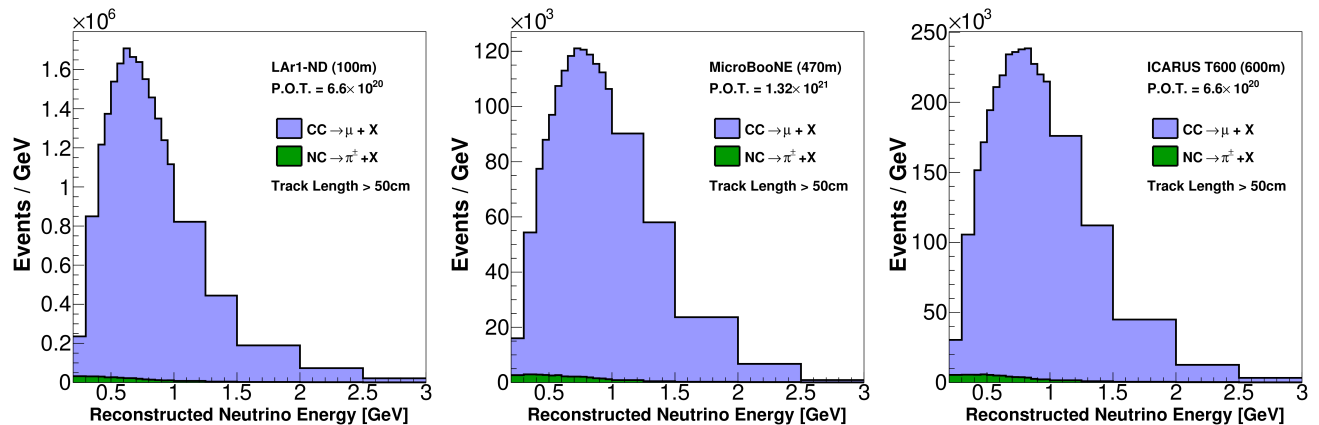


**FIG. 12:** Selected muon neutrino charged-current inclusive candidate events in LAr1-ND (left), MicroBooNE (center), and the ICARUS-T600 (right). Final state muon tracks that are fully contained in the TPC volume are required to travel greater than 50 cm. Muons which exit the active detectors are required to travel  $> 1$  m before exiting. Statistical uncertainties only are shown. Data exposures are indicated on the plots and assume inclusion of the full MicroBooNE data set.

- Secondary interactions of  $p$ ,  $n$ ,  $\pi^\pm$  in the beryllium target and aluminum horn;
- Beam focusing with the magnetic horn.

Primary hadron production uncertainties, whenever available, are taken directly from the measured cross sections which are used to constrain the Monte Carlo. In particular, in the case of  $\pi^+$  and  $\pi^-$  production, the experimental uncertainties reported by the HARP experiment [14, 15] are directly used to set the allowed variation within the beamline simulation.

Secondary interaction uncertainties are also evaluated. Table II summarizes allowed variations on hadron-Be and hadron-Al cross sections in the simulation. The total cross section,  $\sigma_{\text{TOT}}$ ; the inelastic cross section,  $\sigma_{\text{INE}}$ ; and the quasi-elastic cross sections,  $\sigma_{\text{QEL}}$  are varied separately for nucleons and pions interacting with Be and Al. When we vary  $\sigma_{\text{INE}}$  and  $\sigma_{\text{QEL}}$  we fix the cross section of the other to hold the total cross section constant.

**TABLE II:** Cross section variations for systematic studies of secondary hadron interactions in the target and horn. For each hadron-nucleus cross section type, the momentum-dependent cross section is offset by the amount shown [13].

	$\Delta\sigma_{\text{TOT}}$ (mb)		$\Delta\sigma_{\text{INE}}$ (mb)		$\Delta\sigma_{\text{QEL}}$ (mb)	
	Be	Al	Be	Al	Be	Al
$(p/n)$ -(Be/Al)	$\pm 15\%$	$\pm 25\%$	$\pm 5\%$	$\pm 10\%$	$\pm 20\%$	$\pm 45\%$
$\pi^\pm$ -(Be/Al)	$\pm 11.9\%$	$\pm 28.7\%$	$\pm 10\%$	$\pm 20\%$	$\pm 11.2\%$	$\pm 25.9\%$

Beam focusing systematics include uncertainty on the magnitude of the horn current ( $174 \pm 1$  kA) as well as skin depth effects describing where the current flows on the surfaces of the horn. The skin depth effect allows the magnetic field to penetrate into the interior of the horn conductor which in turn creates a magnetic field within the conductor. This will lead to deflections of charged particles which traverse the conductor, especially higher energy particles

**TABLE III:** *Variations in the total flux of each neutrino species in neutrino mode due to the systematic uncertainties [13].*

Source of Uncertainty	$\nu_\mu$	$\nu_e$
$\pi^+$ production	14.7%	9.3%
$\pi^-$ production	0.0%	0.0%
$K^+$ production	0.9%	11.5%
$K^0$ production	0.0%	2.1%
Horn field	2.2%	0.6%
Nucleon cross sections	2.8%	3.3%
Pion cross sections	1.2%	0.8%

which do not penetrate deeply into the horn conductor. The effect can be approximated by modeling an exponentially decreasing field to a depth of about 1.4 mm. To assess the systematic, the field is turned on and off, which leads to an energy dependent effect of 1 to 18% for particles of  $< 1$  GeV to 2 GeV, respectively [13].

We currently don't assess a systematic on hadron interactions with material downstream of the horn (including air, concrete, steel, etc.). These effects have been studied and found to contribute about 1% (2%) to the  $\nu_\mu$  ( $\nu_e$ ) fluxes, so even a large 50% uncertainty would make a negligible contribution to the total errors.

Table II reports the contributions of the underlying systematics to the integrated  $\nu_\mu$  and  $\nu_e$  fluxes along the BNB, revealing total normalization uncertainties of order 15% on both absolute predictions.

Using Eq. 4 we compute the covariance matrix for all the systematic variations in the flux model. The fractional error matrix and flux correlation matrix are shown in Figure 13. We see that the event rates at different detector locations and for both  $\nu_\mu$  and  $\nu_e$  fluxes have large positive correlations. These correlations are, of course, the key to SBN sensitivity. The high statistics measurement made in the near detector, together with the high levels of correlation between the near and far locations will eliminate the large normalization uncertainty highlighted in Table II when performing oscillation searches, a critical motivation for the multi-detector SBN configuration.

#### D. Neutrino Interaction Uncertainties

Uncertainties in the neutrino interaction model are the largest uncertainties affecting the normalization of events in the SBN detectors, but are expected to be highly correlated between detectors because of the use of the same target nucleus (argon). Only through second order impacts of neutrino fluxes or differences in the geometric acceptance of events in the detectors can the correlations be different than 100%.

Neutrino interactions on argon are simulated using the GENIE [73] neutrino event generator. GENIE simulates each stage of the interaction including inclusive and exclusive differential cross sections off individual nucleons and the effects of the nuclear medium on final state particles as they propagate out of the target nucleus (final state interactions). Multi-nucleon correlation effects of the initial state are also a challenge in neutrino interactions and are not part of the present simulation. This is true of other available Monte Carlo packages as well. Incomplete

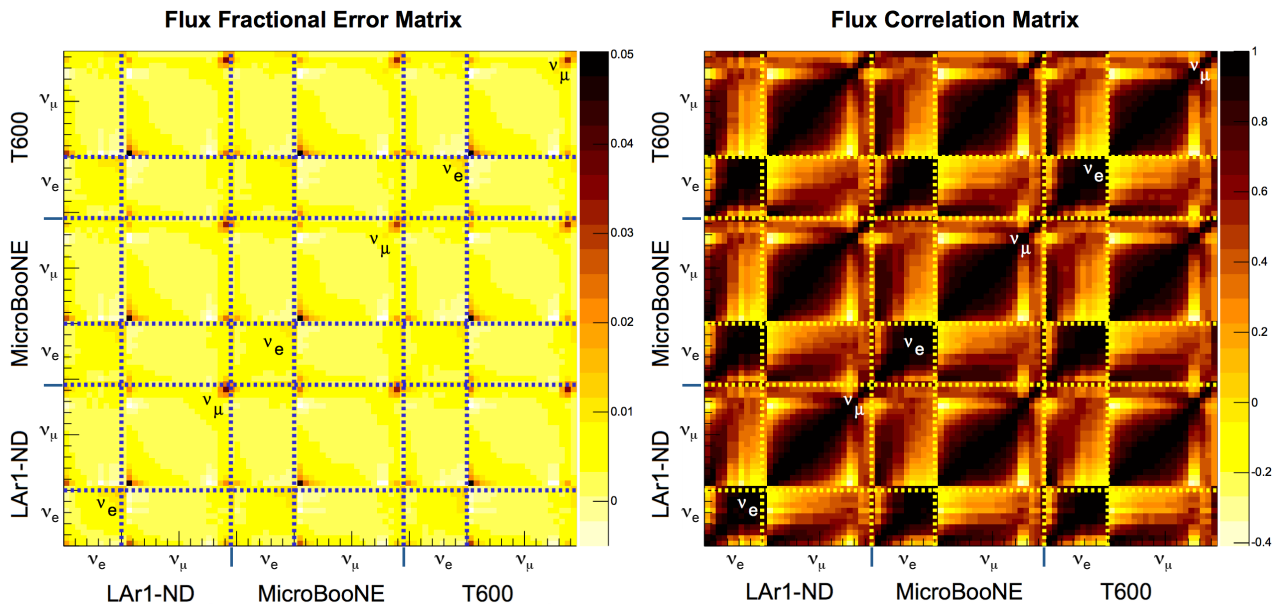


**FIG. 13:** The fractional flux covariance matrix (left) and correlation matrix (right) for the  $\nu_e$  and  $\nu_\mu$  charged-current reconstructed energy distributions. Both the  $\nu_e$  events (11 energy bins from 0.2–3 GeV) and  $\nu_\mu$  events (19 energy bins from 0.2–3 GeV) at all three detector locations are represented; the dashed lines indicate the boundaries in the matrix. For example, the lower left square marked “ $\nu_e$ ” shows the fractional error (left) and correlations (right) within the reconstructed  $\nu_e$  CC event distribution in LAr1-ND. In another example, the square four from the left and two from the bottom shows the correlations between the  $\nu_\mu$  CC event distributions in LAr1-ND and MicroBooNE.

modeling of nuclear effects can lead to biases in neutrino energy reconstruction and is a very active area of both experimental and theoretical research at the moment (see [74] and [75] and the references therein). The data sets of the SBN LAr-TPC detectors will, in fact, be very valuable for studying these effects and improving simulations.

GENIE does provide a built-in framework of event reweighting for evaluating systematic uncertainties and correlations in an analysis. Table IV lists the uncertainties used for this analysis and their nominal percent variation at  $1\sigma$ , according to the GENIE documentation. This is a partial list of the available parameters within the GENIE framework, chosen here for their relevance to the SBN oscillation searches. The analysis does not currently include an estimate of uncertainties on final state interactions.

We simulated 250 different cross section “universes” in which each of the model parameters were varied at random from a Gaussian distribution with a  $1\sigma$  spread equal to the  $1\sigma$  uncertainty in the underlying physical quantity. Much more detail is available from the GENIE manual, chapter 8 [76], on both the underlying physical uncertainties and the methodology for propagating them to observed event distributions. Figure 14 shows the RMS of the 250 simulated universes in the reconstructed neutrino energy bins used in the  $\nu_e$  and  $\nu_\mu$  analyses, indicating absolute neutrino interaction model uncertainties of 10–15%. From these variations, the cross section covariance matrix,  $E^{\text{cross section}}$ , is constructed using Eq. 4. Figure 14 shows the fractional covariance matrix and correlations for the  $\nu_e$  charged-current candidate events that were shown in Figure 11. The off-diagonal blocks of the correlation matrix indicate the correlations between events in different detectors. The diagonal elements within the off-diagonal

Parameter	Description	$1\sigma$ Uncertainty (%)
$M_A^{CCQE}$	Axial mass for CC quasi-elastic	-15%+25%
$M_A^{CCRES}$	Axial mass for CC resonance neutrino production	$\pm 20\%$
$M_A^{NCRES}$	Axial mass for NC resonance neutrino production	$\pm 20\%$
$R_{bkg}^{\nu p, CC1\pi}$	Non-resonance background in $\nu p, CC$ $1\pi$ reactions.	$\pm 50\%$
$R_{bkg}^{\nu p, CC2\pi}$	Non-resonance background in $\nu p, CC$ $2\pi$ reactions.	$\pm 50\%$
$R_{bkg}^{\nu n, CC1\pi}$	Non-resonance background in $\nu n, CC$ $1\pi$ reactions.	$\pm 50\%$
$R_{bkg}^{\nu n, CC2\pi}$	Non-resonance background in $\nu n, CC$ $2\pi$ reactions.	$\pm 50\%$
$R_{bkg}^{\nu p, NC1\pi}$	Non-resonance background in $\nu p, NC$ $1\pi$ reactions.	$\pm 50\%$
$R_{bkg}^{\nu p, NC2\pi}$	Non-resonance background in $\nu p, NC$ $2\pi$ reactions.	$\pm 50\%$
$R_{bkg}^{\nu n, NC1\pi}$	Non-resonance background in $\nu n, NC$ $1\pi$ reactions.	$\pm 50\%$
$R_{bkg}^{\nu n, NC2\pi}$	Non-resonance background in $\nu n, NC$ $2\pi$ reactions.	$\pm 50\%$
NC	Neutral current normalization	$\pm 25\%$
DIS-NuclMod	DIS, nuclear model	Model switch

**TABLE IV:** *Neutrino interaction model parameters and uncertainties. This information is reproduced here from the GENIE manual Section 8.1 [73] for convenience.*

blocks are the correlations between the same energy bins in different detectors and are seen to be near +1.0 in most cases.

### E. Detector Systematics

The response of the different detectors has to be known to a sufficient precision to maximize the experimental sensitivity and avoid introducing artificial detector effects mimicking the sought for oscillation signal. In this respect, the adoption of the same detection technique for all the different detectors and of the same operation conditions, permits to virtually cancel out the impact of the detector response uncertainty on the final measurement. Possible second order effects can arise from differences in the details of the design and implementation of the various detectors. The most relevant physical parameters like the drift field and the TPC structure should be kept as close as possible. Detector systematic effects can be generated by differences between the near and the far detectors, for example:

- The wire orientations in the TPCs;
- TPC readout electronics (shaping, sampling time, S/N ratio, general noise conditions affecting the identification/measurement efficiency);
- Residual differences in the electric drift field (absolute value and homogeneity);



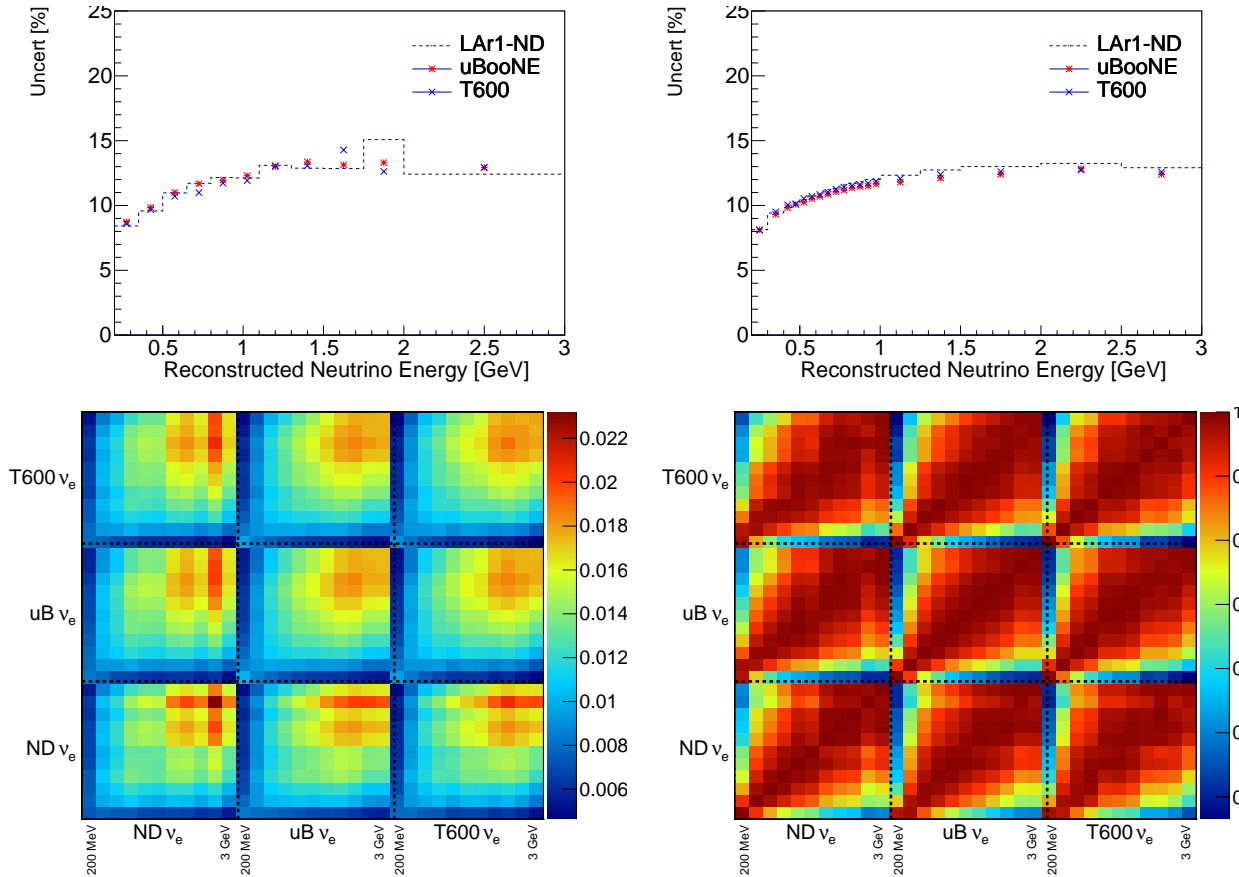


**FIG. 14:** Absolute uncertainties on  $\nu_e$  (upper left) and  $\nu_\mu$  (upper right) event rates at each of the three SBN detectors due to neutrino cross section uncertainties. (Lower left) Fractional cross section covariance matrix,  $E^{cross\ section}$ , for  $\nu_e$  CC candidate events. (Lower right) The correlation matrix for  $\nu_e$  CC candidate events. Inspection of the diagonal elements of the off-diagonal blocks shows the correlations between events in different detectors to be very near 1.0

- Residual differences in the detector calibrations including the light collection systems and the identification of off beam interactions by timing;
- LAr purity levels in the detectors;
- Different drift lengths and space charge effects;
- Residual differences in background levels from dirt events and from cosmic rays including different coverage and efficiency of the cosmic tagging systems;
- Effects induced by the different event rates at the two sites, event selection and identification efficiency including the different aspect ratios of the near and far detectors.

As an example, the impact of the different wire orientation on the electron identification efficiency has been studied with a simulation of the primary electrons produced in  $\nu_e$  CC interactions of the beam, assuming in both detectors the electronic wire signal and noise level actually measured in the T600. The effect of the different collection wire orientation between LAr1-ND and T600 turns out to be negligible on the reconstructed  $dE/dx$  distribution: a  $\sim 0.1\%$

variation in the electron identification efficiency on the first 2 cm of the track is observed in the simulation, having fixed to the same value (3.425 MeV/cm) the maximum accepted  $dE/dx$ . The corresponding multiplicity of occupied collection wires is also affected by the different wire orientations. A 3% difference in the electron identification efficiency is expected when at least 3 collection wires are required for the measurement. Conservatively, assuming to correct the angular dependence of the wire multiplicity to the 20% level using the data themselves, a residual  $< 1\%$  systematic effect in the selection efficiency is expected. This effect would be made further negligible if the induction wire signals could also be exploited in the  $dE/dx$  measurement.

A further example are electric field distortions induced by the accumulation of positive argon ions in the TPC drift volumes from the high cosmic muon fluxes in the SBN detectors located at the surface. Since the distortions depend on the drift length, which are different among the detectors, a potential detector systematic uncertainty could arise. However, today only first estimates of the absolute size of such distortions exist and thus of their affect on tracks and reconstruction. The ICARUS technical run on the surface in Pavia did not see significant track distortions. However, the effect could be more significant in LAr1-ND and MicroBooNE due to their longer drift distances. Different actions can be taken to reduce this effect. Tracks from the high rate of cosmic muons that create the effect can also be used to monitor the distortion in each detector. For the near detector, as in MicroBooNE, a laser calibration system is foreseen to provide information on the actual electric field (see Part II for more details). The laser and cosmic muon tracks allow to generate a correction to be applied in the event reconstruction. MicroBooNE will provide important input on the scale of the effect and the performance of the reconstruction corrections. A possible hardware implementation could stabilize the electric field inside the sensitive volume of the LAr-TPC with the addition of widely spaced shaping wire planes at the voltage of the potentials of the field cage electrodes (see Part III for more details) thus reducing the space charge effect.

It should be noted that all the contributions listed above can be directly measured with the data, monitored during the experiment, and corrected for in the analysis, largely reducing their impact on the measurement. It has been estimated that an overall global detector systematic uncertainty in the 2–3% range would preserve the experimental sensitivity. We assume this systematic level as a requirement for the detectors.

## F. Beam-Induced “Dirt” Events

Neutrinos from the BNB will interact in material surrounding the active detectors, including liquid argon outside of the TPC, the cryostat steel, structural elements or engineering support equipment in the detector hall, the building walls and floors, and the earth outside the detector enclosure. These interactions can produce photons (through  $\pi^0$  decay or other channels) which can enter the TPC and convert in the fiducial volume, potentially faking an electron signal. While it turns out the majority of interactions producing this background occur relatively close to the detector volume, the moniker “dirt” events is kept in analogy to its use in MiniBooNE plots and publications. This description, however, will refer to any backgrounds generated by beam neutrino interactions *occurring anywhere outside of the TPC active volume*. We consider this background only for the  $\nu_e$  analysis as the out-of-detector contamination of the  $\nu_\mu$  charged-current sample is expected to be negligible.

To estimate the dirt background, a Monte Carlo simulation is used which includes a realistic geometry description of the material surrounding the detectors. Due to the large mass but

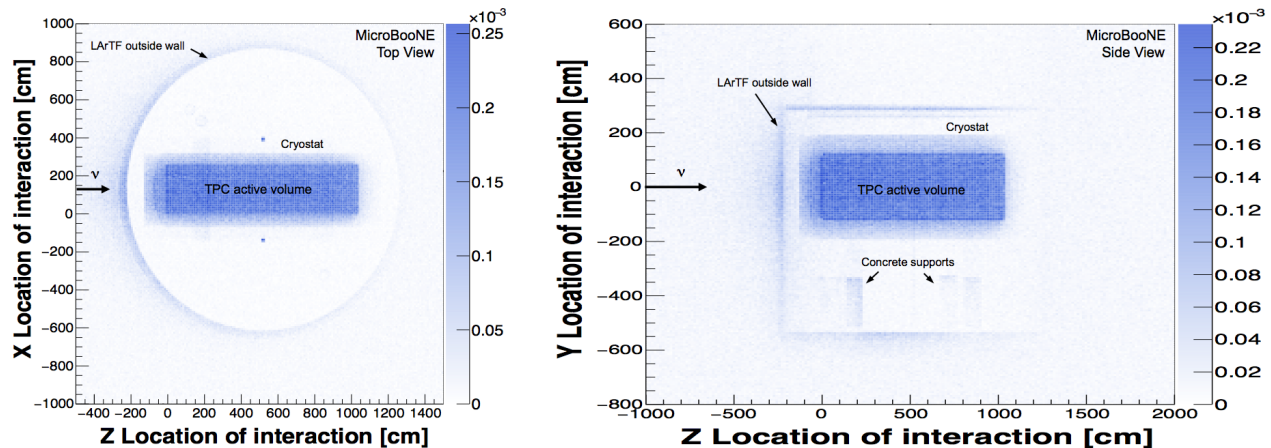


**FIG. 15:** Location of interaction vertices for neutrinos which deposit any energy into the MicroBooNE detector shown from above (left) and the side (right).

small probability for any given interaction to create energy inside the detector, it is challenging to generate large statistics. Substantial effort was put into generating a large Monte Carlo sample using the MicroBooNE simulation where the geometry description is the most detailed. Figure 15 shows the distribution of interaction vertices for BNB neutrinos which deposit any detectable energy into the MicroBooNE detector. The walls of the LArTF building and the soil surrounding it are clearly visible. In the right image, the concrete supports can be seen, but not the foam insulation saddles that sit between the supports and the cryostat. The highest density of vertices is, of course, in the active volume of the detector.

From this sample, events with an interaction vertex outside of the active TPC volume but that generate a photon which converts inside the detector, are selected. Due to the short radiation length in liquid argon ( $X_0 = 14$  cm), the argon volume surrounding the TPC inside the cryostat provides an effective shield for photons trying to enter from beyond the cryostat walls. Most of the interactions capable of creating a photon inside the fiducial volume, therefore, tend to happen in this outer argon region. This can be seen in the upper left panel of Figure 16. The plot shows the creation point of all photons which then convert inside the MicroBooNE active volume, and they clearly pile up in the region just beyond the active volume boundary. Photons entering the detector are likely to interact within a few 10's of centimeters of the TPC boundary, providing a handle with which to minimize this background. The lower panels of Figure 16 show the photon conversion point within the active volume projected onto the  $z$ -axis (the beam direction) and the  $x - y$  plane.

This sample, as with all single photon shower backgrounds, is reduced by analyzing the  $dE/dx$  at the start of the shower and rejecting 94% of pair production interactions. To further reduce out-of-detector dirt photons in the  $\nu_e$  analysis, we restrict the fiducial volume to an inner region of the detector 30 cm from the upstream and 25 cm from the side boundaries of the active TPC region, reducing the number of dirt background events by 80% in MicroBooNE. These fiducial volume boundaries are indicated in the figures for MicroBooNE, but are used uniformly in all three detectors in the analysis.

A similar Monte Carlo sample has been generated for the LAr1-ND detector at 110 m. Figure 17 shows the creation point of all photons which then convert in the LAr1-ND active volume. While the dirt photons in MicroBooNE come in from both the upstream face and the sides of the detector (see Figure 16), in LAr1-ND they are more concentrated at the upstream

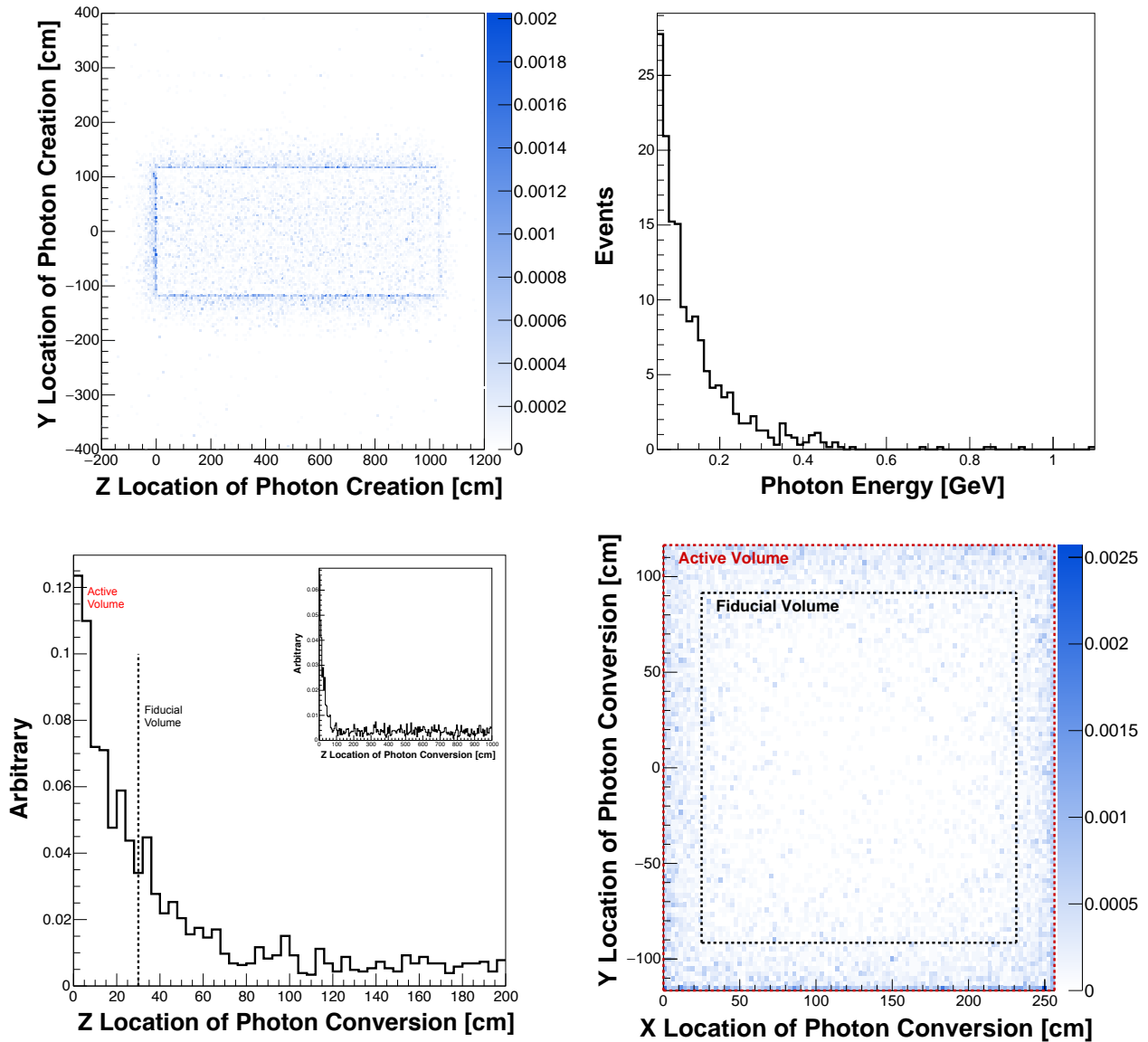


**FIG. 16:** (Top left) Photon creation position in the  $Y$ - $Z$ , side view, projection for photons which then convert inside the MicroBooNE active volume, possibly faking a  $\nu_e$  CC interaction. (Top right) Energy of the photons that convert inside the MicroBooNE detector but came from neutrino interactions outside of the detector active volume. (Bottom left) Photon conversion position inside the MicroBooNE detector projected onto the  $z$ -axis ( $z = 0$  is the start of the TPC active volume; only first 200 cm shown). The vertical dashed line is 30 cm from the front of the TPC. (Bottom right) Photon conversion position in the  $X$ - $Y$ , front view, for photons which convert downstream of  $z = 30$  cm (plot boundary is the TPC active volume; fiducial volume for  $\nu_e$  analysis is indicated).

face of the detector. This difference is due to two factors, *i*) the neutrino flux at the LAr1-ND location is still highly collimated so the event rate is peaked in the middle of the detector and falls off toward the detector sides, while it is uniform across the MicroBooNE detector face, and *ii*) the amount of argon outside of the TPC in the square LAr1-ND cryostat is less than the amount in the cylindrical MicroBooNE cryostat.

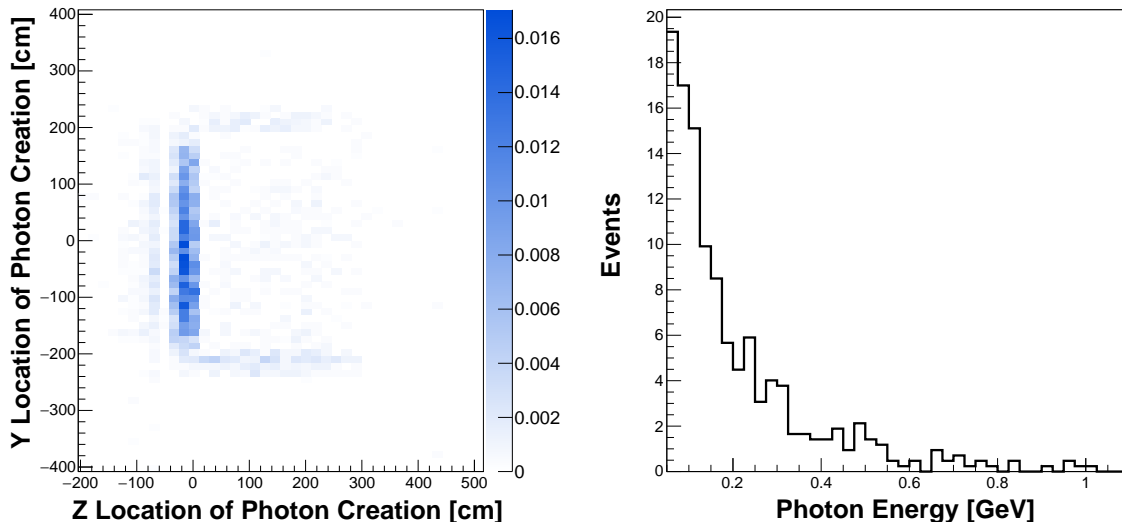


**FIG. 17:** (Left) Photon creation position in the  $Y$ - $Z$ , side view, projection for photons which then convert inside the LAr1-ND active volume. (Right) Energy of the photons that convert inside the LAr1-ND detector but came from neutrino interactions outside of the detector active volume.

A dedicated simulation of out-of-detector interactions at the ICARUS-T600 site has not been generated. Instead, because the 470 m and 600 m locations are both in the region where the flux is wider than the detectors, we can use the MicroBooNE predictions to scale to the far detector site and generate an estimate of the dirt background in ICARUS. We account for the different surface areas of the two detectors and scale the neutrino flux as  $1/r^2$ . To account for any differences in the background rate from photons entering the front vs. the sides of the detectors, we scale events in the beginning 50 cm of the MicroBooNE detector separately from those further downstream:

$$N_{\text{dirt}}^{\text{T600}} = \frac{470^2}{600^2} \times 2 \times \left( \frac{\text{Front Area T300}}{\text{Front Area } \mu\text{BooNE}} N_{\text{dirt}}^{\mu B}(z \leq 50 \text{ cm}) + \frac{\text{Side Area T300}}{\text{Side Area } \mu\text{BooNE}} N_{\text{dirt}}^{\mu B}(z > 50 \text{ cm}) \right) \quad (7)$$

where  $N_{\text{dirt}}^{\mu B}(z)$  is the number of dirt events predicted in MicroBooNE and  $z$  is the distance from the front of the active volume. Table V provides the total number of dirt background events expected in each detector according to the simulations for LAr1-ND and MicroBooNE and using Eq. 7 to estimate the rate in ICARUS. The scaling procedure adopted for the far detector has been checked with a muon neutrino MC event sample. About 40 dirt events induced by neutrino interactions in the passive LAr volume behind the wire planes or in the top/bottom of the detector were found. This result is roughly in agreement with the previously described extrapolation if the events induced in the upstream and downstream passive LAr and in the other materials around the detector are neglected.

In the present analysis, we reduce the dirt background to manageable levels by restricting the fiducial volume used in the  $\nu_e$  analysis. A more sophisticated approach has also been explored that would use the reconstructed shower direction in candidate events to project *backwards* from the vertex and calculate the distance to the nearest TPC boundary in the backwards direction. Cutting on this quantity on an event-by-event basis would allow us to further reduce the dirt backgrounds on all sides without sacrificing fiducial volume. This is referred to as the *backwards-distance-to-wall* variable, and is not used in the current analysis.

**TABLE V:** *Estimated rates of photon induced showers from out-of-detector neutrino interactions faking a  $\nu_e$  CC interaction in a  $6.6 \times 10^{20}$  POT exposure. A  $dE/dx$  cut has been applied to reject 94% of pair production events.*

Detector	Estimated Dirt Background Events ( $6.6 \times 10^{20}$ POT)		
	$z \leq 50$ cm	$z > 50$ cm	Total
LAr1-ND	26.2	17.0	43.2
MicroBooNE	2.38	19.5	21.9
ICARUS-T600	5.15	57.0	62.2

### *Error Matrix Contribution from Dirt Backgrounds*

Finally, we require an estimate of the error matrix associated with dirt backgrounds,  $E^{\text{dirt}}$ . The dirt background rate in each detector can be constrained with data using a sample of electromagnetic shower events near the TPC boundary, or showers where the reconstructed momentum is consistent with the particle having entered the detector. This sample will be enhanced in dirt background events and can be used to validate the simulations. At this time, we conservatively estimate a 15% systematic uncertainty uncorrelated between detectors, but fully correlated within the energy spectrum in each detector. This covariance matrix is constructed as

$$E_{ij}^{\text{dirt}} = \rho_{ij}(0.15 \times N_i^{\text{dirt}})(0.15 \times N_j^{\text{dirt}}) \quad (8)$$

where  $\rho_{ij}$  is 0 if  $i$  and  $j$  bins correspond to different detectors, and 1 if they correspond to the same detector.

## G. Cosmogenic Backgrounds

Another important background to the  $\nu_e$  analysis is created by cosmogenic photons that generate electrons in the detector via Compton scattering or pair production interactions that are misidentified as a single electron. Photons are created either in the atmospheric shower (“primary photons”) or by cosmic muons propagating through the detector and nearby surrounding materials (“secondary photons”). In the case of an un-shielded detector at the surface, the background to a  $\nu_e$  CC sample is mostly due to primary photons, but these can be easily absorbed by a few meters of earth or concrete shielding. In simulations of the far detector, for example, a 3 m rock coverage reduces by a factor 400 the number of primary photons above 200 MeV in the active volume, and secondary photons generated by muons passing through or very near the detectors becomes the dominant source of background. To further reduce the rate, we must identify cosmic showers through topological and timing information in the event.

In an ideal situation where precise timing information is known for every track or shower inside the detector, only cosmogenic events in coincidence with the beam spill can contribute to the background. However, in a realistic situation, interactions occurring anytime within the acquisition time (which corresponds to the maximum electron drift time) may influence the data analysis, as will be explained below. Given the respective detector sizes, the maximum drift times are 1.28 ms in LAr1-ND, 1.6 ms in MicroBooNE and 0.96 ms in ICARUS, to be compared with the 1.6  $\mu$ s duration of the beam spill from the BNB. Potential cosmogenic backgrounds

can be categorized according to their time structure as:

Timing case A: Cosmogenic photon interacts in the detector in coincidence with the beam spill.

Timing case B: Cosmogenic photon interacts anywhere inside the drift time, and a *different* cosmic event (muon or otherwise) is in the detector in coincidence with the beam spill. If the arrival time of the photon is poorly known, it could be mistaken for the in-spill event.

If not properly recognized, neutrino beam interactions occurring in LAr surrounding the TPC active volume or low energy neutral-current interactions that are not identified, can also provide a scintillation trigger in the beam spill leading to a situation similar to timing case B. This effect has been roughly estimated for the far detector, resulting in a very small additional contribution to the cosmogenic background due to the low neutrino interaction rate (Table VIII). Therefore, it is not currently included in the analysis.

Key topological information includes the location of the photon within the detector (just as with dirt events, externally produced  $\gamma$ s will interact near the detector edges) and the proximity to the parent cosmic muon track in the case of secondary photons. Therefore, we identify two main categories of event topology:

Topology I: Cosmogenic photon interacts inside the fiducial volume, and the parent muon also enters the TPC active volume.

Topology II: Cosmogenic photon interacts inside the fiducial volume, but the photon originated from the atmospheric shower (a primary), the parent particle is not visible (e.g. neutrons), or the parent particle does not enter the TPC active volume (e.g. muon misses the active volume).

Estimation of the cosmogenic background rate requires a detailed simulation of the cosmic particle fluxes and their interactions in and around the detectors. As with the dirt backgrounds described in Section II F, a realistic geometry description and significant computational effort is required. For the current analysis, independent simulations have been developed by the MicroBooNE, LAr1-ND, and ICARUS Collaborations. All future analysis of SBN data will, of course, be based on a common simulation, but the current development has provided some important opportunities for cross checks. We provide here brief descriptions of each simulation:

- ICARUS: The ICARUS simulation uses FLUKA [67, 68] for both the cosmic ray showering and the particle transport to and inside the detector. FLUKA is a multipurpose Monte Carlo code used for several years to simulate cosmic showers in the atmosphere. Examples of its performance can be found in the literature, for instance the simulated flux of muons at different depths in the atmosphere agrees with CAPRICE data within experimental errors [77]. Similar agreement [78] is obtained with the muon spectra measured by the L3 experiment, and predicted proton and lepton fluxes in the atmosphere are in very good agreement [79] with the AMS data. The ICARUS simulation is the most complete in that it includes both proton and ion primary cosmic ray sources and generates all particle content in the showers. Primary neutrons, for example, are found to contribute about 10% of electron-like events. The energy spectra of different particle types predicted by the FLUKA simulations at 260 m above sea level (FNAL elevation is 225 m) are shown

in Figure 18. The detector was simulated at the surface (not in a building) with and without 3 m of concrete overburden above the detector as mentioned above. The default in this analysis is *with* overburden.

- **MicroBooNE:** The MicroBooNE simulations are performed with the CRY cosmic-ray shower simulation [80] as a primary particle generator and GEANT4 to transport particles into the MicroBooNE detector. The CRY package provides reasonable results in a fast and easy way, but has known limitations, such as the lack of a contribution from primary ions, a rigid binning structure that sacrifices some spectral details, and an under prediction of neutron, proton, electron, and  $\gamma$  shower content. Comparisons have shown that results obtained with CRY+GEANT4 in MicroBooNE and results scaled from the full FLUKA T600 simulation agree within a factor of two. The detector geometry is the most detailed and includes the LArTF building and substantial infrastructure, so there is some shielding effects from the building and platforms above the detector. The LArTF facility also has the ability to support concrete shielding blocks on the roof, but this is *not* included in the present simulations. Studies are continuing by the MicroBooNE Collaboration to determine if the additional shielding should be added for the upcoming physics run.
- **LAr1-ND:** The LAr1-ND cosmic muon flux is generated using Gaisser’s parameterization [81], with corrections for the Earth’s curvature and the muon lifetime. The muon flux simulation is performed at the Fermilab latitude, and muons are propagated through the LAr1-ND detector and building using GEANT4. The detector is simulated in a pit below grade but without additional shielding above the detector. Only the muon component of the shower is included, but results from both the ICARUS and MicroBooNE simulations, which include all components, show that secondaries from muons are by far the dominant contribution to the background, and the exclusion of primary photons and hadrons in the simulation is nearly equivalent to simulating a detector with some overburden.

To get a sense for the situation, it is instructive to first look at some basic numbers coming from the far detector simulation. Cosmogenic interactions of all kinds depositing more than 100 MeV of energy will occur in the T600 fiducial volume at  $\sim 11$  kHz, implying such an event inside the detector during 1 out of every 50 beam spills. A  $6.6 \times 10^{20}$  POT run represents approximately  $1.32 \times 10^8$  spills at nominal intensity, corresponding to 211 seconds of beam-on time throughout the experiment. ICARUS will, therefore, see  $2.5 \times 10^6$  cosmic events *during the beam spill time* in the run. Further,  $\sim 10$  cosmic muon tracks will enter into the detector volume during the 0.96 ms drift time in each readout of the detector.

Figure 19 (left) shows the energy distribution of cosmogenic photons which interact in the TPC fiducial volume as calculated by far detector simulation (the others look similar, of course). The spectrum is steeply decreasing with energy. For comparison, Figure 19 (right) shows the energy distribution of the electrons produced in  $\nu_e$  charged-current interactions in the far detector by the BNB intrinsic  $\nu_e$  flux. In the following, all background estimates are provided above an energy threshold of 200 MeV.

Cosmogenic photon interaction rates have been estimated in the three detectors using the simulations described above and the results are detailed in Table VI. In each detector, fiducial cuts as suggested by the beam dirt events analysis (Section II F) have been applied, namely 25 cm from the sides of the active volume, 30 cm from the upstream face, 50 cm from the downstream face, and 1.5 cm from the cathode when applicable (for the resulting fiducial masses see Table XXXV). Rates for both topology I and II events occurring within the beam spill (timing category A) are estimated directly from the simulations by scaling the time exposure



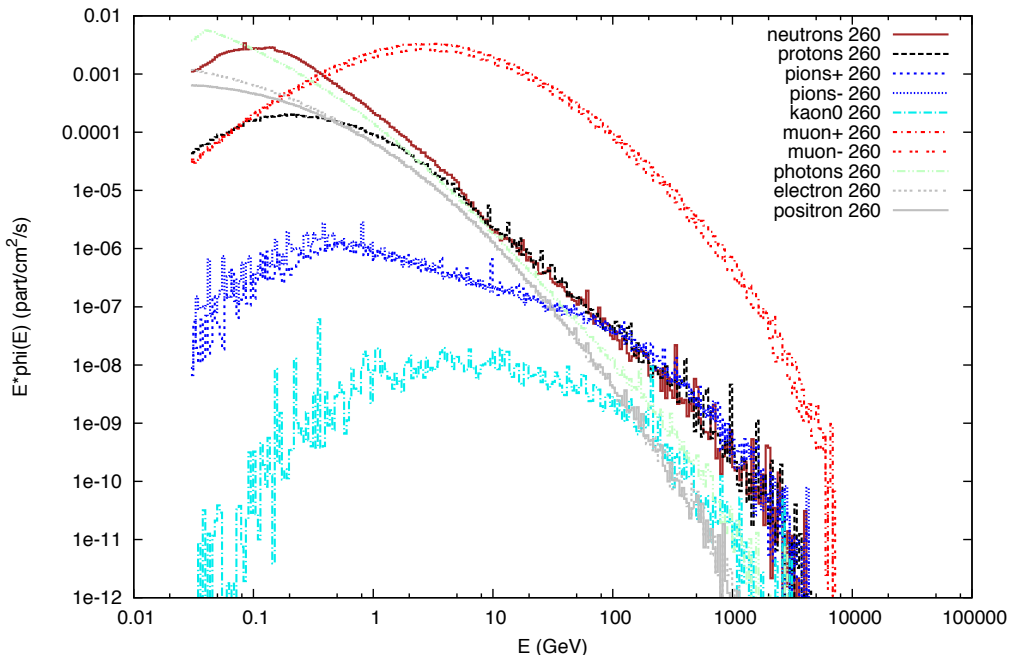


**FIG. 18:** Particle fluxes in the atmosphere at 260 m elevation (FNAL is at 225 m) according to the FLUKA simulation.

represented in each Monte Carlo sample to 211 seconds. Rows 1–4 of Table VI give the raw rates for both Compton and pair producing photons inside the fiducial volume with and without a parent muon that enters the TPC active volume. These numbers reveal several interesting features. First, the ratio of row 1 to row 2 is  $\sim 2\%$  in each case, which is consistent with the size of the Compton scattering cross section in this energy range. Second, a comparison of rows 3–4 to 1–2 indicates that the likelihood of a photon converting in the fiducial volume where the parent muon completely misses the TPC is very small. The 25 cm active buffer around the fiducial volume motivated by the dirt backgrounds is also very effective at absorbing cosmogenic photons entering the detector from outside. And as we will describe below, the presence of the parent muon in the TPC provides a strong handle for rejecting the photon shower as a beam-related event. Finally, comparing the different columns of rows 1–4 does reveal some variability in the predicted cosmic photon rates in the three detectors. Factors of 2–3 may be expected due to differences in the input simulations as described above. The geometry of the detectors plays a role in the expected rates, as well. For example, the probability that a crossing muon produces a photon in the detector will scale as the average muon track length in the detector, and LAr1-ND has the largest average track length due to the detector’s 4 m height.

Rows 5–8 of Table VI present the number of events of timing category B and are calculated directly from rows 1–4. We assume, to first order, that the time signal during the beam spill is produced by a cosmic muon entering the detector. Event category B is reducible if light signals in the argon are able to be correctly matched to the energy deposits that produce them, however, we initially assume this is not done. The number of category B events,  $N_B$ , can then be calculated from the number of category A events,  $N_A$ , that were estimated directly from the simulation. The scale factor ends up being  $N_\mu^{\text{drift}}$ , the average number of muons that enter the

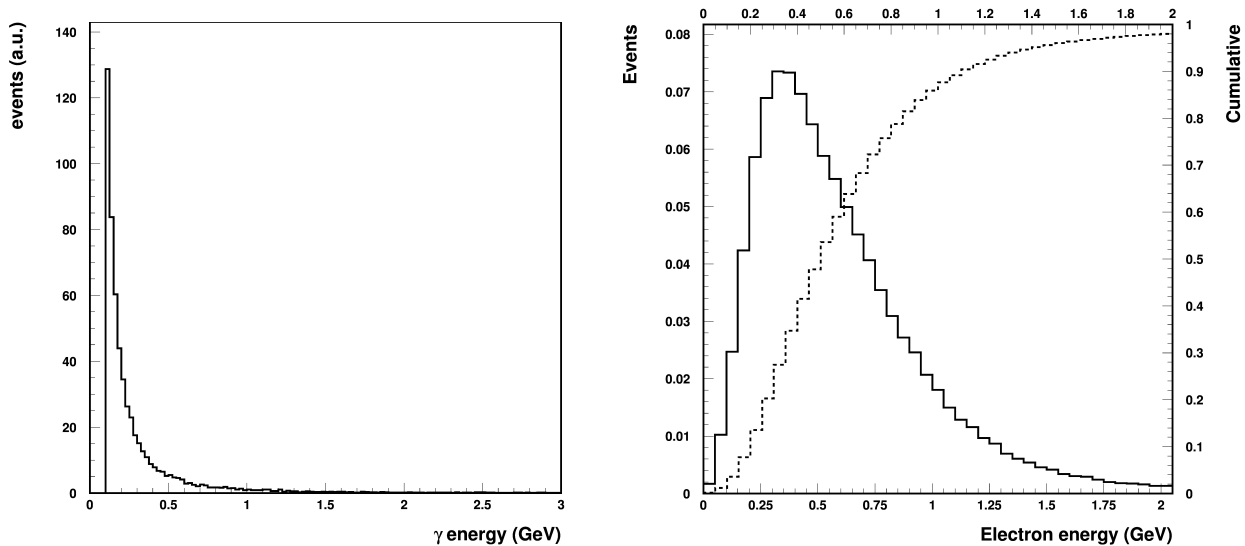


**FIG. 19:** (Left) Energy distribution of cosmic background photons inside the far detector. (Right) Energy distribution of electrons produced in  $\nu_e$  interactions in the far detector.

detector per readout during the full drift time:

$$N_B = P_\gamma^{\text{drift}} \times P_\mu^{\text{spill}} = \left( N_A * \frac{t_{\text{drift}}}{t_{\text{spill}}} \right) \times \left( N_\mu^{\text{drift}} * \frac{t_{\text{spill}}}{t_{\text{drift}}} \right) = N_A * N_\mu^{\text{drift}} \quad (9)$$

where  $P_\gamma^{\text{drift}}$  is the probability of having a cosmogenic photon anywhere in the drift time and  $P_\mu^{\text{spill}}$  is the probability that a muon crosses the detector during the beam spill time. Our simulations indicate that  $N_\mu^{\text{drift-LAr1-ND}} = 2.9$ ,  $N_\mu^{\text{drift-MicroBooNE}} = 5.0$ , and  $N_\mu^{\text{drift-T300}} = 5.5$ . The T300 is the right unit for the ICARUS detector since each T300 module is an optically isolated element of the full T600 detector.

Table VI represents the raw number of cosmogenic photons that interact within the fiducial volumes of each detector during the proposed run. A number of strategies can be applied to reduce the cosmic backgrounds entering the  $\nu_e$  analysis sample. Below we list the strategies being considered. Items 1–5 describe topology based cuts using TPC information only. Items 6–8 use precise timing information to reject events that are not coincident with the neutrino beam or to eliminate TPC beam triggers that are contaminated by cosmic activity in the detector during the beam spill.

- 1)  $dE/dx$ : Pair production events can be rejected with the reconstruction of  $dE/dx$  in the initial part of the shower. Preliminary results show that only 6% of pair conversions present a  $dE/dx$  lower than 3.5 MeV/cm in the first 2.5 cm of the shower.
- 2) Distance from the muon track: Figure 20 shows the distance of the cosmogenic photon conversion point from the parent muon track, whenever it also crosses the detector. Rejecting event candidates with a reconstructed vertex inside a cylindrical volume of 15 cm radius around each muon track rejects >99% of the background photons above 200 MeV. The resulting loss in fiducial volume for the  $\nu_e$  analysis ( $\sum_\mu \pi R^2 L_\mu$ ) is minimal,  $\sim 1\%$

**TABLE VI:** Background rates, assuming 3 years of data taking for a total of  $6.6 \times 10^{20}$  protons on target, delivered in  $1.32 \times 10^8$  beam spills equaling 211 seconds of beam time. Events with at least one photon shower above 200 MeV converting in the fiducial volume are counted in all the  $\gamma$  entries.

Cosmic photon interaction description	Timing Cat.	Topology Cat.	$E_\gamma > 200$ MeV, Pair prod $E_e > 200$ MeV, Compton		
			LAr1-ND	$\mu$ BooNE	ICARUS
1 $\gamma$ Compton in spill, primary $\mu$ enters AV	A	I	887	206	599
2 $\gamma$ Pair prod in spill, primary $\mu$ enters AV	A	I	52,300	11,600	32,000
3 $\gamma$ Compton in spill, primary misses AV	A	II	<1	<3	<4
4 $\gamma$ Pair prod in spill, primary misses AV	A	II	55	82	11
5 $\gamma$ Compton in drift, primary $\mu$ enters AV	B	I	2,550	1,030	3,300
6 $\gamma$ Pair prod in drift, primary $\mu$ enters AV	B	I	150,200	57,950	176,000
7 $\gamma$ Compton in drift, primary misses AV	B	II	<3	12.4	<4
8 $\gamma$ Pair prod in drift, primary misses AV	B	II	160	410	60

per event on average in the far detector considering all muons in one drift time in one module.

- 3) Clustering around muon tracks: Rather than a fixed cylindrical volume around tracks as in strategy 2), a variable volume cut around each muon/charged particle can be defined by the zone of connected electromagnetic activity. The “connection” is built by walking out from the primary track, clustering hits and gathering clusters together. This appears to be a very effective cut, however its stability in different wire orientations and noise conditions has to be further established.
- 4) Activity at the vertex: Requiring the presence of another ionizing track from the vertex would reject all Compton events and a further fraction of the pair production events. However, the same selection on  $\nu_e$  events discards  $\sim 25\%$  of the signal, making this a cut of last resort.
- 5) Backwards distance to the detector wall: This cut was introduced above in our discussion of dirt backgrounds to more efficiently identify showers from photons generated outside of the detector. Using the reconstructed shower direction in candidate events, one can project back from the vertex and calculate the distance to the nearest TPC boundary in the backward direction. Since the cosmogenic background is dominated by photons generated by muons inside the active volume, this cut has limited impact and needs further investigation before being applied.
- 6) Scintillation light: Precise event timing information is available through the detection of scintillation light in the liquid argon. If light detector signals can be matched to the corresponding ionization signals with high efficiency, this would allow a large reduction of backgrounds falling into the timing category *B* introduced above. Studies are ongoing to characterize the matching performance and optimize the light collection systems in both LAr1-ND and ICARUS.
- 7) Proton beam spill time structure: Measurement of event times with  $\sim 1$ -2 ns accuracy would enable the exploitation of the bunched beam structure within the spill ( $\sim 2$  ns wide

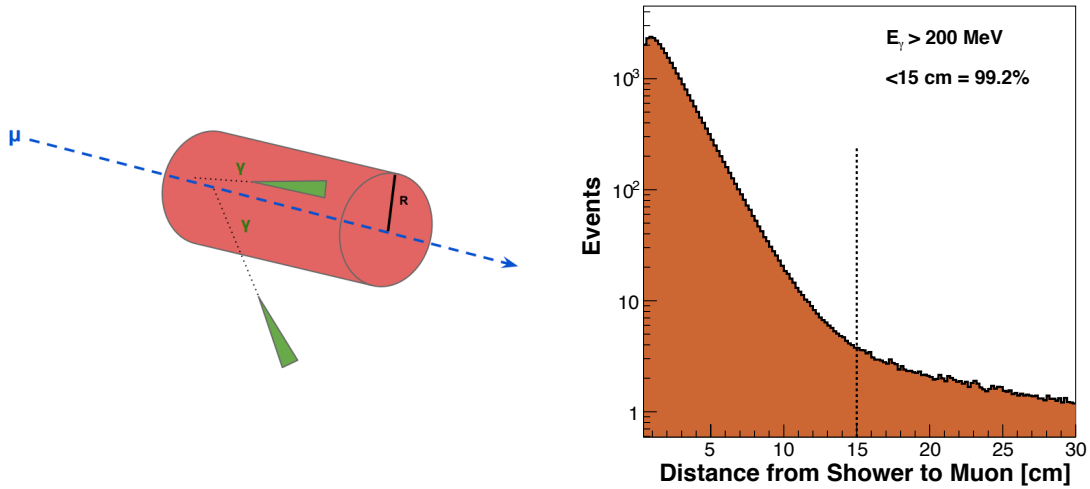


**FIG. 20:** Shortest distance between the conversion point of cosmogenic photons and the parent muon track for photons above 200 MeV.

bunches every 19 ns, see Section IA), to reduce cosmic backgrounds by rejecting events that occur between bunches. The possibility to reduce the number of bunches by a factor of 2-3, while keeping the same number of protons per spill, will also be investigated in order to further increase the rejection ability using precise timing.

- 8) Muon tagging: A powerful way to reduce cosmogenic backgrounds would be to employ a cosmic tagging system external to the TPC volume capable of independently measuring the position and time of entering charged tracks. This information would greatly facilitate the reconstruction and identification of muon tracks in the TPC, leading to a reduction of both type A and B background categories. In the simplest application of this information, an external tagging and tracking system with high (e.g. >95%) coverage of the muon flux that creates potential backgrounds could be used to identify and reject detector readouts when a cosmic  $\mu$  passes near the detector during the proton beam spill. Expected fluxes at the detector locations indicate this would reduce the beam data sets by roughly 1.5%, 2%, and 3% at LAr1-ND, MicroBooNE, and ICARUS, respectively, while reducing the cosmic backgrounds in a very clean way.

Table VII illustrates the performance of topological cuts 1) and 2) applied to the Monte Carlo simulations. In particular, photon showers within 15 cm of the muon path are rejected and 94% of  $\gamma$  pair production showers are rejected corresponding to a  $dE/dx > 3.5$  MeV/cm cut on the first 2.5 cm of the shower. Remaining background levels in the three detectors (order 100 events) are summarized in Table VII, which can be directly compared to Table VI before these cuts. Also, listed for comparison is the expected numbers of intrinsic  $\nu_e$  CC events. In Section III H, we will present predicted event distributions when using these topological cuts, as well as illustrate the power of augmenting these with external muon tagging and timing selections.

**TABLE VII:** Background rates, after topological cuts, assuming 3 years of data taking for a total of  $6.6 \times 10^{20}$  protons on target, delivered in  $1.32 \times 10^8$  beam spills equaling 211 seconds of beam time. The cuts that have been applied relative to Table VI are (distance from the  $\mu$  track)  $< 15$  cm and  $dE/dx > 3.5$  MeV/cm.

Interaction description	Timing Cat.	Topology Cat.	$E_\gamma > 200$ MeV, Pair prod $E_e > 200$ MeV, Compton, $\nu_e$		
			LAr1-ND	$\mu$ BooNE	ICARUS
1 $\gamma$ Compton in spill, primary $\mu$ enters AV	A	I	8	$<3$	$<4$
2 $\gamma$ Pair prod in spill, primary $\mu$ enters AV	A	I	26	6	21
3 $\gamma$ Compton in spill, primary misses AV	A	II	$<1$	$<3$	$<4$
4 $\gamma$ Pair prod in spill, primary misses AV	A	II	$<4$	6	$<1$
5 $\gamma$ Compton in drift, primary $\mu$ enters AV	B	I	22	12	30
6 $\gamma$ Pair prod in drift, primary $\mu$ enters AV	B	I	74	29	113
7 $\gamma$ Compton in drift, primary misses AV	B	II	$<3$	12	$<4$
8 $\gamma$ Pair prod in drift, primary misses AV	B	II	10	19	$<4$
Total Cosmogenic $\gamma$ backgrounds			146	88	164
Intrinsic $\nu_e$ CC			15,800	413	1,500

#### *An Illustration of Cosmogenic Rate Reductions in ICARUS*

As an illustration of the detector capabilities in rejecting the cosmogenic background, the external muon tagging system and event matching to the proton spill time structure (introduced in [82, 83]) can be applied in the first stages of the data selection in order to achieve an effective reduction of the data amount to be fully analyzed (Table VIII).

From the previous calculations of the cosmic ray flux impinging on the T600 detector (see Table VI), the predicted number of triggers produced by cosmics inside the  $1.6 \mu\text{s}$  beam spill is globally  $\sim 2.5 \times 10^6$  events.

The adoption of a full coverage external muon tagging system with a 95% detection efficiency at each muon crossing can directly reduce the number of triggers produced by cosmic rays to  $\sim 2.4 \times 10^4$  events. These resulting surviving events come mainly from the  $\sim 15\%$  fraction of muons either coming to rest or decaying inside the detector since, in the case of double crossing of muons entering and exiting the LAr-TPC, the survival probability is considerably smaller ( $\sim 0.25\%$ ). As a consequence the cosmogenic background events of the ‘‘Timing category A’’ in Table VI associated to the primary crossing muons are suppressed down to 0.25%. Events of category B, triggered by the passing/stopping muons not identified by the tagging system, are instead reduced only to below 1 % level (0.96%). As a result, the predicted fraction of  $\gamma$ -ray conversions per imaging picture is evaluated from the Timing Category A, Topology I and Timing Category B rescaled for the factors 0.0025 and 0.0096 respectively, is about 0.075.

Assuming a factor 3 of reduction can be achieved from the exploitation of the beam spill time structure, a total of 8020 events are retained, out of which  $\sim 600$  contain a converting  $\gamma$  with  $E > 200$  MeV (event topology I). As described above, only 1% of converting  $\gamma$ 's accompanied by a visible muon will satisfy the requirement of a minimal distance of 15 cm of the photon conversion from the muons, leaving  $\sim 6$  events.

In addition, from Table VI,  $<4$   $\gamma$ -ray conversion ( $E > 200$  MeV) events are expected without a visible muon in the TPC's (event topology II) in time with the bunched beam structure and

**TABLE VIII:** *Expected background event reduction in the T600 detector exploiting the muon tagging system and the beam spill time structure. Event topology I refers to events with a muon track crossing the active TPC volume and Event Topology II refers to events with no visible muon in the TPC. The contribution from the non-identified neutrino interactions is also added.*

	Cosmic Background Events	
Total cosmic events in beam spills (211 sec. total)	$2.5 \times 10^6$	
Cosmic triggers after the tagging system	$2.4 \times 10^4$	
Surviving events after the spill structure exploitation	8020	
	Event Topology	
	<u>I</u>	<u>II</u>
$\gamma$ conversions	600	3
After distance from muon cut (15 cm)	6	3
Remaining cosmogenic backgrounds after $dE/dx$ cut	1	
Remaining cosmogenic background in non-identified BNB $\nu$ interactions	18	
Total cosmogenic background after scintillation light exploitation	5	

under the conservative assumption that only 50% of them are recognized by the tagging system. Therefore the surviving 9 event sample is further reduced to  $\sim 1$  events by the reconstruction of the  $dE/dx$  in the initial part of the shower.

If not properly recognized, neutrino beam interactions at low energy occurring both in active volume and in the external LAr could mimic a cosmogenic trigger in time with the beam spill. In such a case cosmogenic photons inside the drift time are expected to contribute to the background escaping any mitigation effect from the muon tagging system and the precise time matching with the beam spill structure. A rough conservative estimation of  $\sim 3 \times 10^5$  events will result in 18 events satisfying the previous selection criteria, namely the requirement of the minimal 15 cm distance from muon and  $dE/dx$  identification.

The resulting total  $\sim 19$  background events could be further reduced to  $\sim 5$  events under the conservative assumption that the scintillation light system is capable to localize the triggering event within  $\sim 4$  m along the beam direction.

The explicit request of absence of muon tagging in the event and the precise time matching with the bunched spill structure are expected to slightly reduce the  $\nu_e$  CC event acceptance by  $\sim 3\%$ . The 200 MeV electron energy threshold will result in a reduction of  $\sim 10\%$  on the electron signal acceptance, while the corresponding reduction for a request of a minimal distance of the event vertex from the cosmic muon tracks is almost negligible, 0.7% on average.

#### *Error Matrix Contribution from Cosmogenic Backgrounds*

We now require an estimate of the error matrix associated with the predicted cosmogenic backgrounds,  $E^{\text{cosmics}}$ , to be used in the sensitivity analysis as discussed in Section II A.

It is important to emphasize that the most important outcome at this time is to understand the approximate scale of the cosmogenic backgrounds in the experiment. The exact rate does not introduce significant *systematic* uncertainty because it will be measured with high precision using off-beam random event triggers. This is a critical aspect of the experiment, and designing the DAQ systems to record sufficient random triggers must be considered. For the sensitivity

analysis, we construct the cosmic error matrix to account for the statistical uncertainty on the predicted sample,  $E_{ii}^{\text{cosmic}} = N_i^{\text{cosmic}}$  and  $E_{ij}^{\text{cosmic}} = 0$  for  $i \neq j$ .

The key thing to demonstrate at this time is that cosmic backgrounds can be reliably reduced to a level where oscillation signals can be observed over them with sufficient statistical significance. The fact that the independent detector simulations have come together to produce predictions consistent within a factor of two gives confidence that the scale is correctly estimated. Common simulations will, of course, be used in the actual analysis, but more importantly the background levels will be tightly constrained *with data* in each detector.

### H. $\nu_\mu \rightarrow \nu_e$ Appearance Sensitivity

We are now ready to bring together the background predictions and uncertainty estimations detailed in the previous Sections to construct the experimental sensitivity to a  $\nu_\mu \rightarrow \nu_e$  oscillation signal. Figure 21 shows the full  $\nu_e$  background predictions in each detector, including intrinsic  $\nu_e$  beam events, neutral-current and  $\nu_\mu$  CC mis-IDs, out-of-detector beam related “dirt” backgrounds, and cosmogenic photon induced electromagnetic shower backgrounds. For comparison, a sample  $\nu_\mu \rightarrow \nu_e$  oscillation signal is also shown for each detector location corresponding to the best-fit parameters from the Kopp et al. analysis [41] of  $\Delta m^2 = 0.43 \text{ eV}^2$  and  $\sin^2 2\theta = 0.013$ .

On the left in Figure 21 is shown the result when using the topological cuts 1) and 2) described in Section II G to reduce cosmic backgrounds. This analysis, using  $dE/dx$  information at the vertex and the 15 cm cylinder cut around crossing muons, demonstrates the power of TPC information alone in reducing these backgrounds, rejecting more than 99% of cosmogenic photons when their parent muon is also visible in the TPC. However, as can be seen in the figures, the cosmogenic backgrounds remain a large contribution to the analysis, particularly at low energies, and additional hardware-based systems that can initially reduce the data sample in a very clean way are considered important additions to guarantee the success of the experiment.

The right column of Figure 21 demonstrates the potential improvement when employing additional hardware solutions such as those introduced in Section II G. Precise timing information, in particular, can augment the TPC data by rejecting triggers where the 1.6  $\mu\text{s}$  beam spill time is contaminated by a cosmic event in the detector. To generate the right hand distributions of Figure 21, it is assumed that the combination of strategies 6–8 from Section II G are applied to remove 95% of cosmogenic events in the first stages of data analysis, before entering into automated reconstruction and event selection algorithms. Given the dominance of muons passing very near the detectors as the source of cosmic backgrounds, most of this reduction should be straightforwardly achievable with a properly implemented external tracking system. Further rejection capabilities will come from precise event timing information from the internal scintillation light collection systems. The required level of rejection can be taken as a design requirement on these systems, determining the necessary coverage of the external tagging systems and the time resolution of the internal light collection, but this factor of 20 reduction is a fairly conservative estimate of the power of strategies 6–8 combined.

Table IX lists the integrated event totals represented in the histograms of Figure 21. The  $20\times$  reduction from additional cosmic tagging discussed above is indicated in parenthesis. Vetoing of events with cosmic activity in the beam spill using timing results in a reduction of all beam related event categories of  $\sim 1.5\%$ ,  $2\%$ , and  $3\%$  in LAr1-ND, MicroBooNE, and ICARUS, respectively. This reduction is not shown in the Table (for clarity) but is accounted for in Figure 21 (right) and in the final sensitivity. One thing to note in Table IX is that the event

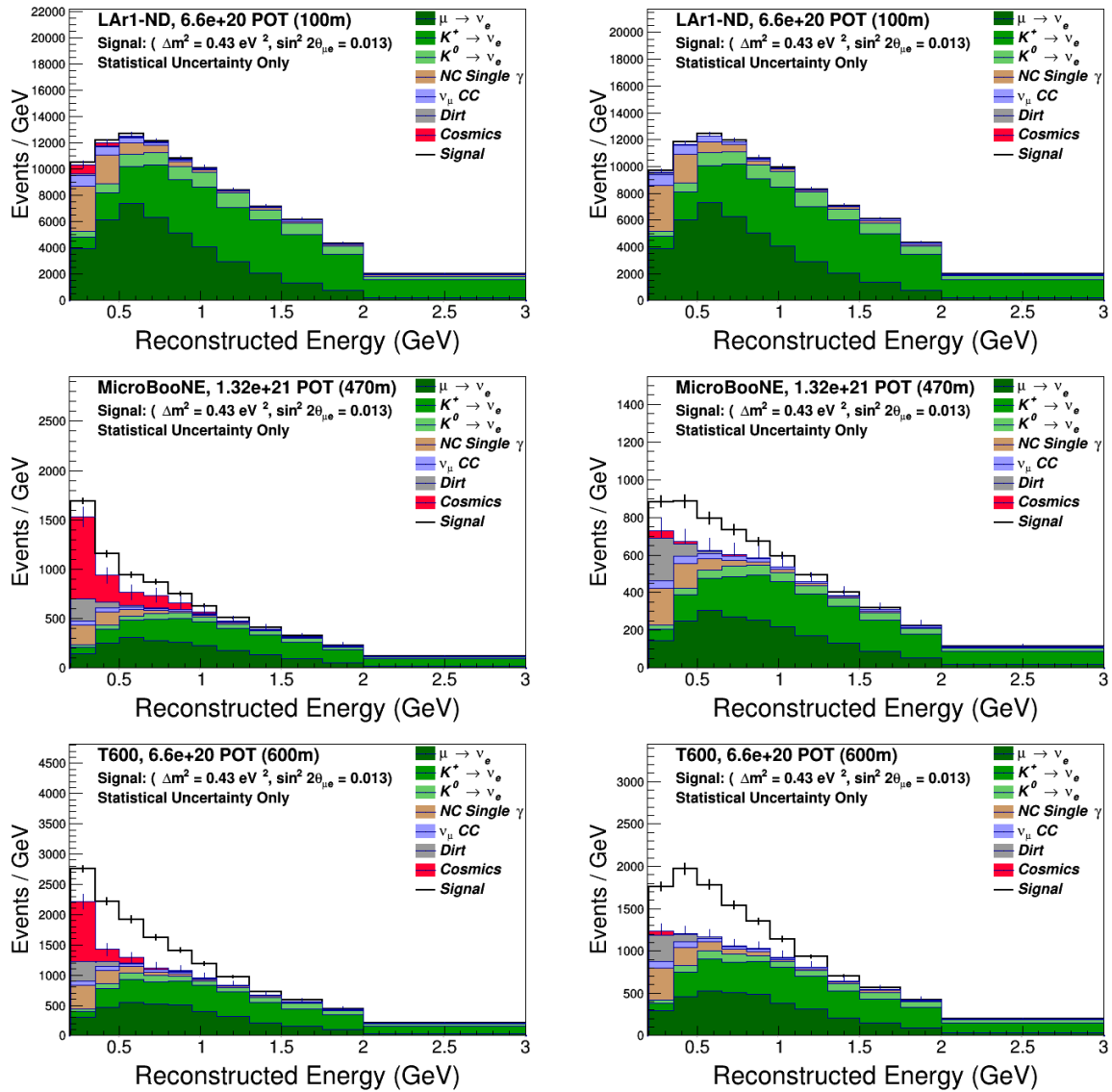


**FIG. 21:** Electron neutrino charged-current candidate distributions in LAr1-ND (top), MicroBooNE (middle), and ICARUS-T600 (bottom) shown as a function of reconstructed neutrino energy. All backgrounds are shown. In the left column, only muon proximity and  $dE/dx$  cuts have been used to reject cosmogenic background sources. In the right column, a combination of the internal light collection systems and external cosmic tagger systems at each detector are assumed to conservatively identify 95% of the triggers with a cosmic muon in the beam spill time and those events are rejected. Oscillation signal events for the best-fit oscillation parameters from Kopp et al. [41] are indicated by the white histogram on top in each distribution.

counts listed for Dirt and Cosmogenic events are larger than those given in Sections II F and II G. This is a result of energy smearing effects which are properly simulated in the final sensitivity analysis ( $15\%/\sqrt{E}$ ), but not in the earlier stages of simulations where true energies were used to display the predictions. The predicted background energy spectra are provided well below the 200 MeV cutoff value used in the analysis such that events can be properly smeared in both directions. Because both backgrounds are steeply falling functions of photon



**TABLE IX:** *Event rates in the  $\nu_e$  charged-current candidate sample in the range 200–3000 MeV reconstructed neutrino energy for  $6.6 \times 10^{20}$  protons on target in LAr1-ND and the ICARUS-T600 and  $13.2 \times 10^{20}$  protons on target in MicroBooNE. The numbers listed correspond to the application of topological cuts 1) & 2) for reducing cosmogenic backgrounds. In parentheses are indicated the reduced cosmogenic background rate when a 95% efficient time-based ID system is used to reject contaminated triggers. Vetoing of these events results in a reduction of all beam related event categories of 1.5%, 2%, and 3% in LAr1-ND, MicroBooNE, and ICARUS, respectively, which is not shown (for clarity) but is accounted for in Figure 21 and 22.*

	LAr1-ND $6.6 \times 10^{20}$ p.o.t.	MicroBooNE $13.2 \times 10^{20}$ p.o.t.	ICARUS-T600 $6.6 \times 10^{20}$ p.o.t.
$\mu \rightarrow \nu_e$	6,712	338	607
$K^+ \rightarrow \nu_e$	7,333	396	706
$K^0 \rightarrow \nu_e$	1,786	94	180
NC $\pi^0 \rightarrow \gamma\gamma$	1,356	81	149
NC $\Delta \rightarrow \gamma$	87	5	9
$\nu_\mu$ CC	484	35	51
Dirt events	44	47	67
Cosmogenic events <sup>a</sup>	170 (9)	220 (11)	204 (10)
Signal ( $\Delta m^2 = 0.43 \text{ eV}^2$ , $\sin^2 2\theta = 0.013$ ) [41]	114	136	498

<sup>a</sup>These predictions exclude a small correction from the case where an unidentified neutrino interaction provides the scintillation trigger, as discussed in Section II G.

energy, more events smear into the analysis range than smear out. This is properly handled in the analysis and leads to an increase in event count relative to the earlier values which cut on generated photon energies.

Figure 22 presents the experimental sensitivity of the proposed Fermilab SBN program to  $\nu_\mu \rightarrow \nu_e$  appearance signals in the  $(\Delta m^2, \sin^2 2\theta)$  plane compared to the original LSND allowed region [26]. The sensitivity shown includes the additional 95% cosmic background rejection coming from timing information described above and illustrated on the right in Figure 21. We compare this to the case using only TPC topology cuts to identify cosmogenic events below. The LSND 99% C.L. allowed region is covered at the  $\geq 5\sigma$  level above  $\Delta m^2 = 0.1 \text{ eV}^2$  and  $> 4.5\sigma$  everywhere. Note that the region below  $\Delta m^2 = 0.1 \text{ eV}^2$  is already ruled out at more than  $5\sigma$  by the previous results of ICARUS at Gran Sasso (see Figure 8).

The sensitivity results presented in Figure 22 incorporate all background sources and related uncertainties described in this proposal except detector related systematics as introduced in Section II E. Each of the rate predictions and other systematic uncertainties (i.e. flux and cross section) in the analysis are built using advanced, sophisticated simulation programs, while current estimates of detector related systematics come from hand scanning of events, empirical experience with these and other detectors, or toy Monte Carlo studies, and so are difficult to incorporate with the same sophistication at this time. Instead, studies to investigate the level of uncorrelated detector systematics that can be tolerated while preserving the experimental sensitivity have indicated that total uncertainties in the 2–3% range are acceptable. All studies performed to date suggest these can be well controlled for a multi-detector experiment, with individual studies coming in at  $\leq 1\%$  (see Section II E).

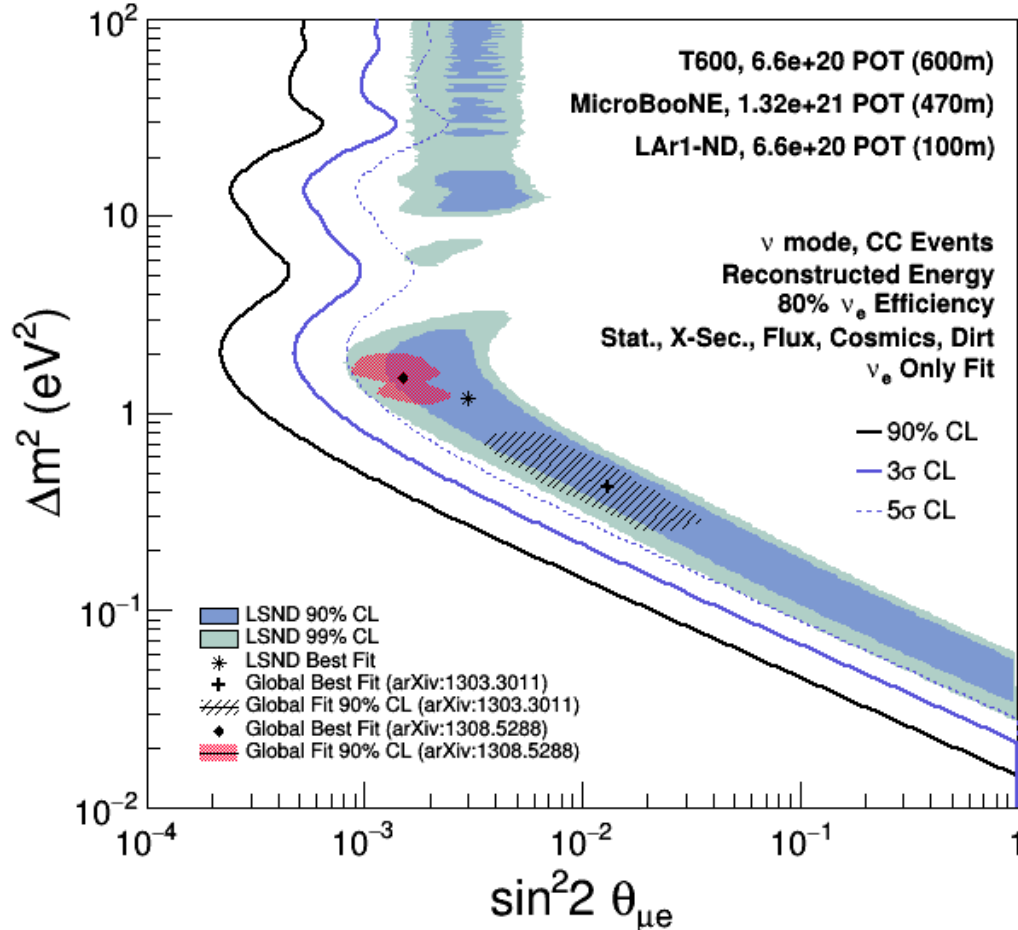


**FIG. 22:** Sensitivity of the SBN Program to  $\nu_\mu \rightarrow \nu_e$  oscillation signals. All backgrounds and systematic uncertainties described in this proposal (except detector systematics, see text) are included. The sensitivity shown corresponds to the event distributions on the right in Figure 21, which includes the topological cuts on cosmic backgrounds and an additional 95% rejection factor coming from an external cosmic tagging system and internal light collection system to reject cosmic rays arriving at the detector in time with the beam.

In Figure 23, we present the sensitivity in a different way that facilitates easier comparison between different results. Rather than displaying fixed confidence level contours (90%,  $3\sigma$ ,  $5\sigma$ ) in the  $(\Delta m^2, \sin^2 2\theta)$  plane, we plot the significance with which the experiment covers the 99% C.L. allowed region of the LSND experiment as a function of  $\Delta m^2$ . The curves are extracted by asking what  $\chi^2$  value the analysis produces at each point along the left edge of the 99% C.L. LSND region. The gray bands correspond to  $\Delta m^2$  ranges where LSND reports no allowed regions at 99% C.L.

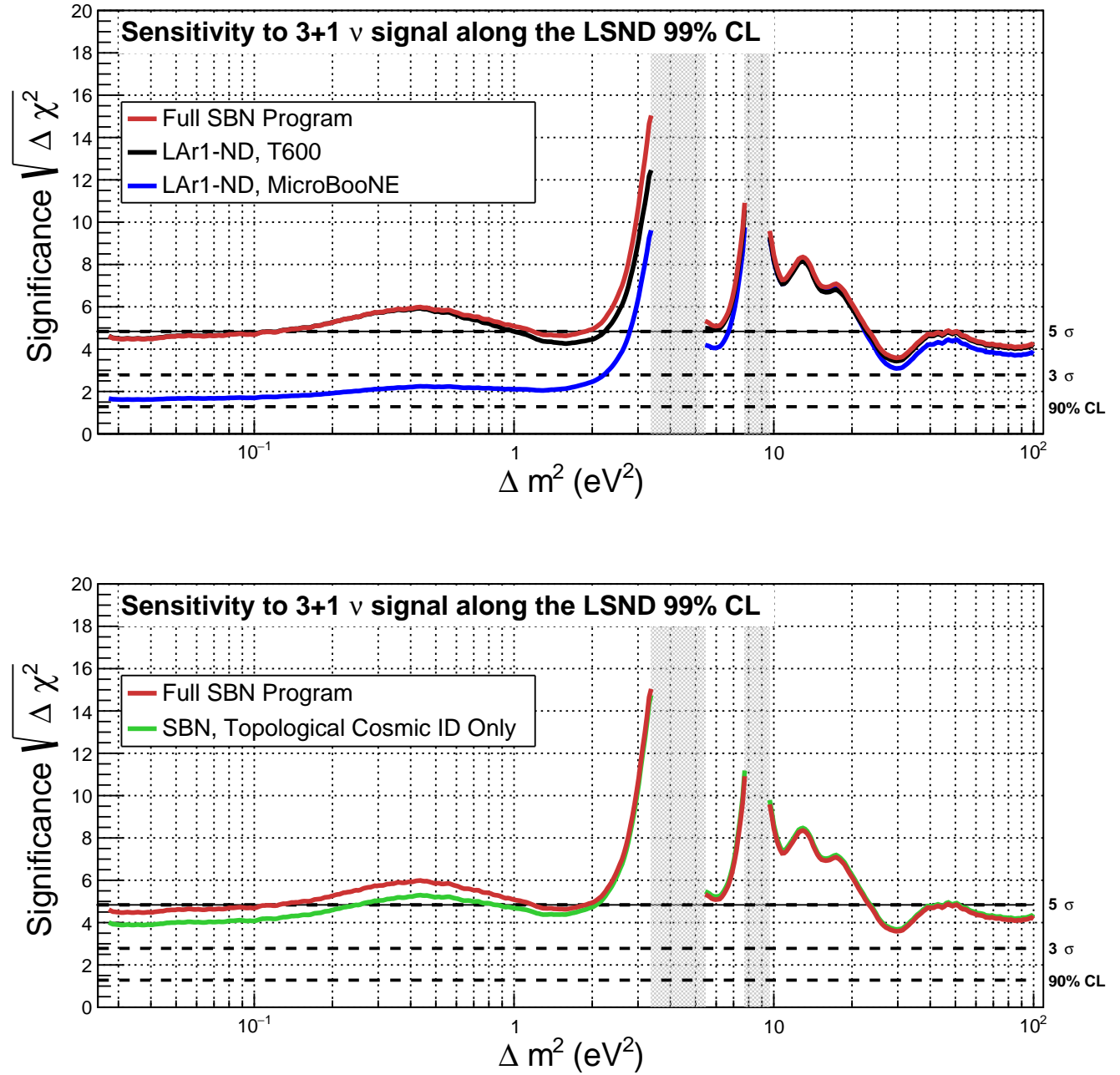
Two versions of this plot are shown in Figure 23. The top presents the significance at which the LSND region would be covered for the different possible combinations of SBN detectors: LAr1-ND + MicroBooNE only (blue), LAr1-ND + ICARUS only (black), and all three detectors in combination (red). This presentation makes clear the contributions of the MicroBooNE and ICARUS-T600 detectors as far detectors in the oscillation search. The presence of the large mass added by the ICARUS-T600 detector is imperative to achieving  $5\sigma$  coverage. In addition,

MicroBooNE, by starting to run several years earlier, makes a valuable contribution particularly in the important  $1 \text{ eV}^2$  region.

The bottom plot shows the full program sensitivity compared to the result when only topological information from the TPC is used to reject cosmogenic backgrounds as described above. This is equivalent to comparing the cases depicted in the left and right columns of Figure 21. The backgrounds at low energy impact the low- $\Delta m^2$  region most and the ability to further suppress cosmic backgrounds through precise timing information clearly represents an improvement in the sensitivity at low  $\Delta m^2$  of about  $0.75\sigma$ .

We note that the selection criteria used here for the rejection of the dirt and cosmogenic backgrounds were chosen to illustrate the sensitivity of the proposed program in a conservative way. For example, the fiducial cut on dirt backgrounds was chosen to aggressively remove this background but also reduces the fiducial volume (signal statistics) significantly. A detailed optimization would likely result in a looser fiducial cut, allowing for an increase in signal statistics. Similarly, a conservative rejection factor of 20 has been assumed for the combination of an external veto system and timing from the light detection systems. Achieving a higher rejection factor from these systems would have significant positive impact on the program.

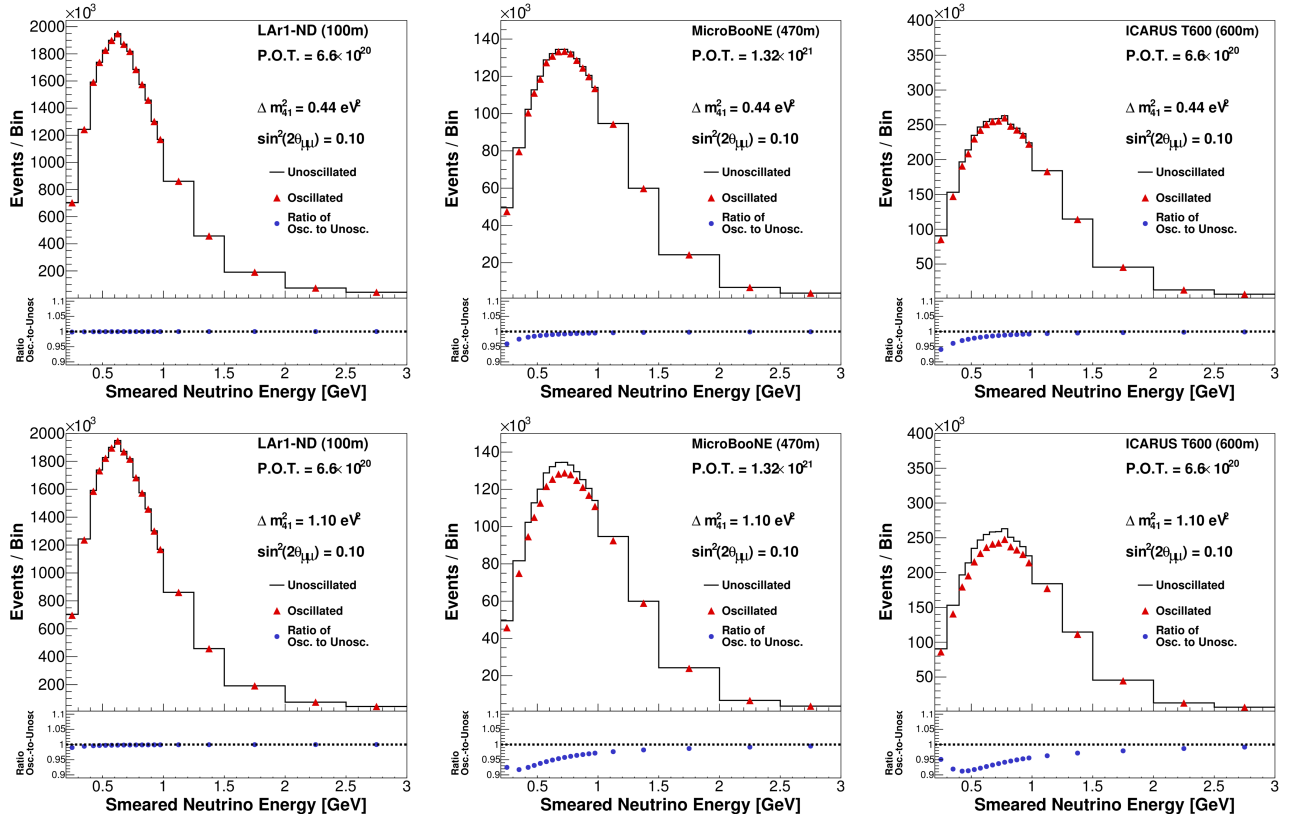
Finally, we note that this is a statistically limited measurement. An increase in the number of neutrino interactions either through delivery of more protons to the target or a more efficient target and horn system would greatly benefit the program. For this reason, we propose the further study of BNB improvements like those described in Part V of this proposal.



**FIG. 23:** Sensitivity comparisons for  $\nu_\mu \rightarrow \nu_e$  oscillations including all backgrounds and systematic uncertainties described in this proposal (except detector systematics, see text) assuming  $6.6 \times 10^{20}$  protons on target in LAr1-ND and the ICARUS-T600 and  $13.2 \times 10^{20}$  protons on target in MicroBooNE. (Top) The three curves present the significance of coverage of the LSND 99% allowed region (above) for the three different possible combinations of SBN detectors: LAr1-ND + MicroBooNE only (blue), LAr1-ND + ICARUS only (black), and all three detectors (red). (Bottom) Comparison of the sensitivity with only topological cosmic background rejection and with additional suppression from timing information (see text).

### I. $\nu_\mu \rightarrow \nu_x$ Disappearance Sensitivity

The  $\nu_\mu$  disappearance sensitivity for the SBN Program is also estimated. The background evaluation is not as complete as for the  $\nu_e$  analysis, in particular possible contributions from dirt or cosmogenic sources are not considered, but they are expected to be small compared to the high  $\nu_\mu$  CC rate. The critical aspects to this evaluation are the neutrino flux and interaction model uncertainties described in Sections II C and II D. The absolute flux and cross section uncertainties in any detector along the BNB are larger than 10%, but the high correlations between the near detector and the MicroBooNE/ICARUS-T600 event samples along with the excellent statistical precision of the LAr1-ND measurements will make the SBN program the most sensitive  $\nu_\mu$  disappearance experiment at  $\Delta m^2 \sim 1 \text{ eV}^2$ .



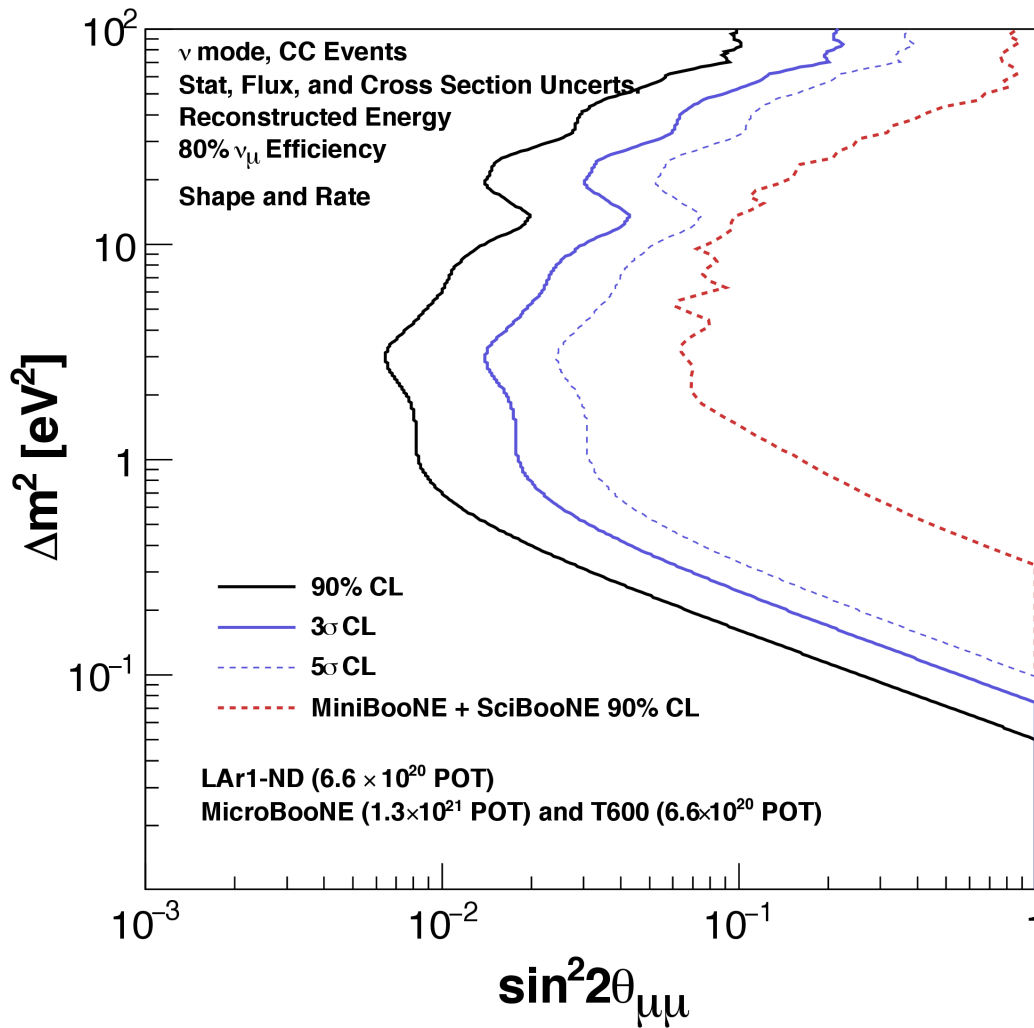
**FIG. 24:** Examples of  $\nu_\mu$  disappearance signals in the SBN detectors for  $\Delta m^2 = 0.44 \text{ eV}^2$  (top) and  $\Delta m^2 = 1.1 \text{ eV}^2$  (bottom).

Figure 25 presents the  $\nu_\mu$  disappearance sensitivity assuming  $6.6 \times 10^{20}$  protons on target exposure in LAr1-ND and ICARUS-T600 and  $13.2 \times 10^{20}$  protons on target in MicroBooNE. The red curve is the 90% confidence level limit set by the SciBooNE and MiniBooNE joint analysis [42] and is to be compared to the solid black curve (also 90% C.L.) for the LAr SBN program presented here. SBN can extend the search for muon neutrino disappearance an order of magnitude beyond the combined analysis of SciBooNE and MiniBooNE. Figure 24 shows two examples of  $\nu_\mu \rightarrow \nu_x$  oscillation signals (for  $\Delta m^2 = 0.44 \text{ eV}^2$  and  $1.1 \text{ eV}^2$ ) in the three detectors for the exposures given above.

The  $\nu_\mu$  disappearance measurement is a critical aspect of the SBN program and is needed to confirm a signal, if seen in  $\nu_e$  appearance, as oscillations. A genuine  $\nu_\mu \rightarrow \nu_e$  appearance can

also be accompanied by a disappearance of the intrinsic  $\nu_e$  beam component, since the three oscillation probabilities are related through a common mixing matrix. As an example, in the case of one additional sterile neutrino,  $\sin^2 2\theta_{\mu e} \leq 1/4 \sin^2 2\theta_{\mu\mu} \cdot \sin^2 2\theta_{ee}$ , which is valid for small mixing angles.

The ability to perform searches for oscillation signals in multiple channels is a major advantage for the FNAL SBN oscillation physics program. By collecting the  $\nu_\mu$  and  $\nu_e$  event samples in the same experiment at the same time, correlations between the samples can be well understood and many systematics are common. This implies that a simultaneous analysis of  $\nu_e$  CC and  $\nu_\mu$  CC events will be a very powerful way to explore oscillations and untangle the effects of  $\nu_\mu \rightarrow \nu_e$ ,  $\nu_\mu \rightarrow \nu_x$ , and  $\nu_e \rightarrow \nu_x$ , if they exist, in this mass-splitting range.



**FIG. 25:** Sensitivity prediction for the SBN program to  $\nu_\mu \rightarrow \nu_x$  oscillations including all backgrounds and systematic uncertainties described in this proposal (except detector systematics, see text). SBN can extend the search for muon neutrino disappearance an order of magnitude beyond the combined analysis of SciBooNE and MiniBooNE.

### III. Other SBN Physics

The SBN program of three LAr-TPC detectors along the Fermilab Booster Neutrino Beam delivers a rich physics opportunity in addition to the oscillation searches detailed in Section II. We only briefly introduce some of them here. In some cases, more details can be found in the individual detector Design Reports, Part II (LAr1-ND) and Part III (ICARUS-T600) of this proposal.

#### A. Neutrino-Argon Interactions

Precise neutrino-nucleus cross section measurements are a fundamental prerequisite for every neutrino oscillation experiment, including the future LAr long-baseline neutrino program. In the GeV energy range, as a result of competitive physical processes and complicated nuclear effects, neutrino interactions on argon include a wide variety of final states. These can range from the emission of single or multiple nucleons to more complex topologies with multiple pions or other hadrons, all in addition to the leading lepton in charged-current events. Liquid argon TPC technology is particularly well suited to studying these interactions because of its excellent particle identification capability and calorimetric energy reconstruction down to very low thresholds.

The SBN Program provides an ideal venue to conduct precision cross-section measurements in the few hundred MeV to few GeV energy range using the well characterized fluxes of the BNB [13]. The detectors will collect neutrino samples with high statistics and will make the world's best measurements of  $\nu_\mu$ -Ar and  $\nu_e$ -Ar scattering. MicroBooNE will lead with initial measurements and pave the way for the T600 and LAr1-ND to follow with even larger data sets for increased precision, including for rarer processes such as  $\nu e$  scattering, strange particle production, multi-nucleon and multi-pion production, and coherent scattering with an argon nucleus. Analysis of the different data sets will enable important cross-checks and each brings valuable additions to the physics reach. The larger dimensions of the T600 will mean more complete containment of event final states including high energy muons and neutrons, leading to improved particle identification and energy reconstruction for some event classes. MicroBooNE and ICARUS will both also record large samples of events from the off-axis flux of the NuMI neutrino beam [84] with its higher electron neutrino content and different energy spectrum. LAr1-ND, due to its proximity to the BNB source, will contribute the largest statistics, recording millions of neutrino interactions in a few year run. In Part II of this proposal a table is provided that details the event rates for different event categories in the near detector (Table I).

#### B. Additional Searches

If short-baseline neutrino oscillations are observed in charged-current channels, then it will be possible to “prove” the existence of sterile neutrinos by searching for the disappearance of NC  $\pi^0$  scattering events,  $\nu_\mu Ar \rightarrow \nu_\mu \pi^0 X$ , in MicroBooNE and ICARUS-T600 relative to LAr1-ND. As demonstrated by the MicroBooNE experiment [85], this is a clean event sample with little background. Although the incident neutrino energy is not determined (the outgoing neutrino typically carries off most of the incident neutrino energy), a decrease in this event rate in the MicroBooNE and ICARUS-T600 detectors would indicate the oscillation of active neutrino states into sterile neutrino states.

SBN experiments will have good sensitivity to possible sterile neutrino decay. For the scenario of reference [86, 87], an active neutrino interacts by a neutral-current process inside the detector and produces a heavy neutrino (with a mass of a few hundred MeV) that quickly decays into a photon and a lighter neutrino. The signature, therefore, is an interaction vertex in the upstream portion of the detector and a single photon in the downstream portion of the detector, where the photon does not point back to the interaction vertex. With the superb spatial resolution and high event rates, this process can be searched for with good sensitivity. The near detector has the advantage of high statistics, while MicroBooNE and the T600 have longer volumes for observing the decay.

SBN will also be able to search for sub-GeV dark matter (mass less than a few hundred MeV) [88–90] by running in beam-dump mode, where the 8 GeV proton beam is steered above the beryllium target and into the 50 m (or 25 m) downstream absorber. Beam-dump mode reduces the neutrino flux by a factor of  $\sim 50$ , which makes the experiments more sensitive to low mass dark matter coming from  $\pi^0$  and  $\eta$  decay or from proton bremsstrahlung in the steel beam dump. The existence of low mass dark matter can then be inferred from the enhancement of neutral-current events relative to charged-current  $\nu_\mu$  events compared to this ratio in normal beam-on-target running. Three different neutral-current channels can be studied: neutrino-electron elastic scattering, neutrino-nucleon elastic scattering, and neutral-current  $\pi^0$  production ( $\nu Ar \rightarrow \pi^0 X$ ). For each channel, low mass dark matter scattering on carbon will look just like neutral current neutrino scattering on carbon, and this will result in an enhancement of neutral current events. As a proof of principle, the MiniBooNE experiment just completed a one-year beam-dump run to search for low mass dark matter, and results are expected in 2015.



**A Proposal for a Three Detector  
Short-Baseline Neutrino Oscillation Program  
in the Fermilab Booster Neutrino Beam**

---

*Part 2: LAr1-ND Conceptual Design*

---

## I. Introduction

The Fermilab Short Baseline Neutrino program includes the construction of a Liquid Argon Near Detector, LAr1-ND, at 110 m from the Booster neutrino source in a new enclosure. Leveraging the advanced design work performed for LBNE and the very recent experience of the MicroBooNE detector construction, the LAr1-ND project has the potential to move forward quickly. As described in Part I, LAr1-ND serves as the near detector in a three LAr-TPC experiment capable of definitively addressing existing anomalies in neutrino physics and making precision measurements of high- $\Delta m^2$  neutrino oscillations through both appearance and disappearance searches.

Due to the high event rate of neutrino interactions at the near location, significant physics output can be achieved with a relatively short run of the LAr1-ND experiment. In addition to the physics program, LAr1-ND, following the MicroBooNE model, will have a development program serving as an engineering prototype for LAr-TPCs for long-baseline CP-violation searches in the future.

This Conceptual Design Report for the LAr1-ND detector is organized as follows. Section II briefly reviews the LAr1-ND stand alone physics program. A short introduction to the LAr1-ND detector design and dimensions is given in Section III. Section IV presents the TPC design, while the TPC electronics, DAQ and trigger systems are described in Section V. Section VI describes a UV laser-based field calibration system. Different options for the scintillation light collection system under consideration are described in Section VII. An external cosmic ray tagging system will complement the experiment, as reported in Section VIII.

## II. Physics of LAr1-ND

While LAr1-ND, in conjunction with MicroBooNE and the ICARUS-T600, is a critical part of the oscillation physics program described in Part I, as a stand alone detector it enables a large number of relevant physics results. In this section we will discuss a sub-set of the physics measurements that can be performed with LAr1-ND. These include studies of a possible MiniBooNE-like low energy excess of electromagnetic events that does not depend on the distance.

### A. MiniBooNE Low Energy Excess

Looking for the low energy excess observed by the MiniBooNE experiment [91] and characterizing its nature is the main physics goal of the MicroBooNE experiment [92]. This excess of electromagnetic events could be due to neutrino interactions with either a single-electron or single-photon in the final state. Observation of a low energy excess signal by MicroBooNE in the years leading up to the beginning of LAr1-ND data taking would immediately lead to the question of whether that excess is intrinsic to the beam or appears over the 470 m distance between source and detector.

LAr1-ND, at 110 m from the BNB target, can search for the same excess in a relatively short time. Here we estimate the significance with which LAr1-ND would observe *the same* MiniBooNE-like electromagnetic excess in the  $\nu_e$  candidate sample. The methods used to estimate signal predictions for LAr1-ND for the model described above follows those of a study performed by the MicroBooNE Collaboration [93]. Specifically, the excess of events observed

from MiniBooNE is scaled to the LAr1-ND predicted reconstructed rates. This is done accounting for the MiniBooNE reconstruction and particle identification efficiencies as reported in [94] to correct the raw excess event rates in MiniBooNE as a function of  $(E_{lep}, \theta_{lep})$ , and subsequently using the Monte Carlo predicted 2D matrix  $[E_{\nu}^{true}, E_{lep}]$  for charged current inclusive events on argon in order to properly correct for the cross-section dependence of Ar versus CH<sub>2</sub> and the flux ratio at LAr1-ND with respect to MiniBooNE. Because only the lepton energy and angle are available in MiniBooNE data, we investigate the excess in LAr1-ND as a function of the ‘lepton candidate’ energy (after accounting for shower energy smearing).

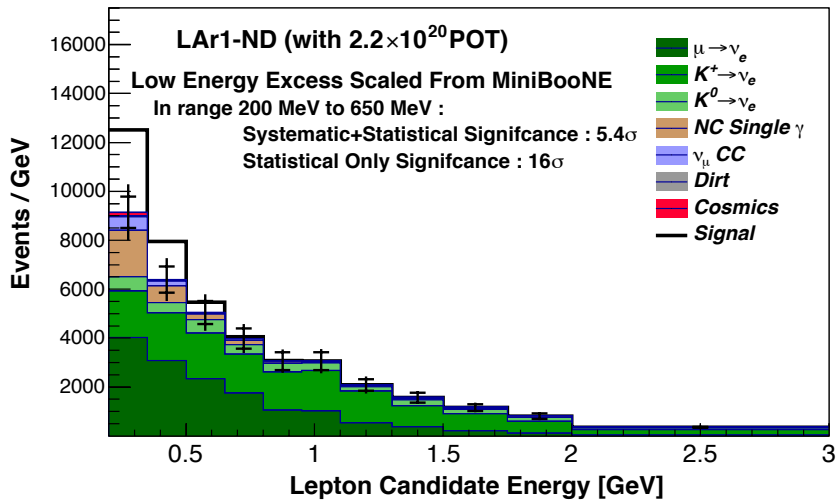


**FIG. 26:** Scaled MiniBooNE low energy excess events as a function of the lepton candidate energy in LAr1-ND for an exposure of  $2.2 \times 10^{20}$  protons on target and using the same fiducial volume and backgrounds as the  $\nu_e$  appearance analysis described in Part I of the proposal. The signal prediction assumes the effect observed by MiniBooNE is electrons but is not distance dependent. For the uncertainty on the background distribution the inner bars represent the statistical uncertainty and the outer bars represent the statistical + systematic uncertainties (see Part I).

Using the  $\nu_e$  charged current inclusive backgrounds and systematic uncertainties discussed in Part I, we quantify the significance of a MiniBooNE-like excess in LAr1-ND. In Fig. 26, we report the excess events stacked on top of the expected backgrounds. In the 200–650 MeV range in lepton energy, 803 excess events are expected, compared to a background of 3,177 events for an exposure of  $2.2 \times 10^{20}$  protons on target. This is a  $5.4\sigma$  signal including both systematic and statistical uncertainties. Considering only statistical uncertainties, the excess sits  $> 10\sigma$  above the background.

If MicroBooNE observes an excess of photons which are due to an as-yet unknown source of neutral current interactions producing single photons in the final state, LAr1-ND at 110 m will immediately confirm that the excess is intrinsic to the beam (i.e. that it is due to some un-modeled neutral current interaction). Also, the event rate with which LAr1-ND will be able to study these events will be more than one order of magnitude larger than MicroBooNE. Such a sample will enable a measurement of this reaction with great precision and inform the development of cross section models in this energy range to include this process.

## B. Neutrino Cross Section Measurements

As discussed in Part I, neutrino-nucleus interactions are critical to understand in neutrino oscillation experiments, including the future liquid argon long-baseline program. LAr1-ND provides an ideal venue to conduct precision cross section measurements in the GeV energy range. The experiment will collect enormous neutrino event samples and, continuing the studies done by MicroBooNE and ICARUS, will make the world's highest statistics cross section measurements for many  $\nu$ -Ar scattering processes.

Table X shows the expected rates of  $\nu_\mu$  and  $\nu_e$  events separated into their main experimental topologies for an exposure of  $6.6 \times 10^{20}$  protons on target (POT). A novel approach based on the event categorization in terms of exclusive topologies can be used to analyze data and provide precise cross section measurements in many different  $\nu_\mu$  and  $\nu_e$  exclusive channels. Included for reference, we also show the classification by physical process from Monte Carlo truth information.

The largest event sample corresponds to a  $\nu_\mu$  charged-current 0 pion final state, where there is an outgoing  $\mu^-$ , one or more recoil nucleons, and no outgoing pions or kaons. This cross section for scattering off nuclei largely depends on final state interactions and other nuclear effects and LAr1-ND data will allow the study of nuclear effects in neutrino interactions in argon nuclei with high precision.

In LAr1-ND more than 2 million neutrino interactions will be collected per year in the full active volume (assuming  $2.2 \times 10^{20}$  POT), with 1.5 million  $\nu_\mu$  and 12,000  $\nu_e$  charged current (CC) events. One year exposure of LAr1-ND will provide an event sample 6-7 times larger than will be available in the full MicroBooNE phase I run.

Comparison of  $\nu_e$  CC and  $\nu_\mu$  CC cross sections is very important. By lepton universality, the cross sections should be the same after correcting for the outgoing charged-lepton mass. A difference in the cross sections would indicate a new process that violates lepton universality.

LAr1-ND will also see several hundred  $\nu_\mu e \rightarrow \nu_\mu e$  elastic scattering events in  $6.6 \times 10^{20}$  POT. These events are easily identified by an outgoing electron along the neutrino beam direction with  $\cos\theta > 0.99$  and with no recoil nucleons. With this event sample, a measurement of  $\sin^2\theta_W$  can be made at relatively low energy to be compared with the world average.

We expect approximately a quarter million NC elastic scattering events identified by a single nucleon (proton or neutron) recoil track. If the recoil proton events can be cleanly separated from the recoil neutron events, then it may be possible to make a competitive measurement of  $\Delta s$ , the strange quark contribution to the proton spin.

Finally, by using the same neutrino beam that was used by the MiniBooNE experiment, we will be able to directly compare neutrino cross sections off carbon ( $A = 12$ ) and argon ( $A = 40$ ) targets and search for a nuclear dependence of the cross section.

## III. Overview of the LAr1-ND Detector

The design of the LAr1-ND detector [7] builds on many years of LAr TPC detector R&D and experience from design and construction of the ICARUS-T600, ArgoNeuT, MicroBooNE, and LBNF detectors. The basic concept of the LAr1-ND detector, based on LBNF-type technology, is to construct a membrane-style cryostat at 110 m from the Booster neutrino source in a new enclosure adjacent to and directly downstream of the existing SciBooNE hall. The membrane cryostat will house multiple cathode plane assembly (CPA) and anode plane assemblies (APAs) to read out ionization electron signals. The APAs located near the beam-left and beam-right

Process		No. Events	Events/ ton	Stat. Uncert.
$\nu_\mu$ Events (By Final State Topology)				
CC Inclusive		5,212,690	46,542	0.04%
CC 0 $\pi$	$\nu_\mu N \rightarrow \mu + Np$	3,551,830	31,713	0.05%
	· $\nu_\mu N \rightarrow \mu + 0p$	793,153	7,082	0.11%
	· $\nu_\mu N \rightarrow \mu + 1p$	2,027,830	18,106	0.07%
	· $\nu_\mu N \rightarrow \mu + 2p$	359,496	3,210	0.17%
	· $\nu_\mu N \rightarrow \mu + \geq 3p$	371,347	3,316	0.16%
CC 1 $\pi^\pm$	$\nu_\mu N \rightarrow \mu + \text{nucleons} + 1\pi^\pm$	1,161,610	10,372	0.09%
CC $\geq 2\pi^\pm$	$\nu_\mu N \rightarrow \mu + \text{nucleons} + \geq 2\pi^\pm$	97,929	874	0.32%
CC $\geq 1\pi^0$	$\nu_\mu N \rightarrow \mu + \text{nucleons} + \geq 1\pi^0$	497,963	4,446	0.14%
NC Inclusive		1,988,110	17,751	0.07%
NC 0 $\pi$	$\nu_\mu N \rightarrow \text{nucleons}$	1,371,070	12,242	0.09%
NC 1 $\pi^\pm$	$\nu_\mu N \rightarrow \text{nucleons} + 1\pi^\pm$	260,924	2,330	0.20%
NC $\geq 2\pi^\pm$	$\nu_\mu N \rightarrow \text{nucleons} + \geq 2\pi^\pm$	31,940	285	0.56%
NC $\geq 1\pi^0$	$\nu_\mu N \rightarrow \text{nucleons} + \geq 1\pi^0$	358,443	3,200	0.17%
$\nu_e$ Events				
CC Inclusive		36798	329	0.52%
NC Inclusive		14351	128	0.83%
Total $\nu_\mu$ and $\nu_e$ Events		7,251,948	64,750	
$\nu_\mu$ Events (By Physical Process)				
CC QE	$\nu_\mu n \rightarrow \mu^- p$	3,122,600	27,880	
CC RES	$\nu_\mu N \rightarrow \mu^- \pi N$	1,450,410	12,950	
CC DIS	$\nu_\mu N \rightarrow \mu^- X$	542,516	4,844	
CC Coherent	$\nu_\mu Ar \rightarrow \mu Ar + \pi$	18,881	169	

**TABLE X:** Estimated event rates using GENIE (v2.8) in the LAr1-ND active volume (112 t) for a  $6.6 \times 10^{20}$  exposure. In enumerating proton multiplicity, we assume an energy threshold on proton kinetic energy of 21 MeV. The  $0\pi$  topologies include any number of neutrons in the event.

walls of the cryostat will each hold 3 planes of wires with 3 mm wire spacing. The wire readout arrangement is identical to MicroBooNE, with banks of cold electronics boards at the top and one vertical side of each APA. The total number of readout channels is 5,632 per side (11,264 in the entire detector). The CPAs have the same dimensions as the APAs and are centered between them. Each pair of facing CPA and APA hence forms an electron-drift region. The open sides between each APA and the CPA are surrounded by 4 Field Cage Assembly (FCA) modules, constructed from FR4 printed circuit panels with parallel copper strips, to create a uniform drift field. The drift distance between each APA and the CPA is 2 m, such that the cathode plane will need to be biased at -100 kV to create an electric field of 500 V/cm. Accurate mapping of the electric field in the drift region will be performed through a UV laser-based calibration system. The active volume is 4.0 m (width)  $\times$  4.0 m (height)  $\times$  5.0 m (length), containing 112

tons of liquid argon. The LAr1-ND design will additionally include a light collection system for the detection of scintillation light and the detector will be complemented by an external cosmic ray tagging system. In addition, we are looking into the possibility of placing shielding over the near detector should it be deemed necessary to reduce cosmogenic backgrounds.

Overall, the design philosophy of the LAr1-ND detector is to serve as a prototype for LBNF that functions as a physics experiment. While the present conceptual design described here is an excellent test of LBNF detector systems sited in a neutrino beam, the LAr1-ND collaboration is exploring innovations in this design and the opportunity to further test them in a running experiment.

### A. Detector Dimensions

The LAr1-ND detector size has been optimized with respect to the preliminary design described in the LAr1-ND proposal [7]. In the original proposal the detector was designed to be located in the existing experimental enclosure that previously housed the SciBooNE experiment, at 100 m from the BNB target. The dimensions of the detector were dictated by the size of the enclosure, leading to an active volume of 4.0 m (width)  $\times$  4.0 m (height)  $\times$  3.6 m (length), containing 82 tons of liquid argon. Studies reported in Ref. [10] indicated the advantage of locating the near detector in a new enclosure, directly downstream of the existing SciBooNE enclosure at 110 m. A new building opens the question of the detector dimensions and optimizing it for physics. Enlarging the dimensions in the transverse directions has not been considered in order to maintain the 2 m maximum drift length and the height of the detector (to avoid larger excavation costs). However, Monte Carlo studies of muon containment and photon background rejection as a function of the detector length in the beam direction have been performed.

Figure 27 shows the breakdown of the fate of muons produced in  $\nu_\mu$  CC interactions in a fixed fiducial volume as a function of the overall active detector length. In a 4.0 m (width)  $\times$  4.0 m (height)  $\times$  3.6 m (length) detector, 53% of muons are contained (so muon momentum can be measured through calorimetric reconstruction with very good accuracy), 35% exit with a track longer than 1 m (so muon momentum is measured by multiple scattering, with less accuracy), and the remaining 12% exit with a track shorter than 1 m (so muon momentum cannot be measured). Increasing the length of the detector in the direction of the beam to 5 m increases the fraction of fully contained muons to 62%, a 17% fractional increase. The 11% minimum on the fraction of exiting muons shown in the plot is due to tracks that leave the volume through the sides of the detector, and can be reduced by tightening the fiducial volume definition.

## IV. TPC Design

The conceptual design for LAr1-ND is shown in Figure 28a which shows the TPC housed inside a membrane-style cryostat. The LAr active volume is a rectangular parallelepiped with dimensions of 4 m vertically, 4 m horizontally, and 5 m along the beam direction. The TPC consists of four anode plane assemblies (APAs) and two central cathode plane assemblies (CPAs), as indicated in Figure 28b. The APAs and CPAs are large-scale elements with an area of 4 m  $\times$  2.5 m each. The overall dimensions of the individual APAs are restricted to be increments of the top (192 mm) and side (222 mm) readout board dimensions. The TPC is oriented

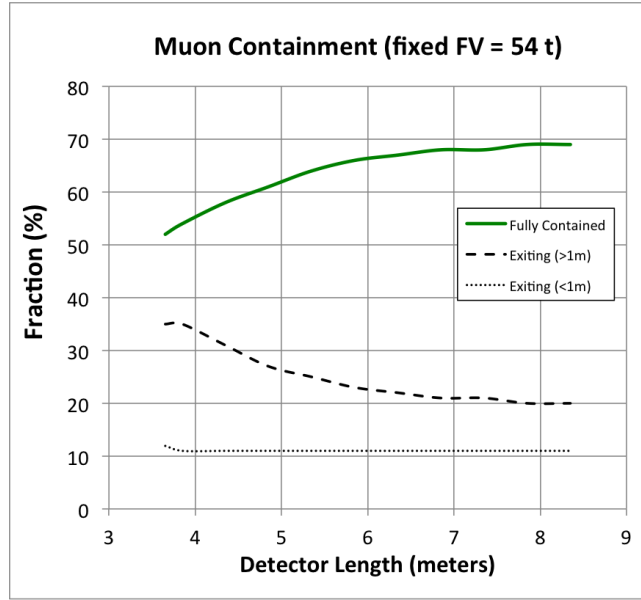


**FIG. 27:** Muon containment as a function of the detector length in the beam direction.

such that the Booster neutrino beam passes perpendicular to the drift direction. The TPC key design parameters are summarized in Table XI.

The main requirements of the TPC are:

1. The TPC volume is large enough to achieve the physics goals of the experiment. The 4 m × 4 m dimensions of the TPC active volume in the transverse (perpendicular to beam) directions and 5 m dimension in the longitudinal (along beam) direction are determined based on studies of signal containment and background rejection (see Section III A).
2. The 3 mm wire pitch is chosen, as in the MicroBooNE and ICARUS-T600 detectors, to enable electron/photon separation to be achieved with identical efficiency.

**TABLE XI:** LAr1-ND TPC key design parameters.

TPC Parameter	Value
TPC active volume	5 m (L) × 4 m (H) × 4 m (W), 112 metric ton active LAr mass
Number of TPC cells	2 drift volumes, 2 m drift length in each
Maximum drift time	1.28 ms
Anode Plane Assembly	2.5 m × 4 m active area, with cold electronics mounted on 2 sides
Wire properties	150 μm, CuBe
Wire planes	3 planes on each APA, U & V at ±60° to vertical (Y)
Cathode bias	-100 kV at 500 V/cm drift field
Number of Wires	2816 channels/APA, 11264 wires total in TPC
Wire tension	0.5 kg at room temperature

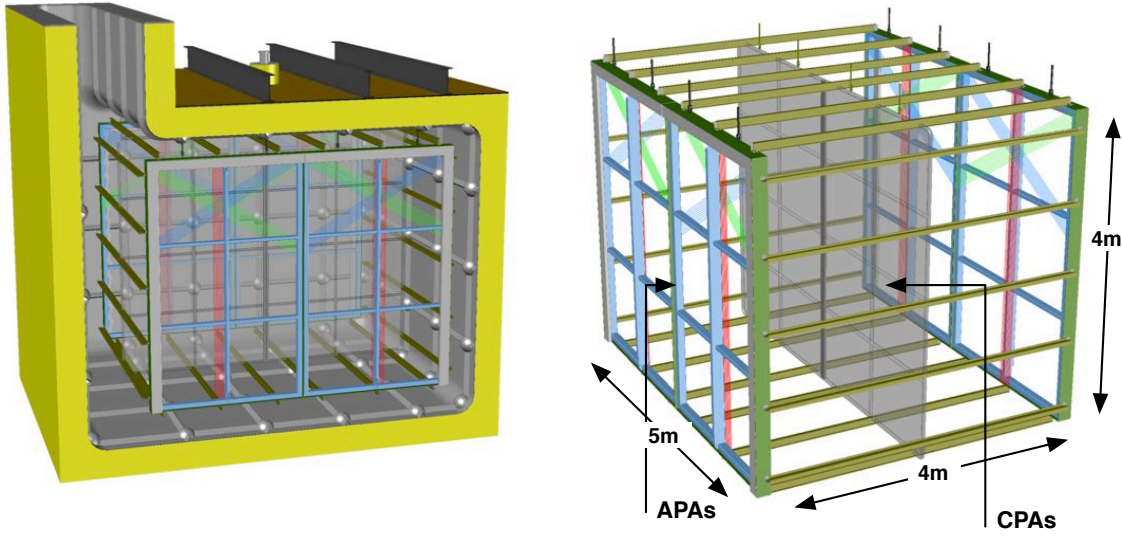


**FIG. 28:** (Left) A conceptual design of the LAr1-ND. (Right) A model of the TPC, showing the four bridged APAs and the central CPAs.

3. The APAs are constructed in a manner that guarantees no wires will break during the operational life of the experiment.
4. The high voltage system and field cage provides a uniform and stable drift field in order to capably image the entire fiducial volume.
5. The electric field everywhere inside the cryostat must not exceed 40 kV/cm to prevent breakdown [95].

### A. The Anode Plane Assembly

Each LAr1-ND APA will consist of 3 planes (referred to by the direction they are oriented: Y, U and V) of 150  $\mu\text{m}$  diameter Copper-Beryllium (CuBe) wires. The wire pitch and plane spacing is 3 mm, with the collection planes vertical (Y), and the two induction planes (U,V) each have wires at angles of  $\pm 60^\circ$  from the vertical. Bias voltages of approximately -200 V, 0 V, and +500 V will be applied to the (U,V,Y) wire planes, respectively, to provide the 100% transparency condition necessary to allow all electrons to pass through the U and V planes and be collected by the Y plane.

All wires in the APAs are bonded mechanically with epoxy and terminated electrically with solder onto bonding boards made out of G10, which also provide connection to the readout electronics. The APA uses the same wire bonding method developed for the LBNF APAs, but without the continuous helical wrapping. Each wire will be tensioned at 0.5 kg per wire when the APA is at room temperature. The wires would acquire an additional 0.7 kg if suddenly cooled to liquid argon temperatures while the support frame structure is still warm, therefore a controlled cooldown rate is needed. Since CuBe has a nearly identical CTE as that of the stainless steel, the nominal wire tension will be restored once the entire APA is cooled down. This CuBe wire has a break load of approximately 3 kg at the LAr temperature, so the wire tension will be comfortably below this threshold.



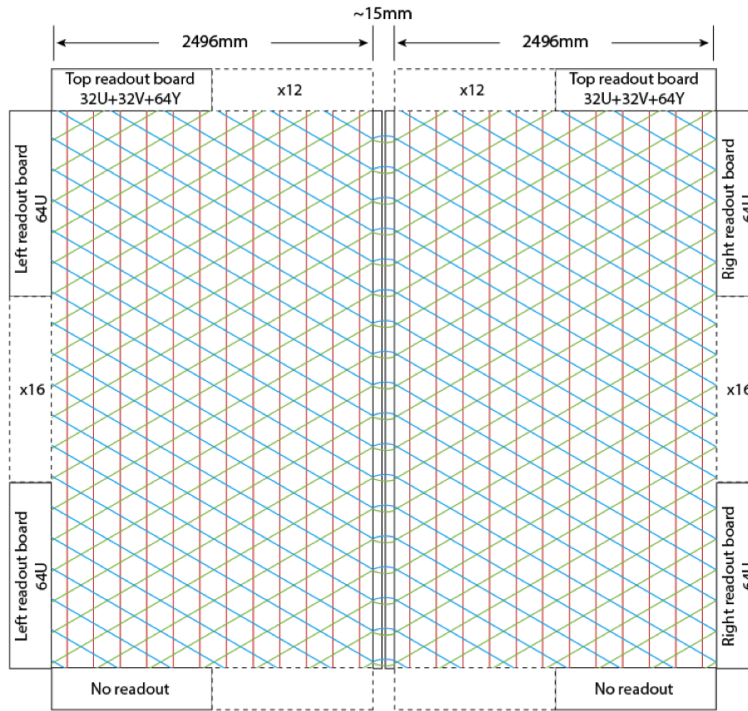


**FIG. 29:** A schematic of the bridged APAs.

In order to minimize the cost of the readout electronics, each APA has cold readout electronics on two edges only. The U wires of the two APA's observing the same drift volume are electrically connected at the joining edges via flexible jumper cables (see Figure 29). Similarly for the V wires. The installation/access of the jumpers should be done before the installation of the cold electronics to avoid ESD damage to the ASICs. The jumper cables use industry standard gold plated pin and socket connections, similar to all electrical interconnects between the cold electronics boards. Although the jumpers may increase the risk of open circuit on the wire readout somewhat, its benefits in the reduction of readout channel count, and the APA size outweigh the risks. Nevertheless, one of our early design efforts will be the selection and evaluation of the interconnect components at the cryogenic temperatures. A special set of readout electronics may be needed to read out the joining edge of an APA during individual APA testing.

In this design there is a gap of 15 mm between the two active apertures of the APAs which creates a “dead” readout region. To overcome this issue there is an option to insert a printed circuit board in the gap between the two APAs, and bias the circuit board strips with a voltage distribution such that the incoming electrons will be deflected away from this gap and land in the active region of the wire frame. In this field configuration, there will be no electron loss, but reconstructed inclined tracks will appear distorted at this gap. As this region has a fixed distortion, it can be easily mapped out and corrected (see Figure 30). This field shaping concept will be implemented at one section of the LBNE 35ton TPC and evaluated during the LBNE 35ton Phase II operation.

Figure 31 is a view of an upper outer corner of an APA. Three layers of wire bonding boards are stacked on the front face of the frame. The wires are bonded to each board at the leading edge with epoxy, and then soldered to copper pads on the boards. Copper traces on the wire bonding boards bring the wire signal to the cold electronics boards mounted on the two outside

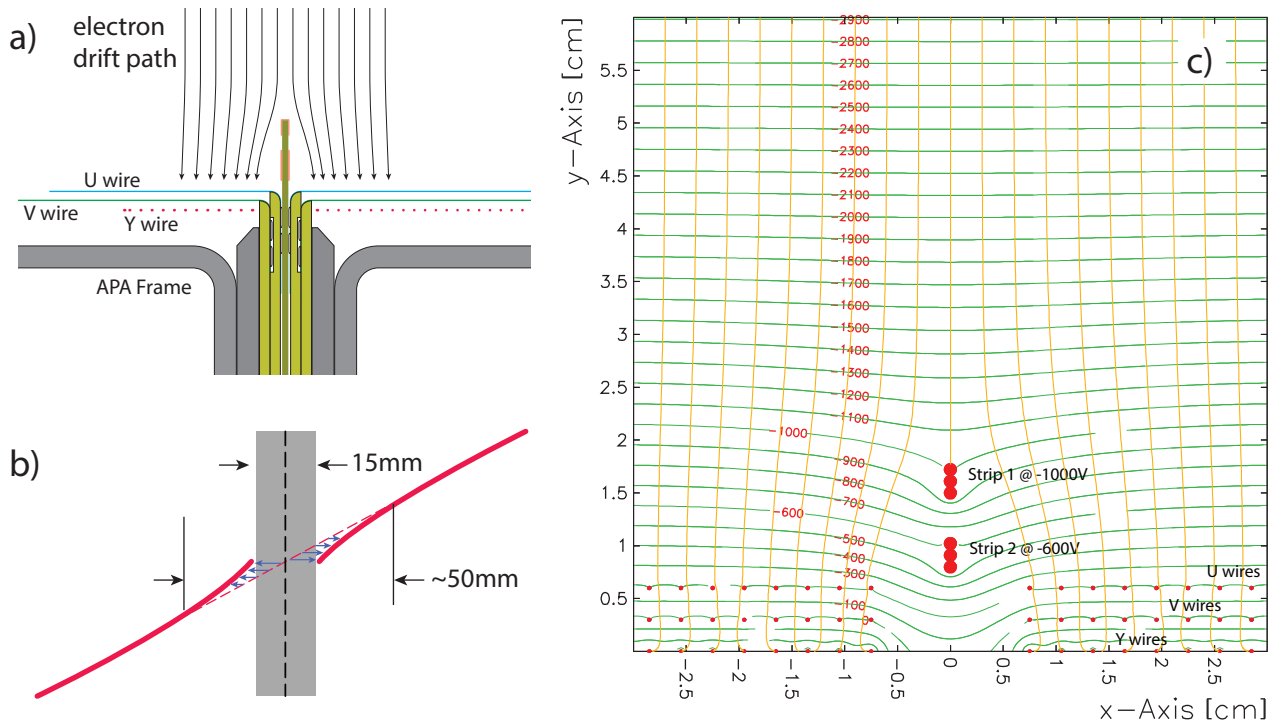


**FIG. 30:** a) A concept to eliminate the dead region between the two APAs by adding a few properly biased electrodes at the center of the gap to divert the electrons to the nearby active regions. b) The distortion on the reconstructed tracks. c) A Garfield simulation of the electron drift lines in a two strip configuration.

edges of the frame. Only the wires on the joining edge of the APA are bonded on “LBNE” style grooved boards (Figure 30a, 32). This configuration minimizes the number of grooved boards which are labor intensive to fabricate, while maintaining a relatively small dead space between APAs.

High voltage capacitors and high value resistors are needed for each readout channel with a bias voltage (U & Y). These components can be integrated on the wire bonding boards (MicroBooNE style), or mounted on intermediate CR boards between the wire bonding boards and the FEE boards (LBNE style).

The four stainless steel APA frames are required to be flat and to have rigid tolerances. The distributed load on the frame is calculated to be 250 kg/m. Since this load is applied to one side of the frame only, it has the tendency to bow the frame. This in turn could make the wire plane spacing non-uniform over the entire opening, resulting in different electron transparency. The transparency can be restored by over biasing the wires, but we should keep the flatness of the frame to better than  $\sim 0.5$  mm to avoid very high bias voltages. Since the APA frames are outside of the TPC’s active volume, it is straightforward to design the frames to be stiff against such distortions. Adjustment of the wire bonding boards can also be made at APA assembly time to further improve the wire plane precision over fabrication tolerances in the APA frames.

A prototype LBNE type frame with dimensions 1.5 m  $\times$  0.5 m has been designed and fabricated at Sheffield University to prototype the manufacturing process, which minimizes distortions and leads to significant improvements in flatness. For the full LAr1-ND APA frame, a four-stage process is envisioned: i) secure the whole assembly to a purpose built fabrication

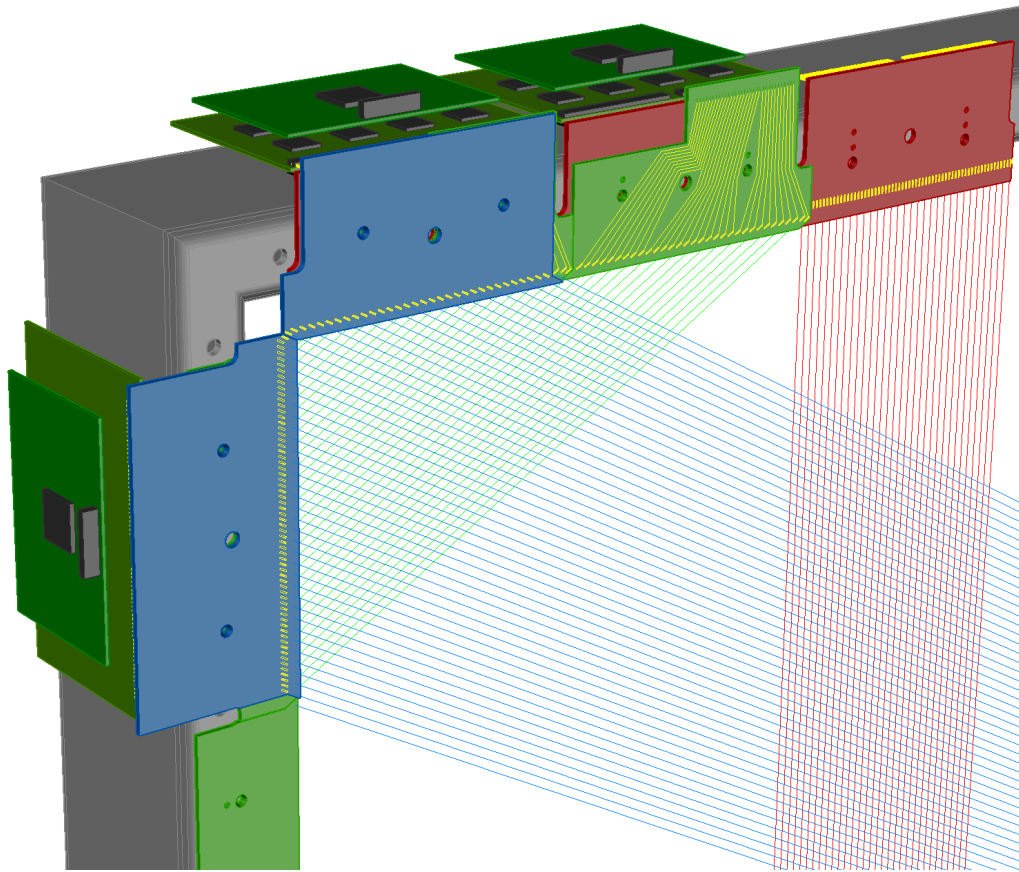


**FIG. 31:** A conceptual design of an upper outer corner of an APA showing the different layers of wire bonding boards on the top end side of the APA frame. The cold electronics boards are connected to these wire bonding boards. Metal covers may be installed over the electronics boards to reduce noise pickup and contain the boiled argon bubble streams.

jig during tack welding; ii) normalization of the structure (stress relief) to prevent buckling; iii) machine and drill all mounting points for additional components; and iv) chemical passivation to remove contaminants.

## B. The Cathode Plane Assembly

The CPA has the same dimensions as the APA and consists of a stainless-steel framework. The surface of the CPA panels will be either a solid stainless steel sheet or a highly transparent wire-mesh-plane. The requirements of the light collection system will dictate which CPA surface is used. For example, a double layer mesh cathode module enables TPB coated reflector foils to be mounted in between the mesh planes. This configuration allows the polymer foils to contract freely during cool-down.

During manufacture, all the CPA surfaces will be carefully polished in order to avoid any sharp edges that could lead to electrical discharge. If a transparent type CPA is chosen the mesh will be tensioned and mounted between two steel frames in order to enclose the sharp edges of the mesh (see Figure 33). G10 mounting connectors will be pre-installed on the outer edges of the CPA to allow integration of the CPA and the Field Cage Assembly (FCA) modules.

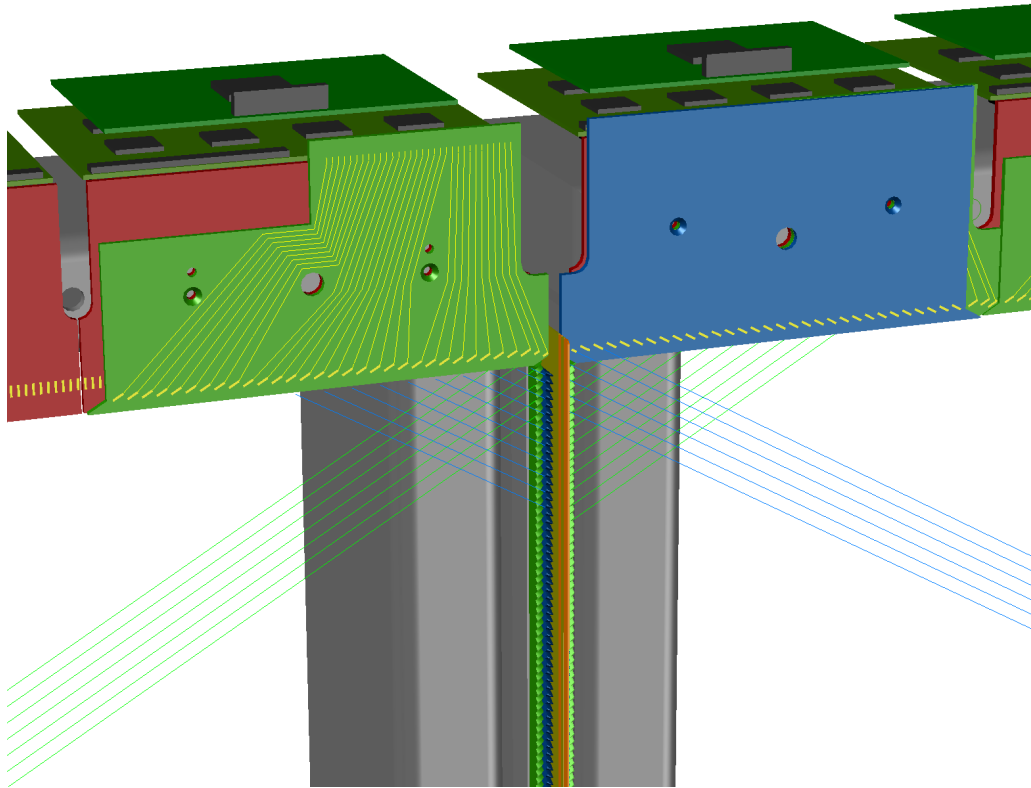


**FIG. 32:** A closeup view of the gap between the two APAs showing a possible implementation of the electron diverter concept

Finally, a HV cup will be integrated to allow connection of the HV feedthrough to the CPA.

### C. The High Voltage Feedthrough

A single high voltage feedthrough is installed through a cryostat penetration to connect the high voltage power supply to the CPA. To provide the 500 V/cm drift field over the 2 m drift distance the CPA will sit at a potential of -100 kV. To ensure safe and reliable operation, the HV feedthrough is constructed with a HV rating of no lower than 120 kV in liquid argon. The design of this feedthrough is based on the design of the ICARUS/ MicroBooNE feedthrough. To avoid outgassing of impurities, the feedthrough uses a central stainless steel conducting core within an Ultra-High Molecular Weight Polyethylene (UHMW-PE) insulator surrounded by a stainless steel grounding sheath. UHMW-PE has a high dielectric strength, ensuring a compact feedthrough design, and its high-thermal expansion coefficient relative to stainless steel allows the vacuum seal to be cryo-fitted. The outer stainless steel sheath will terminate prior to the contact to the CPA to prevent electrical breakdown. As in the ICARUS/MicroBooNE design, the feedthrough will be removable from outside of the cryostat in the event that it needs to be replaced. A 150 kV power supply (Glassman LX150R12) in conjunction with a noise filter will be utilized as in MicroBooNE.

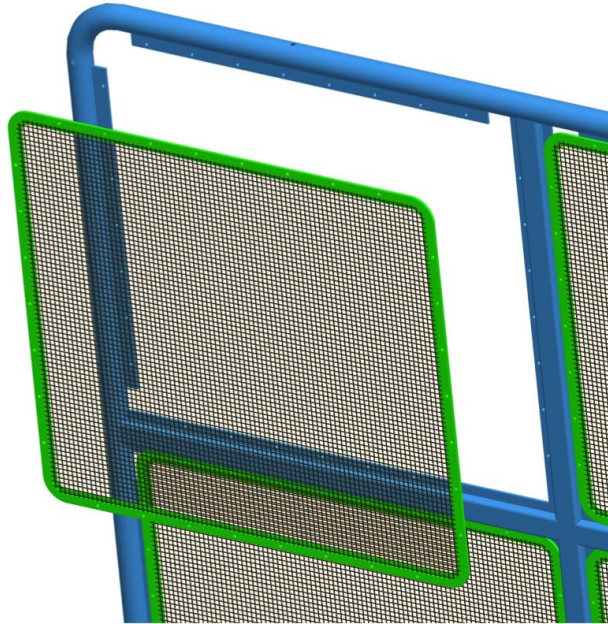


**FIG. 33:** A model of the CPA corner, showing the mesh into the frame assembly.

#### D. The Field Cage

The HV drift cage must provide a uniform 500 V/cm electric field over the TPC active volume to maintain linearity between drift distance and time of ionization. The field cage gradually steps the voltage from the -100 kV applied to the CPA up to ground voltage. It will be made from 1.6 mm double sided Cu clad FR4 PCBs, similar to the 35t LBNE prototype. The double sided Cu cladding effectively ensures that the inter-strip capacitance is increased thus minimizing over voltage conditions between the CPA and field cage strips in the event that the CPA or the field cage discharge to ground. A photo of the 35t field cage panels is shown in Figure 34. Slits between the Cu etched strips ensure good liquid argon flow. Additionally, in order to accommodate the laser beam calibration system (see Section VI) the side field cage walls will have two openings 50 mm ID in each drift volume at the half-height. A resistor divider chain will supply the potential for the field cage electrodes. To reduce the field distortion caused by a possible resistor failure, four equal value 1 G $\Omega$  resistors, with each resistor rated at 5 kV and 1 W, will make parallel connections between neighboring electrodes. These resistors will be located on the inner wall of the TPC since the electric field in this volume is lower than that outside the TPC.

Surge protection elements will be placed in parallel with the resistor divider chain to provide redundant protection to the resistors should a catastrophic voltage condition begin to arise in the chain. This technique was instigated by the MicroBooNE collaboration and shown to provide a reliable method of handling high-voltage breakdown issues [96].

#### E. Installation Procedure

There are two installation options for the TPC. One option is to pass all TPC components through the cryostat chimney; this would require completion of the cryostat prior to the TPC

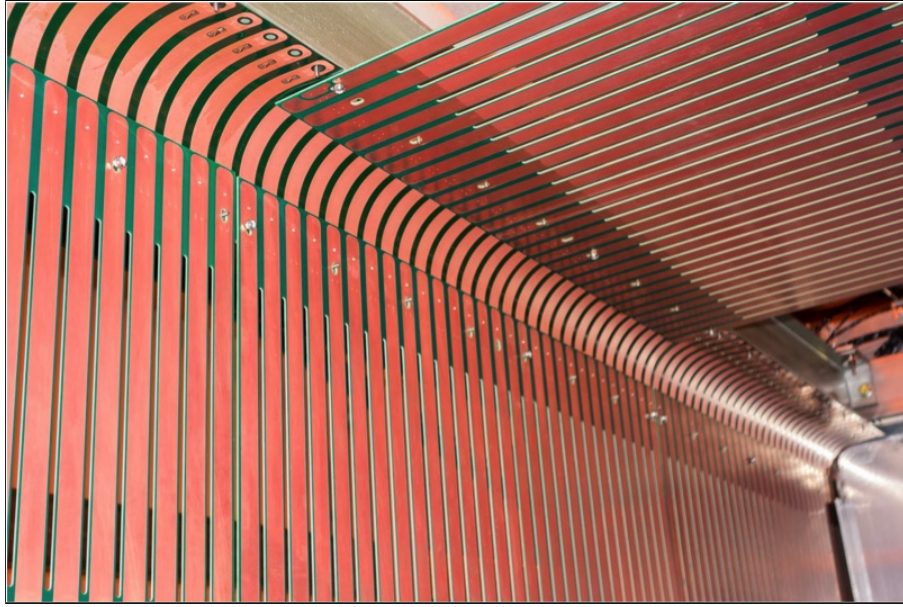


**FIG. 34:** *A photo of the 35 ton LBNE prototype field cage.*

installation and the dimensions of all internal components would be restricted by the size of the chimney. The second and more favorable option is to hang all the TPC assembly from a main lid before sealing. This option allows for parallel construction of the TPC and cryostat. However, this creates the necessity for the building housing the detector to be tall enough and an adequate load capacity crane would be needed.

#### F. Quality Control and Quality Assurance

A QA program will be performed at Lancaster University to confirm the APAs constructed in the UK behave as expected when cooled to 77K using liquid nitrogen. These results will verify the design and manufacturing process of all APAs. Cold tests will be carried out in a purpose-built  $\sim 3 \text{ m} \times 4 \text{ m} \times 0.2 \text{ m}$  thermal cryo-vessel, large enough to contain the full-scale APA. The vessel will be constructed from stainless steel with polystyrene insulation. The vessel, with the APA inserted, will be cooled with gaseous nitrogen prior to filling with liquid nitrogen. The thermo-mechanical measurements will include: a survey of the bending and distortion of the APA frame structure and comparison with FEA calculations; vibration frequency based APA wire tension measurements; and resistance measurements to test electrical integrity.

Travelers will be provided for all TPC components shipments detailing contents and relevant instructions.

#### G. Risks

Breakage of a single wire can jeopardize the detector's functionality, so a QA procedure will be followed to ensure the tension of the wires is never higher than that of their desired warm tension of 0.5 Kg, and wires are not subject to any kinking that could reduce their strength. The tension of each wire installed on the APAs will be measured using a laser feedback system developed as part of the LBNE 35-ton project, and subsequently used by both MicroBooNE

and LArIAT during TPC construction.

Breakdowns in the liquid argon volume can produce over-voltage conditions across resistors in the field cage, which if damaged could produce distortions in the drift-field. Surge protection devices, as developed by the MicroBooNE experiment, will be present mitigating the risk to the resistors.

## V. TPC Electronics, DAQ and Trigger

### A. Introduction

The aim of the TPC readout is to digitize, compress losslessly and record the TPC signals upon the reception of a variety of triggers such as neutrino beam and cosmic rays triggers generated by the light detection system as well as external scintillation counters, calibration and random strobe triggers. In order to fully reconstruct cosmic rays entering the drift space during an event drift time, data arriving from -1.28 msec before the trigger to +2.56 msec after the trigger (a total of 3 maximum drift times) will be recorded and compressed losslessly at each event. In a parallel stream, and as useful R&D for LBNF, the readout will continuously record data, compress it and store it for a few hours awaiting for a possible supernova alert from the SNEWS network.

The block diagram of a single TPC readout channel is outlined in Figure 35. The signal from each wire is pre-amplified and shaped by a CMOS analog front end ASIC, then digitized by a CMOS ADC ASIC inside the cryostat. The digitized signal is sent to an FPGA, which aggregates data from multiple ADC chips and multiplexes it to high speed serial links. The serial data is sent over cold cable through a feed-through to the warm interface board installed outside the cryostat on top of the signal feed-through. The warm interface board receives the electrical serial data from the cold electronics and converts it to optical signals for transmission over a fiber optical link to the TPC readout module, housed in a crate. Once the signal arrives at the TPC readout module, it is processed in an FPGA for compression, reduction, and storage. Processed data is buffered on board temporarily and then transmitted to DAQ PCs through the crate backplane and optical links. Data received on PCs is stored in hard drives for further analyses.

The design of the front end electronics, the TPC readout and the trigger is described in the next sections. A summary of the numbers of modules needed and of the spares as well as their distribution is reported in Table XII.

### B. The Front End Electronics

The LAr1-ND front end electronics is comprised of three parts: cold electronics, warm interface electronics and signal feed-through. The cold electronics will be installed on the TPC anode assembly and operated in LAr. The digitized detector signal will be sent to the warm interface electronics over cold cable. The warm interface electronics will be installed on the top signal feed-through assembly, and interface to both cold electronics and back end readout electronics and the DAQ system.

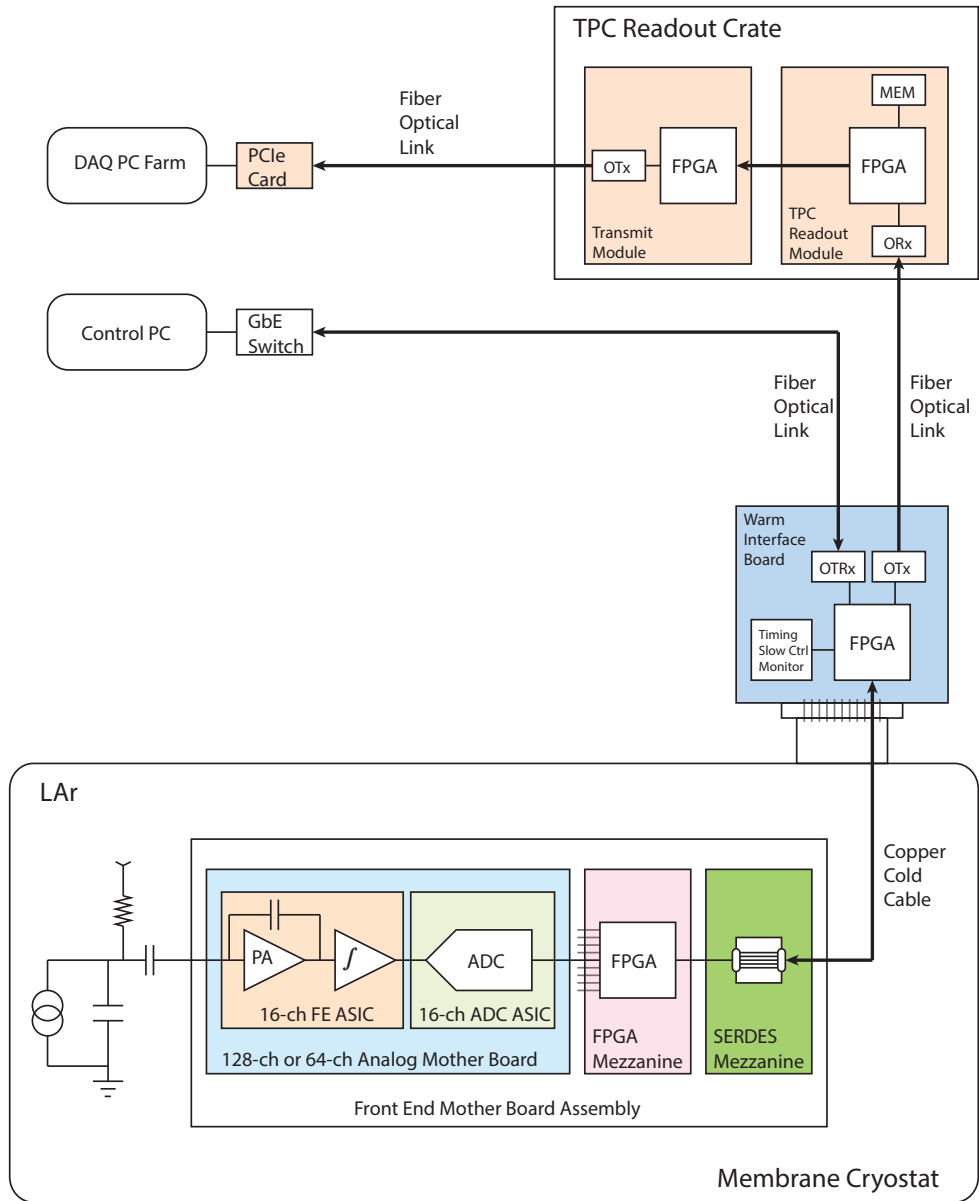


**FIG. 35:** Information flow of a single TPC readout channel.

*Cold Electronics*

The LAr1-ND TPC will have two APA modules, on each side with 5,632 channels, a total 11,264 readout channels for the whole TPC. The large number of readout channels required to instrument the LAr1-ND TPC motivates the use of CMOS ASICs for the electronics. Both analog FE ASIC and ADC ASIC, to a large extent, have already been developed for LBNE, and analog FE ASIC is being used in MicroBooNE. The entire front end electronics chain is immersed in the LAr and operates at 87 K to achieve an optimum signal to noise ratio. It is



Module	Channels per Module	Distribution	Number of Modules needed	Number of Spare Modules	Number of Modules
Front End Modules (FEM)	64 wires/FEM	16 FEM/crate	176	18	194
Crates			11	2	13
Backplane		1 Backplane/crate	11	2	13
XMIT		1 XMIT/crate	11	2	13
Crate Controller (CC)		1 CC/crate	11	2	13
PCIe		3 PCIe/crate	33	4	37
Trigger module			1	2	3
Analog FE ASIC	16 wires		704	96	800
ADC ASIC	16 wires		704	96	800
128-ch Mother Board	128 wires		52	6	58
64-ch Mother Board	64 wires		72	8	80
FPGA Mezzanine	128 or 64 wires		124	14	138
SERDES Mezzanine	128 or 64 wires		124	14	138
Warm Interface Board	704 wires		16	4	20
Service Board	2,816 wires		4	2	6
Signal Feed-through	2,816 wires		4	2	6
Cold Cable	2,816 wires		4	2	6

**TABLE XII:** *Numbers of modules needed and of spares as well as their distribution.*

composed of a 16-channel analog FE ASIC providing amplification and shaping, a 16-channel ADC ASIC implemented as a mixed-signal ASIC providing digitization, buffering and the first stage of multiplexing, a FPGA providing the second multiplexing stage, and voltage regulators. Analog FE ASICs, ADC ASICs plus a FPGA implementing multiplexer, clock, control and monitoring circuitry comprise a single 128-channel or 64-channel front end mother board assembly. The FPGA on each motherboard will transmit data out of the cryostat on twinax copper pairs running at multiple Gbit/s through a feedthrough to the warm interface electronics, and receive programming instructions and timing information from the warm interface electronics as well.

Each side of the TPC has two APA modules, which are interconnected along the adjacent side. Each APA module will have 31 front end mother boards on two sides. 13 boards will be located on top of the TPC with each board processing 128 channels. 18 boards will be on the side without interconnection, with each board housing 64 channels. A block diagram of the 128-channel front end mother board is shown in Figure 36. Both analog FE ASIC and ADC ASIC have been designed and fabricated in a commercial CMOS process (0.18  $\mu\text{m}$  and 1.8 V). This guarantees a high stability of the operating point over a wide range of temperatures, from room temperature to 77 K. The ASICs are packaged in a commercial, fully encapsulated plastic QFP 80 package. A minor revision of the analog front-end ASIC, to further improve the robustness and simplify the system design, including internal pulse generator, smart reset and improved input protection is being planned. It will greatly simplify the design of the electronic calibration system.

The Cold FPGA will interface to analog FE ASICs and ADC ASICs on the analog mother board. It will control and monitor ASICs, and receive data from ADCs. Once data arrives at the FPGA, a second stage multiplexer will be implemented to further reduce the number

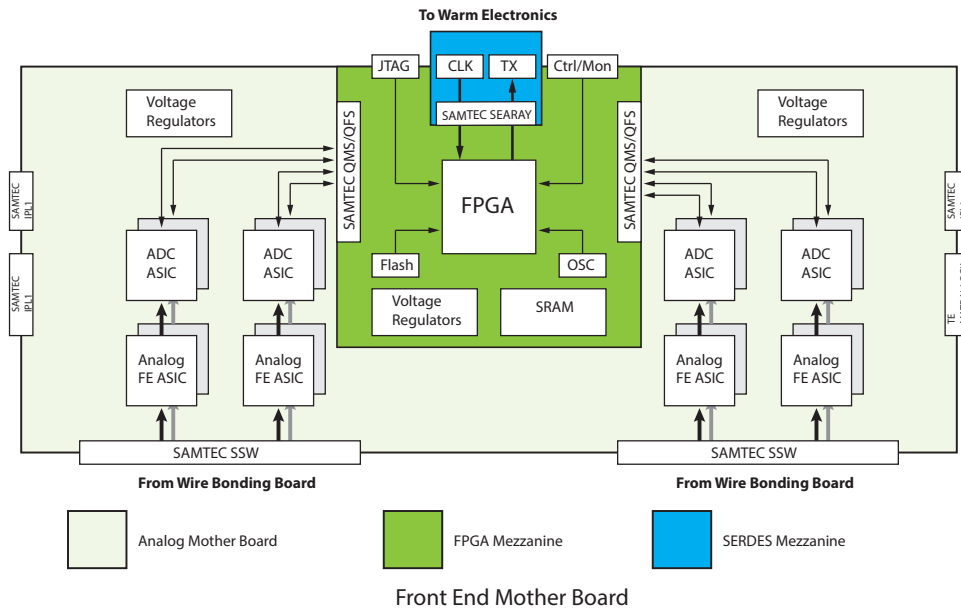


**FIG. 36:** Block Diagram of Front End Mother Board Assembly.

of data links to outside of the cryostat. The design is to support transparent data readout without any compression over 2Gbit/s serial links. An efficient zero-suppression scheme can be implemented in the FPGA to greatly reduce the total data volume if proven to be feasible and necessary. Each mother board processes 128 or 64 detection channels. The clock will come in through RX links while data is sent out over TX links. Voltage regulators used on board have been qualified in liquid Nitrogen. On the board, SRAM is used to temporarily buffer events if a more sophisticated algorithm is used to process data. A commercial SRAM chip working in cryogenic temperature has also been identified. The estimated power dissipation is 20 mW/channel. The ALTERA Cyclone IV GX FPGA will be used in the FPGA mezzanine design. It has been tested in LN<sub>2</sub> successfully, both fabric logic and a high speed transmitter are working properly at cryogenic temperature.

The prototype front end mother board is being designed for the LBNE 35 ton prototype. The picture of the prototype 128-ch analog mother board is shown in Figure 37 and prototype FPGA mezzanine is shown in Figure 38. SERDES mezzanine is a passive adapter board, which will be plugged on the FPGA mezzanine to interface to cold cable. The candidate cold cable is made by Gore using twinax cable and ERNI hard metric connector. The 50ft Gore twinax cable has been tested with feed-through pin carrier running at 2 Gbit/s successfully.

### Warm Interface Electronics

The detector signal is digitized inside the cryostat. After multiplexing in FPGA, it is sent out of the cryostat over copper serial link to the warm interface electronics installed on the top of the signal feed-through. The warm interface board will be the bridge between the cold electronics and back end readout electronics and DAQ system.

The warm interface board will use ALTERA Cyclone V FPGA, which will receive high speed serial link coming out of cryostat, perform data preparation, then send the data to the

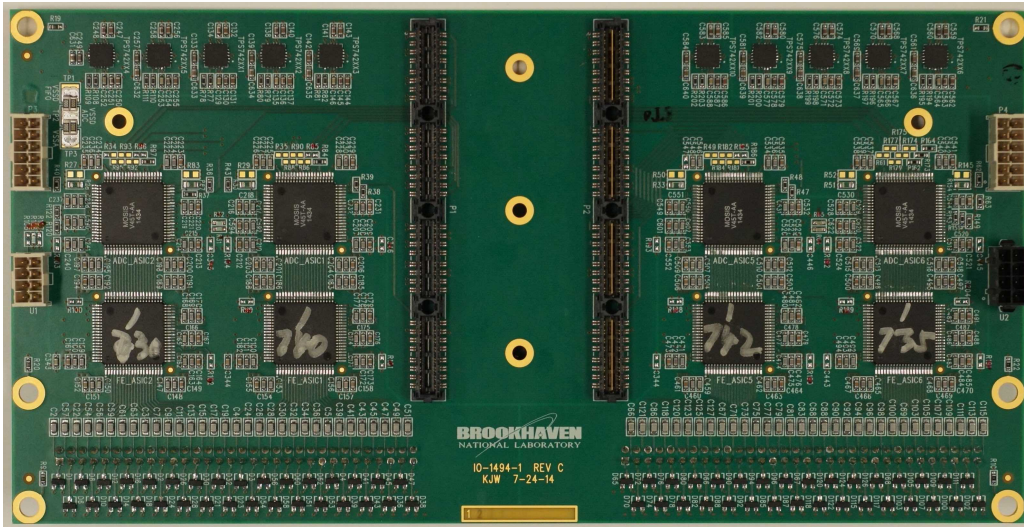


**FIG. 37:** *Prototype 128-ch analog mother board designed for LBNE 35ton prototype TPC.*

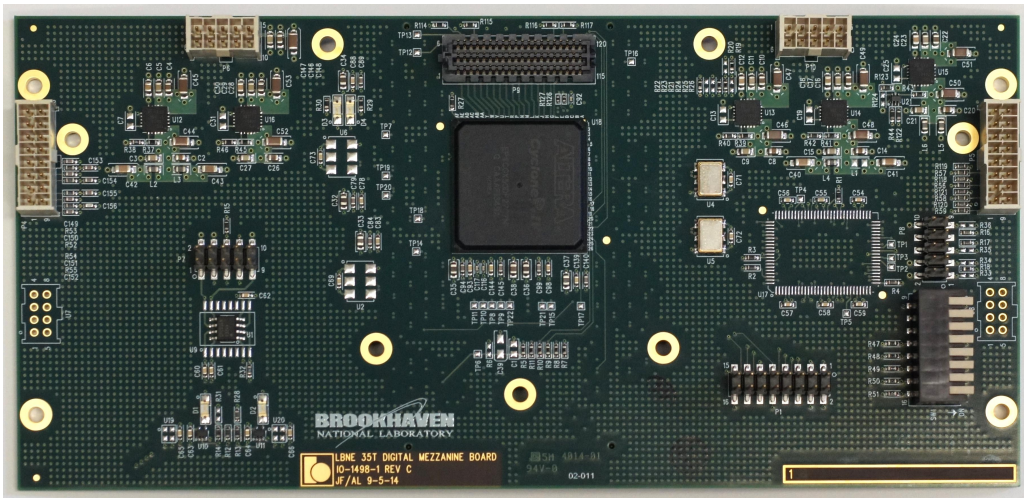


**FIG. 38:** *Prototype FPGA mezzanine designed for LBNE 35ton prototype TPC.*

readout and DAQ system through fiber optical links. On board FPGA has computing power to do further data processing if necessary before sending the data to downstream electronics. By default, data interface board will send data over a 2 Gbit/s link to the TPC readout module, which processes un-compressed 64-ch worth of data. The whole TPC will require 176 fiber optical links to carry data from 11,264 TPC channels. A 12-ch parallel fiber optical link will be used to minimize the volume required on board, requiring a total of 16 fiber bundles. This will ease the design of the electronics assembly on the top of the signal feed-through.

Timing, control and monitoring are also functions of the warm interface electronics. The system clock and synchronization signal will be distributed from warm interface board to the front end mother board assembly. Slow control and monitoring information will also be communicated between the warm interface board and the front end mother board assembly, using an I2C like protocol. The front end mother board assembly can be remotely programmed and monitored through a control PC. The communication between the warm interface board and control PC is by Gigabit Ethernet over a fiber optical link.

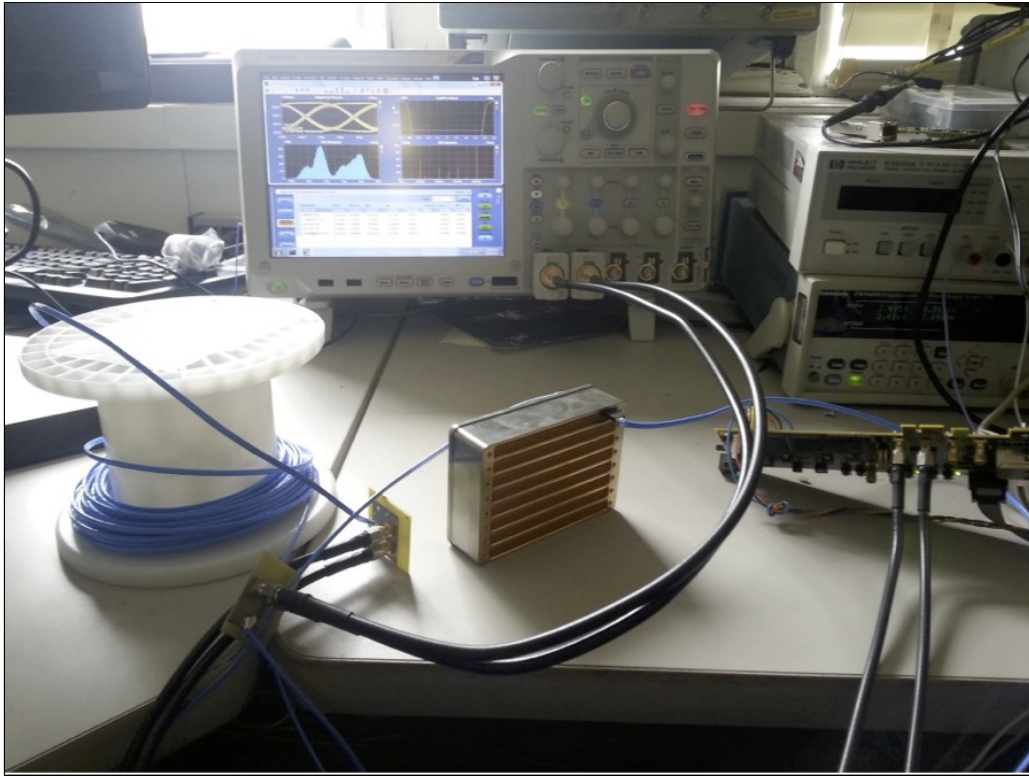


**FIG. 39:** *ATLAS pin carrier is tested with Gore cable for 2 Gbit/s signal transmission.*

The front end analog ASIC has a built in calibration capacitor, to facilitate the electronic calibration. With plans to revise the front end analog ASIC adding a built-in calibration pulse generator, there is no need to distribute the calibration pulse signal from outside the cryostat. This will greatly simplify the system design.

The link between warm interface electronics and back end readout electronics and control system is only through fiber optical links. This effectively eliminates the possibility to have ground loops between the detector and the DAQ system.

Both cold electronics and warm interface electronics will be powered by a floating low voltage power supply. It is planned to have a service board installed on the top of the signal feed-through. The service board will be responsible for power management and distribution.

#### *Signal Feed-through*

The signal feed-through design has to consider two important factors: 100% hermeticity and high speed signal transmission capability. The ATLAS style pin carrier [97] shown in Figure 39 is designed for a LAr Calorimeter and its hermeticity has been certified. It has also been used for the MicroBooNE signal feed-through design. Since the pin carrier design is available, no additional engineering design is needed. The pin carrier is suitable for both warm flange and cold flange if LAr1-ND decides to use double flanges setup to improve the efficiency of the purification system. The manufacturer of the pin carrier has been contacted; they are still available and capable of building the same type of pin carriers with reasonable cost.

Two 8-row pin carriers and two 7-row pin carriers will be welded on a 14-inch conflat flange with a Faraday cage mounted on the top to provide the shielding for warm interface electronics.

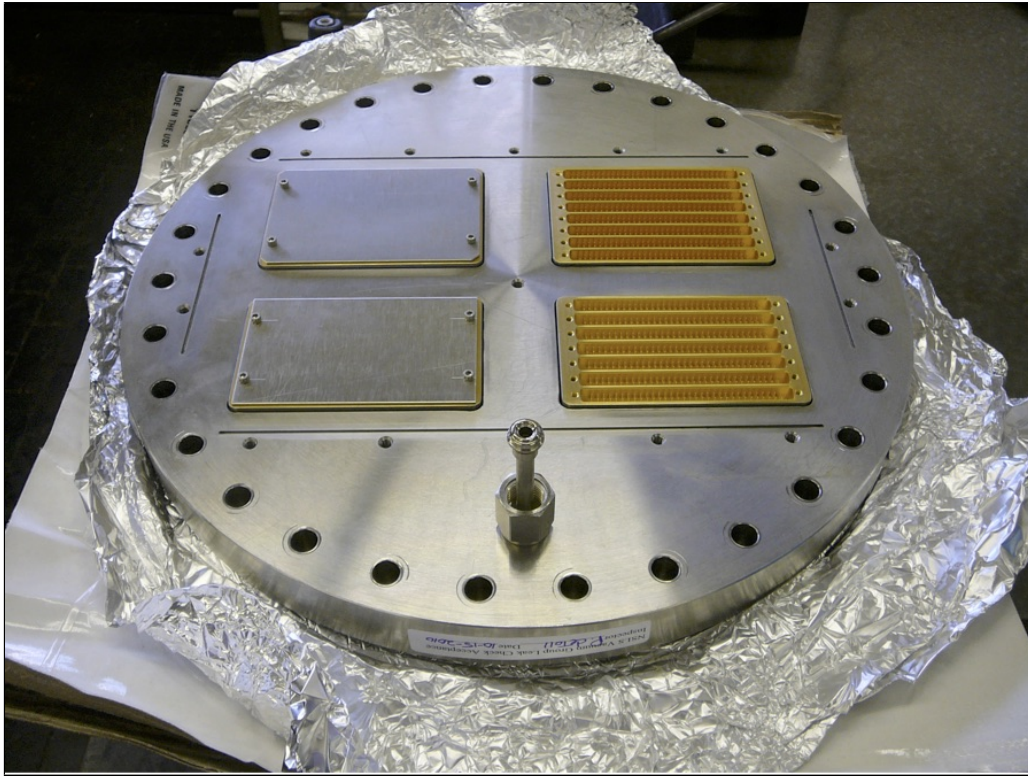


**FIG. 40:** *ATLAS pin carriers are welded on flange.*

A picture of the flange with pin carriers welded on is shown in Figure 40. There will be four signal feed-throughs for LAr1-ND TPC readout. Each feed-through is used to read out one APA of 2,816 channels. A total of 44 serial links on each feed-through will come out of the cryostat running at 2 Gbit/s. Considering redundancy, ground pins and fiber organization, it will require 8 64-pin rows. The warm interface board will need proper cooling; it is envisioned that each board will occupy two pin carrier rows to allow sufficient air flow. The service board will occupy another two rows for power management and distribution. Therefore, the signal feed-through flange with 1920-pin, 30-row pin carriers is enough to handle one full anode plane assembly. It will be investigated if the readout of two APAs on one side of TPC could be fit on the one signal feed-through assembly.

### C. The TPC readout

In MicroBooNE, the TPC signals are digitized outside of the cryostat in a board developed by BNL and joined to a Nevis board, the FEM, that provides the compression, storing and trigger application. In LAr1-ND the signals will be digitized within the cryostat and after emerging from the feedthrough, will go through a copper to optical transceiver and arrive on optical fibers at an adaptation of the MicroBooNE FEM Nevis boards. The FEMs will each receive signals from 64 wires and will be modified to include an optical to copper converter AFBR-59R5LZ and a deserializer TLK2501IRCP. The signals will then be treated in exactly the same way as in MicroBooNE, thus capitalizing on the extensive Nevis hardware and firmware design and development performed for MicroBooNE

A total of 176 FEMs will be required and will be housed in eleven 6U crates, sixteen 64-

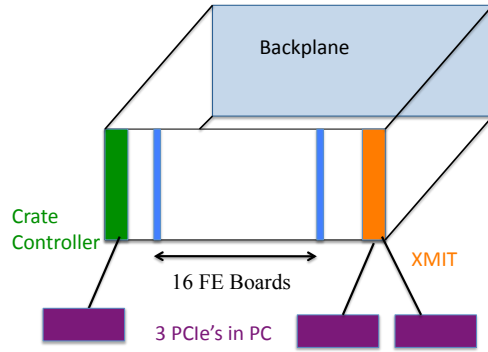


**FIG. 41:** A readout crate showing, from left to right, the crate controller, up to 16 FEM modules, the XMIT and the 3 PCIe cards used for communicating with the crate and resident in a PC.

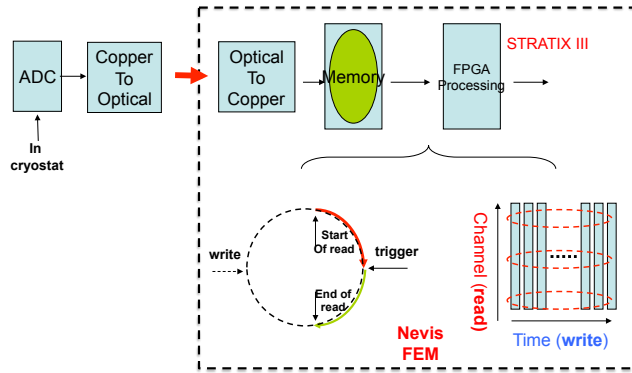


**FIG. 42:** The Nevis FEM data flow, showing the circular buffer and the "write" in time order and "read" in channel order scheme.

channel FEMs per crate. The crates each also house a fast data transmission module (XMIT) and a crate controller (CC) used for parameter transmission to the FEMs and for a slow debugging mode readout. A MicroBooNE crate layout is shown in Figure 41.

The digitized data stream is shown in Figure 42. The FPGA stores the data from 64 wires sequentially in time in a 1M x 36 bit 128 MHz SRAM memory, grouping two ADC words together in each 36 bit memory word. This requires a data storage rate of  $(64/2) \times 2 \text{ MHz} = 64 \text{ MHz}$ . Since data reduction and compaction algorithms rely on the sequential time information of a given wire, the data readout out from this SRAM memory takes place in wire order in alternate clock cycles, again at the rate of 64 MHz. The SRAM chip size and memory access speed permit continuous readout of the TPC data. The data is arranged in frames of 1.28 ms, the maximum drift time. Since the readout clock is not synchronous with the accelerator spill time, the 3.84 ms worth of data relevant to an accelerator neutrino event spans four 1.28 ms long frames. In order to reduce the amount of data being transmitted, the FPGA trims the four frames to span the exact 3.84 ms required. Experience with a Fermilab test stand demonstrates that on any given wire, successive data samples vary relatively slowly in time. In most cases, two adjacent data samples either coincide or differ by one ADC count. Huffman coding provides for lossless data compression by taking advantage of this slow variation of the data stream. For accelerator neutrino events, lossless Huffman coding compression yields a compression factor of

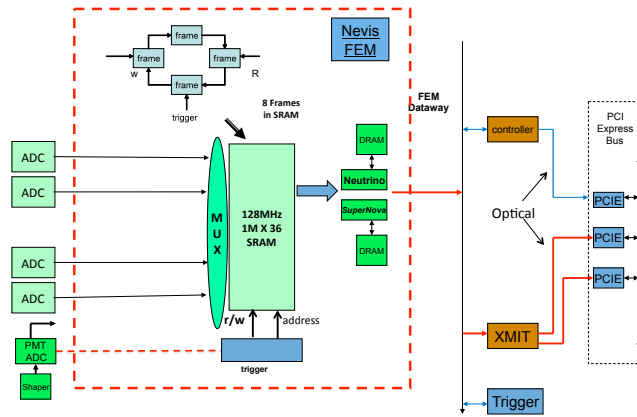


**FIG. 43:** The Structure of the Nevis readout system: FEMs, databay, XMIT, crate controller and three PCIe cards PC resident.

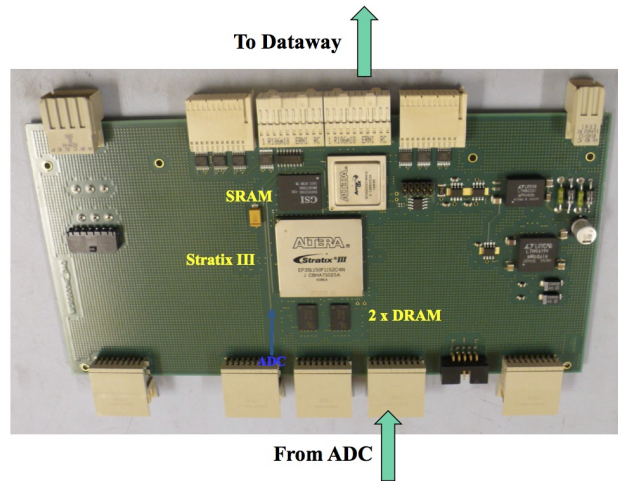


**FIG. 44:** The MicroBooNE Nevis FEM.

eight to ten and proves sufficient; but for the continuous supernova data, further compression by about an additional factor of ten, is necessary to limit the size of the data sample and to match disk writing speeds, resulting in unavoidable data loss. A method called dynamic decimation (DD) handles this case. The DD scheme relies on recognizing regions of interest (ROI) in the data stream that contain waveforms corresponding to drift charges. Parts of the data stream not containing ROI contribute to pedestal determination. In DD the FPGA samples the ROI data at the same rate as accelerator data, but reduces the pedestal sampling to a much lower rate (e.g. 1/16). The final data record of a wire contains full coverage in time, with or without drift signals from a charged track. A too-high threshold for ROI can result in loss of resolution for small signals, but the data still appear as pedestal, although sampled at a lower rate. An independent Huffman coding stage further reduces the data volume after dynamic decimation. After going through their respective compression schemes, the beam and supernova data are stored in two separate DRAM buffers as shown in Figure 43. The data is then transmitted to the crate backplane databay on connectors shown on the right of the schematic. A photograph of the Nevis FEM board currently in use in MicroBooNE is shown in Figure 44. The transmission is controlled by the XMIT module. Each XMIT module includes two optical links, one used

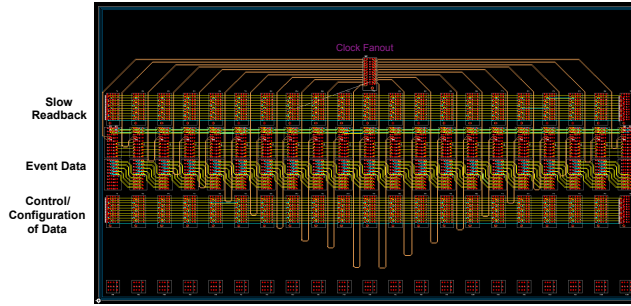


**FIG. 45:** *The Readout crate backplane.*

for the triggered data stream and the other for the continuous supernova data stream. These links connect to optical transceivers housed on two PCI Express interface cards developed at Nevis for use in ATLAS and resident in a PC. Each crate is connected to a dedicated PC (the sub-event PC). The two transceivers on the interface cards handle 6.4 GB/s traffic and connect to a 4-lane PCI Express bus, with each lane accommodating 2.5 GB/sec. The XMIT module transmits data to the PC based on the token passing technique. The XMIT module generates the token and passes it to the first FEM module. This module receives the token and transmits its data, if any. The data transits from one board to the next on the crate backplane until it reaches the XMIT module. The token passes on to the next FEM module when an active FEM finishes transferring its data. Since a module only drives the data to its neighbor, it forms a point-to-point short link. Data can flow at rates up to 512 MB/sec on this path, a factor of ten faster than the expected traffic on this dataway. Figure 45 shows the layout of the crate backplane. In addition to the token passing dataway, a secondary bus serves to download the FPGA codes and initiate data/parameter readback via the crate controller and a third PCI Express card in the PC. This slower readback can be used to read out the FEM without the XMIT, a useful feature for system development, for operating a lightweight test stand, and for other purposes.

An additional PC, the event-building PC, collects the triggered data sent to it by the eleven sub-event PCs and builds triggered events through a switch. Each sub-event PC also stores the supernova data in circular buffers large enough to accommodate a few hours of continuous data. The buffers are resident in disk drives that can accommodate 100 MB/sec writing speeds, but for which we have assumed a more conservative 50 MB/sec by providing an overall supernova compression factor of 80-100.

#### D. The Trigger Board

The trigger board (TB) flags time frames that must be treated differently than those for continuous reading of supernova events. The light detection system generates one or more triggers based on the detector signals. Example trigger conditions include: sum of all light detector pulse heights above a threshold, sums of groups of light detector pulse heights above a lower threshold, and number of light detectors above the threshold satisfying a multiplicity requirement. Each trigger condition receives a code ranging from 1 to  $n$ , with  $n$  likely not exceeding 7, and 0 meaning no trigger. This code is transmitted serially one bit at a time to the TB on one cable as shown in Figure 46. A second cable carries a marker to identify the first bit of a trigger code transmission.



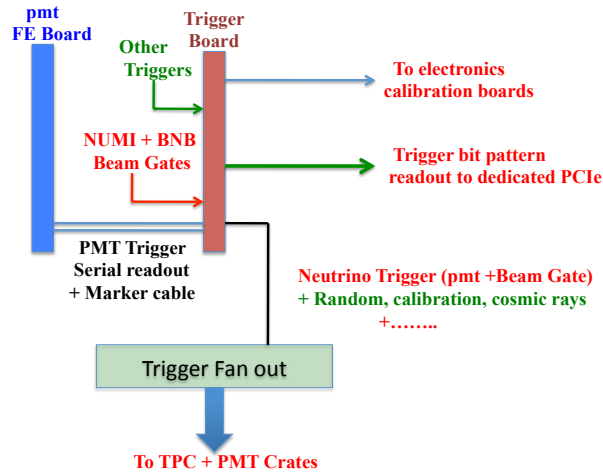


FIG. 46: *The MicroBooNE trigger scheme.*

Booster and NUMI beam gates also input to the TB, where they can be placed in coincidence with light detector triggers to flag neutrino interaction candidates. Valid light detector triggers enter a logical OR with other utility triggers sent to the trigger board to form calibration triggers for the electronics, random triggers for noise measurement, off-beam triggers for cosmic ray response studies, and others as deemed necessary. All inputs to the trigger board will be via front panel LEMO connectors, as will the trigger output. An OR of all triggers passes to a fan-out module on a single cable, and from there is distributed to all crate controllers, and, through the crates backplane dataway, to the FEMs. Upon receiving a trigger, an FEM inhibits its supernova readout mode with its associated decimation, initiates the finer-grained readout scheme and directs the data to the appropriate readout path. Activation or masking of each of the trigger modes will be computer controlled as will the setting of the various trigger thresholds and conditions. The actual cause of the trigger will be available at the event building stage and off-line, as this information will be read out as a bit pattern from the TB via an optical fiber connected to a PCIe card resident in the sub-event PC connected to the crate housing the TB.

### E. An Alternative Scheme

An alternative scheme of TPC front end electronics, readout and DAQ system is shown in Figure 47. The front end electronics could adopt the cold digital ASIC which will be developed for LBNE, if it becomes available in time. The only change is the FPGA mezzanine will be replaced by a cold digital ASIC mezzanine. It is also possible that a small section of TPC readout to be instrumented by a digital ASIC for R&D purposes if the design is not sufficiently mature will be installed on the detector. The alternative TPC readout module will use a more advanced FPGA to process 256 channels of detector signals, it will greatly simplify the system design and the number of readout crates will be reduced by a factor of 2-3. Also the modern USB 3 link could be used to replace the optical fiber link with a custom designed PCIe card, for data transmission to a DAQ PC farm.

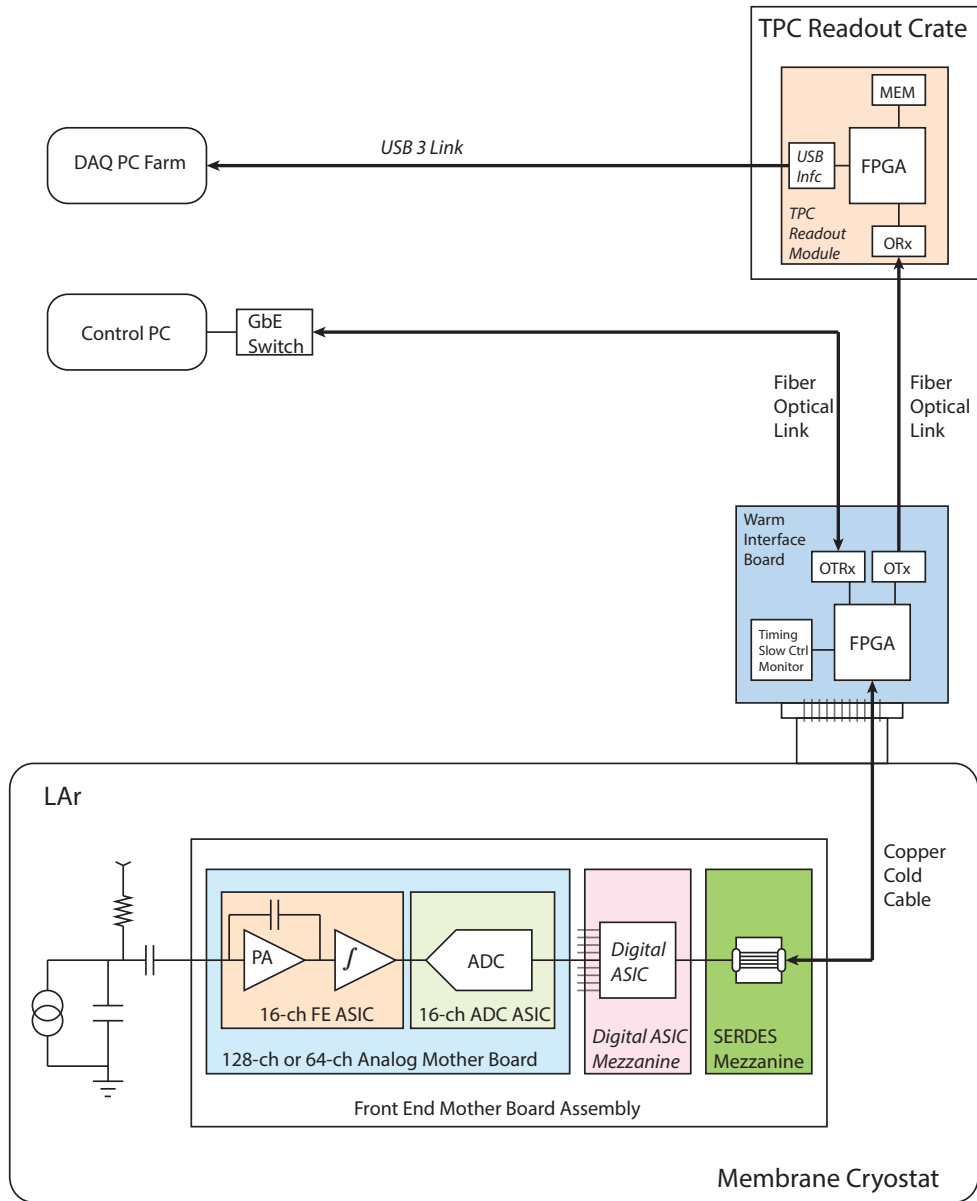


FIG. 47: Information flow of a single TPC readout channel.

## VI. UV Laser-Based Field Calibration System

### A. Calibration of Drift Field by UV Laser Beam

The knowledge of the electric field inside the drift volume of a TPC is a key aspect for performing subsequent event reconstruction. Since distortions of particle tracks due to field non-uniformities are indistinguishable from particle multiple scattering, they affect the accuracy of the particle momentum reconstruction based on track scattering angles. Deviations of the

field map from perfectly uniform in a LAr-TPC may arise due to accumulation of positive argon ions in the drift volume. Ions are created by ionizing particles produced in neutrino interactions as well as by cosmic rays. While free electrons are quickly (within a few milliseconds) swept towards the readout system, ions have significantly lower mobility, and their drift velocity in a LAr detector at nominal drift field is of the order of 0.5 cm/s. The rate of cosmic muons in the fiducial volume of the LAr1-ND detector is estimated to be  $\sim 2200 \mu/s$  (or roughly  $110 \mu/m^2/s$ , considering only the top surface area). Positive ion charge is therefore produced by cosmic ray muons at a rate of  $\sim 1.7 \text{ nC/s}$ . These ions are continuously neutralized at a cathode. An example of positive ion charge distribution in equilibrium for a LAr1-ND-like geometry is shown in figure 48, Left. Such accumulated volume charge leads to distortion of the drift field and, consequently, deviation of reconstructed track coordinates from the true ones by up to 2.5 cm (see figure 48, Right). Ion drift velocity is comparable to local argon flow velocities, produced by global argon re-circulation flow and thermal convection. Therefore, the resulting distribution of positive space charge inside the drift volume of the LAr1-ND TPC may show a sophisticated dynamic behavior.

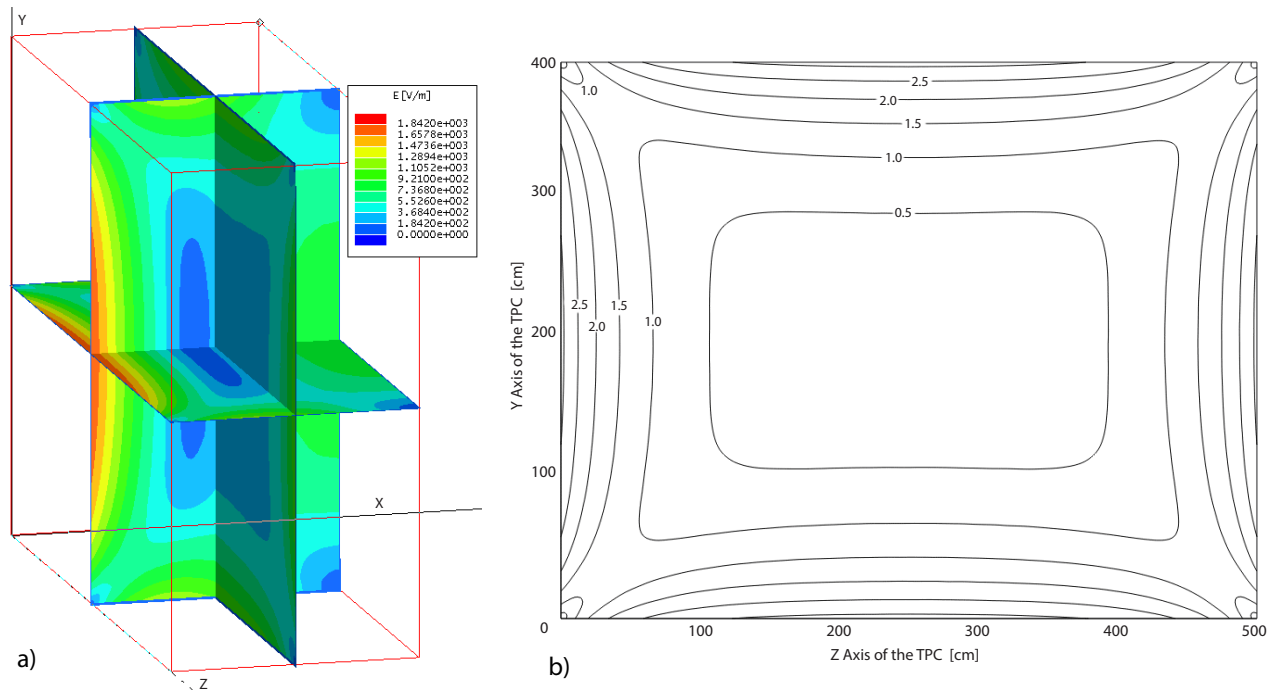


**FIG. 48:** (Left) Electric field strength of the accumulated space charge on 3 orthogonal cut planes inside a drift volume of the one half of LAr1-ND (red outlined box). In this view the beam goes into the page (parallel to the z-axis), the cathode is on the left and anode is on the right. The nominal 500V/cm drift field is not included. This distorting field is high at the middle of the cathode, and middle of the wire planes, causing longitudinal distortions along the drift. The field is also relatively high at the middle of the field cage walls, causing transverse distortions. (Right) Maximum transverse distortion (lensing effect) in the TPC for electrons originating from the cathode surface. The magnitude of the distortion decreases when the electron starting point is closer to the wire planes.

Analyzing the curvature of initially straight ionization tracks allows to reconstruct the distribution of the drift field vector across the whole volume of the detector [98]. This method was successfully exploited in the ARGONTUBE long drift TPC [99–101] to derive non-uniformity

of the electric field along its 5 m long drift volume. The method to generate straight ionization tracks at defined locations in liquid argon is described in [102]. The thin photon beam from the pulsed UV laser with  $\lambda=266$  nm ionizes argon via multi-photon absorption. The resulting ionization track is straight, characterized by low electron density, and therefore practically not subjected to charge recombination losses, unlike cosmic muon tracks. Those tracks are also free of  $\delta$ -electrons, which complicate track reconstruction in the case of muons. For the MicroBooNE detector a set of such tracks are required in order to cover the whole sensitive volume to reconstruct field distortion. Such tracks are created one-by-one by steering pulsed laser beams with the use of a custom-designed opto-mechanical feed-through (see [103]). The pulse rate of the laser generator is 10 Hz, capable of producing the minimum required set of 100 tracks within one minute (taking into account steering time).

### B. Laser Beam Arrangement and Beam Optics

A typical scheme of producing a fan of straight ionization tracks from one laser source in a TPC is shown in Figure 49. A Nd:YAG laser (Surelite I-10) from Continuum, Inc. emitting light at a wavelength of 1024 nm is used as the primary light source. Inside the laser head nonlinear crystals are installed in the beam line for frequency doubling and summing, resulting in a wavelength of 266 nm, needed for ionization of liquid argon. The pulse maximum energy at this wavelength is 60 mJ and the pulse duration is  $\approx 5$  ns. The maximum repetition rate is 10 Hz. The beam has a divergence of 0.5 mrad and the diameter of about 5 mm.

The beam is delivered to the top of the rotating optical feed-through via a beam conditioning optics. This optics allows to set the beam attenuation and diameter and allows computer-controlled adjustment of the beam direction within few degrees. The feed-through brings the beam into the cryostat and provides a capability of steering it across the whole detector active volume. The arrangement of the four optical rotating units in the LAr1-ND cryostat is shown in Figure 49, Right.

The four steerable mirrors are located at half-height of the TPC active volume in front of corresponding beam entry apertures in the TPC field-shaping structure, as shown in Figure 51. Each aperture has a diameter of 50 mm in order to maximize the deflection angle for the laser beam.

### C. Rotating Feed-Through

To deliver undistorted UV laser beam into the active volume of the LAr1-ND detector, a rotating optical feed-through with the steerable mirror has been designed. The mirror is mounted on a horizontally rotatable support structure. A rack and pinion construction, where the mirror is mounted on the front side of a half gear (pinion) provides the necessary freedom for the vertical movement. All movable components are motorized to allow for remote control and automation of the mirror movement. The mirror support structure was fabricated out of polyamide-imide (Duratron T4301 PAI), which has a very low outgassing rate, low thermal expansion coefficient and is certified for operation at 87 K. To minimize the probability of discharges due to the close location of the feedthrough to the field cage, no conductive parts were used in the support structure. The two principal parts of the feedthrough are shown in Figure 50. At the left, the top rotating unit, operating at room temperature is seen. The steerable mirror, mounted at the bottom of the feedthrough support column, is shown at the

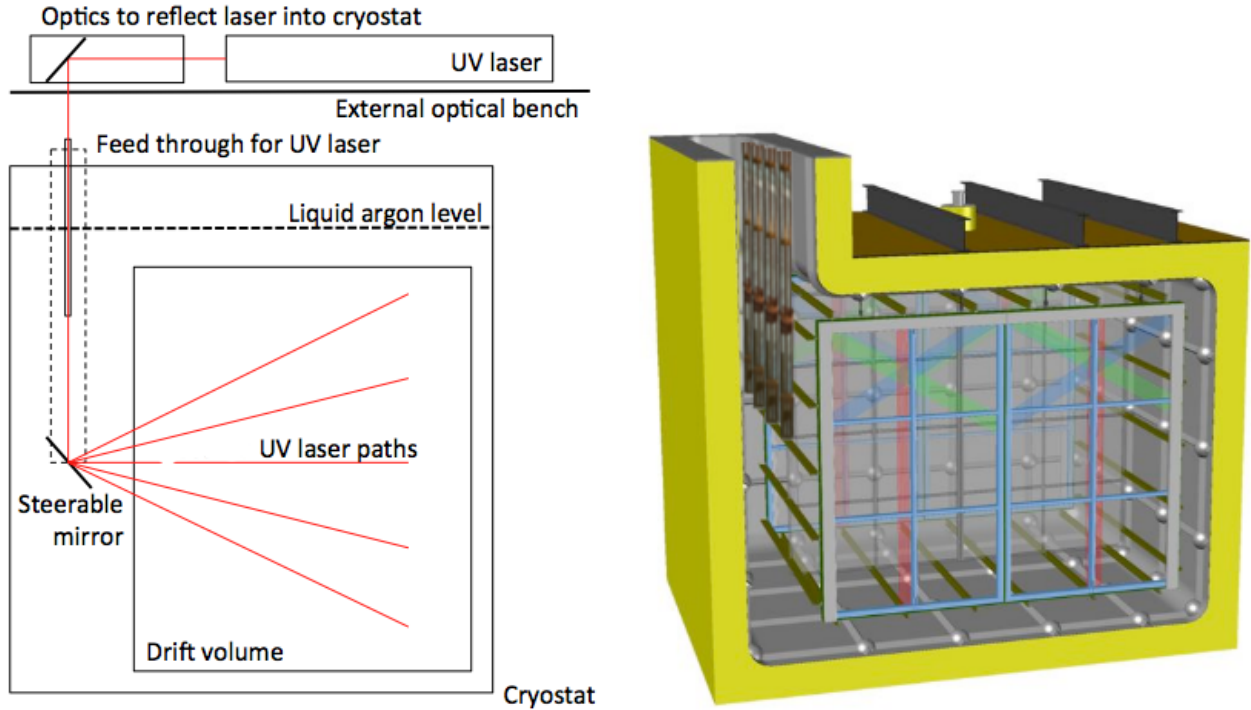


**FIG. 49:** *Left: a typical scheme of producing a fan of straight ionization tracks from one laser source in a TPC. Right: arrangement of four rotating optical feed-through in the LAr1-ND cryostat.*

right. In Figure 51 steerable mirrors mounted on the TPC field-shaping cage are shown. These units operates in liquid argon at the temperature of 87 K.

#### D. Expected Performance

An algorithm of field calibration has as input an array of detector events with one straight ionization track in each. The result of the algorithm is the coordinate correction map, which converts apparently curved track images back to true coordinate system, where they are straight. The algorithm is iterative with optimizable iteration step and therefore reconstruction accuracy. An example of simulated reconstruction in 2-D space is shown in Figure 52 for the case of a similar laser system that has been implemented in MicroBooNE. The distortion magnitude is reduced down to a few millimeters in 99% of the detector volume. A similar performance is anticipated for the LAr1-ND laser calibration system.

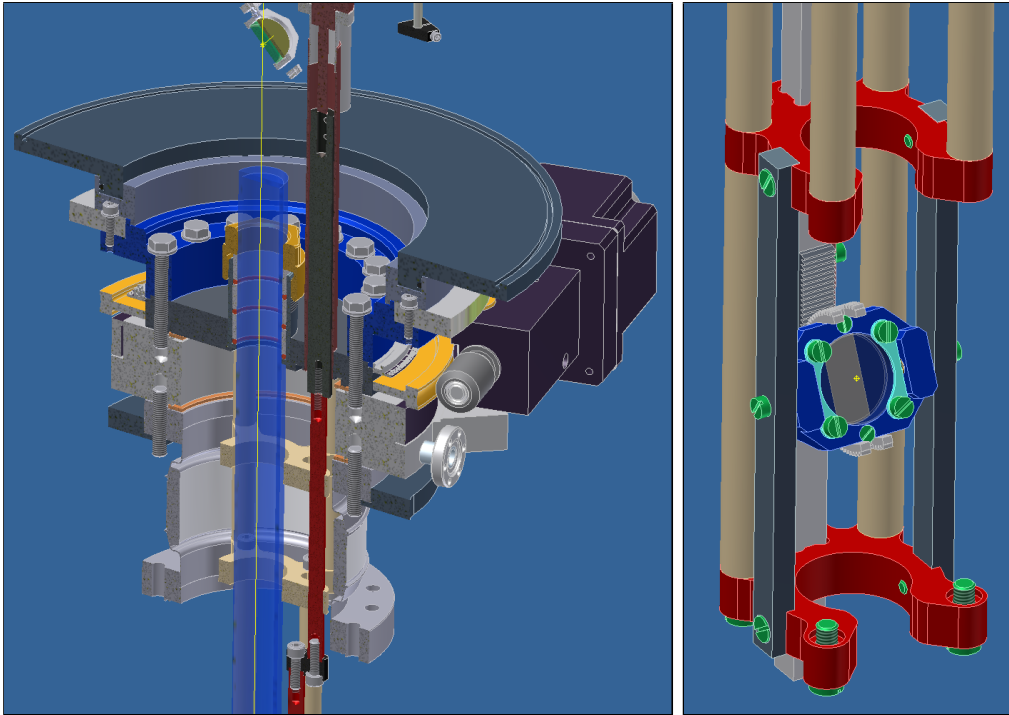


**FIG. 50:** *Left: CAD cutaway drawing of the feedthrough construction is shown. The yellow line indicates the path of the UV laser beam. Right: the cold mirror including the support structure.*

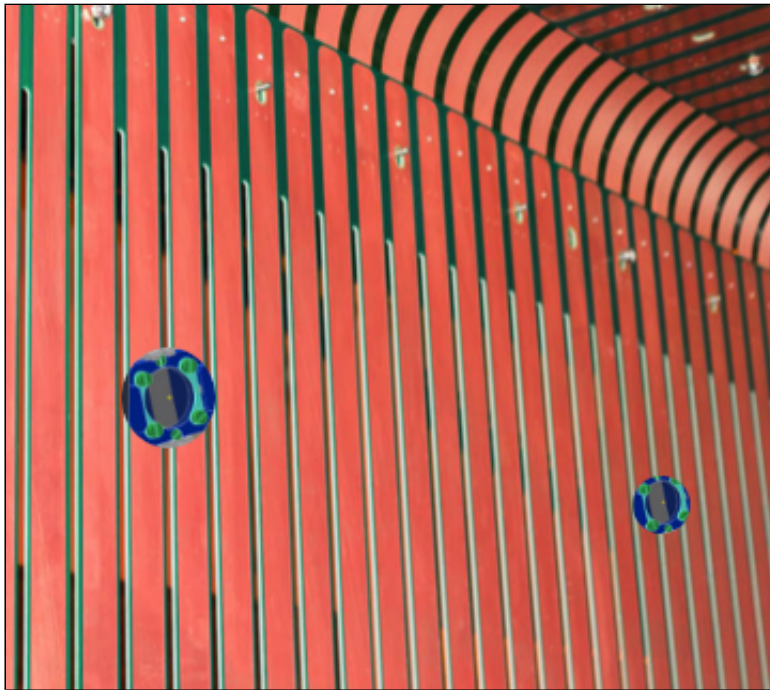


**FIG. 51:** *Steerable mirrors as seen through the 50 mm apertures in the TPC field-shaping cage.*

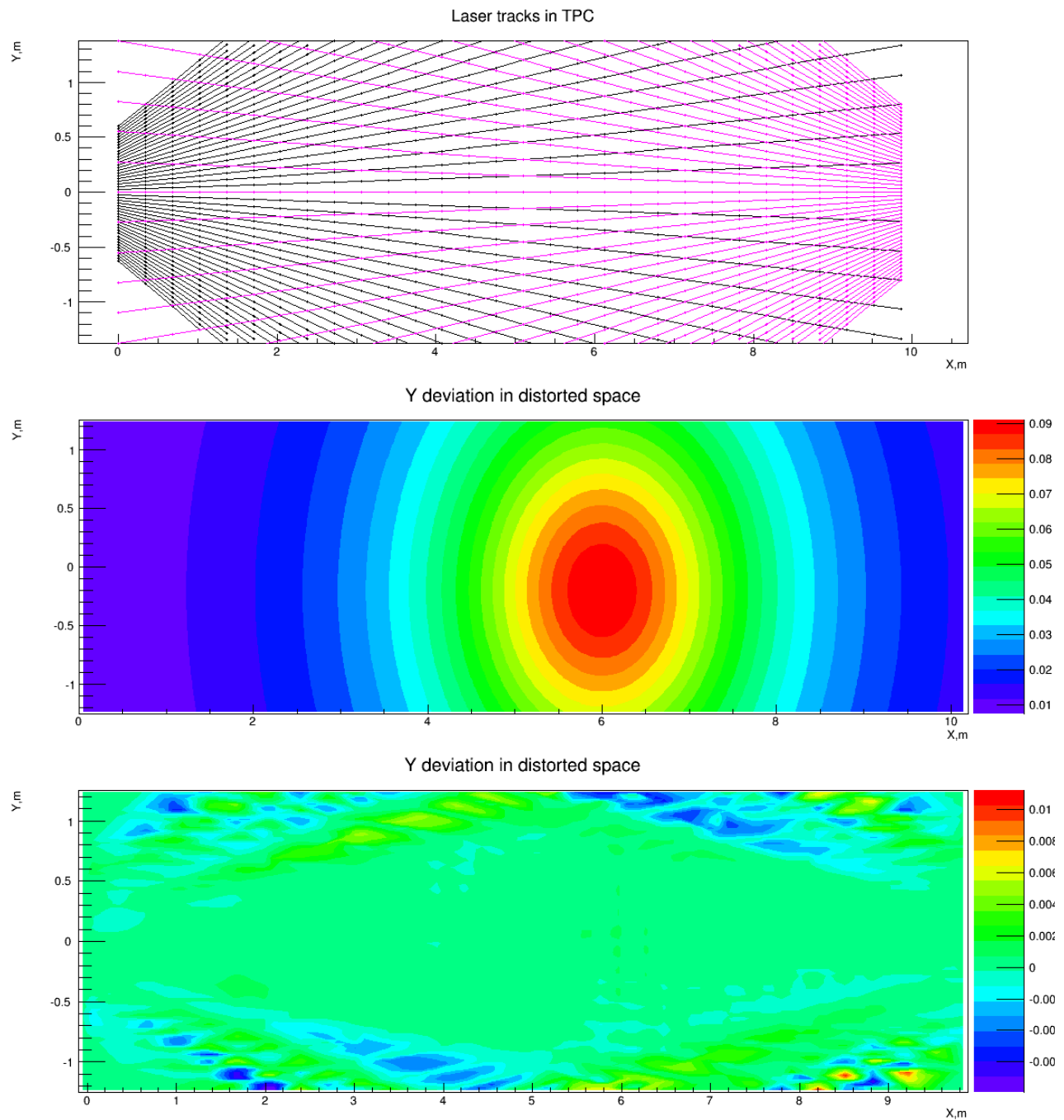


**FIG. 52:** Example simulation based on MicroBooNE showing the performance of the laser calibration system. (Top) True laser beam trajectories in the MicroBooNE LAr-TPC. (Middle) map of  $Y$  coordinate of track deviation under influence of an ad-hoc non-uniform electric field, which in this example is slightly offset from center. (Bottom) map of the residual  $Y$ -coordinate deviation from the true ones after application of the reconstruction correction based on the laser tracks. The color scale in the lower two plots is in units of meters.

## VII. Light Detection System

### A. Introduction and Motivation

Ionized and excited argon molecular states in the LAr volume will produce 128 nm vacuum ultraviolet (VUV) scintillation photons through recombination and de-excitation processes. The scintillation light includes a nanosecond-scale fast component (from singlet  $\text{Ar}_2^*$  decay with a lifetime  $\sim 6$  ns) as well as a microsecond-scale slow component (from triplet  $\text{Ar}_2^*$  decay with a lifetime  $\sim 1.6$   $\mu\text{s}$ ). Since recombination rates are reduced with higher electric field strength, a change in the field strength has opposite impacts on the amount of free ionization and scintillation light available for detection. At typical TPC field strengths, energy deposition by ionizing radiation is shared approximately equally between free ionization electrons and VUV scintillation photons, yielding approximately  $2.9 \times 10^4 e_{free}^-/\text{MeV}$  and  $2.4 \times 10^4 \gamma/\text{MeV}$  with a 500 V/cm electric field. It thus appears very appealing and natural to further optimize LAr-TPC detector performance by combining information from the available scintillation light with that from the ionization charge.

To be detected, scintillation photons are usually shifted from the vacuum ultraviolet to the visible to match the quantum efficiencies of available photodetectors, which typically peak around 430–450 nm. In most systems, this has been achieved using a fluorescent material to downshift the direct scintillation light (such as Tetraphenyl Butadiene, TPB) either coated on the surface of cryogenic photomultiplier tubes (as in ICARUS) or on plates mounted in front of the PMTs (as in MicroBooNE). PMTs must be located outside of electric field regions in the detector, thus in ICARUS and in MicroBooNE the PMTs are located just outside of the wire planes which are held close to ground. The resulting small photocathode area and limited solid angle coverage results in a relatively low light yield ( $\sim 1$  phe/MeV for the past ICARUS system and  $\sim 2$  phe/MeV for MicroBooNE).

Detection of scintillation light can play several important roles in LAr-TPCs, depending on the time, energy, and position resolution performance of the light detection system (LDS) that is implemented. Increased collection efficiency could result in the improvement of all three performance metrics and enable improved background rejection and access to additional physics topics.

For a surface detector in a beam, prompt light signals provide a ‘trigger’, indicating when an interaction has occurred in coincidence with the neutrino beam. In LAr1-ND, neutrino interactions in the active TPC volume are expected in about 5% of the 1.6  $\mu\text{s}$  long BNB beam spills. With a LDS time resolution of 1–2 ns, neutrino events could further be correlated with the 53 MHz Booster beam RF substructure (81  $\sigma=1.15$  ns wide pulses spaced 19 ns apart), leading to a potential 3-4 $\times$  reduction in random cosmogenic backgrounds in the  $\nu_e$  event sample (see Part I: Oscillation Physics Program). Figure 53 shows the BNB RF structure as measured by the MiniBooNE Cerenkov light detector. Also shown is the MiniBooNE time reconstruction of CCQE muon neutrino events relative to the beam RF time of the first proton pulse as determined by the Resistive Wall Monitor (RWM) discriminator. The CCQE muons exhibit the same time structure as the RF pulse, with a total time resolution of  $\sigma_t = 1.75$  ns. The extra spread is due to RWM timing jitter and event reconstruction time resolution.

Good timing reconstruction resolution, in conjunction with the beam RF structure, can also be used to tag neutron events that are produced by neutrino interactions in the surrounding dirt. Due to the extended interaction geometry and subluminal speed of the neutrons, they interact in the detector out of phase with the beam RF time structure. This produces a flat time



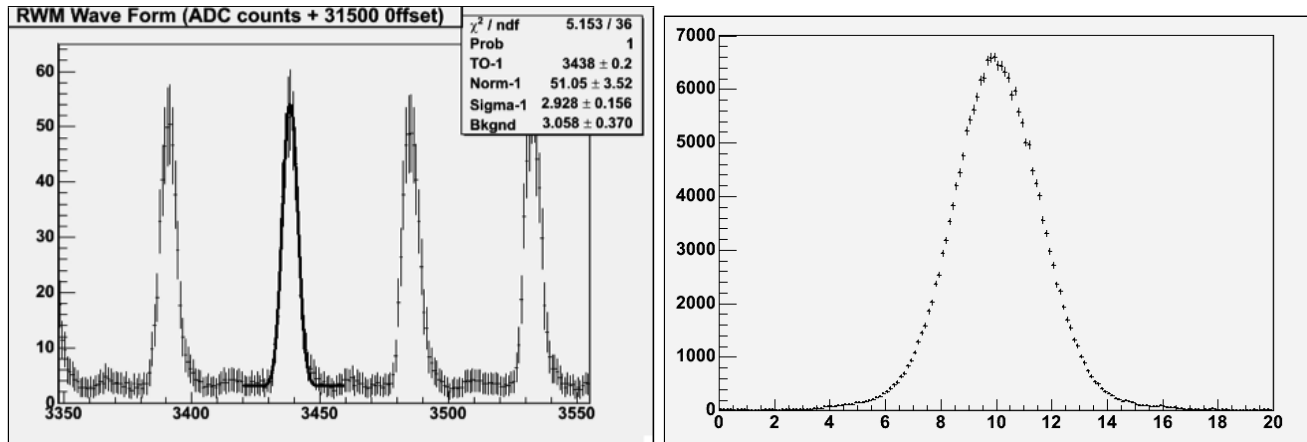


**FIG. 53:** *Left: The Booster-BNB 53MHz RF beam structure (2.5 counts/nsec). Right: the absolute time (nsec) reconstruction for CCQE muon neutrino candidates in MiniBooNE with all 81 bunches overlaid on top of each other, demonstrating that with good track timing, the RF structure of the beam can be reconstructed.*

response in the reconstructed bunch time (right plot of Figure 53), which can aid in background rejection and/or measurement of the neutron-dirt rate.

Prompt light signals also provide the unknown event  $t_0$  necessary to reconstruct non-beam related events such as cosmic rays or supernova neutrinos. A system capable of associating multiple light pulses with their sources in the detector permits identification and 3D reconstruction of different events occurring throughout the 1.28 ms TPC readout window. The  $t_0$  of each interaction in the detector is necessary to determine the location of the ionization along the drift direction and get an accurate reconstruction of the energy deposited along a track (by accounting for attenuation along the drift). The ability to identify the time of individual events will further contribute to rejecting cosmogenic backgrounds in the  $\nu_e$  analysis. An average of 2.9 cosmic muons are expected in the TPC volume per readout window, distributed across the 20 m<sup>2</sup> area of the TPC (see Part I of this proposal). A position resolution of the LDS of better than 1 m would be needed to enable association of light signals with different activity in the detector. It should be noted, however, that the association with entering muons will be significantly aided by the external cosmic ray tagging system described in Section VIII B.

A LDS with increased detection efficiency could improve the reconstruction threshold of argon neutrino detectors to as low as a few MeV, enabling access to whole new fields of study such as low-energy nuclear effects. This requires a more uniform light collection as well as at least a ten-fold improvement in the collection efficiency compared to existing LAr neutrino detectors. In addition to lowering the threshold, using the scintillation light for calorimetric reconstruction allows the compensation of charge recombination effects, thereby increasing the linearity of the overall energy resolution in the detector. The improvement in resolution obtained by higher light collection has been demonstrated in simulation [104, 105] and an example of the power of such a combined energy calculation in xenon has been shown by the EXO collaboration [106].

An enhanced light readout system can also contribute to particle identification. The PID will derive from pulse shape discrimination (PSD) methods used in dark matter noble liquid detectors which effectively distinguish nuclear recoils from minimally ionizing particles (MIPs) using the time structure of the scintillation light alone. In neutrino interactions, this would aid in the separation of neutron interactions (which produce heavily ionizing recoil protons) from

gamma scatters (that produce minimally ionizing electrons).

Sufficient light collection may also provide a way of determining the sign of the incoming neutrino without using a magnetic field through improved tagging of Michel electrons coming from stopping muons, including those at lower energies. Efficient reconstruction of this very well known process is particularly helpful in argon because negatively-charged muons have a 75% capture rate on argon atoms, in which case there is no Michel electron emitted at the end of a muon track, whereas this capture does not happen for positively-charged muons. Ref. [105] shows that light detection systems with efficiency  $\sim 1 \times 10^{-3}$  can isolate a sample of  $\mu^-$  events with relatively little  $\mu^+$  contamination. This capability will be essential in raising the sensitivity in anti-neutrino running both in sterile neutrino searches and CP-violation searches in LBNF due to the large wrong-sign component of the anti-neutrino beam.

### B. A Light Collection System for LAr1-ND

The relatively small volume of LAr1-ND makes it an excellent test-bed for new light detection system designs being considered for future LAr neutrino detectors, especially LBNF. The collaboration is committed to taking full advantage of this opportunity without incurring undue risk to the science goals of the SBN program. Hybrid systems that provide redundancy and side-by-side performance comparisons are also being considered and would fit well with the R&D goals of the experiment. LDS approaches currently being evaluated for LAr1-ND include: a system based on acrylic light guide bars read out at the ends with SiPMs, a system based on TPB-coated reflector foils to increase collection efficiency without increasing the number of photodetectors, and a traditional TPB-coated PMT based system.

Detailed MC simulations of the light generation and detection are being developed to compare reconstruction performance criteria such as track time, calorimetric energy, and position resolution. These results will inform the final design choice and determine the feasibility of a hybrid system comprised of elements from more than one of the present concepts. Studies are in progress and will be completed to enable a technology decision early in 2015.

#### *Light Guide Bar Light Detection System*

A light guide bar based light detection system has been initially proposed for LAr1-ND [7], based on a design originally developed for LBNE. In the LBNE design the system is positioned inside the APAs with wrapped wires. Thin profile light guides, measuring  $100 \text{ cm} \times 2.54 \text{ cm} \times 0.64 \text{ cm}$ , with wavelength shifter (WLS) deposited on their surface are used to collect the 128 nm LAr scintillation light. The WLS converts the VUV photons to  $\sim 425 \text{ nm}$  photons, some of which enter the bar. The downshifted photons are internally reflected to the end where they are detected by 3 SensL SiPMs whose QE is well matched to the  $\sim 425 \text{ nm}$  photons (See Fig. 54). This design allows one to collect light over a larger area with a relatively small number of readout channels. Four cast acrylic bars are assembled into “paddles”. Each LBNE APA measures  $7 \text{ m} \times 2.5 \text{ m}$  and contains 20 of these light guide paddles. The solid angle subtended by an LBNE APA from a point displaced 2 m from its center is 15% and the fraction of the APA surface covered by light guides is 12%. A total of 108 APAs are used in each of 2 cryostats, totaling  $108 \times 2 \times 20 \times 4 = 17,280$  light guide bars in LBNE.

The light guide photon detection system being considered for LAr1-ND aims to maximize the active area of the light guide bars to have both a high photon detection efficiency and

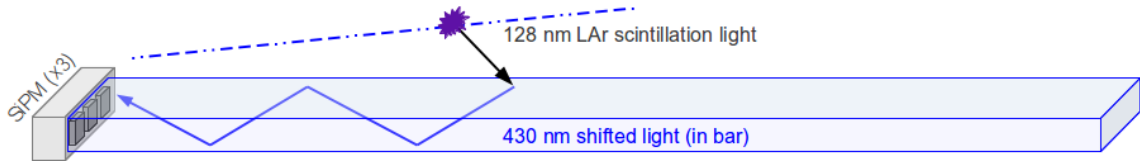


**FIG. 54:** *Cartoon of LAr scintillation light detection with a light guide coated with WLS.*

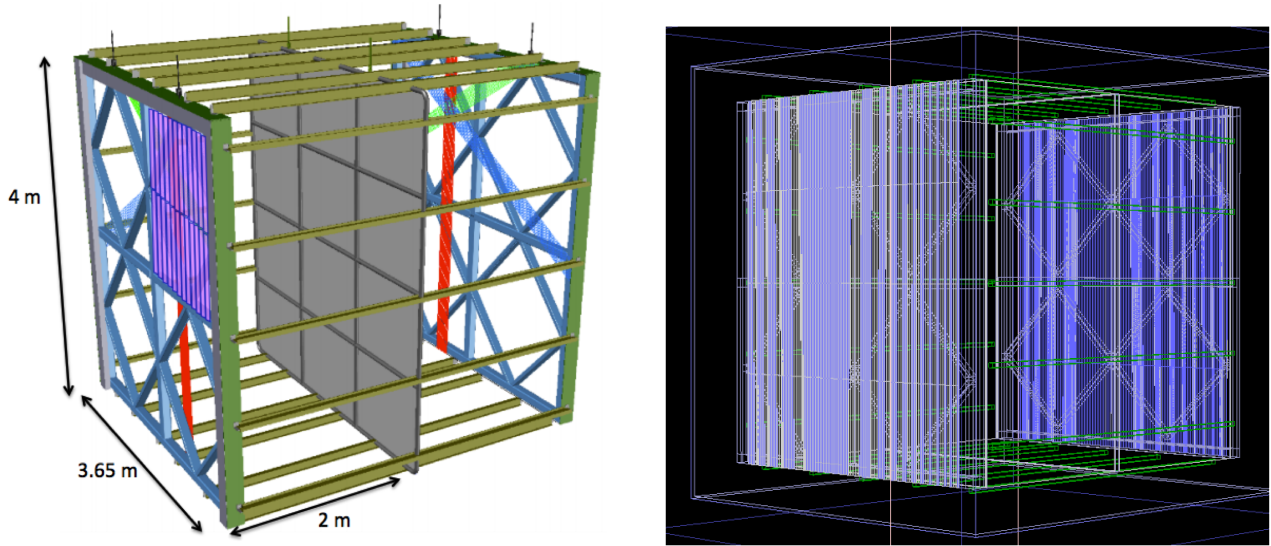


**FIG. 55:** *Left: Cartoon of the light guide design for LAr1-ND. Right: Light guide design implemented in Geant4.*

good granularity for timing and position resolution, which are especially valuable for a detector operating at the surface. The present design consists of 1,000 acrylic light guide bars coated with WLS embedded acrylic, each measuring  $100\text{ cm} \times 2.54\text{ cm} \times 0.64\text{ cm}$ , mounted behind the LAr1-ND wire planes, as shown in Fig. 55. The solid angle subtended by a LAr1-ND APA from a point displaced 2 m from its center is 16% and the fraction of the APA surface covered by light guides is 87%. Both ends of each bar will be read out by an array of 3 SiPMs, smoothing out the position-dependent response of each bar and improving the overall light collection efficiency of each bar by a factor of  $\sim 2$  relative to the LBNE design. Furthermore, LAr1-ND will use new low-noise SensL SiPMs (MicroFC-60035-SMT), which have an order of magnitude lower dark rate.

The LAr1-ND light guide photon detection system builds off the LBNE design and therefore benefits directly from LBNE-related R&D efforts. Measurements of light guide bars in LAr have yielded valuable information on their performance and led to significant improvements in their design and quality. In particular, as an improvement over hand-painting the bars, the WLS solution is now applied to the surface by dip-coating the acrylic bars and then allowing them to dry in a low humidity environment. Recent measurements of these improved light guides have shown that attenuation lengths of over 100 cm are routinely achievable. Furthermore, preliminary data from studies of these light guides in pure LAr suggests that the global quantum efficiency (defined as the number of photoelectrons divided by the number of incident 128 nm photons) 50 cm from one end of the bar is  $\sim 0.5\%$ . Therefore, the global quantum efficiency when reading out both ends of the bar is expected to be  $> 1\%$ . Preliminary estimates indicate that

the light guide based photon detection system will collect 24 phe/MeV from a point displaced 2 m from its center and more than 24 phe/MeV when averaged over the entire TPC volume. A full MC simulation is in progress to confirm these performances.

### *TPB-coated Reflector Foil Light Detection System*

A second design, based on a concept adapted from liquid argon dark matter detectors, proposes the installation of TPB-coated reflector foils inside the TPC volume to enhance light collection. The higher quantities of light collected would open the door to exploring physics topics not accessible to LAr-TPCs with standard readout schemes. By trapping light within the volume using TPB-coated reflective foils, light yield is enhanced naturally with less need to increase the number of DAQ readout channels as compared to solutions that achieve similarly-high light yields by scaling up photocathode coverage. A smaller number of readout channels allows for easier and more practical implementation of high-speed signal digitization, which would immediately improve the timing resolution of the system.

A system of this type is currently implemented in the LArIAT experiment (LAr-TPC In A Test Beam). LArIAT's light readout system collects many more scintillation photons than typical liquid argon neutrino experiments, with simulations estimating about 40 phe/MeV at zero field – substantially higher than the reach of both current and planned liquid argon neutrino detectors ( $\sim 1$  phe/MeV for ICARUS,  $\sim 2$  phe/MeV for MicroBooNE, and  $\sim 0.2$ - $0.3$  phe/MeV for the proposed LBNE system). The light yield simulation was cross-checked against available analytic predictions [107] and has been recently validated through measurements on a small-scale prototype where two high-QE cryogenic PMTs were used to collect and read out scintillation light in argon. Bench tests of SiPMs mounted to custom on-board preamps are also underway at FNAL and early results are encouraging. The forthcoming LArIAT test beam run will provide information both on technical and physical aspects of a reflective foil enhanced efficiency light system for LAr-TPCs.

The LArIAT optical system, with reflectors covering 60% of the active volume's inner surfaces and a photocathode coverage of 0.35%, appears scalable up to the LAr1-ND dimensions with no need to transition through a dedicated R&D phase. A zero-field light yield on the order of 100 phe/MeV (corresponding to 0.5% photon detection efficiency) is the target for the LAr1-ND design. Preliminary simulations indicate a photocathode coverage of approximately 0.4% coupled with 70% inner surface coverage of TPB-coated reflector foil is required to reach this level. For a LAr1-ND half-module, this translates to 1900 cm<sup>2</sup> of distributed photocathode area and about 50 m<sup>2</sup> of TPB-coated foil covering the inner surfaces of the field cage and cathode. A full MC simulation is in progress to confirm these specifications.

The wavelength-shifting TPB film (200  $\mu\text{g}/\text{cm}^2$ ) is deposited by vacuum evaporation on a substrate like Vikuiti ESR, a highly reflective and non-metallic foil made by multi-layer polymer technology. Each foil is 65  $\mu\text{m}$  thick, and can be fashioned in a variety of different sizes (for example, 50  $\times$  50 cm<sup>2</sup>) and mounted to thin, rigid supports with comparable coefficients of thermal expansion to create modular TPB-coated reflector tiles. These tiles can then be installed in an array to cover the inner surfaces of the field cage, and may also be easier to work with in the TPB deposition process.

The choice of photosensor is restricted to high-QE cryogenic PMTs, SiPMs, or a combination of the two. Adequate photocathode coverage could be provided by about 50 3-inch diameter PMTs positioned in an array behind the wire planes, or by about 1600 1.4 cm<sup>2</sup> SiPMs distributed behind the wire planes and possibly onto the field cage. Silicon photomultipliers offer several

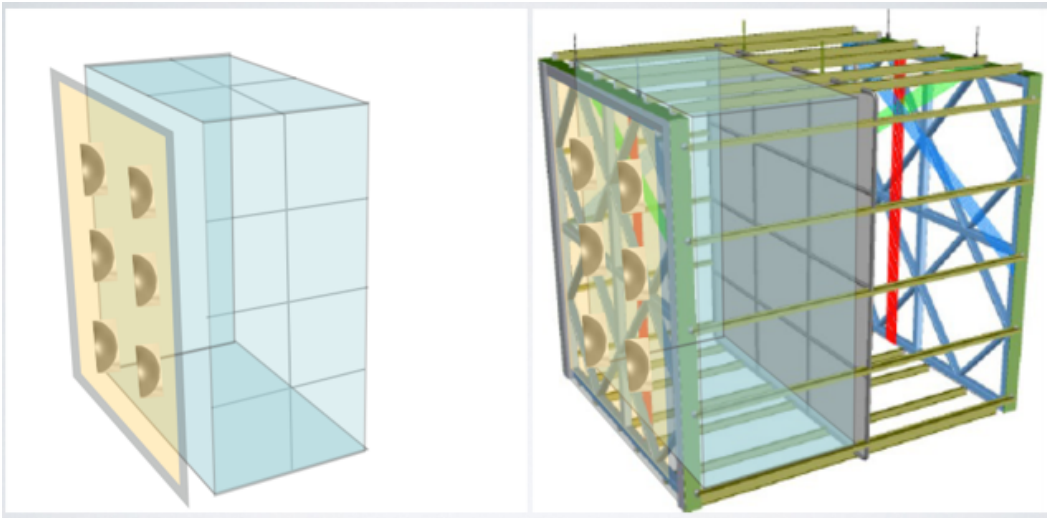


**FIG. 56:** Schematic view of an enhanced efficiency light detection system in LAr1-ND. Shown on the left is the photosensor array behind the wire plane as well as modular TPB-coated reflector tiles lining the inner field cage of one half-module of the LAr1-ND detector.

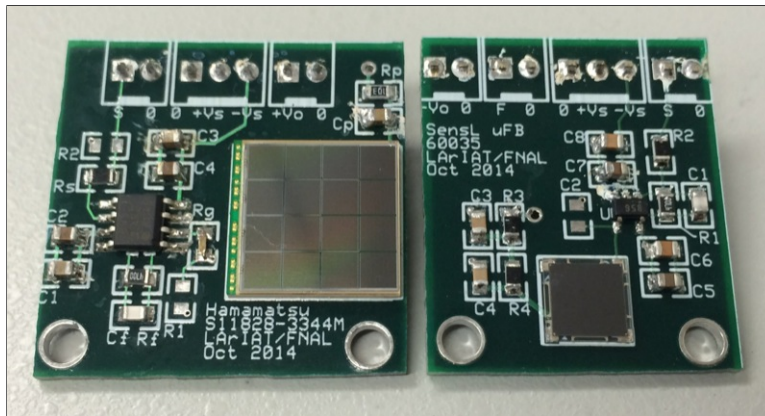


**FIG. 57:** Custom readout electronics developed by LArIAT. Boards include bias voltage filtering, preamp, and readout for the Hamamatsu S11828-3344M, a  $4 \times 4$  SiPM array with a total active area of  $1.2 \times 1.2 \text{ cm}^2$  (left), and for the SensL MicroFB-60035 single SiPM channel with area  $0.6 \times 0.6 \text{ cm}^2$  (right).

notable advantages over PMTs, given their high QE coupled with small occupancy and low bias voltage. The forthcoming LArIAT run will provide full characterization of the SiPM response to LAr scintillation light in operating conditions to compare directly to PMT performance. Electronics for reading out SiPM arrays (groups of 16 SiPM channels) as well as single channel SiPM chips, which include on-board bias voltage filtering and preamp/shaping circuitry as shown in Figure 57, have been developed. Further modifications to optimize the gain and timing response of the boards will be investigated. The TPB-coated reflector tiles described above may provide the necessary support for mounting variations of these miniature SiPM boards onto the field cage walls if such a layout proves advantageous.

The choice of the DAQ system for the TPB-coated reflector foil light detection system depends on the photosensor adopted, and in the case of PMTs, the limited number of readout

channels and the fast signal formation enables the use of fast waveform digitizers like the CAEN V1751 (10 bit, 1 GS/sec ADC) currently used in LArIAT. However, their use would require full and detailed engineering and augmented DAQ performance due to the potential increase in readout channels. The Silicon Photomultiplier signal Processor module described in Sect. VII B seems an appropriate solution for the SiPM option, offering 14-bit, 150 MS/sec ADC for digitizing signals. This module have full waveform-recording capabilities with flash ADC, but also allows for flexible FPGA data processing algorithms needed for real-time pulse height and area measurements.

#### *PMT-based Light Detection System*

Light detection using TPB-coated cryogenic PMTs is known to work well in modest-sized LAr-TPCs, like the ICARUS T600 and MicroBooNE. This design is not easily scalable to big detectors, and different systems, like the ones reported in the previous sections, have been developed in view of larger LAr-TPCs for future applications.

In a PMT-based system, by using fast PMTs and good pixelization, the goal is to detect as much prompt and delayed scintillation light information (time and charge) as possible. This will then provide good event time and position reconstruction and track matching with the TPC. The preference is to have a transparent cathode to maximize the prompt light collection. A PMT-based system designed for LAr1-ND would use Hamamatsu R11065 3" diameter PMTs with 25% QE, and 6.5 ns transit time spread (full width at half max) at LAr temperatures. The PMTs are flat face and would have a 3" TPB wavelength shifter affixed to the surface. The combined PMT+TPB efficiency at 128 nm is expected to be 12.5% .

The LAr1-ND detector instrumented with 121 PMTs on each side arranged in an  $11 \times 11$  grid over a  $4 \text{ m} \times 4 \text{ m}$  frame would have 1% total photocathode coverage, or 6.7% on each of the instrumented sides. Light yield in this configuration is estimated to be 13 phe/MeV for a source 2 m away from the the center of an APA, where about 25% (50%) comes as prompt light for lightly (heavily) ionizing particles. A full MC simulation is in progress to confirm these performances. The option to instrument the outer veto region (LAr outside the active TPC boundaries) is being investigated as well.

#### *Electronics for the Light Detection System*

Several options exist for reading out SiPM or PMT signals, each of which has its own relative merits. These options include a direct signal digitization or the signal digitization after SiPM/PMT pulse shaping. Fast (direct) digitization of SiPM pulses has been implemented by the HEP Electronics Group at Argonne National Laboratory (ANL) to support the development of the photon detection systems for LBNE. The FEE developed at ANL is being adopted for SiPM readout, but the implementation is flexible and may be modified for use with PMTs, if desired.

Each SSP (SiPM Signal Processor) module (Fig. 58) consists of 12 readout channels packaged in a self-contained 1U module. Each channel contains a fully-differential voltage amplifier and a 14-bit, 150 MSPS analog-to-digital converter (ADC) that digitizes the waveforms received from the SiPMs. The digitized data is then processed by a Xilinx Artix-7 Field-Programmable Gate Array (FPGA). The FPGA implements an independent Data Processor (DP) for each channel. The processing incorporates a leading edge discriminator for detecting events and a

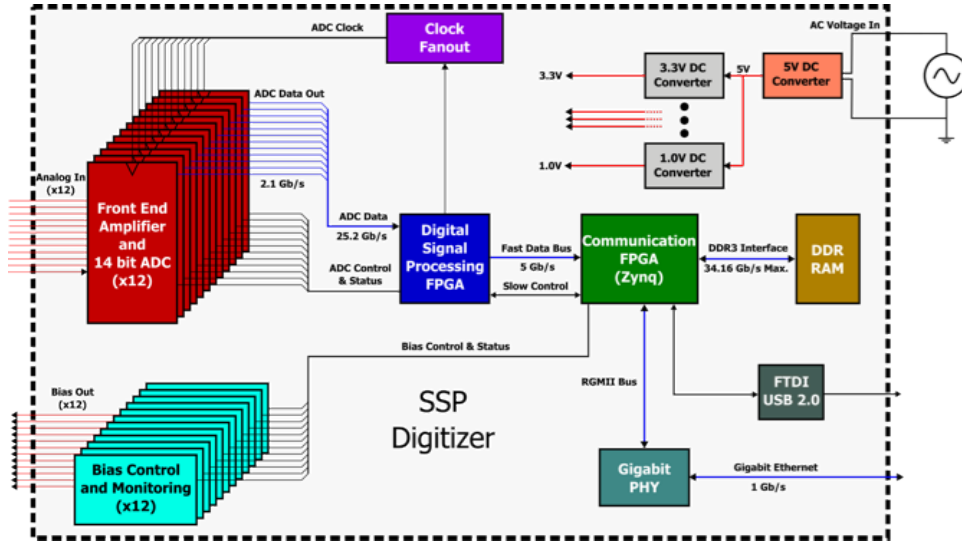


**FIG. 58:** Block diagram and physical realization of the prototype SSP module.

constant fraction discriminator (CFD) for sub clock timing resolution. In the simplest mode of operation, the module can perform waveform capture, using either an internal trigger or an external trigger. As an alternative to reading full waveforms, the Data Processors can be configured to perform a wide variety of data processing algorithms, including several techniques for measuring amplitude, and also timing of the event with respect to a reference clock.

If a faster timing response becomes one of the requirements of the photon detection system, a faster ADC with a shaper will be incorporated into the front-end electronics to achieve improved timing resolution. The present system samples the waveforms at 150 MSPS, and achieves  $\sim 2$ -3 ns resolution on single photo-electron signals. Given that the time constant of the prompt light is 6-7 ns, it may become necessary to improve the timing resolution to the sub-nanosecond level. This would require the use of faster ADCs and possibly pulse shaping. This is not part of the system specifications currently, but would be an R&D activity should the performance be required.

## VIII. Cosmic Ray Tagging System

As described in Part I of this Proposal, cosmic ray muons are the most abundant background in a LAr-TPC at surface. Although muons do not contribute significantly to the background for the sterile neutrino search, they produce  $\delta$ -rays, which in turn produce photons by Bremsstrahlung. These photons, via Compton scattering or pair production, could possibly mimic a  $\nu_e$ -like interaction signature.

The addition of a cosmic ray tagging system, that detects cosmic ray muons and measures their time and position relative to events internal to the TPC, is a way to mitigate the cosmic ray background.

From Monte Carlo simulations, the average number of cosmic muon tracks, seen in each of the LAr1-ND TPC events is about 3. Each muon track is surrounded by tracks of electrons and positrons, originating from Bremsstrahlung of delta-electrons produced by muons, and, for rare very high energy muons, by muon Bremsstrahlung in the liquid argon. The cosmic ray tracker system chosen for the LAr1-ND detector is composed of scintillators external to the LAr1-ND

cryostat providing  $4\pi$  solid angle coverage.

### A. Scintillating Tracker Design and Operation

The LAr1-ND cosmic ray tracker is composed of scintillating planes, each consisting of an array of  $1 \times 10 \times 400$  cm scintillating bars as shown in Figure 59. One plane provides coordinate resolution in X - and the adjacent plane provides resolution in Y coordinate. In the following description each such sandwich is referred to as X-Y tracker plane.

Each bar is made of BC-440 (or similar) plastic scintillator with the emission maximum at 434 nm and bulk attenuation length of  $>400$  cm. The bar is wrapped in a diffuse reflector foil (Tyvek) to make the light field inside the bar more uniform and, additionally, in an aluminum-coated Mylar foil. The insensitive gap between two adjacent bars is about 0.5 mm.

In order to provide a more efficient and uniform collection of scintillation light along the bar, two wavelength-shifting fibers (1 mm diameter multi-clad Kuraray WLS Y11(200) S-type [108]) are glued into the scintillating bar near its edges at both lateral sides. The light is transmitted by the fibers to the bar edge, where it is detected by the Hamamatsu S12825-050P multi-pixel Geiger avalanche photo-diodes (MAPDs, also known as SiPMs). Matching of the Y-11 emission spectrum to the SiPM sensitivity is illustrated in Figure 60.

In order to mitigate cosmic ray events, a  $4\pi$  solid angle coverage of the TPC is highly desirable. On the top, where the flux of cosmic rays is maximum, an additional X-Y plane is installed at the distance of 2 m above the X-Y plane covering the top surface of the TPC as shown in Figure 61. These two planes in combination form a telescope, that provides coordinate resolution of  $10/\sqrt{12} \approx 2.9$  cm at the detector planes and angular resolution of  $2 \times 2.9/200 \approx 0.03$  rad.

In order to increase the rejection of the EM background and the detection efficiency of  $\nu_e$  CC interactions the following algorithm is proposed. The time distribution of the muon-related signal from the scintillating tracker is compared to that of the internal TPC light detection system and to the beam gate. Muon tracks, detected in the TPC are extrapolated to the scintillating planes. The time distribution of the signal from the scintillating tracker channels, that are crossed by the extrapolated muon trajectories is used to build correspondence with the internal TPC light collection system signals. Those tracks, that are seen by the tracker and internal light collection system outside of the beam gate are unambiguously identified as cosmic muons, The remaining event with the signature of no signal in scintillating tracker and the signal in the TPC light collection system in time with the beam gate can be identified as the beam-related. All 7 X-Y planes of the scintillating tracker are essential for this procedure.

### B. Electronic Readout System

As mentioned above, in the proposed design the Hamamatsu S12825-050P photodiodes are used to convert wavelength-shifted scintillation light to the electronic analog signal. The most relevant parameters of these diodes are shown in Figure 62 as a function of the over-voltage (the difference between the applied reverse-bias voltage and the breakdown voltage). At the over-voltage of 2.0 V the PDE at the maximum of the spectral sensitivity is about 32% and the gain exceeds  $10^6$ . The pulse frequency at the threshold allowing to detect single photons is of the order of 100 kHz at 20°C. The signal from photodiode is amplified and shaped by a CITIROC multi-channel front-end ASIC, designed by Omega. The analog signals are discriminated at



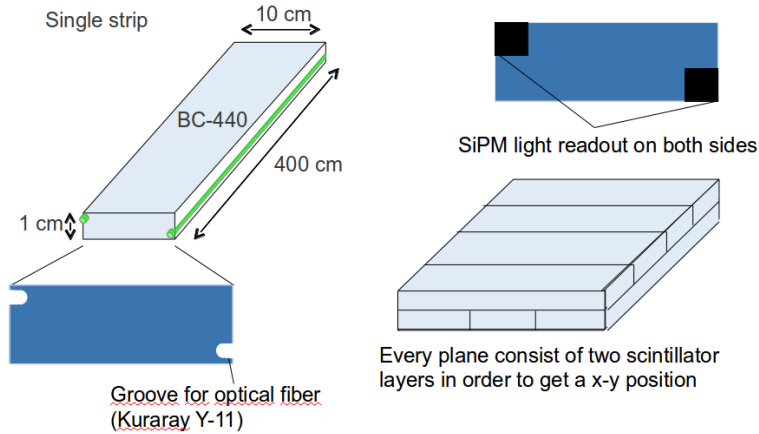


**FIG. 59:** Veto plane composition: scintillating bars with WLS fibers glued into grooves along strip sides. The material for the bars is BC-440 or similar plastic scintillator. Scintillation light is collected with Kuraray Y-11 WLS fibers and transmitted to the bar edge, where it is detected by Hamamatsu S12825-050P SiPMs.

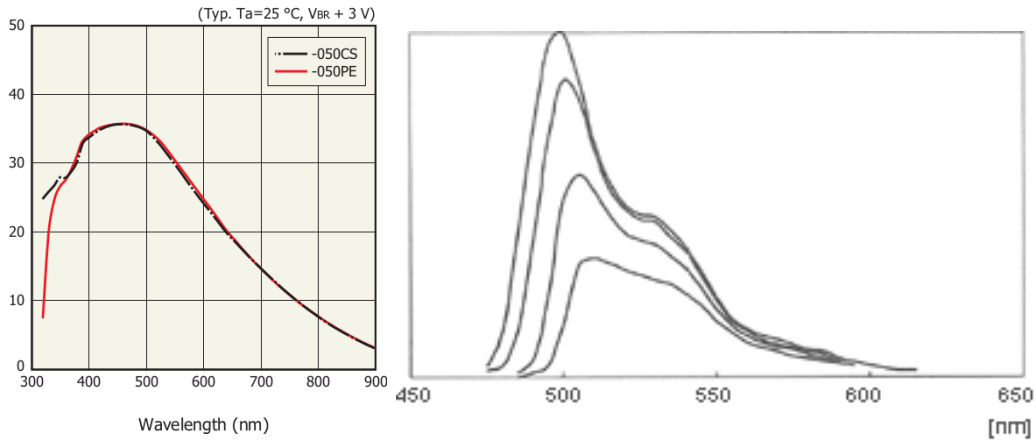


**FIG. 60:** SiPM spectral sensitivity (left), and emission spectrum from Y11 WLS fiber (right).

the level of a 1.5 of single photo-electron response. To suppress the dark current rate the logic coincidence is used at each end of the scintillating bar, between the signal from two diodes glued to two WLS fibers at each side of the bar. The resulting logic signals together with digitized peak values of the shaped analog signals and time stamp are stored in a FIFO buffer and eventually transmitted via Ethernet link to the experiment DAQ system for event building and storage.

### C. Expected Performance

The performance of the proposed tracker configuration is estimated on the base of the experimental data published in reference [109]. The authors studied the light yield and timing characteristics of a similar scintillating tracker with 16 m long scintillator bars, Kuraray Y-11(200)S WLS fiber and Hamamatsu S10362-13-050C photodiodes, very similar to S12825-050P used in the present proposal. The thickness of the bars studied was 7 mm and the width from

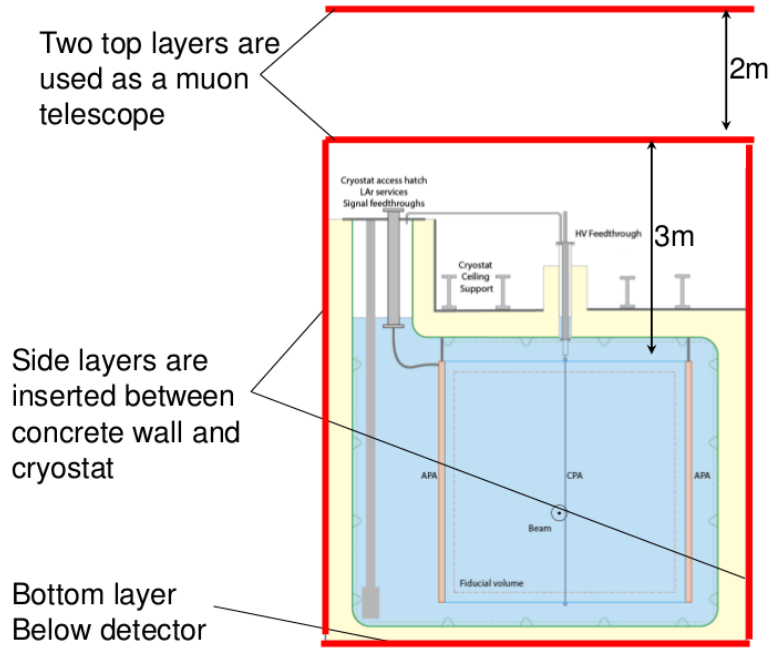


FIG. 61: Veto planes arrangement around the detector.

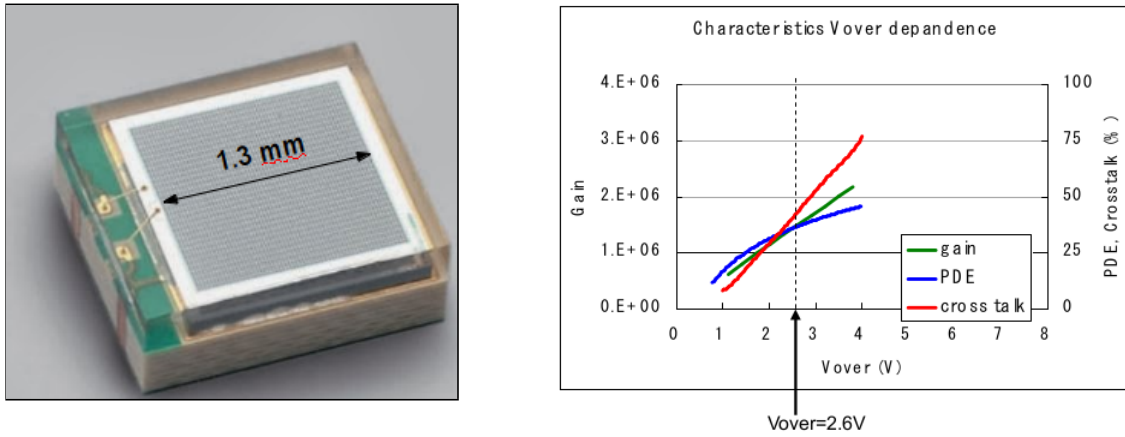


FIG. 62: Hamamatsu S12825-050P SiPM (left), photon detection efficiency (PDE), noise and pixel cross-talk as a function of over-voltage at 408 nm (right).

1 cm to 4 cm. The effective attenuation length was found to be  $\approx 4.2$  m. Extrapolating their data to the case of  $1 \times 10 \times 400$  cm bars yields the expected data on light yield, shown in the table XIII. The detection inefficiency in each channel is calculated as a Poisson probability to obtain a signal lower than 2 p.e. The single end trigger inefficiency is given by the logic AND between left and right channels at each end of the bar.

The velocity of the re-emitted light propagation in the Y11 fiber is found to be  $16.00 \pm 0.08$  cm/ns and the decay time of Y11 fiber  $12 \pm 0.5$  ns [109]. Therefore the coincidence window for left and right discriminated signals is conservatively chosen to be about 100 ns (defined by CITIROC FE ASIC timing characteristics). The rate of dark current pulses above the 1.5 p.e. threshold is about 10 times lower than that for single photo-electron [110], that is of the order of 10 kHz. The resulting rate of accidental left-right coincidence is about 10 Hz. Such a low

**TABLE XIII:** *The summary on the expected MIP light yield and detection efficiency for the proposed cosmic ray tracker. The data is obtained by extrapolation of experimental results published in [109].*

	Near end (1.0 m)	Far end (4.0 m)
Light yield, p.e.	22	11
Detection inefficiency	$6.4 \times 10^{-9}$	$2.0 \times 10^{-4}$
Single end trigger inefficiency	$1.2 \times 10^{-8}$	$4.0 \times 10^{-4}$
Single channel dark count rate	10 kHz	10 kHz
Single end trigger dark count rate	10 Hz	10 Hz

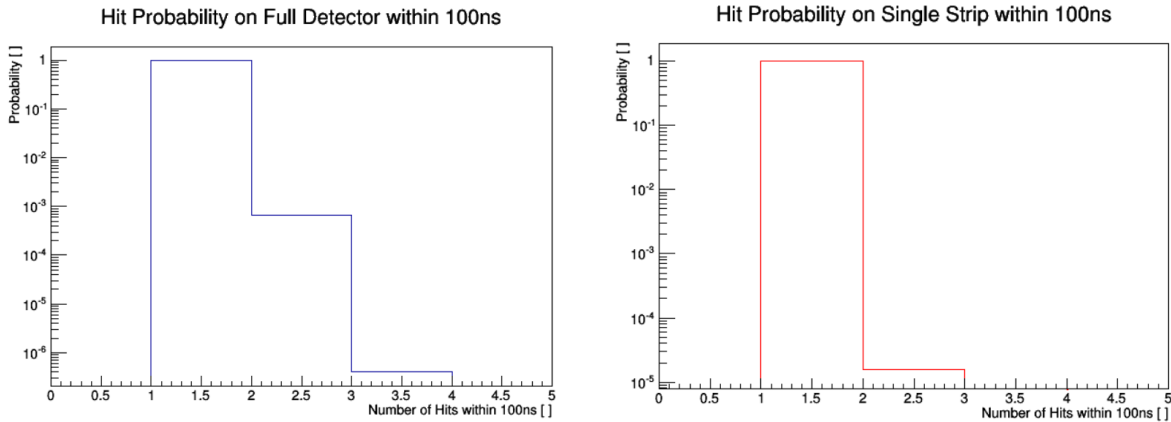


**FIG. 63:** *The expected muon multiplicity over the whole top scintillator plane (left) and over one  $1 \times 10 \times 400$  cm scintillator bar.*

rate allows us to minimize the useless part of the data flow from the scintillating tracker and to use inexpensive low-rate transmission channels from the tracker planes to the processing unit. At the processing unit a more sophisticated logic of correlation of the signals from both ends of the bar, as well as with the signals from the perpendicular bars can be implemented.

The expected minimum sum of the signal from both ends of the bar is 36 p.e. on each of the left and right WLS fiber channels. The total sum per bar is therefore 72 p.e. The minimum total sum of the dark count pulses is  $2 \times 4 = 8$  p.e. Setting a constraint of having the total sum per bar of at least 20 p.e will bring the rate of fake hits per bar down by more than ten orders of magnitude, making it negligible. The additional inefficiency introduced by such cut is of the order of  $10^{-13}$ , therefore, also negligible.

The probability of the multiple muons hitting the same scintillator channel is estimated from the Monte-Carlo simulation of cosmic muon flux at the detector surface by CRY simulation package. The resulting multiplicities are shown in Figure 63. The graph at the left shows average multiplicity of muon tracks in the whole top  $4 \times 4$  m<sup>2</sup> surface of the tracker X-Y plane, while the right plot shows the multiplicity in each single scintillating bar within 100 ns of the signal integration period. The probability to have more than one hit per bar is of the order of  $10^{-5}$ .

Since the detection inefficiency of the proposed light readout system is negligible, the total detection efficiency of the tracker is limited by the 0.5 mm thick insensitive gaps between adjacent scintillating bars. The detection efficiency of one coordinate plane is therefore about 99.5%. If the coincidence of X and Y planes is required, the detection efficiency drops to 99%

per X-Y plane.

### IX. The LAr1-ND Detector: A Development Toward LBNF

LAr1-ND presents an excellent opportunity for the continued development of the LAr-TPC technology toward the LBNF program. The design of the LAr1-ND detector is largely based on current LBNF-type technology, but alternate solutions can also be pursued where it is valuable to inform final choices for the LBNF detector. The designers of LAr1-ND systems are, in many cases (i.e. cryostat, cryogenics, TPC, cold electronics), the same teams working on LBNF designs, ensuring good communication of ideas and lessons learned. LAr1-ND's location 110 m from the Booster Neutrino Beam target will provide a unique opportunity to test specific components and new concepts in a high-rate neutrino beam.

Tables [XIV](#), [XV](#), and [XVI](#) compare different systems of the LAr1-ND and LBNF detector designs, highlighting key similarities and differences.

A comparison of the LAr1-ND and LBNF design of the cryostat and cryogenic systems is reported in Table [XIV](#). The same membrane-style cryostat is used. One difference is the location of the cryogenic pumps. Also, in LAr1-ND, there is the possibility that the liquid completely fills the main volume, touching the top plate, in order to minimize the outgassing from the surface and cabling. This choice is currently under study.

Table [XV](#) compares the features of the LAr1-ND and LBNF TPC designs and many similarities exist. The main difference is that the LAr1-ND design does not wrap the readout wires around the APA frames since this is not needed with the drift volume only on one side.

As reported in Table [XVI](#) the LAr1-ND electronics is largely based on an already developed LBNF design. The choice of the cold FPGA for digital processing is due to the long lead time needed to develop a dedicated ASIC for this task. This work is underway, and could be tested in the detector in a future phase of running.

Finally, as discussed in Section [VII](#), LAr1-ND provides an excellent test-bed for light collection systems in a LAr detector. The TPB coated acrylic light guide design is based on concepts developed for LBNF, and LAr1-ND will be a direct test of this approach in a running neutrino experiment. Other approaches are being developed in attempt to enhance light collection with increased collection efficiency and improved time resolution. LAr1-ND provides an opportunity to test new approaches, possibly side-by-side, with the goal of informing an optimized design for LBNF in the future.

<b>Cryostat/ Cryogenics</b>	<b>LAr1-ND</b>	<b>LBNF</b>	<b>Comparison</b>
Cryostat Technology	Membrane	Membrane	Same commercial technology using passive foam insulation
LAr pump	Outside cryostat	Inside cryostat	Test alternate concept
Ullage space	In the cryostat OR confined to a region over inactive region	In the cryostat	Isolated expansion region being considered; allows the main cryostat to be completely filled with LAr, reducing outgassing from warm surfaces inside the cryostat
Purification	Dual phase during filling, gas phase thereafter	Dual phase throughout	With the warm ullage in a separate area in LAr1-ND, a much smaller scale purification system can be used in the small gas volume during the normal operation of the TPC

TABLE XIV

<b>TPC</b>	<b>LAr1-ND</b>	<b>LBNF</b>	<b>Comparison</b>
Construction	Pre-fabricated/tested modules assembled in cryostat or on-site	Pre-fabricated/tested modules assembled in cryostat	Same concept, different implementation
TPC Support	Suspended under cryostat roof	Suspended under cryostat roof	Same concept, different implementation
TPC configuration	CPA in the middle, single sided APAs against the walls	CPAs against the walls, double sided APAs in the middle	Avoid a costly fiducial cut around the non-active thickness of the APA in the center of the active region. The APAs can be placed closer to the cryostat walls to maximize active region in the limited available space.
APA configuration	Single sided, no helical wire wrapping, readout on 3 edges	Double sided, helical wire wrapping on two induction planes, readout on one edge	LAr1-ND's APA design avoids the wire wrapping, while allowing APA tiling on all 4 sides. Learn from LBNF 35 ton TPC prototype. The LAr1-ND design provides a verified alternative to the LBNE APAs.
APA wire configuration	3 sense wire planes, +/- 60 degree, 3mm wire pitch, identical to MicroBooNE	3 sense wire planes, +/- 45 degrees, 4.5-5mm wire pitch	LAr1-ND's wire configuration is identical to MicroBooNE
APA wire bonding	CuBe wires epoxyed and soldered to PCB with notched edges	CuBe wires epoxyed and soldered to PCB with notched edges	Same design
CPA design	Stainless steel frame + conductive sheet	Stainless steel frame + conductive sheet	Same design concept, light transmission TBD
Field cage design	Cu strips on FR4 panels	Cu strips on FR4 panels	Similar design

TABLE XV

<b>Electronics</b>	<b>LAr1-ND</b>	<b>LBNF</b>	<b>Comparison</b>
Analog Front-End	ASIC	ASIC	Same design
ADC	ASIC	ASIC	Same design
FE Digital Processing	FPGA	FPGA or ASIC	LAr1-ND will use FPGA to meet fast schedule
Front End Board	Analog Mother Board + Digital Mezzanine	Analog Mother Board + Digital Mezzanine	Similar design, different mechanical dimension and channel density
Cold Cable	Twinaxial Cable	Twinaxial Cable	Same design
Signal Feed-through	ATLAS Pin Carrier	Flange Board or ATLAS Pin Carrier	LAr1-ND will use already developed technology ATLAS pin carrier.
Warm Interface Board	FPGA + Optical Transceiver	Optical Transceiver and/or FPGA	LAr1-ND will use FPGA to study data compression and trigger algorithm, and keep the capability to stream all data out
Data Concentrator Board	Commercial PCIe Card	SLAC RCE	LAr1-ND will use commodity hardware in DAQ system, focus efforts on algorithm, firmware and software development

TABLE XVI

**A Proposal for a Three Detector  
Short-Baseline Neutrino Oscillation Program  
in the Fermilab Booster Neutrino Beam**

---

*Part 3: T600 Design and Refurbishing*

---

## I. Introduction

Imaging detectors have always played a crucial role in particle physics. In the past century successive generations of detectors realized new ways to visualize particle interactions, driving the advance of physical knowledge and the discovery of unpredicted phenomena, even on the basis of single fully reconstructed events. In particular, bubble chamber detectors were an incredibly fruitful tool, permitting to visualize and study particle interactions, providing fundamental contributions to particle physics discoveries. Gigantic bubble chambers, like Gargamelle [111, 112] (3 tons of mass), were extraordinary achievements, successfully employed in particular in neutrino physics. Two major limitations of bubble chambers in the search for rare phenomena are the impossibility to scale their size towards much larger masses, and their duty cycle which is intrinsically limited by the mechanics of the expansion system.

In 1977 C. Rubbia [113] conceived the idea of a Liquid argon Time Projection Chamber (LAr-TPC), i.e. the calorimetric measurement of particle energy together with three-dimensional track reconstruction from the electrons drifting in an electric field in sufficiently pure liquid argon. The LAr-TPC successfully reproduces the extraordinary imaging features of the bubble chamber, its medium and its spatial resolution being similar to those of heavy liquid bubble chambers, with the further feature of being a fully electronic detector, potentially scalable to huge masses (several kton). In addition the LAr-TPC provides excellent calorimetric measurements and has the big advantage of being continuously sensitive and self-triggering.

The ICARUS-T600 cryogenic detector is the biggest LAr-TPC ever realized, with the cryostat containing 760 tons of LAr (476 tons active mass). Its construction finalized many years of R&D studies by the ICARUS Collaboration [114–118], with prototypes of growing mass developed both in laboratory and with industry involvement. Nowadays, it represents the state of the art of this technique and it marks a major milestone in the practical realization of large-scale LAr detectors.

The pre-assembly of the ICARUS T600 detector began in 1999 in Pavia (Italy); one of its two 300-tons modules was brought into operation in 2001. A test run lasting three months was carried out with exposure to cosmic rays on the surface, allowing for the first time an extensive study of the main detector features [20]. After the test, the detector was de-commissioned and, in 2004, the two cryostats housing the internal detectors were transported to their final site, in the Hall B of the underground Gran Sasso National Laboratories (LNGS). A number of activities on the ICARUS-T600 plant were then necessary for the completion of the detector assembly in its underground site. In the first months of 2010 the T600, see Fig. 64, was finally brought into operation [9] taking data with the CERN to Gran Sasso (CNGS) neutrino beam and with cosmic rays. The ICARUS experiment has operated with a remarkable detection efficiency and it has successfully completed a three years physics program being exposed to the CNGS beam from October 2010 to December 2012. Neutrino events have been collected, corresponding to  $8.6 \times 10^{19}$  protons on target with an efficiency exceeding 93%. Additional data were also collected with cosmic rays, to study atmospheric neutrinos and proton decay. From the technological point of view, the T600 run was a complete success, featuring a smooth operation, high live time, and high reliability. A total of about 3,000 CNGS neutrino events has been collected and is being actively analyzed.

The successful operation of the ICARUS-T600 LAr-TPC proves the enormous potential of this detection technique, addressing a wide physics program with the simultaneous exposure to the CNGS neutrino beam and cosmic-rays [39, 48, 119, 120]. Moreover, the solutions adopted for the argon recirculation and purification systems permitted to reach an impressive result in terms of argon purity, which is one of the key issues for the superb detector performance.



A corresponding free electron lifetime exceeding 15 ns has been obtained, a milestone for any future project involving LAr-TPCs. This result [121] demonstrates the effectiveness of the single phase LAr-TPC detectors [122, 123], paving the way to the construction of huge detectors with longer drift distances: for example, with the achieved purity level, at 5 m from the wire planes the maximum signal attenuation is only 23%.

The T600 decommissioning process started in June 2013, with the cryostat emptying phase lasting less than one month in a safe and smooth way. A warming-up phase followed, that brought the cryostats to room temperature in about one month. The T600 dismantling started in September 2013 and globally lasted about 10 months. After it was concluded, the cryostats were opened, to recover the internal TPC detectors and the cryogenic plant and electronics to be re-used in future projects.

The movement of the two T600 modules to CERN has been already completed. The ICARUS-T600 TPCs are ready for their complete overhauling (CERN WA104 project), preserving most of the existing operational equipment, while upgrading some components with up-to-date technology in view of the T600 future non-underground operation at FNAL.

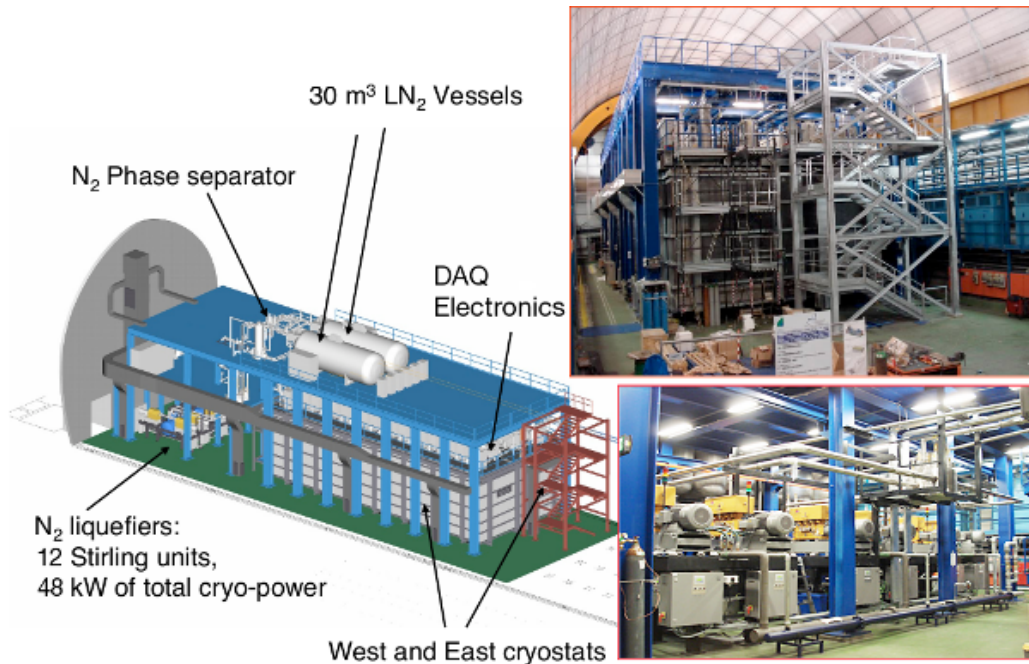


**FIG. 64:** *Left: schematic view of the whole ICARUS-T600 plant in Hall B at LNGS. Right-top: photo of the detector installation. Right-bottom: details of the cryo-cooler plant.*

This Design Report is organized as follows. Sec. II, after recalling the SBN experimental program, briefly reviews the potential of the ICARUS-T600 standalone physics program with the NuMI beam. Requirements for the detector to operate at shallow depths are resumed in Sec. III. The present ICARUS-T600 detector configuration is described in Sec. IV, while the T600 overhauling activities foreseen at CERN as WA104 program are shown in Sec. V, with particular emphasis on the new Light Collection System, the new Electronics and the new Cryogenic and Purification systems. The possibility to complement the detector with an external cosmic ray tagging system is discussed in Sec. VI.

## II. Physics of Far Detector

### A. The SBN experimental program

In recent years, several experimental “anomalies” have been reported which, if confirmed, could be hinting at the presence of additional “sterile” neutrino states with larger mass-squared differences participating in the mixing [23–29]. An important contribution to the sterile neutrino search has been already given by the ICARUS Collaboration with the T600 detector running in the underground INFN-LNGS Laboratory and exposed to the CNGS neutrino beam [9, 39, 48].

As already described in details in the Part I of this Proposal, the future short-baseline experimental configuration is proposed to include three LAr-TPC detectors located on-axis along the Booster Neutrino Beam (BNB). The Near Detector (LAr1-ND) will be located in a new building directly downstream of the existing SciBooNE enclosure, 110 m from the BNB target. The MicroBooNE detector, which is currently in the final stages of installation, is located in the Liquid argon Test Facility (LArTF) at 470 m. The Far Detector (the existing ICARUS-T600) will be located in a new building, 600 m from the target, between MiniBooNE and the NO $\nu$ A Near Detector surface building. The challenge of predicting absolute neutrino fluxes in accelerator beam experiments, and the large uncertainties associated with neutrino-nucleus interactions, strongly motivate the use of multiple detectors at different baselines, to reduce systematic uncertainties in the search for oscillations.

The observed set of anomalous results in neutrino physics calls for a conclusive new experiment capable of exploring the parameter space in a definitive way and to clarify the possible existence of eV-scale sterile neutrinos.

### B. T600 Physics with the NuMI beam

The physics outreach of the T600 detector as a stand alone detector can be enhanced with the study of neutrino cross-sections and interaction topologies at energies relevant to the Long Baseline Neutrino Facility (LBNF) program, exploiting the off-axis neutrinos from the NuMI beam.

The NuMI beam-line is fed by 120 GeV protons with  $4 \times 10^{13}$  protons per pulse. The secondary beam includes a double-horn focusing system which allows for different variable energy configurations producing a neutrino beam directed, towards the far MINOS detector, with a slope of  $\sim 50$  mrad.

Given the NuMI repetition rate (0.53 Hz) and its spill duration (8.6  $\mu$ s), one trigger every 12 s is expected in the T600, mainly due to cosmic rays occurring in the coincidence gate. About 1 neutrino event from the NuMI beam every 150 s is also foreseen.

The T600 will collect a large neutrino event statistics in the 0–3 GeV energy range with an enriched component of electron neutrinos (several %) from the dominant three body decay of secondary  $K$ . A careful and detailed analysis of these events will be highly beneficial for the future LBNF LAr program, allowing to study very precisely detection efficiencies and kinematical cuts in all neutrino channels and event topologies.

A FLUKA-based Monte Carlo simulation [68, 69, 124] of the NuMI beam line has been set up according to the available technical drawings [125] for the low energy beam configuration. The obtained neutrino fluxes have been compared with those published by the MINOS collaboration at the MINOS near detector position. Even if not all the geometry details were available and/or included in the simulation, our results agree with the MINOS ones within 20%, indicating that

reliable prediction of neutrino rates at off-axis positions is possible.

Muon neutrino event rates are comparable with the ones from the Booster beam, while the electron neutrino component is enhanced in the off-axis beam.

This amount of data would allow a detailed evaluation of detection efficiency and background reduction at the energy of the second oscillation maximum in the LBNF expected signal.

### III. Requirements for Detector Performance

The ICARUS-T600 detector in the present configuration is already well suited for sterile neutrino searches at FNAL. Nonetheless, it was designed for the low background, deep underground conditions of LNGS laboratory, where the single prompt trigger has always ensured the unique timing connection to the main image of the event. However, the situation will be substantially different for a detector of this magnitude if placed at shallow depths (a few meters deep), since several additional and uncorrelated triggers (due to cosmic rays) will be generally occurring continuously and at different times during the  $\sim 1$  ms duration of the T600 readout window [126]. This represents a new problem since, to reconstruct the true position of the track, it is necessary to precisely associate the different timings of each element of the image to their own specific delay with respect to the trigger. The specific investigation of the oscillation anomalies at shallow depths is based on the search of a signal with the presence of a neutrino-induced, single ionizing electron (or positron). High energy cosmic muons creating secondary showers may also produce single ionizing background electrons or positrons with similar energies. At the neutrino energies of the FNAL Booster Beam, the intrinsic  $\nu_e$ CC contamination occurs at the very low rate of  $\sim 500$   $\nu_e$ CC/y, while a possible LSND-like oscillation signal will produce a few hundred  $\nu_e$ CC/y (e.g.  $\sim 170$  ev/y for  $\Delta m^2 = 0.43$  eV<sup>2</sup>,  $\sin^2 2\theta = 0.013$ ). On the other hand, as already described in details in Part I of this Proposal, the cosmic ray background is very prolific of events: in a pit covered by 3 m of concrete, cosmic muon rates in coincidence with the beam trigger window of 1.6  $\mu$ s, will produce the huge rate of  $0.83 \times 10^6$  cosmic per year (c/y). Moreover, during the 1 ms long duration of each readout window,  $\sim 11$  cosmic ray tracks are expected over the full T600, in agreement with the ICARUS measurements at surface carried out in 2001 test run [20]. It is concluded that in its original configuration the ICARUS LAr-TPC detector cannot perform a practical search for LSND-like anomalies at shallow depths, since the cosmic trigger events are too much frequent. As already pointed out in Part I, depending on the background type, several reduction strategies can be applied. In addition to offline analysis techniques for background reduction, mostly based on electron/photon discrimination through dE/dx evaluation, the T600 detector will require the implementation of the following three features:

- the realization of a new light collection system, to allow a more precise event timing and localization;
- the exploitation of the BNB bunched beam structure, lasting 1.15 ns (FWHM  $\sim 2.7$  ns) every 19 ns, to reject cosmic events out of bunch as proposed in a SBN note [127];
- the realization of a cosmic ray tagging system, external to the LAr fiducial volume, to automatically identify entering charged tracks with position and timing information: this would greatly facilitate the reconstruction and identification of muon tracks. It has to be reminded that crossing muons can be identified by the 3D reconstruction software, however the 3D reconstruction itself needs the information on the track absolute time  $t_0$ .

#### IV. The T600 Detector: present configuration

The ICARUS-T600 detector consists of a large cryostat split into two identical, adjacent modules, with internal dimensions  $3.6 \times 3.9 \times 19.6 \text{ m}^3$  each, filled with about 760 tons of ultra-pure LAr. The modules will be referred in the text as *West module* (the oldest one) and *East module* (the newest one), with respect to CNGS beam coming from the North. A uniform electric field ( $E_{drift} = 500 \text{ V/cm}$ ) is applied to the LAr bulk: each module houses two TPCs separated by a common cathode.

Charged particles, generated for example by a neutrino interaction in LAr, produce ionization along their path. Thanks to the low transverse diffusion of charge in LAr, the images of the tracks (produced by ionization electron clouds) are preserved and, drifting along the electric field lines, are projected onto the anode, as illustrated in Fig. 65. The TPC anode is made of three parallel planes of wires, 3 mm apart, facing the 1.5 m drift path. Globally, 53,248 wires with length up to 9 m are installed in the detector. By appropriate voltage biasing, the ionization charge induces signals in non-destructive way on the first two planes (Induction-1 and Induction-2), then it is finally collected by the last one (Collection plane).

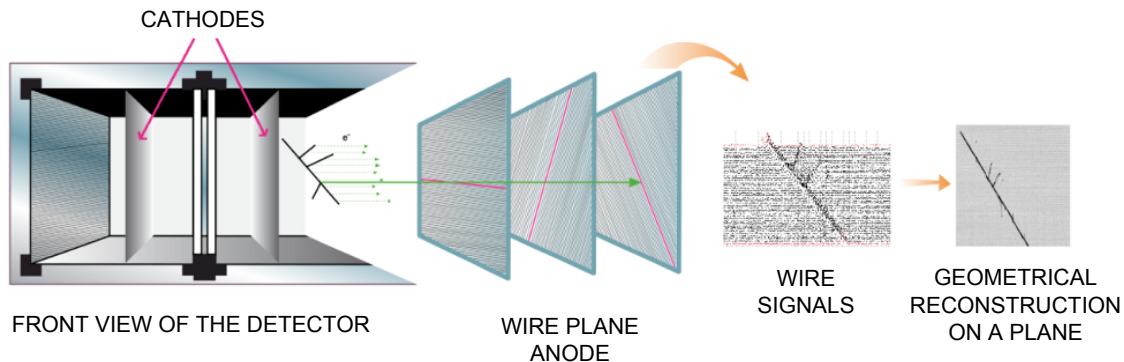


**FIG. 65:** Illustration of the ICARUS-T600 working principle: a charged particle ionization path in LAr and its geometrical reconstruction.

Wires are oriented on each plane at a different angle ( $0^\circ$ ,  $+60^\circ$ ,  $-60^\circ$ ) with respect to the horizontal direction. Therefore, combining the wire/drift coordinates on each plane at a given drift time, a three-dimensional reconstruction of the ionizing event can be obtained. A remarkable resolution of about  $1 \text{ mm}^3$  is uniformly achieved over the whole detector active volume ( $340 \text{ m}^3$  corresponding to 476 t).

The measurement of the absolute time of the ionizing event, combined with the electron drift velocity information ( $v_{drift} \sim 1.6 \text{ mm}/\mu\text{s}$  at  $E_{drift} = 500 \text{ V/cm}$ ), provides the absolute position of the track along the drift coordinate. The determination of the absolute time of the ionizing event is accomplished by the prompt detection of the scintillation light produced in LAr by charged particles. To this purpose, arrays of cryogenic Photo Multiplier Tubes (PMTs), coated with wavelength shifter to allow the detection of Vacuum Ultra-Violet (VUV) scintillation light ( $\lambda = 128 \text{ nm}$ ), are installed behind the wire planes.

The electronics was designed to allow continuous read-out, digitization and independent waveform recording of signals from each wire of the TPC. The read-out chain is organized on a 32-channel modularity. A Decoupling Board receives the signals from the chamber and passes them on to an Analogue Board via decoupling capacitors; it also provides wire biasing voltage and the distribution of the test signals. Digitization is performed by 10-bit fast ADCs, which

continuously read data and store them in circular buffers. Stored data are read out by the DAQ when a trigger occurs. The trigger relies on the detection of scintillation light by the PMTs, in coincidence with the CERN-SPS proton extraction time for the CNGS beam.

This Section is organized as follows: Par. IV A describes in details the main component of the ICARUS-T600 internal detectors: the mechanical structure, the wire planes, the cabling and the High Voltage system. Par. IV B shows the present layout of the Light Collection System, while the Electronics and DAQ in the LNGS configuration are described in Par. IV C. Finally, Cryogenics and Purification systems are presented in Par. IV D.

## A. TPC design

### *TPC mechanical structure*

Each one of the two LAr cryostats hosts a mechanical structure that sustains the different internal detector subsystems and the control instrumentation, namely: (1) the TPC wire planes and the relative HV electrode system (cathode and field-shaping electrodes), (2) the PMT system for the scintillation light detection and (3) sensors and probes of the slow control system. Once the cryostat is filled, the structure is totally immersed in LAr.

All materials of the mechanical structure were chosen and treated to guarantee high LAr purity and minimal radioactive contamination: the main components (beams and pillars) have been built with AISI 304L stainless steel; other parts (supports, spacers, etc.) are made of PEEK™. The stainless steel structure has dimensions of 19.6 m in length, 3.6 m in width and 3.9 m in height, for a total weight of  $\sim 20$  tons, see Fig. 66 and 67.

To cope with the different thermal shrinking between aluminum and stainless steel, the stainless steel structure leans on the cryostat aluminum floor by means of 10 adjustable feet positioned on corresponding reinforced pads, and rigidly linked to it only in two pads at half-module length. In this way, the structure is practically independent from deformations of the cryostat induced by cooling and by the different operating conditions (vacuum and overpressure). Moreover, the sustaining structure is self-supporting and is rigid enough to allow for transportation.

Rocking frames to hold the TPC wires are positioned on the vertical long sides of the mechanical structure. The latter was dimensioned in such a way to sustain the total mechanical tension of the wires applied to the two wire frames, whose design is based on the concept of the variable geometry design (weight bridge). This is based on movable and spring loaded frames, to set the proper tension of the wires after installation, see Fig. 68 and Fig. 69. This system allows for a precise detector geometry and planarity, compensating for any possible over-stress during the cool-down and LAr filling phases, and counteracting the flexibility of the structure.

### *TPC wire planes*

The anode of each TPC consists of a system of three parallel wire planes (of  $17.95 \times 3.16$  m<sup>2</sup> surface), 3 mm apart from each other, for a total of 13312 wires/chamber, see Fig. 70; a total of 53,248 wires is mounted on the whole T600 detector (four chambers). Wires are made of AISI 304V stainless steel with a wire diameter of 150  $\mu$ m; wire length ranges from 9.42 m to 0.49 m depending on the position of the wire in the plane itself. Thirteen windings (slipknots) around two gold-plated stainless steel ferrules at both ends of each wire are realized, in a "guitar chord"

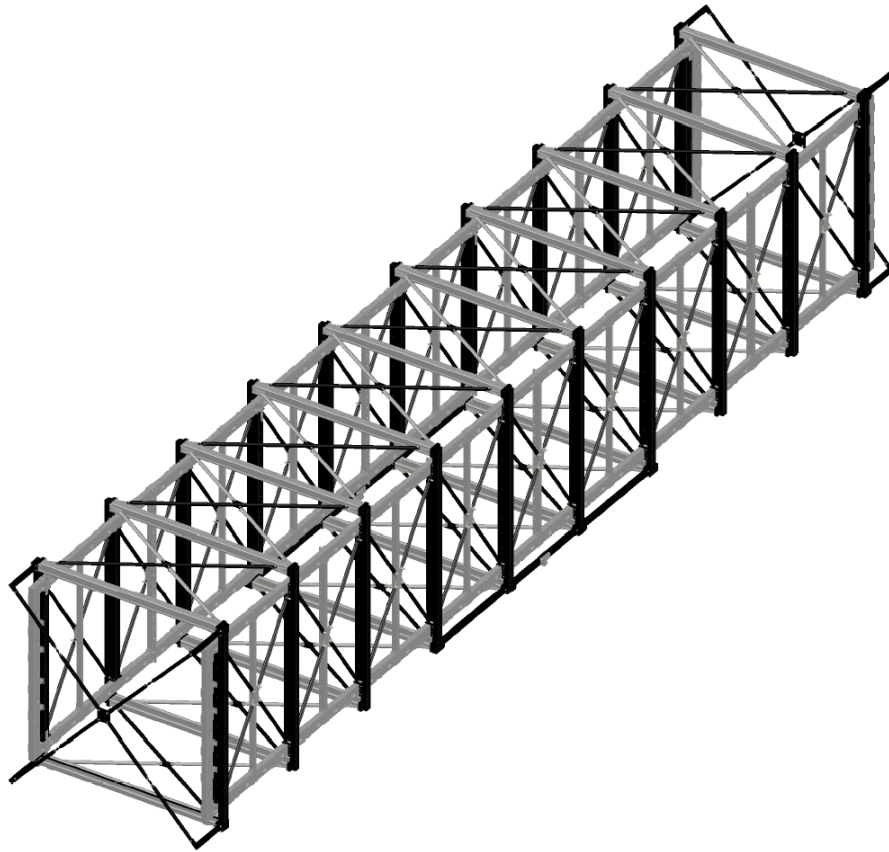


**FIG. 66:** Drawing of the bare inner mechanical structure of one T600 module, working as a support for all the internal detector subsystems.



**FIG. 67:** The internal sustaining structure of a T600 module.

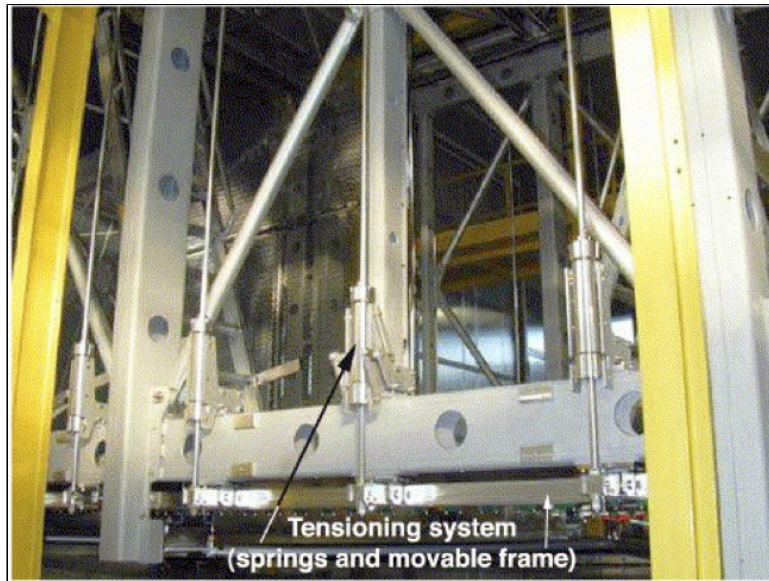


**FIG. 68:** Detail of the wire tensioning mechanics: a 2 m long portion of the wire frame equipped with three tensioning springs.

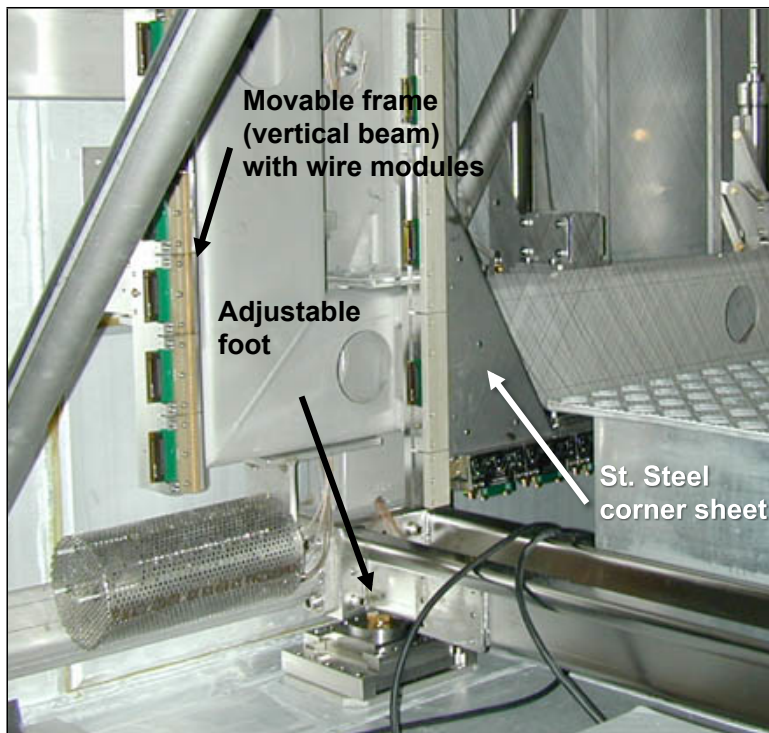


**FIG. 69:** Detail of the internal structure showing an adjustable foot and the wires at the corner.

configuration, see Fig. 71. In this way a very safe holding is guaranteed by the wire friction itself. From the mechanical point of view, wires are strung with a nominal tension of 12 N (5 N for the longest wires), which is high enough to limit sagittas (due to gravity and to electrostatic forces) to values negligible with respect to the distance between the wires. The wire elongation is still well below the elastic limit (39 N nominal value).

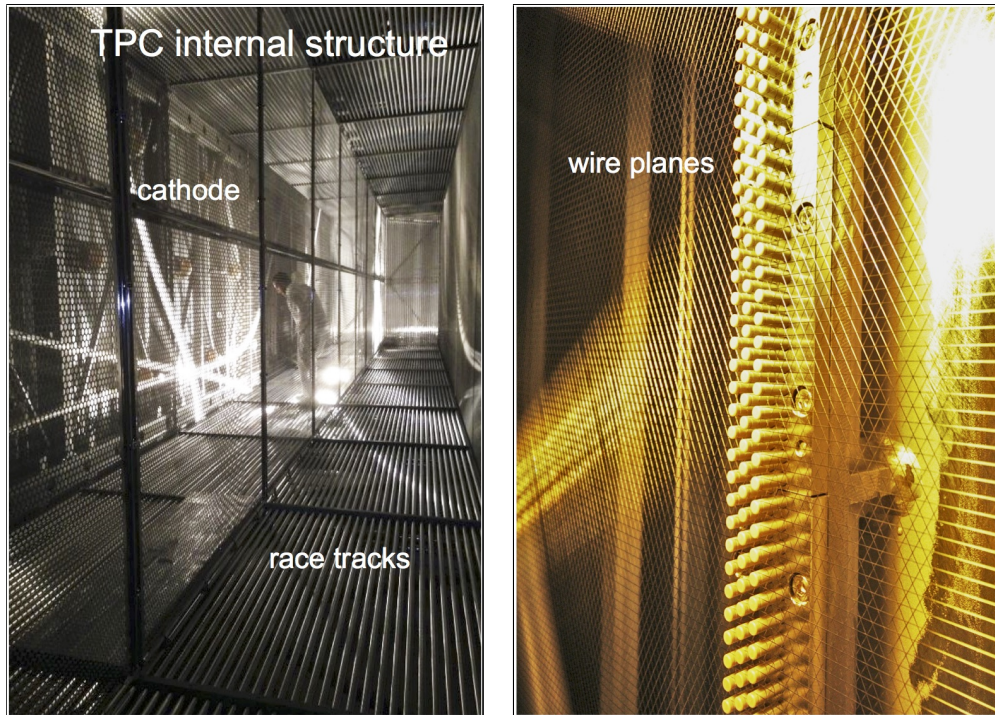


**FIG. 70:** *Left: internal TPC structure: cathode, race tracks and wire planes are highlighted. Right: detail of the three wire plane structure.*

The variable geometry design demonstrated its reliability since none of the wire broke and no damages at the wire chamber structure occurred: in the 2001 Pavia test run; during the transport of the two modules from Pavia to LNGS; during all the installation movements on site; during the commissioning, run and de-commissioning at LNGS. The wires are stretched in the elastic frame sustained by the mechanical structure, as described above. Two coplanar, adjacent sets of horizontal wires (1056 units), 9.42 m long, form the Induction-1 plane, stretched between the vertical beams of the wire frame and a central fixed beam. For both the Induction-2 and Collection planes (wires inclined at  $\pm 60^\circ$ ) the standard length of the wires stretched between the upper and lower beams of the frame is 3.77 m (4640 wires per plane), whereas wires of decreasing length (960 wires per plane) are used in the triangular-shaped portions, between one vertical and one horizontal beam, at the corners of the planes (Fig. 69). The single wire capacitance in the various planes has been calculated to be 20 pF/m for the first (Induction-1) and third (Collection) plane, and 21 pF/m for the intermediate (Induction-2) plane.

The wires are anchored by special holders onto the wire frame in groups of 32 units (the *wire modules*). Each holder is formed either by one or two (according to the different cases) PEEK™ combs contained in stainless steel supports which also embed one or two printed circuit boards. The wire ferrules, held by the PEEK™ shell at both ends of the wire module, are hung on the comb pins. The printed circuit board establishes the electric connection between the 32 pins of the comb and a single connector also mounted onto the board. Fig. 72 shows the technical design of the mechanical system holding 2 wire modules for the wires at  $\pm 60^\circ$ .

The wire modules are individually mounted onto the beams of the elastic frame (de-tensioned position). The elastic frame is schematically subdivided into portions about 2 m long. Each portion comprises  $18 \times 2$  combs/connectors. After the installation of the wire modules was



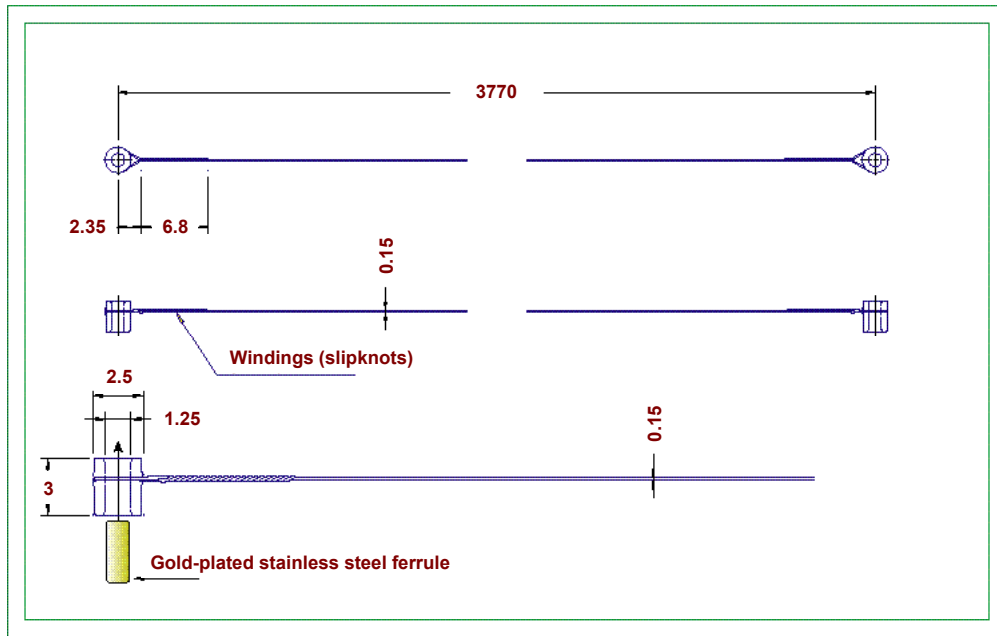


**FIG. 71:** Schematic of the Wire holding structure, with detail of the winding in a "guitar chord" concept.

completed, wires were tensioned by loading the springs of the movable frame, see Fig. 68.

### Cabling

The individual wire signal transfer to the read-out electronics outside the cryostat is provided by twisted-pair flat cables (34 pairs, flexible, halogen free). Thirty-two pair lines (pairs 1÷32) of the 68 available contacts are dedicated to wire signals, one to the test-pulse signal and the last pair, referred to ground, is used as a screen between signal and calibration conductors. Inside the cryostat the flat cables, suitably terminated with male connectors at both ends, are plugged at one end to the female connectors (32-wire channels + 1 test pulse channel + 1 screen channel) mounted onto the printed boards of the wire modules. At the other end, the cables are plugged to similar connectors embedded (inner side) in specially designed vacuum tight feed-through flanges. Flanges are mounted on the top of the cryostat, at the end of the way-out chimneys. Each one of the 96 feed-through flanges installed in the T600 detector can provide signal transmission for 18 wire modules (576 wires) and for cables for test pulse calibration. The complete connection layout from wires to the read-out electronics is schematically displayed in Fig. 73. A refurbishment of the internal detector cabling is foreseen during the T600 overhauling activities at CERN, see Par. V.

### TPC HV system

The HV system has to produce a stable and uniform field over the  $1.50 \times 3.16 \times 17.95 \text{ m}^3$  entire drift volume. The system is made of several components, the most important of which are the cathodes, the field-shaping electrodes and the HV feed-throughs.

In the present configuration the cathodes are built up by an array of nine panels (Fig. 74 and

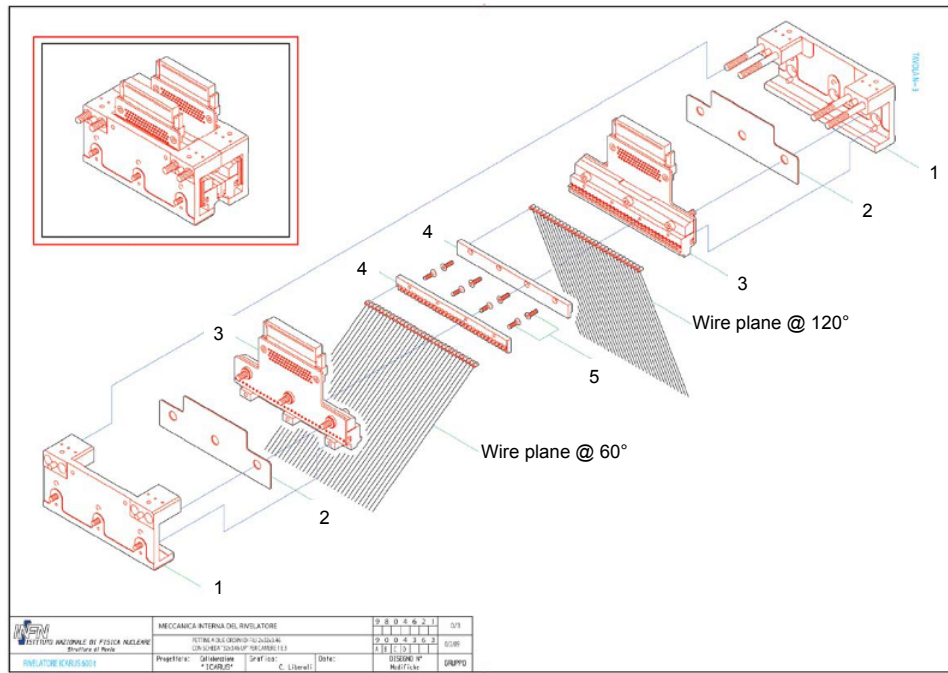


**FIG. 72:** Technical design of the mechanical system holding the 32-wire modules at  $\pm 60^\circ$ : detail of the components (from left to center and reverse): mechanical support, spacer, printed board with connector, PEEK™ shell with 32-wire ferrules, PEEK™ comb (and reverse).

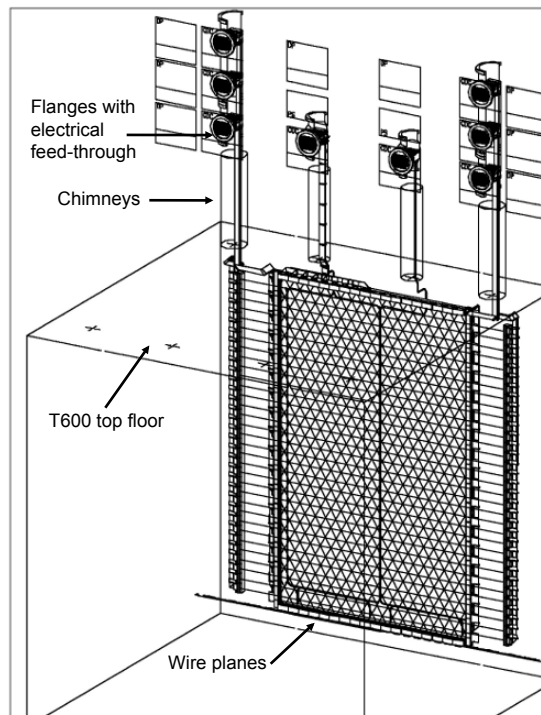


**FIG. 73:** Wires, cables, chimney and feed-through layout. The back side of the electronic racks (LNGS configuration) is indicated. Note that the wire chamber longitudinal dimension is not in scale, i.e. the figure includes only the non-repetitive portions of the TPC.

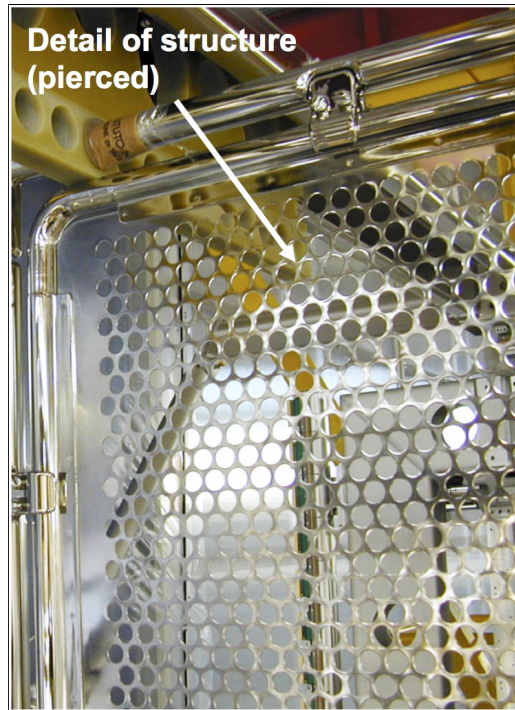


**FIG. 74:** *Detail of one cathode panel in the LNGS run configuration.*

Fig. 75) made of pierced stainless steel sheets. This solution implies an optical transparency between the two drift regions, which allows the detection of the scintillation light by means of all PMTs positioned between the wire chambers and the cryostat walls.

The electric field in each drift volume is kept uniform by means of the field-shaping electrodes (*race tracks*, see Fig. 76 and Fig. 77). These consist of 29 rectangular rings ( $18.1 \times 3.2 \text{ m}^2$ ) for each wire chamber, made of 2 m long stainless steel tubular elements (34 mm diameter, 0.8 mm thick) connected by two welded terminals. The distance between race tracks is 49.6 mm. In the upper part, between the race tracks and the gaseous Ar (GAR) phase, a grounded metallic shielding is interposed. The race tracks are set at a potential linearly decreasing from the cathode value to the first wire plane voltage, to ensure uniform electric field and hence constant drift velocity inside the volumes. The biasing potentials of the race tracks are obtained through resistive voltage degraders. The HV degrader is based on four resistor chains, one for each drift volume, with the “hot” end connected to the cathode and the “cold” end set to ground. Resistor chains are made of 30 steps. Intermediate contacts are connected to the field-shaping electrodes. The resistance for each step is  $25 \text{ M}\Omega$ , obtained by connecting four  $100 \text{ M}\Omega$  resistors in parallel. For a  $0.5 \text{ kV/cm}$  drift field the voltage across each resistor is 2.5 kV.

The HV generated by an external power supply is brought to the internal cathode via an hermetic feed-through. A feed-through coaxial geometry has been adopted: the design is based on an inner conductor (HV) and an outer conductor (ground) insulated by UHMW PE (ultra-high-molecular-weight polyethylene) as shown in Fig. 78. The outer conductor, made of a stainless steel tube, surrounds the insulator extending inside the cryostat up to the LAr level. By such a geometry the electric field is always confined in regions occupied by high dielectric strength media (UHMW PE and LAr). The inner conductor is made of a thin wall stainless steel tube, to minimize the heat input and to avoid the creation of argon gas bubbles around the HV lower end. A female contact, welded at the upper end for the connection to the HV cable,

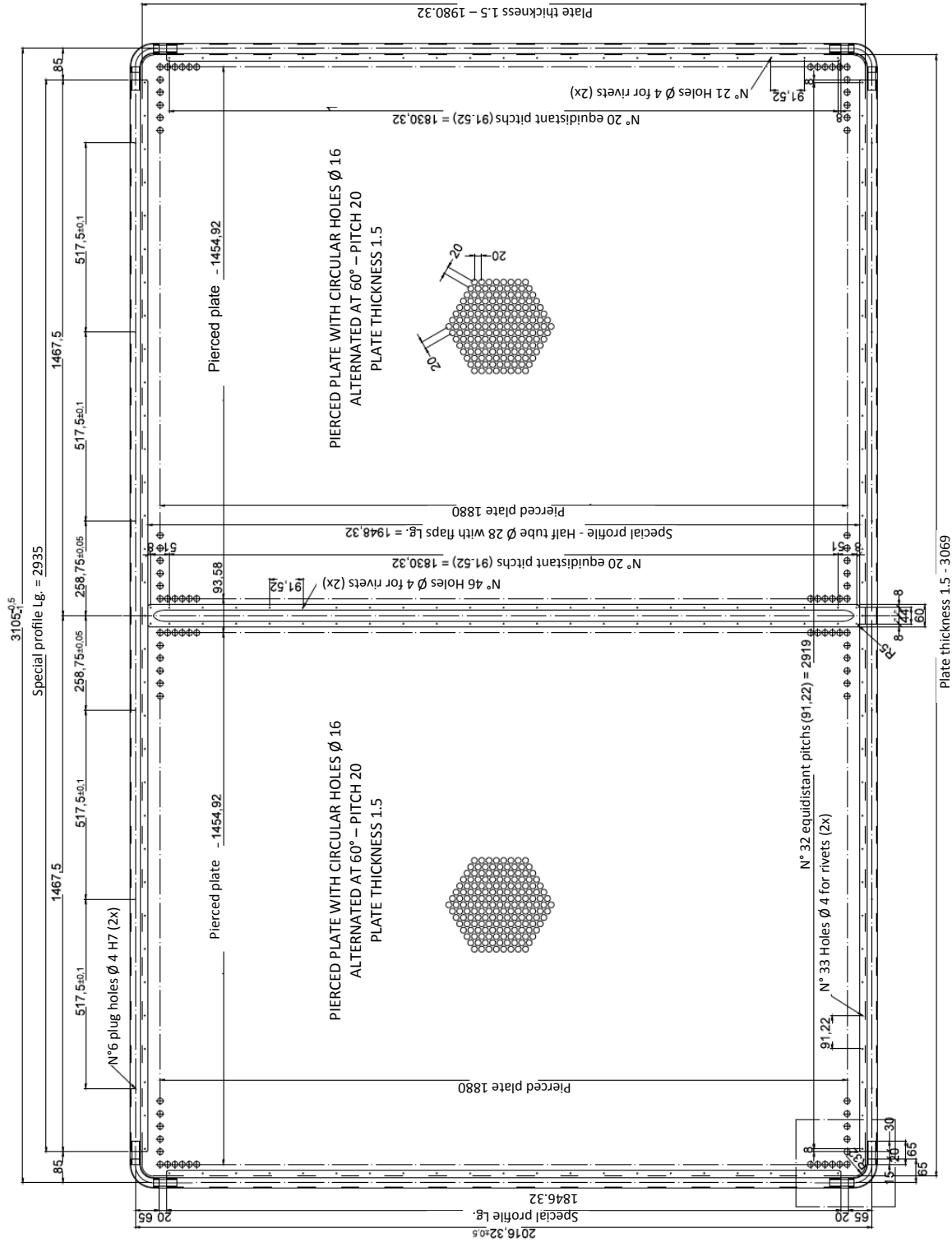
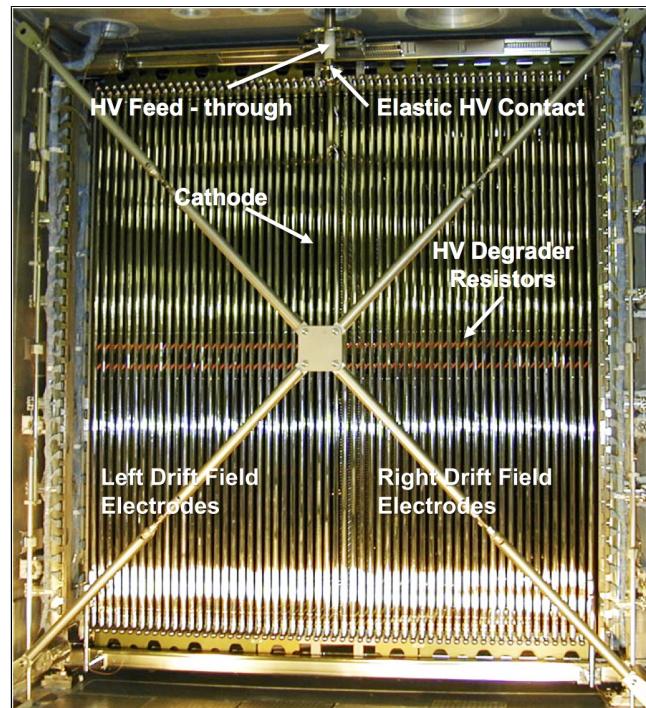
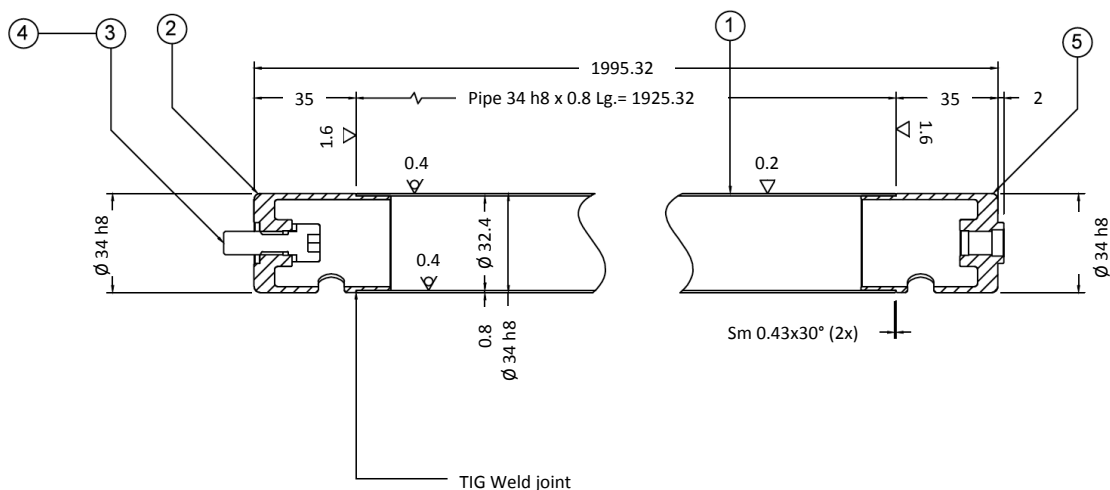


FIG. 75: Technical drawing of one cathode panel in the LNGS run configuration.



**FIG. 76:** The first half-module of the T600 detector before closing. Some components of the HV system are visible: feed-through, cathode, field electrodes (race tracks), voltage divider.



**FIG. 77:** Technical drawing of one race track element.

and a round-shaped elastic contact for the connection to the cathode, screwed at the lower end, complete the inner electrode. Special care has been taken in the assembling to ensure the complete filling with the PE dielectric of the space between the inner and the outer conductors and to guarantee leak tightness at ultra-high-vacuum level.

The HV system of ICARUS-T600 had no failures during the three years of run at LNGS, at the operating voltage of 76 kV. Moreover, in the last days of the LNGS run few tests were

carried out with an operating voltage about twice its nominal value (150 kV, corresponding to  $E_{drift} \simeq 1$  kV/cm), with no failures for five days. After this the HV system was switched off to allow the T600 decommissioning procedures to start.

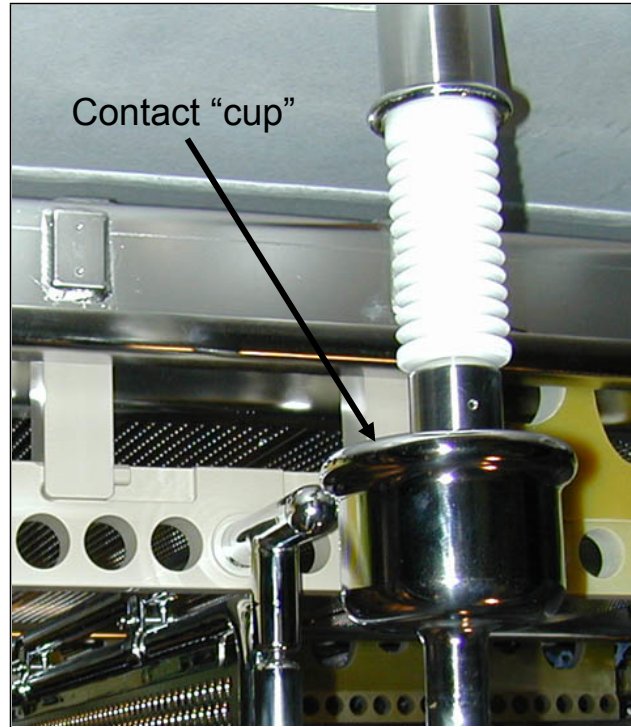


**FIG. 78:** Picture of the HV feed-through. The "cup" for the contact to the cathode panels is also visible.

The main characteristics of the present T600 TPC internal detector configuration are resumed in Tab. XVII.

### B. Light Collection system

Charged particles deposit energy in liquid argon mainly by excitation and ionization of Ar atoms, leading to scintillation light emission and free electron production, respectively. Additional scintillation light comes from the recombination of electron-ion pairs, which is inversely proportional to the strength of the electric field applied to the detector active volume. As a consequence, free-electron yield rises with the field value while photon yield decreases. In both cases saturation occurs, for minimum ionizing particles, at  $E_{drift} > 10$  kV/cm. At the nominal drift field applied in ICARUS-T600, approximately the same amount of photons ( $\sim 4,000$   $\gamma$ /mm) and free electrons ( $\sim 5,000$  ion-electron pairs per mm) are produced for minimum ionizing particles (m.i.p.) [128].

Scintillation light emission in LAr is due to the radiative decay of excited molecules ( $Ar_2^*$ ) produced by ionizing particles, releasing monochromatic VUV photons ( $\lambda \sim 128$  nm) in transitions from the lowest excited molecular state to the dissociative ground state. A fast ( $\tau \sim 6$  ns decay time) and a slow ( $\tau \sim 1.6$   $\mu$ s) components are emitted; their relative intensity depends on  $dE/dx$ , ranging from 1:3 in case of minimum ionizing particles up to 3:1 in case of  $\alpha$ -particles. This isotropic light signal propagates with negligible attenuation throughout each TPC vol-

Number of read-out chambers (TPC) in T600	4
Number of wire planes per chamber	3
Distance between wire planes	3 mm
Wire orientation with respect to horizontal	0°, ±60°
Wire diameter	150 μm
Wire length	
Horizontal wires	9.42 m
Wires at ±60°	3.77 m
Wires at the corners (±60°)	3.81-0.49 m
Wire pitch (normal to the wire direction)	3 mm
Wire capacitance Ind.-1, Ind.-2, Coll.	20, 21, 20 pF/m
Wire nominal tension	12 N (5 N for hor. wires)
Number of wires/wire module	32
Number of wire modules/chamber	
Horizontal wires	66
Wires at ±60°	2 × 145
Wires at the corners ±60°	2 × 30
Number of wires/chamber	
Horizontal	2112
At ±60°	2 × 4640
At the corners (±60°)	2 × 960
Total	13312
Total number of wires in T600	53,248
Wire plane voltage biasing (typical)	-220 V, 0 V, +280 V
Cathode HV (nominal)	75 kV
Cathode to Collection plane distance	1.50 m
Sensitive volume/chamber	85 m <sup>3</sup>
Length	17.95 m
Width	1.50 m
Height	3.16 m
Maximum drift length in LAr	1482 mm
Maximum drift time in LAr (at nominal field)	950 μs

**TABLE XVII:** *Main characteristics of the ICARUS-T600 TPCs.*

ume. Indeed, LAr is fully transparent to its own scintillation light, with measured attenuation length in excess of several tens of meters and Rayleigh-scattering length of the order of 1 m. Because of their short wavelength the scintillation photons are absorbed by all materials inside the detector without reflection.

The design of the T600 detector PMT system, in the LNGS configuration, resulted from dedicated R&D activities on the LAr scintillation light detection, carried on during the second half of the 90's [117]. The adopted solution is based on the large surface Photo-Multiplier 9357FLA Electron Tube, a 12-stage dynode PMT with hemispherical glass window 200 mm (8") diameter, manufactured to work at cryogenic temperatures [129]. The PMT sensitivity to

VUV photons (128 nm) was achieved by coating the glass window with Tetra-Phenyl-Butadiene (TPB), which acts as fluorescent wavelength shifter from VUV wavelengths to the PMT sensitive spectrum. A TPB coating of thickness  $0.2 \text{ mg/cm}^2$  on sand-blasted glass guarantees a conversion efficiency better than 90% and good adhesion after immersion in LAr, resulting in a PMT response with 4% overall quantum efficiency [130].

PMTs are located in the 30 cm space behind the wire planes of each TPC, at 5 mm distance from the Collection wires, with a dedicated sustaining structure specially designed to compensate the thermal stresses occurring during the cooling of the T600 cryostat (Fig. 79 Left). Three rows of 9 PMTs, spaced by 2 m, found place in the East module behind each wire chamber for a total amount of 27+27 photo-devices. In the West module only the two central rows were deployed; two additional PMTs were placed in the top and bottom positions in the Right chamber at the center of the longitudinal direction, for an overall amount of 20 PMTs (Fig. 79 Right). Despite the small number of PMTs deployed inside the T600 detector in the LNGS configuration, the PMT system allowed to get a 100% trigger efficiency for CNGS-induced events above 300 MeV of deposited energy, with a remarkable stability during the three years of data taking [131].

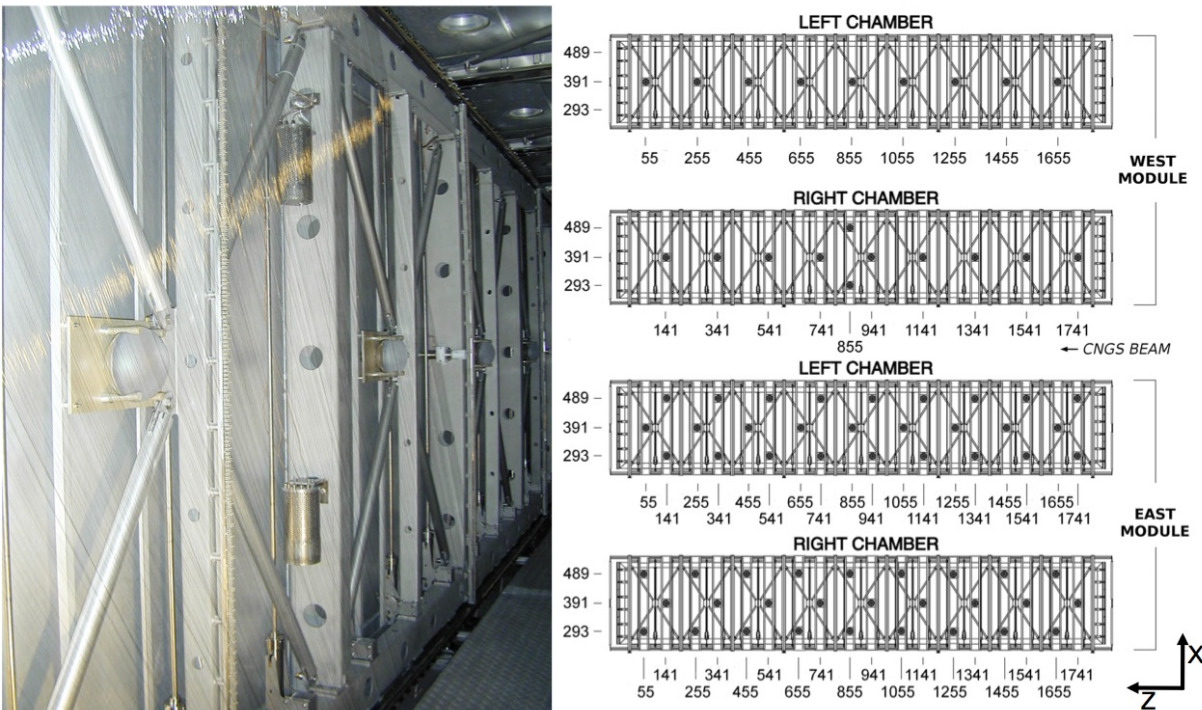


**FIG. 79:** *Left: internal view of one TPC, with a few PMTs clearly visible together with their sustaining structure. Right: PMTs deployment in the two ICARUS-T600 cryostats. PMT coordinates in cm are related to the reference frame used in Hall B.*



### C. Electronics, DAQ and Trigger

#### *Electronics and DAQ*

The present T600 electronics is designed to allow continuous read-out, digitization and independent waveform recording of signals from each wire of the TPC. The read-out chain is organized on a 32-channel modularity. A Decoupling Board receives the signals from the chamber and passes them to an Analogue Board via decoupling capacitors; it also provides wire biasing voltage and the distribution of the test signals.

The Analogue Board hosts the front-end amplifiers and performs 16:1 channel multiplexing and 10-bit ADC digitization at 400 ns sampling time per channel. The overall gain is about 1,000 electrons per ADC count, setting the signal of minimum ionizing particles to 15 ADC counts, with a dynamic range of about 100 times the signal of one m.i.p. A  $3 \mu\text{s}$  decay constant is used for the unipolar signals coming from the Collection and Induction-1 wires, while a  $100 \mu\text{s}$  decay constant is used for the bipolar current signals (Induction-2 wires). A digital Board hosts a 10 bit waveform recorder, which continuously reads the data, stores them in multievent circular buffers, each covering a full drift distance. When a trigger signal occurs, the active buffer is frozen, following data are written to the next free buffer, and the stored data are read out by the DAQ. This configuration guarantees no dead time, until the maximum DAQ throughput (1 full-drift event per second) is reached. The average electronic noise achieved with the specially designed low noise front-end is well within expectations: 1,500 electrons r.m.s. to be compared with 15,000 free electrons produced by a minimum ionizing particle in 3 mm ( $S/N \sim 10$ ).

#### *LNGS run Trigger*

Two different trigger systems based on the detection of scintillation light and ionization charge produced by charged particles in LAr have been realized for the ICARUS-T600 detector LNGS run [131]. They exploited the PMT system and the new S-Daedalus FPGA boards, spanning few orders of magnitude in event energy deposition. The main ICARUS-T600 trigger for detecting CNGS beam related events required the coincidence of the PMT *local trigger* in at least one of the four TPC chambers with a  $60 \mu\text{s}$  gate opened in correspondence of the proton spill extraction delayed for the  $\sim 2.44$  ms CNGS neutrino time-of-flight. The mentioned PMT local trigger is obtained, separately for each TPC, as the linear sum of the collected PMT signals, properly discriminated in order to account for the different number of devices deployed in the two modules.

The combined analysis of the performance of the PMT and S-Daedalus independent trigger systems demonstrated an almost full PMT trigger efficiency for CNGS neutrino events above 300 MeV energy deposition on the full T600 active volume. Efficiency remains at  $\sim 98.5\%$  down to 100 MeV. The stability of the trigger system was verified within the measurement uncertainty, comparing different data sets collected during the CNGS run [131].

The T600 LNGS run Trigger Manager, built in a commercial National Instrument PXI crate, handled the different trigger sources: scintillation light collected by PMTs, timing synchronization with the CNGS extractions, charge signal collected on wires and test pulses for calibration. The system consisted of a Real Time (RT) controller (PXIe-8130) and two FPGA boards (PXI-7813R and PXI-7833). The RT controller implemented all the features that implied communication with external devices, such as the DAQ process or the CNGS Early Warning reception. Communication with the DAQ was implemented in handshake between the DAQ

main process and the trigger manager. The RT controller also monitored the number of available buffers in the digital boards and prevented the generation of new triggers in case all the buffers were full. The maximum number of buffers available for full drift recording was 8. The DAQ throughput, for full drift event recording, was limited to 0.8 Hz mainly because of the adopted VME architecture. The FPGA boards implemented time critical processes, like the synchronization with the LNGS time, the opening of CNGS gate and the time stamp of each trigger. They also kept record of the trigger source and the trigger mask, monitored trigger rates from each source and controlled the overall system stability.

In the architecture of the ICARUS-T600 DAQ system adopted for data taking at LNGS [131], all the 96 readout units work autonomously pushing their own data to 4 receiving workstations, one per TPC chamber. This segmentation and parallelization of the data stream allowed reaching a  $\sim 1$  Hz building rate on the whole T600, safely exploiting the data link at half of the  $\sim 50$  MB/s available bandwidth.

#### D. Cryogenics and Purification systems

The ICARUS-T600 cryogenic plant was mainly installed in the North end of Hall B of LNGS, i.e. behind the cryostat when entering the Hall. The final design of the system was driven by compliance to strict requirements on efficiency, safety, anti-seismic constraints and reliability for several years of operations in a confined underground location. A schematic view of the apparatus has been shown in Fig. 64 Left. The technical requirements for the plant, and its components, were developed requesting fulfillment of strict conditions in terms of mechanics, electronics, radiochemical and electronegative purity, and are summarized below:

- full cryogenic containment for safety needs;
- extremely high LAr purity: residual contamination of electronegative molecules such as water and oxygen lower than 0.1 part per billion, to allow ionization electrons to drift over several meters;
- extremely precise control of the components differential temperature during detector cool-down, in order to avoid stresses on the TPC precision mechanics. In particular the requests were of  $\Delta T < 50$  K on the wire-chamber structures,  $\Delta T < 120$  K on the cold vessels;
- fast cooling to liquid argon temperature, to ensure good starting purity;
- very high temperature uniformity in steady state conditions ( $\Delta T < 1$  K in the main volume) to guarantee uniform electron drift velocity;
- thermal losses as low as possible, to reduce operation costs and minimize power consumption in emergency situations;
- very high stability and operation reliability to fulfill the strict underground safety requirements (this point will be re-discussed to fit the different FNAL safety standards and rules);
- full redundancy, to assure uninterrupted operation over several years.

The T600 detector is made by two adjacent aluminum LAr containers (parallelepipedal in shape), each with an inner volume of  $275 \text{ m}^3$ . The two modules are independent from the point of view of LAr containment and purification plants, while nitrogen cooling system and thermal insulation are common to both. The main design and construction of the cryostats was carried on in collaboration with Air Liquide Italia Service (ALIS) Company [132]. The two cold vessels containing the TPCs are realized with 15 mm thick aluminum honeycomb panels, mechanically reinforced by extruded profiles. The external and internal skins work as double cryogenic containment. The external dimensions of the vessels are  $4.2 \times 3.9 \times 19.9 \text{ m}^3$ , i.e. the maximum size allowed for fitting the boxes into the LNGS underground laboratory. This solution, though unconventional, was preferred mainly for its lightness and rigidity to stand stresses during the emptying phase, and the overall LAr and detector weight. A single thermal insulation vessel surrounded the two modules. The insulation was designed to behave as an additional tight container in case of cryogenic liquid spillages. Every insulation wall is composed of separated metallic boxes, with outer skin made of stainless steel. The inner and side skins are instead of Pernifer™, to avoid thermal shrinking. The boxes were filled with insulating honeycomb panels (0.4 m thick of Nomex™ or equivalent material) and super-insulation layers placed on the inner cold surface.

A thermal shield was placed between the insulation vessel and the aluminum containers, to intercept the residual heat losses through the insulation walls, thus avoiding boiling of the LAr bulk. Boiling nitrogen was circulated in the thermal shield, with a gas/liquid ratio equal to 1:5. This solution guarantees a fast cooling-down phase with thermal gradients within specification, and it forces LAr de-stratification during normal operations, thus maintaining uniform and stable temperature in the LAr bulk.

The argon and nitrogen circulation lines will be now detailed in the following, while a comprehensive view of the cryogenic system is drawn in Fig. 80.

In order to maintain high LAr purity in the active volume, each T600 module is equipped with two GAR and one LAr recirculation units. The gas recirculation system collects argon gas coming from the chimneys hosting the read-out cables and the feed-through flanges. The gas on the T600 top is warm and dirtier than the liquid from being in contact with hygroscopic plastic cables; moreover it could be further polluted by possible small leaks due to the presence of several joints on each chimney. The collected gas is re-condensed and then made to drop into a LN<sub>2</sub>-cooled Oxysorb™ filter, placed after the re-condenser. Newly purified LAr is injected back into the main volume right below the liquid/gas interface. The condenser is normally fed with LN<sub>2</sub> at the temperature required for efficient re-condensation of the gas, by means of forced circulation.

During LNGS data taking, gas recirculation was usually kept at the maximum available rate of  $25 \text{ GAR Nm}^3/\text{h}/\text{unit}$ . Gas recirculation is specially helpful during the filling phase, as it allows purification of the dirty warmer gas, while the outgassing rate decreases exponentially with temperature. On the other hand the system acts as detector pressure stabilizer during steady state operations.

Continuous liquid recirculation is used to massively purify LAr and to reach and maintain purity levels as high as possible after initial filling. It can also be exploited to rapidly restore argon purity in case of accidental pollution during operations. LAr is extracted from the main volume at about 2 m below the liquid surface on one of the 4 m long sides of the T600 modules (endcaps); it is then reinjected on the opposite side, 20 m apart, at the module floor level, through a horizontal pierced pipe that provides uniform distribution over the vessel width. Recirculation is forced by means of immersed cryogenic pumps placed inside independent dewars. Before reinjection, LAr is sent through a battery of four Oxysorb/Hydrosorb™ filter

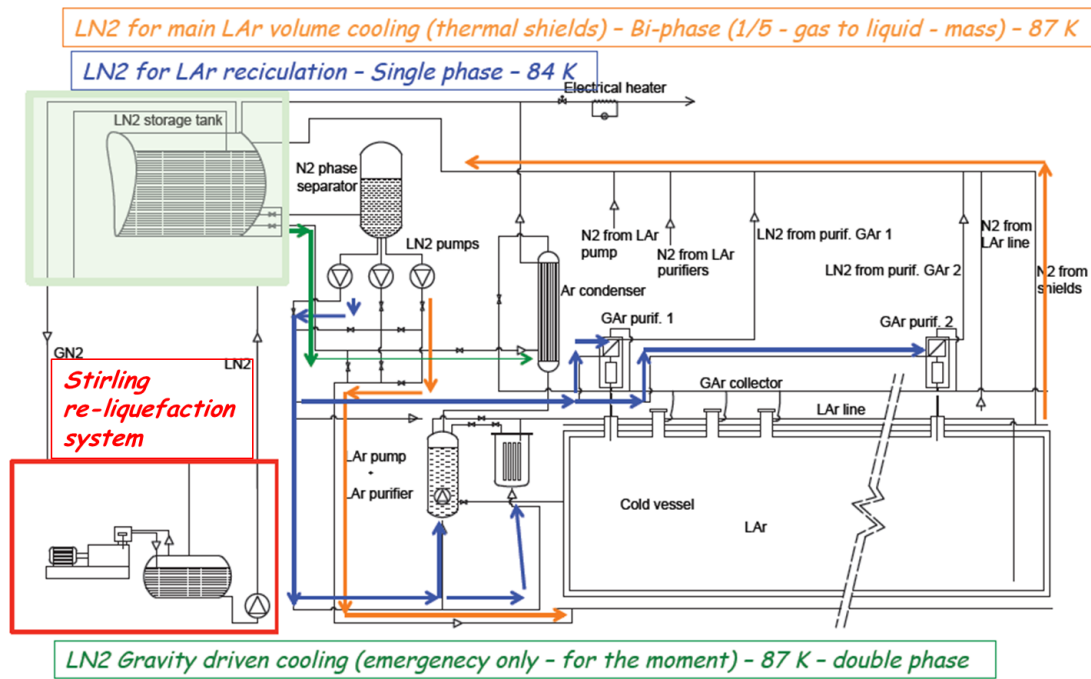


**FIG. 80:** Drawing of the existing plant of the ICARUS-T600 detector, containing all main elements of the system: LN<sub>2</sub> lines and storage tanks, GAr/LAr recirculation, Stirling re-liquefaction system. LN<sub>2</sub> lines are color-coded for clarity.

cartridges, connected in parallel. Each set of filters has a nominal O<sub>2</sub> absorption capacity exceeding 200 normal liters, which is enough to purify an entire module, starting from standard commercial liquid argon (O<sub>2</sub> concentration  $\sim 0.5$  ppm). The maximum recirculation rate of 2 m<sup>3</sup>/h can be achieved, resulting from the pump throughput and the filter set impedance: with this value, one full-volume recirculation can be carried on in about six days. LN<sub>2</sub> is used to cool the pump vessel, purifier cartridges and all the Ar transfer lines.

Two-phase nitrogen coming from thermal screen, together with nitrogen employed in GAr/LAr recirculation, is sent back to a  $\sim 1$  m<sup>3</sup> phase separator connected to two 30 m<sup>3</sup> liquid nitrogen storages, filled up to about 80%. All the residual nitrogen gas produced in the various processes was converted back into liquid by a dedicated re-liquefaction system. This was designed to work in closed loop for safe operation in confined place; however operation in open circuit, with liquid nitrogen delivery by trucks, was also foreseen in case of prolonged emergency stops of the apparatus. The re-liquefaction system consists of twelve Stirling [133] Cryogenics BV SPC-4 (4-cylinder) cryo-coolers, delivering 4.1 kW of cold power each at 84 K with a nominal efficiency of 10.4%. The units operate independently, and automatically switch on/off to keep the nitrogen pressure at a fixed point, thus only delivering the actual cold power needed by the system.

Such required cold power can be determined by the consumption due to the insulation losses (heat input through joints, cryostat feet and cables), the nitrogen screen cooling (circulation pump and distribution lines) and the GAr/LAr recirculation-purification systems. During steady-state operations the cryogenic plant performed very well, successfully undergoing several safety, efficiency, redundancy tests and it demonstrated stability over the whole operating

period. The average request of cold power was around 24 kW, mainly due to insulation losses. This was largely within the capability of the re-liquefaction system, as on average never more than 10 of the twelve Stirling units were found operational simultaneously.

The capability of the cryogenic plant allowed also performing a smooth detector commissioning: in order to ensure an acceptable initial LAr purity, the cryostats were evacuated to a pressure lower than  $10^{-4}$  mbar, before commissioning. Vacuum phase lasted for three months, after which the cryostats could be cooled down to a temperature of 90 K within 7 days from start. Finally filling phase took place, lasting about two weeks, with the use of commercial LAr, pre-purified in-situ before being injected in the detector, at a rate of  $\sim 1$  m<sup>3</sup>/hour/cryostat. During the whole period the GAr recirculation was operating at maximum speed to intercept outgassing from the inner walls. One month after filling, LAr recirculation and purification was started on both cryostats.

Operations at LNGS demonstrated the very high reliability of the existing cryogenic plant, in particular for what concerns argon purification and stability of the system. As a matter of fact it was clearly shown in [121] how, for most of the data taking period, argon purity could be kept at a level corresponding to a free electron life-time higher than 7 ms. Furthermore at the end of the LNGS run the value of 16 ms (increasing) was reached, thanks to the use of a new recirculation pump that was tested in one of the two modules (for details please refer to [121], and see Fig. 81 below).

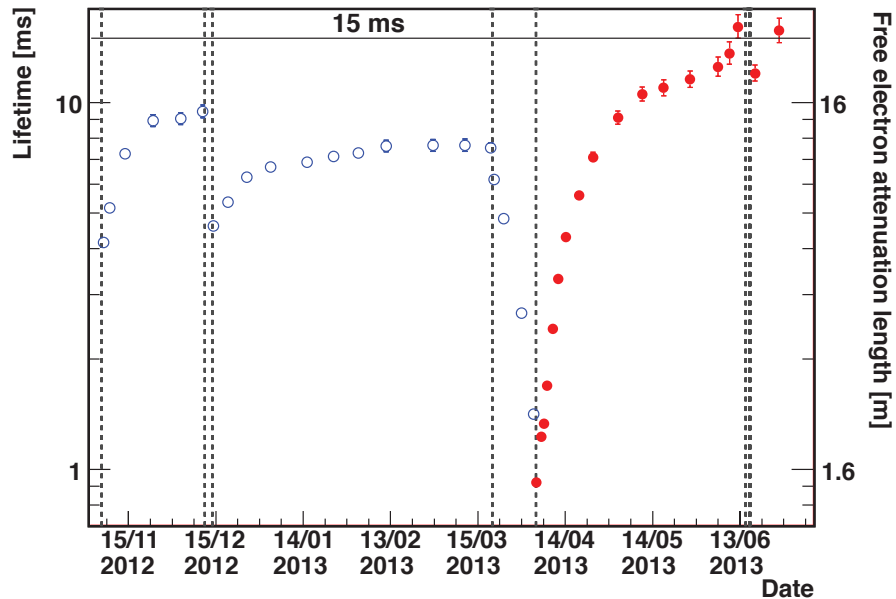


**FIG. 81:** Detail of the LAr purity in the East module of the T600 detector, as measured in the last months of operation. The high value of the electron life-time can be appreciated, as well as the ever-increasing trend in the last days of data taking achieved with a new model of circulation pump. Drops in purity correspond to stops of the recirculation for pump maintenance/substitution.

Other cryogenic parameters affecting the LAr-TPC performance were also accurately monitored during steady-state detector operations. In particular, the internal temperature in the two modules, directly connected to the electron drift velocity, was found to be stable and uniform at

a level better than 0.25 K, well within the requirements (see Fig. 82). The same behavior was confirmed by the data on the internal absolute pressure (see Fig. 83): a very high stability was measured, with variations contained within around 10 mbar, far lower than those of ambient pressure, despite various stops of the recirculation system due to pump maintenance.

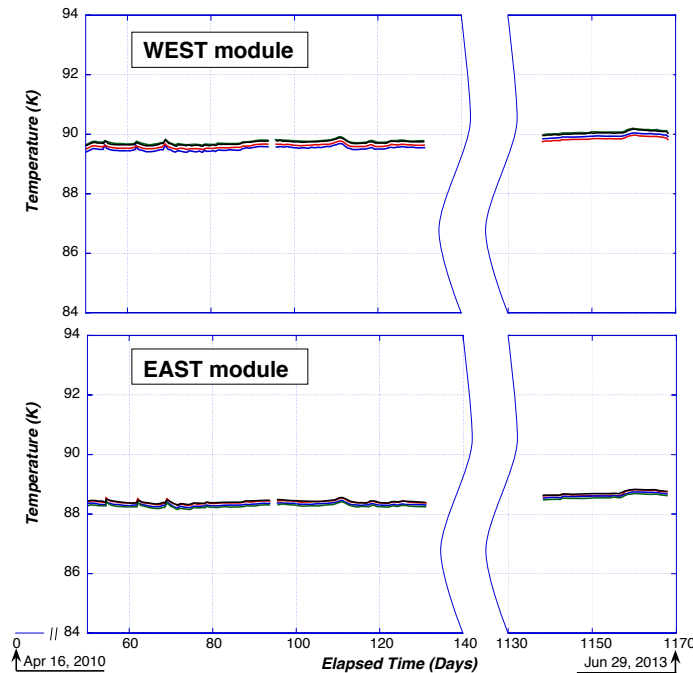


**FIG. 82:** Trend of the temperature in the two modules, measured in three different positions (bottom, middle height, top) during two periods of the LNGS run, one at its beginning in 2010, and the second in 2013, close to the end of data taking.

In general, the cryogenic system of the T600, repeatedly pre-tested against different types of emergencies, performed very well during operations in limiting conditions (deep underground location), and it allowed obtaining unprecedented results on argon purification. This result largely justifies the decision of carrying most of the plant and its design on to the next stage of the detector life within the Fermilab SBN program (see details in Section VD).

## V. Overhauling of the T600 Detector: WA104

The ICARUS-T600 detector has been moved to CERN for a complete overhauling, preserving most of the existing operational equipment, while upgrading some components with up-to-date technology in view of its future non-underground operation. The refurbishing (CERN WA104 project) will include the following main activities:

- substitution of the present cathodes with new ones of improved planarity;
- implementation of a new light collection system, to allow a more precise event localization and disentangle beam events from the background induced by cosmic rays;

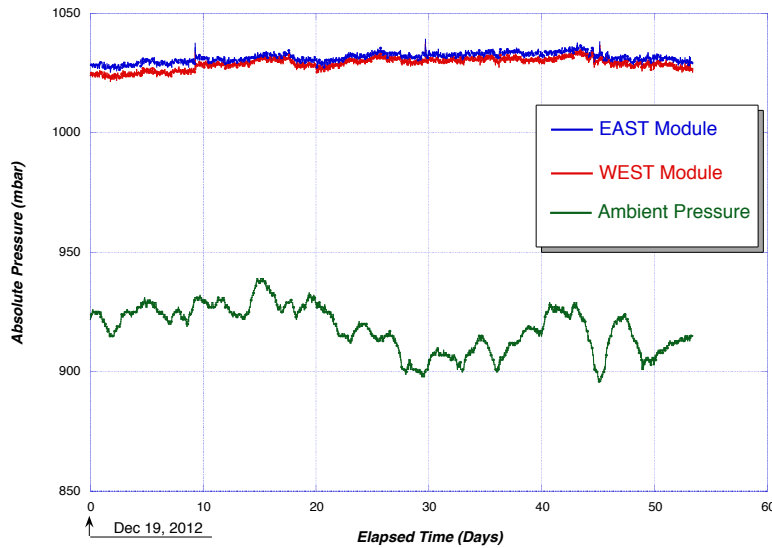


**FIG. 83:** Absolute internal pressure in the two modules during a two-month period between the end of 2012 and the beginning of 2013. Data can be compared with the trend of ambient pressure.

- implementation of new readout electronics;
- other internal TPC updating: slow control system and cabling;
- realization of new vessels for LAr containment and new thermal insulation, based on a similar technology, as foreseen for LBNF and the SBN Near Detector;
- complete review and maintenance of the cryogenics and purification systems.

The transfer of the two T600 TPCs to CERN has been already completed: after the positioning of the first module into its transport vessel (see Fig. 84, Fig. 85 and Fig. 86), the first cargo has arrived to CERN at the middle of November 2014 (see Fig. 87). Movement operations at LNGS proceeded smoothly, with 4 to 6 people continuously involved for three weeks during October 2014. After the arrival of the second transport vessel at LNGS in November 2014, also the second T600 TPC was moved to CERN, being on site at the middle of December 2014.

All overhauling activities will be carried on at CERN building 185, which has been outfitted accordingly, with all necessary services (e.g. electrical, ventilation, heating, air recirculation in clean room). A dedicated clean room, to house the TPCs during operations, has been already completed (see Fig. 88). Since December 19<sup>th</sup> 2014, the first transported module is inside the clean room, while the second one has been stored inside the building (see Fig. 89)

This Section is organized as follows: Par. VA describes the main modifications of the ICARUS-T600 internal detectors. Par. VB shows the new layout of the Light Collection System, while the Electronics and DAQ in the FNAL configuration are described in Par. VC. Finally, Cryogenics and Purification new systems are presented in Par. VD.



**FIG. 84:** *Transport vessel positioning in front of the TPC at LNGS.*

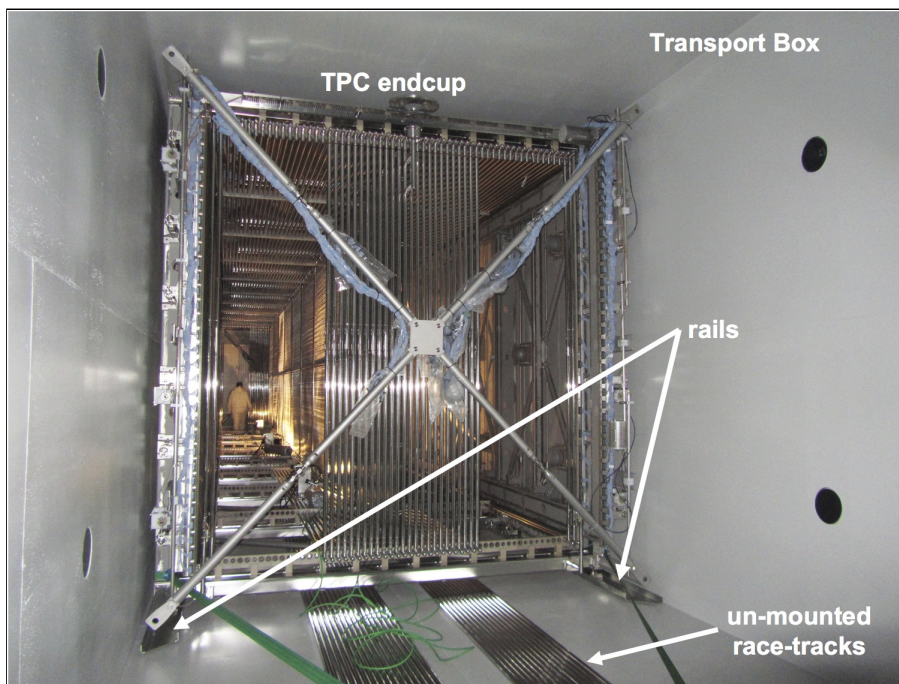


**FIG. 85:** *Start of movement of the TPC inside the transport vessel.*

### A. TPC modifications

Minor changes are expected to be implemented, for what concerns the T600 TPC internal structure, with respect to the present configuration.

Distortions in the uniformity of the electric field in the drift volume of the T600, due to positive ion charge accumulation induced by cosmic rays, have been investigated within the ICARUS collaboration. According to our estimates for ICARUS at shallow depths, the effect could be at most of a few mm, in agreement with the data collected in the 2001 technical run on surface in Pavia. To correct these distortions by making the electric field more uniform, some additional widely spaced shaping wire planes could be installed inside the sensitive volume, at the voltage of the potentials of the field cage electrodes. For instance, two arrays of wires (with





**FIG. 86:** *The transport vessel on its way to CERN.*



**FIG. 87:** *The transport vessel in front of building 185 at CERN.*

a pitch of the  $\sim 10$  cm) at 50 cm and 100 cm from the HV plane, anchored to the corresponding two field cage electrodes, could reduce the field distortion by almost an order of magnitude.

Moreover, small deviations from the linearity of the drift field have been found in the region close to the cathode plane on both modules. This is due to the not perfect planarity of the cathodes, owing to their pierced structure. This was confirmed by visual inspection after the first cryostat opening in October 2014, where displacements from planarity of the order of 5 mm were found. Thus, in view of the SBN experiment at FNAL, it has been decided to change the present cathodes with new ones of improved planarity. The cathode surface could be either opaque or transparent to the scintillation light, depending on the request to perform the coincidence of the light signals from the two PMT arrays at either sides of the cathode. The

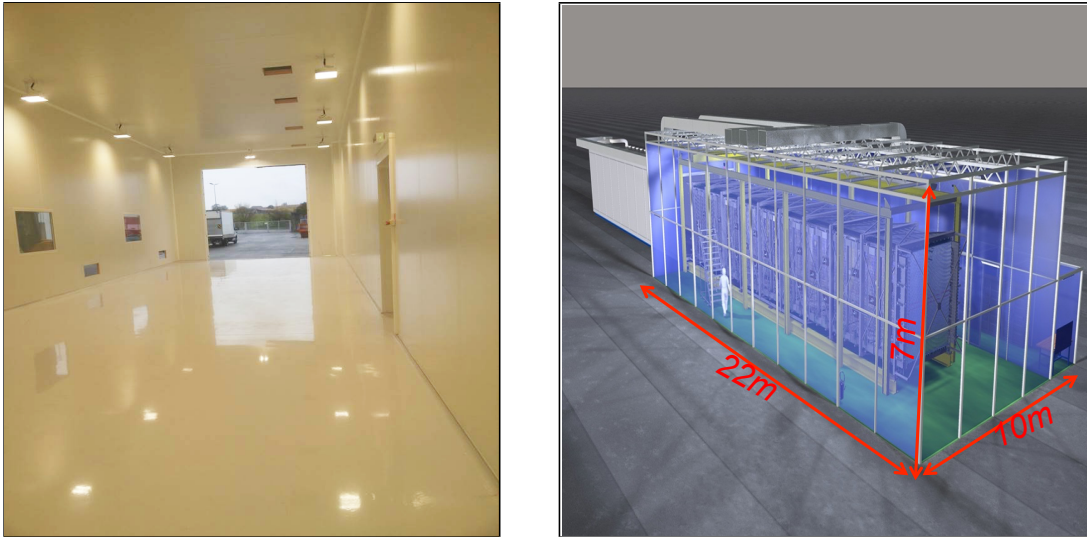


**FIG. 88:** *Left: Clean room implemented inside CERN building 185, adapted for the T600 overhauling. Right: Sketch of the clean room housing the T600 TPCs.*

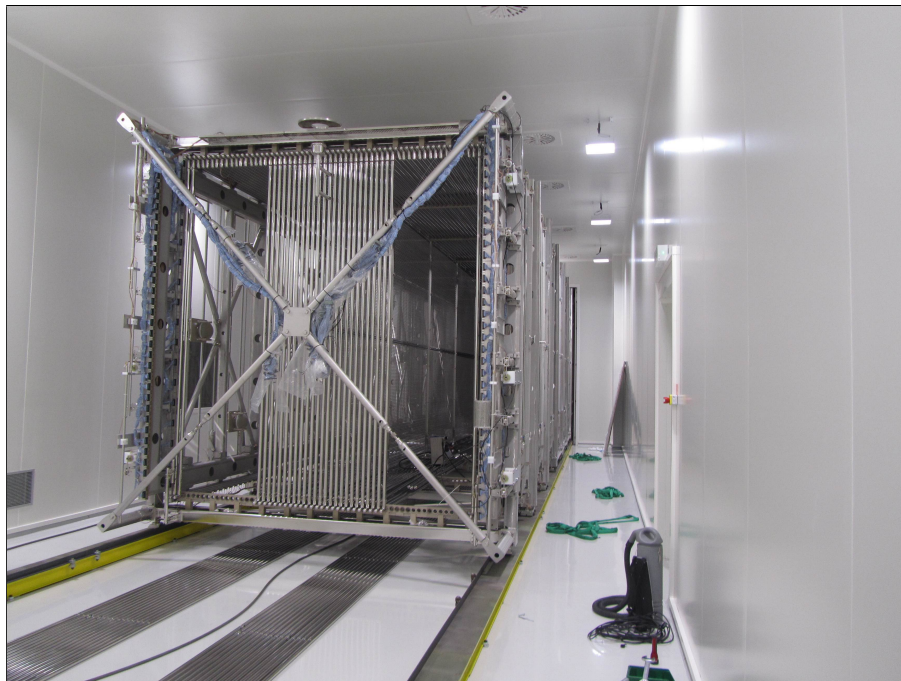


**FIG. 89:** *The first transported module inside the clean room at CERN.*

detailed design of the new cathodes is currently under completion. Other activities on the T600 TPCs concern the updating of the slow control system for temperature, pressure and cryostat wall deformation monitors, as well as the design of new cabling for internal wires, PMTs and slow control sensors.

## B. New Light Collection System Layout and Implementation

The future operation of the ICARUS LAr-TPC at the FNAL BNB at shallow depths requires an improved light collection system, able to detect with full efficiency the prompt scintillation light from events with energy depositions down to  $\sim 100$  MeV.

The renovated T600 photo-detector arrangement should again collect the VUV scintillation signal which is present in the LAr simultaneously to the ionization, converting it to visible light.

The detection process in the LAr-TPC is initiated by the trigger signal opening a long “imaging” readout window, in which tracks are recorded in a time sequence, collected serially by the readout planes, while the electrons travel towards the end of the drift path. The full image of the event is therefore progressively extracted from the drift time distributions and from the many readout wires.

As already mentioned in Sec. III, the fast scintillation light signal in LAr must be put in coincidence with the  $1.6 \mu\text{s}$  beam trigger gate, giving the huge rate of  $\sim 0.83 \times 10^6$  c/y. Moreover, during the long duration of each readout window, there will be on average 44 cosmic ray-induced scintillation light signals spread over the whole T600, four times the number of the cosmic tracks in a single TPC (accounting for the cathode transparency and because the time interval during which a light signal can be linked to a charge deposition is twice the maximum drift time).

The new light collection system has to be able to localize the track associated with every light pulse along the 20 m of the longitudinal detector direction, with an accuracy better than 1 m, which is smaller than the expected average spacing between cosmic muons in each TPC image.

In this way, the light collection system would be able to provide unambiguously the absolute timing for each track; and to identify, among the several tracks in the LAr-TPC image, the event in coincidence with the neutrino beam spill. The time accuracy of the incoming event with the new light collection system is expected to be at 1 ns level, allowing the exploitation of the bunched beam structure, lasting 1.15 ns (FWHM  $\sim 2.7$  ns) every 19 ns, to reject cosmic events out of bunch as described in a SBN note [127]. An overall time resolution of 1.3 ns would then allow a background reduction of a factor  $\sim 4$  by rejecting cosmic events occurring outside the RF buckets with a  $2\sigma$  accuracy.

### *Tests on new cryogenic PMT models*

The baseline solution for the T600 photo-detection system will rely on large surface Photo-Multiplier Tubes with hemispherical glass window of 200 mm (8”) diameter, manufactured to work at cryogenic temperature. First tests were carried out to choose the most suitable PMT model. Three new large area PMTs, Hamamatsu R5912 Mod and R5912-02 Mod, and ETL 9357 KFLB, have been characterized both at room and at cryogenic temperature [134].

Tested PMTs have a borosilicate glass window and a bi-alkali photo-cathode ( $\text{K}_2\text{CsSb}$ ) with platinum undercoating, to restore the photo-cathode conductivity at low temperature. Hamamatsu R5912 Mod and R5912-02 Mod PMTs have 10 and 14 dynodes, respectively, while the ETL 9357 KFLB has 12 dynodes. Photo-cathode uniformity, gain, linearity, dark count rate and Quantum Efficiency (QE) for LAr scintillation light have been measured.

For gain, linearity and uniformity measurements, PMTs were illuminated with a 405 nm NICHIA NDV1413 laser diode, using an Avtech AVO-9A-C-P2-LARB pulse generator and an optical fiber (7  $\mu\text{m}$  core diameter, 3 m long). An appropriate support was used to maintain the

fiber in a fixed orientation, normal to the PMT window, while allowing to move it in various positions on the window itself. A CANBERRA 2005 pre-amplifier and an ORTEC-570 amplifier were used to form PMT signals, then acquired with an ORTEC-Easy-8k,12 bit Multi Channel Analyzer. PMTs dark count rate has been measured with a different acquisition system, i.e. with a CAEN V812 discriminator and a CAEN V560 counter. The discrimination threshold was gradually increased from 1 to 255 mV, with 1 mV steps.

To test them at cryogenic temperature, the PMTs were directly immersed in liquid nitrogen ( $T = 77$  K), to simulate real experimental conditions. Measurements were carried out after a couple of days of rest in the cryogenic bath. The same setup and acquisition system described above were used, with the fiber and the other cables allowed to enter by a proper feed-through, used to preserve darkness conditions and thermal insulation (see Fig. 90).

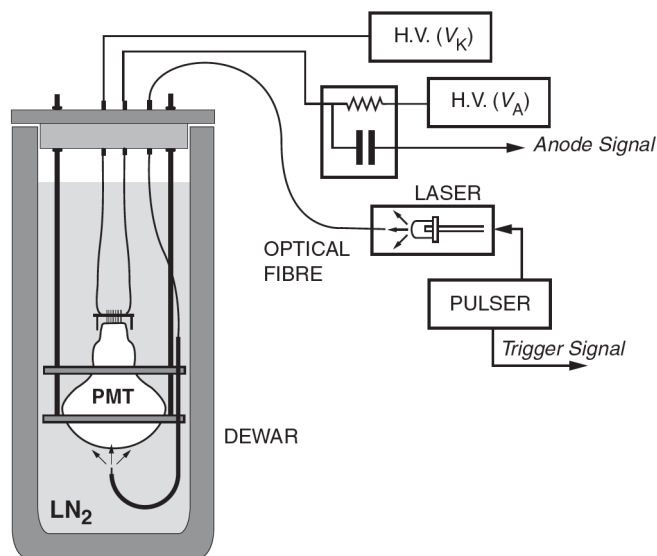


**FIG. 90:** *Experimental setup for the characterization of PMTs immersed in liquid nitrogen.*

Hamamatsu PMTs showed a good uniformity, within 10%, up to 10 cm from the tube axis, where a gain reduction occurs, probably due to the electric field non-uniformity in the peripheral region of the tube. While this behavior does not occur with ETL 9357 KFLB, lower uniformity is measured,  $\sim 20\%$ ; furthermore a very low signal has been measured in a specific region of the photo-cathode for this model: this can be explained by a degradation of the photo-cathode for the specimen under test. Due to this problem and after discussions with the manufacturer, it was decided not to test the ETL 9357 KFLB at cryogenic temperature, pending further tests by the producer.

The gain of the devices was estimated from Single Electron Response (SER) as a function of the applied voltage and operating temperature. The gain reduction occurring at 77 K is evident for both Hamamatsu devices, being  $\sim 70\%$  in the R5912 and  $\sim 35\%$  in the R5912-02 with respect to room temperature data (see Fig. 92 Left). Hamamatsu R5912 MOD remains linear up to 400 phe, while R5912-02 MOD reaches again the saturation regime after a few photo-electrons, about only 10 phe.

In general both photo-detectors showed a good behavior and are suitable for cryogenic application.

A different experimental setup was used to measure the QE of the photo-cathodes in the VUV light region. To make them sensitive to VUV light, the PMT sand-blasted glass windows

were deposited with a TPB coating of  $\sim 0.2 \text{ mg/cm}^2$ .

The measured QE accounts then for: the shifting efficiency of the TPB, a geometrical factor (on average half of the photons will be re-emitted in the opposite direction with respect to the photo-cathode) and the QE of the PMT for blue light. As shown in Fig. 91, the PMT under test was placed inside a steel chamber optically connected to a McPHERSON 234/302 VUV monochromator.

The experimental setup included a McPHERSON 789A-3 scanner, a McPHERSON 632 Deuterium lamp, a rotating Al+MgF<sub>2</sub> mirror, an AXUV-100 reference photo-diode and collimating optics. The whole system was kept under vacuum, down to  $10^{-4}$  mbar, to prevent ultraviolet light absorption. Thanks to the rotating mirror, the light spot was directed alternatively on the PMT surface or on the reference photo-diode. The QE was obtained by comparing the current measured with the PMT and the same collected with the reference diode, keeping the light constant. Measurements were carried out by means of a picoammeter. Results for LAr (128 nm) and LXe (165 nm) emission peaks are reported in Fig. 92 Right. ETL 9357 KFLB has, at 128 nm, a  $\text{QE} = 4.7\% \pm 0.7\%$ , while Hamamatsu PMTs present a higher value,  $\text{QE} = 7.0\% \pm 0.6\%$ .

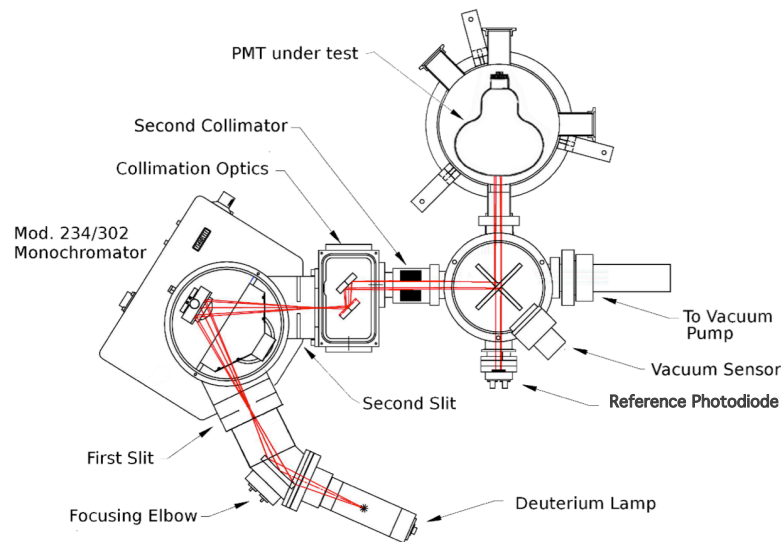


**FIG. 91:** *Experimental setup for the evaluation of the response of PMTs to the VUV light.*

#### *New Light Collection System Layout*

After the choice of the PMT model and the purchase of the devices, a careful evaluation of the performance of each PMT before its final mounting inside the T600 detector will be carried out. Measurements will be focused on the main PMT parameters which are temperature dependent, to isolate possible defects in the devices. In particular, the following features will be characterized: shape of the anode pulse, SER of the anode pulse, gain, single-electron transit time (spread, pre- and late-pulsing), after-pulses, dark-count rate and spectrum. To this purpose a test facility will be setup in a dedicated INFN laboratory.

PMTs will be located in the 30 cm space behind the wire planes with sustaining structures: the sustaining system will allow the PMT positioning behind the Collection wire planes according to the geometrical planned disposition. PMTs induce spurious signal on wire planes: to

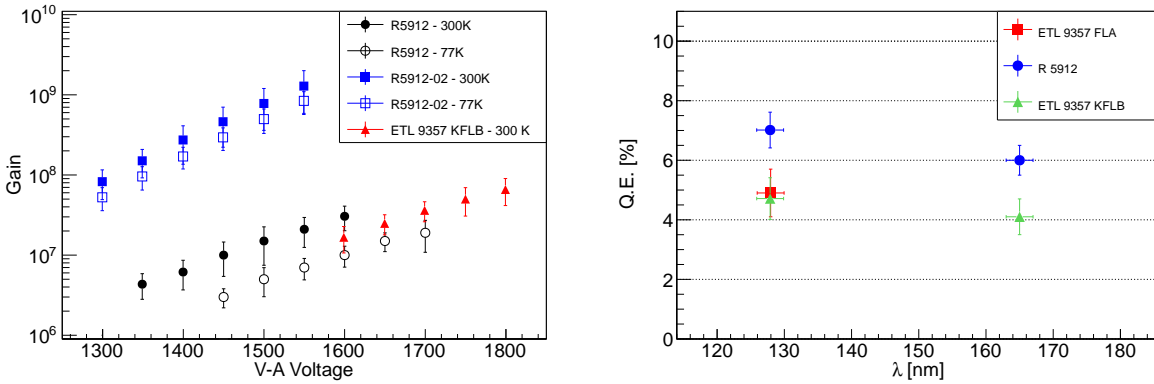


**FIG. 92:** *Left: gain trends for tested PMTs at room (full spots) and at cryogenic (empty spots) temperature as a function of the voltage between anode and cathode. Right: Quantum Efficiency of the tested devices at LAr emission peak (128 nm) and LXe emission peak (165 nm).*

reduce this drawback, still under investigation, each PMT will be surrounded by an electrostatic shield. A drawing to show a 90-PMTs layout behind the wire planes is presented in Fig. 93.

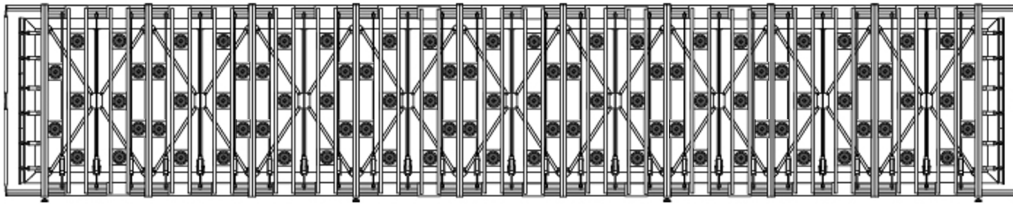


**FIG. 93:** *Drawing showing a 90-PMTs layout behind the wire planes. PMTs are depicted as dark circles. This design yields a 5% photo-cathode coverage.*

To prevent any impedance mismatch in the signal lines, PMT negative biasing will be adopted. This scheme will adopt two cable for each device, one for the DC HV power supply and one for the signal. The main disadvantage is the operation with photo-cathodes at HV voltage close to the collecting wire planes. Despite electric fields of about 600 V/cm are expected, the TPC electric field and the electron collection on the wire planes will be not altered. Moreover, the adoption of a fine-mesh grid in front of each PMT should avoid any interference between charge collection and light detection.

Fast waveform digitizers are required to exploit the bunched beam structure. 1 GHz waveform digitizers with zero suppression will be adopted, preventing the use of shaping pre-amplifiers; the input dynamics must permit the recording of the scintillation light fast component pulses and, at the same time, of the single photons arriving from the slow component de-excitation. A PMT timing calibration/monitoring system will also be implemented. The baseline solution consists of pulsed laser diodes and optical diffusors installed at various locations in front of the PMTs, possibly on the TPC cathodes. Short pulses ( $< 1$  ns) of laser light will be transmitted inside each TPC, by means of optical fibers and feed-throughs, to each of the diffusors. This will allow the PMTs lighting with approximately uniform intensity. A dedicated R&D activity is foreseen to evaluate the timing performance of this system and to optimize the optical fiber feed-through implementation.

Dedicated calculations have been set up to evaluate the performance of the upgraded ICARUS light collection system, in terms of event localization for both cosmic muons and electromagnetic showers. Cosmic muon tracks in the active liquid argon volume are simulated as straight lines with directions distributed as  $\cos^2 \theta$  around the vertical axis, where  $\theta$  is the zenith angle. About 40,000 VUV photons/cm (corresponding to the amount of scintillation light from 2.1 MeV/cm energy deposition of a minimum ionizing particle in a field of 500 V/cm) are produced uniformly along the muon tracks and are emitted isotropically. Rayleigh scattering and the presence of delta rays in a 15 cm radius cylinder surrounding the muon path are also included in the simulation.

Electromagnetic showers are simulated as clusters containing single 1 MeV points ( $\sim 21,000$  photons) up to the deposited energy. No reflection and diffusion on walls have been simulated, since the LAr VUV scintillation photons are absorbed by all materials. The number of detected photons is derived in terms of solid angle calculation.

To estimate the localization capability of the light collection system, a Monte Carlo simulation has been carried out. For each simulated event the barycentre of the light emission has been calculated, by averaging on the coordinates of the PMTs and weighing on the different signal intensities. This was done both for the vertical and horizontal coordinates. The spatial resolution of the system, evaluated as the difference between the simulated track barycenter and the same quantity reconstructed as described above, is found to be better than half a meter, as shown in Fig. 94. This will allow to strongly narrow the LAr region in which to search for neutrino beam-induced events.

### C. New Electronics, DAQ and Trigger

#### *Electronics*

The ICARUS-T600 electronics was designed starting from an analogue low noise warm front-end amplifier followed by a multiplexed (16 to 1) 10-bit AD converter and by a digital VME module that provides local storage, data compression, and trigger information. The overall architecture, based on VME standard, was appropriate for the experiment, taking into account that the T600 electronics design started in 1999. The first production was carried out in 2000 and tests, at surface on the first T600 module, were successfully performed in 2001.

The present architecture (essentially a waveform recorder followed by circular buffers switched by trigger logic) is still valid, however possible improvements are now conceivable, taking advantage of new more performing and compact electronic devices.

The analogue front-end amplifier, used in the T600 LNGS configuration, is perfectly adequate: the only proposed change is the adoption of a smaller package for the BiCMOS (see Fig. 95) custom amplifier, dual channel, which is already available. The possibility to have the front-end in LAr is also considered.

The amplifier serial input noise,  $e$ , linearly increases with detector and cable capacitance,  $C_d$ , and decreases with input stage transconductance,  $g_m$ :

$$e^2 = \frac{C_d^2}{g_m}. \quad (10)$$

Transconductance is 26% higher at LAr temperature (86 K), see Fig. 96, and, together with the reduction of cable length, an improvement of S/N is expected with cold amplifiers. However, in the case of large mass LAr-TPCs, a detector lifetime in the order of tens of years

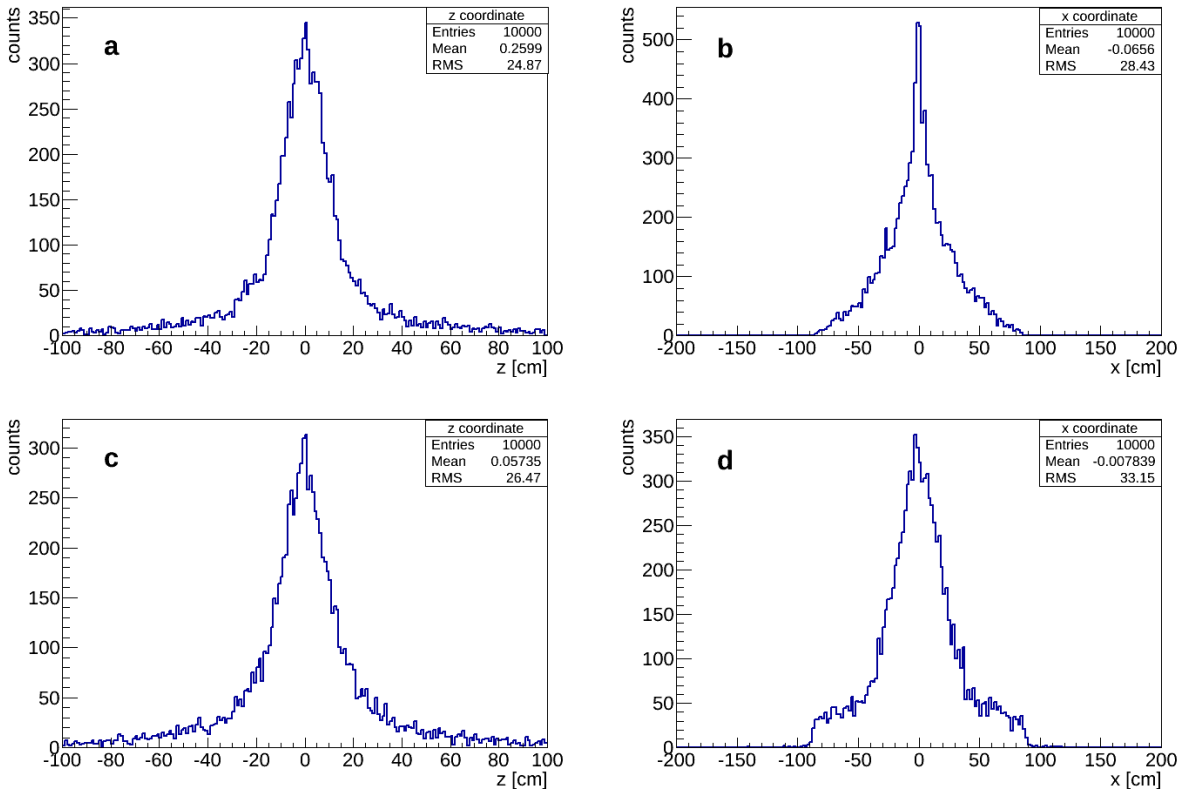


**FIG. 94:** Monte Carlo evaluation of the residuals from the correct position, both along the beam direction  $z$  and along the vertical coordinate  $x$ , for electromagnetic showers of about 200 MeV (a,b) and cosmic rays (c,d). In plot (d) the residual distribution is affected by the detector boundaries along the  $x$  coordinate.

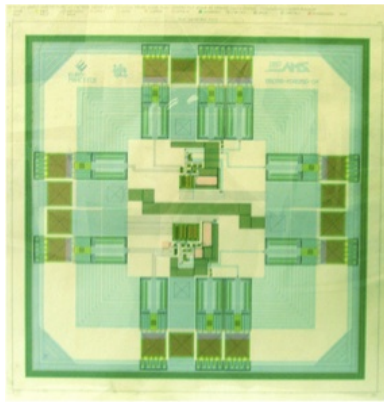


**FIG. 95:** BiCMOS dual channel custom analog pre-amplifier.

is expected. In this period, it is natural to foresee improvement programs in the electronics, because of its constant evolution and progress. An architecture allowing for major and easy upgrading with an accessible electronics has been then chosen.

The gain of the front-end amplifier and filter is  $\frac{1V}{164fC}$ . The 10 bit ADC input range is 1 V, therefore the least count is equivalent to 1,000 electrons. This value matches with the amplifier



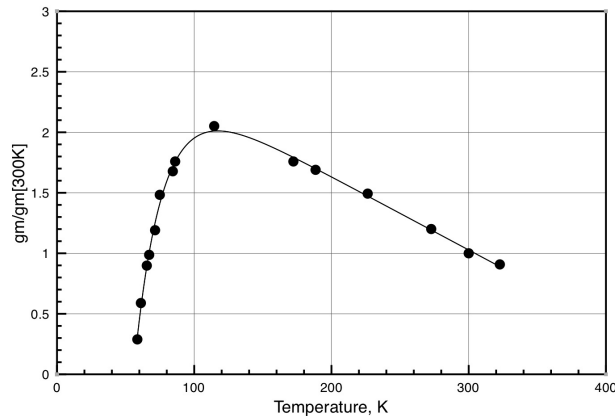


**FIG. 96:** Typical variation of the input stage transconductance  $g_m$  with temperature for junction *Fet*.

noise of  $\sim 2,000$  electrons, given a detector capacitance of 450 pF (signal wires plus cables).

The T600 run at LNGS on the CNGS neutrino beam confirmed a S/N better than 10 for m.i.p. on about 53,000 channels. A relevant change, in the new electronics design, concerns the adoption of serial ADCs (one per channel) in place of the multiplexed ones used at LNGS. The main advantage is the synchronous sampling time (400 ns) of all channels of the whole detector, not to mention compactness and price. A very reliable and cost effective new flange (CF200) has been developed for the T600 future operations, see Fig. 98 Left. The internal structure of a via in this CF200 flange is shown in Fig. 97. The external contacts, on both sides, not visible in Fig. 97, are on a different plane respect to the via, and allow for SMD connectors use. The white squares are brass disks that reinforce the flange structure, in order to stand atmospheric pressure without deformation in case of use in vacuum vessels.

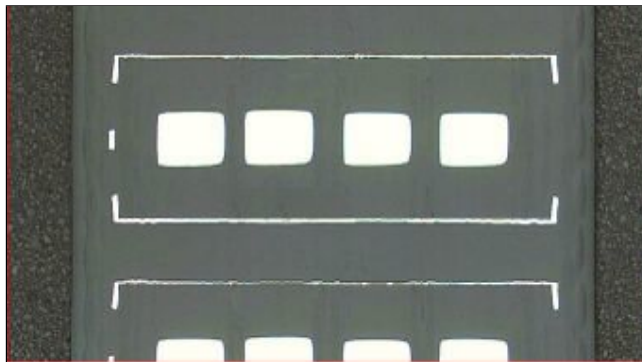


**FIG. 97:** Section of signal flange (5 mm): the copper via contact (white lines in the photo) is fully embedded in solid G10.

This flange allows the connection of 16 cables (512 channels), to exploit the external side of the flange as an electronics cards backplane in a special crate (Fig. 98 Right). The connectors on the external side allow for direct insertion of electronics boards, where both analogue and digital electronics, with a compact design, are housed.

In Fig. 99 the first working prototype board is shown. It serves 64 channels and uses serial optical links. The 8 boards of one flange may use the same serial optical link as it is shown

in the block diagram of Fig. 100. The digital part is fully contained in a high performance FPGA (Altera Cyclone V) that allows easy firmware upgrading. Behind the FPGA, sockets for front-end amplifiers are visible together with the direct insertion connectors that convey wire signals. In Fig. 101 the pre-amplifiers are shown. The board is scored so the amplifiers will be snapped in eight sets of eight pre-amplifiers.

Performance, in terms of throughput of the read-out system, has been improved replacing the VME (8 - 10 MB/s) and the sequential order single board access mode inherent to the shared bus architecture, with a modern switched I/O. Such I/O transaction can be carried over low cost optical Gigabit/s serial links.

As mentioned before, the cold electronics option could be considered, provided a suitable design is found. The ICARUS collaboration does not have a ready-to-use cold pre-amplifier, even if in the past many tests, eventually abandoned, were carried out for this solution [135]. If such cold pre-amplifier is found, one should adapt a pre-amplifier board inside the cold vessel, close to the wire support, modulo 32 or 64, and substitute the piggy back 8-channel amplifier boards, described before, with suitable receivers, maintaining the digital part as it is and the 400 ns sampling time.

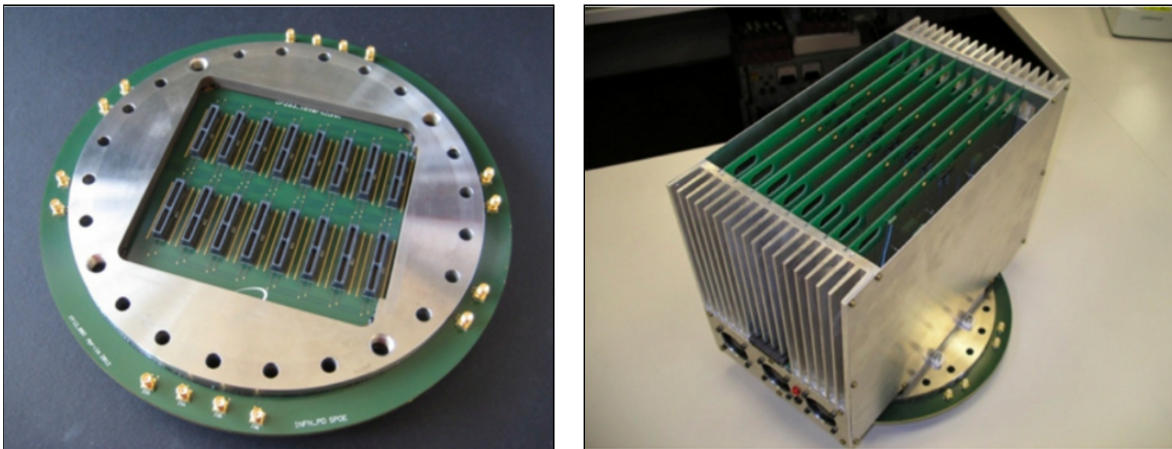


**FIG. 98:** *Left: the new T600 flange without the cards cage. Right: the new T600 flange with the cards cage and 8 boards inserted without front panels.*

### *Trigger and DAQ*

The trigger system of the T600 detector will exploit the coincidence of the prompt signals from the scintillation light in the LAr-TPC, recorded by the PMT system, with the proton spill extraction of the BNB within a  $1.6 \mu\text{s}$  gate.

PMT digitized pulses are sent to a front end dedicated board to be processed by FPGA modules, requiring a logic on multiple PMT signals for the generation of the trigger. Discrimination thresholds have to be set to guarantee the detection of all the event associated to each neutrino interaction with energy  $E > 100 \text{ MeV}$ .

The PMT trigger signal will be then sent to the T600 Trigger Manager, where it will be combined with the time information from the beam spill to initiate the readout of all the TPCs. A multi-buffer event recording will be adopted with a 3-level veto, as for the CNGS beam exploitation, able to give different priorities to different trigger sources, thus minimizing



**FIG. 99:** *First working new electronics prototype board.*

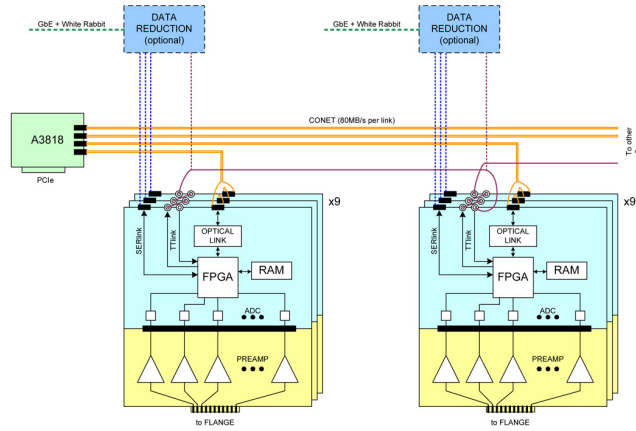


**FIG. 100:** *Arrangement of the read-out boards on different flanges.*

DAQ dead-time. The system, similar to the LNGS run one described in Sec. IV C, will consist of a Real Time (RT) controller and FPGA boards, communicating with the DAQ in handshake mode. The RT controller will monitor the number of available buffers in the digital boards, preventing the generation of new triggers in case they are full. The FPGA boards will implement time critical processes, like the opening of Booster Beam gate and the time stamp of each trigger. FPGA boards are also expected to record the trigger source and mask, to monitor the trigger rates and to control the overall system stability. The T600 Trigger Manager will also allow combine in the trigger logic the signals coming from the new cosmic ray tagging system (see Sec. VI).

At the nominal BNB intensity of  $5 \times 10^{12}$  pot/spill,  $\sim 1$  neutrino interaction, either charged or neutral current, every 180 spills is expected to trigger the T600 detector at the far position with vertex in the LAr-TPCs (1 neutrino every 240 spills considering charged currents only). A slightly lower trigger rate, one every 210 spills, will come from beam-associated events; the dominant trigger source, 1 over 55 spills, is expected from cosmic rays. Globally, about 1 event every 10 s is foreseen in the T600 LAr-TPC at the standard 4 Hz repetition rate of the Booster Neutrino Beamline. This  $\sim 0.1$  Hz trigger rate is well within the 50 MB/s DAQ throughput already realized for the CNGS data taking at LNGS. Actually, the significant improvement in

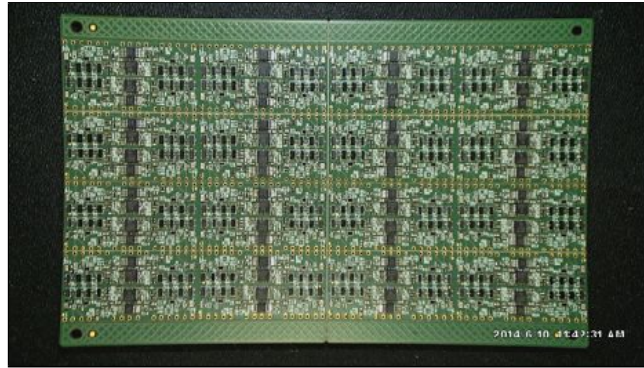


**FIG. 101:** 64 front-end amplifiers before snapping in 8 sets of 8 amps.

the readout throughput achievable with the new serial optical links will ensure an even better performance. Therefore, the present DAQ is largely adequate to operate without dead-time not just with the standard 4 Hz repetition rate of the Booster Beam, but also up to the  $\sim 15$  Hz maximum repetition rate.

Provided that a precise beam extraction signal is available, the trigger and DAQ system is also well suited to the exploitation of the bunched beam structure, accounting for the 1 GHz sampling of the PMT waveforms and the precise spatial reconstruction of the neutrino interaction vertex in the TPCs. The excellent performance in event timing achievable with the ICARUS-T600 detector has been proven by the precision measurement of the neutrino velocity on the CNGS beam [119, 120]. This result relied mainly on:

- the waveform of the extracted proton beam time-structure signal, recorded at CERN with a 1 GHz sampling triggered by the kicker magnet signal;
- an absolute GPS-based timing signal, distributed by LNGS laboratory to the ICARUS-T600 detector via a  $\sim 8$  km optical fiber, synchronized with the CERN absolute timing within few ns;
- the waveform of the PMT trigger signal recorded with a 1 GHz sampling;
- the evaluation, with  $\sim 1$  ns accuracy, of the time corrections corresponding to the distance of the event from the closest PMT and the position of the interaction vertex along the  $\sim 18$  m of the detector length. Note that the time corrections also include the contribution of the PMT transit time, different for each device.

A similar strategy could be adopted at FNAL as well, if the waveform of the fine bunched structure of the Booster beam will be provided with  $\sim 1$  ns resolution. As a further simplification, a precise matching of the neutrino interaction in the T600 active volume with the corresponding bunch could be obtained without need for an absolute timing, if the beam extraction signal will be delivered directly to the T600 detector exploiting the recently successfully developed White Rabbit timing protocol [136].

#### D. New Cryogenic and Purification systems

The SBN program provides a first opportunity for the CERN and FNAL engineering groups to collaborate on the design of LAr-TPC infrastructure. Once established, this collaboration

could have a significant impact on designs for other short and mid-term projects leading to a long-baseline neutrino facility. While most of the components of the T600 detector will be reused after overhauling at CERN, the LN<sub>2</sub> delivery system is expected to be replaced and a completely new cryostat and cryogenic layout will need to be developed. The following describes the cryostat and cryogenic needs for the Far Detector.

New cryostats will host the refurbished T600 detector. LAr will be contained in two mechanically independent vessels, of about 270 m<sup>3</sup> each. According to the past experience, to efficiently outgas the internal surfaces and obtain an appropriate LAr purity, the cold vessels must be evacuated to less than 10<sup>-3</sup> mbar. Therefore the vessels need to be tight to better than 10<sup>-5</sup> mbar l s<sup>-1</sup>. The new T600 vessels will be parallelepipedal in shape with internal dimensions 3.6 (w) × 3.9 (h) × 19.6 (l) m<sup>3</sup>. Aluminum welded extruded profiles (see Fig. 114) will be employed, designed in collaboration with industries and Milano Politecnico (Italy): they are requested to be super clean, vacuum-tight and to stand a 1.5 bar maximal operating internal overpressure. Executive design for both the profiles and welding (mounting) procedures has already been procured: further details are shown in Fig. 106, Fig. 107 at the end of the section.

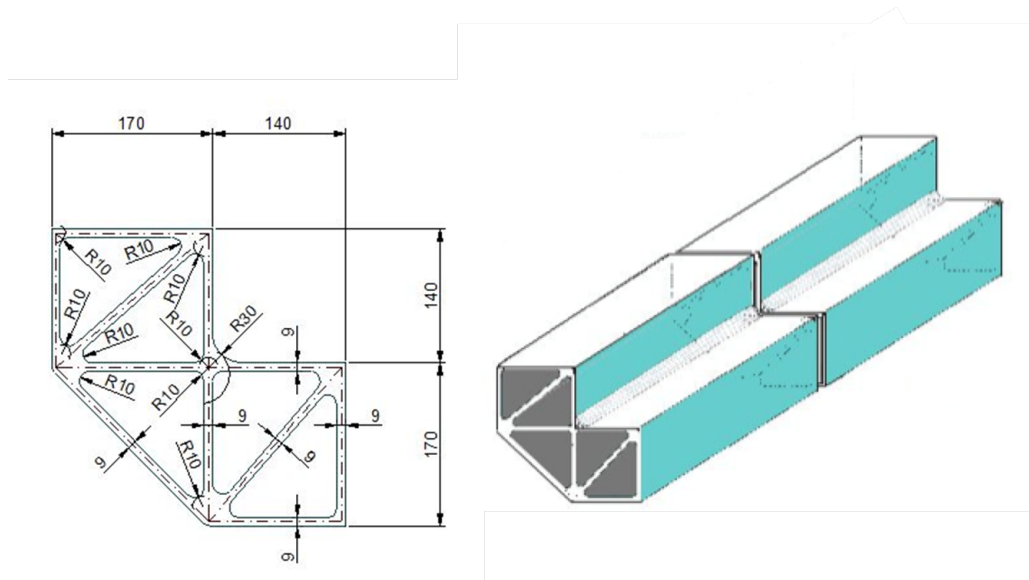


**FIG. 102:** Detail of an aluminum extruded profile corner, 2D and 3D. More drawings are shown at the end of the section.

Such new solution represents a significant simplification with respect to the aluminum honeycomb used in the LNGS run, whereas it implies a slight increase in the cryostat weight, 30 t each. Use of aluminum LAr vessels is also particularly attractive as it offers very good shielding against external electronic noises, and it provides large thermal conductivity that improves the temperature uniformity inside the LAr. As in the LNGS run, walls are double-layered and can be evacuated, leading to efficient leak detection and repair.

The cold vessels will be enclosed inside a common heat exchanger (thermal shield) in which two-phase (gas+liquid) nitrogen is circulated. As in the past run, a mass ratio less than 5:1 will be kept between the liquid and the gas phases, which ensures temperature uniformity all along the shield.

A purely passive polyurethane foam is chosen for insulation, based on the membrane tanks technology. This technique has been developed for 50 years and is widely used for large industrial storage vessels and ships for liquefied natural gas [137, 138]. The solution has been adapted to the ICARUS design by the GTT firm, and it is similar to the one to be used for the membrane cryostat of the Near Detector. In Fig. 110 and Fig. 104 details of the insulation elements and expected thermal gradients respectively are shown, as an example. In Tab. XVIII the thermal flux through the various elements is listed. An insulation thickness of 600 mm will be used for the bottom and lateral sides; for the top-side a maximum thickness of about 400 mm will be used. With this configuration, the expected average thermal losses will be of around  $10 \text{ W/m}^2$ , resulting in a heat loss through the insulation of  $\sim 6.6 \text{ kW}$ . All the external heat contributions (cables, pumps, transfer lines, etc.) can be accounted for a value not exceeding  $5.4 \text{ kW}$ , leading to a total heat load of about  $12 \text{ kW}$ .

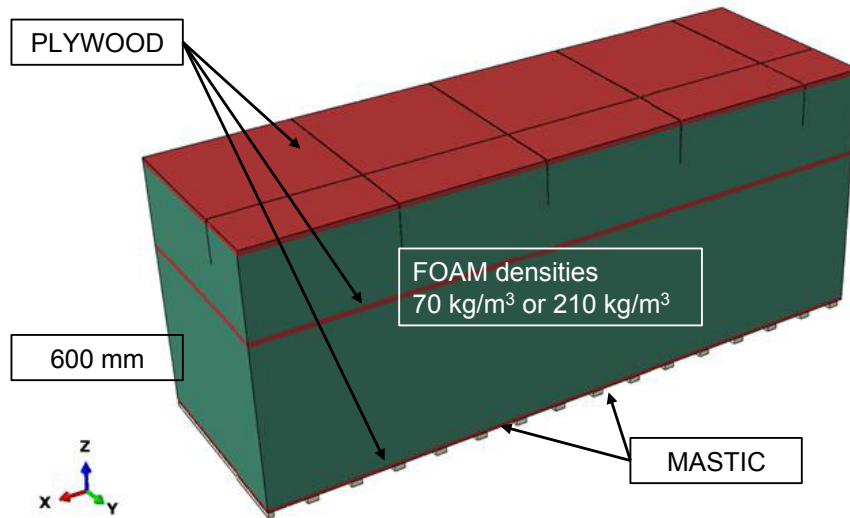


**FIG. 103:** 3D model of the newly-proposed T600 insulation. 600 mm element displayed

Panel thickness (mm)	Foam density ( $\text{kg/m}^3$ )	Total heat (W)	Surface ( $\text{m}^2$ )	Thermal flux ( $\text{W/m}^2$ )
400	70	7.800	0.750	10.40
400	210	13.530	0.750	18.04
600	70	5.200	0.743	7.00
600	210	9.026	0.743	12.15

**TABLE XVIII:** Thermal flux through the insulation elements, as a function of thickness and foam density, from GTT study. The foam density will be usually of  $70 \text{ kg/m}^3$ , while amounting to  $210 \text{ kg/m}^3$  in correspondence to the feet of the detector.

The Far Detector renovated cryogenic design is being developed, wherever possible, with a focus on commonalities with the Near Detector one, to be used across both experiments and also as a stepping stone for LBNF collaborative efforts. With this idea in mind, this system

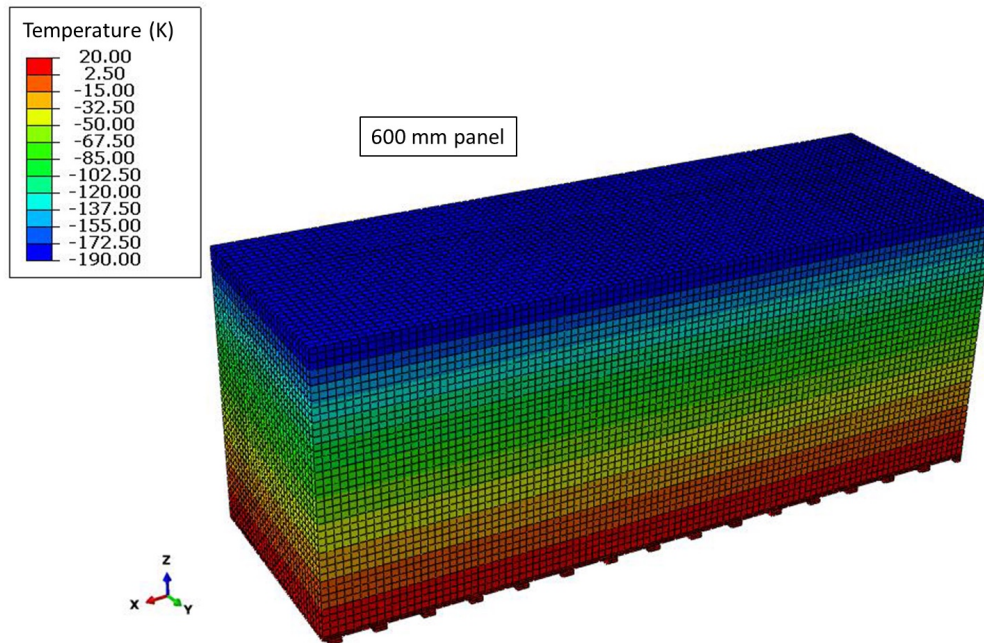


**FIG. 104:** *Finite elements study of the thermal gradient in the 600 mm thick element. Note that on this picture ambient temperature is on the lower side of the element*

is expected to be modular in design, able to be enlarged for future projects, and portable, i.e. constructed on skids that can be tested separately, prior to delivery to FNAL for installation.

The original scheme of ICARUS-T600 cryogenics and LAr purification systems will be preserved, and most of the present plant, INFN property, will be reused. In the same way, the requirements will remain the same, with respect to the past, as described in Sec. [IV D](#).

One main difference, with respect to the previous LNGS run, will be in the logistics, due to the different location of the detector (at shallow depths). If further updates were needed, they would be carried on by the hosting laboratories, following the specification given by the ICARUS Collaboration. On the other hand, during the different stages of the program (overhauling and, later, commissioning and data taking) it will be responsibility of the hosting laboratory to conceive and take care of the necessary maintenance of circuitry and control systems. The same goes for what concerns the plants-related logistics.

At Fermilab, the cooling circuit will be operated in open loop: the Stirling re-liquefaction will not be used. Fig. [105](#) shows once again the existing cryogenic system on the ICARUS-T600 detector, this time highlighting the Stirling re-liquefaction system that will be discarded with the implementation of the open-loop LN<sub>2</sub> delivery system.

Further discussions on specific technical aspects of the cryogenic system are underway, mainly regarding the purification system (filters), best re-condensation strategy, ullage conditions. However, given the already discussed very successful operation of the existing plant (see Sec. [IV D](#)), the ICARUS Collaboration intends to maintain the choices made in its previous experience, with the exceptions described above, and carry them on to the coming SBN program at FNAL.

The envisioned schedule for the development of the ND/FD cryogenic systems is related

to the request to have the Near and Far Detectors ready for commissioning in fall 2017, with data taking starting in April 2018. LAr Cryogenics groups are being formed both at CERN and FNAL, and are set to collaborate to meet the goals.

Fig. 105 shows once again the existing cryogenic system on the ICARUS-T600 detector, this time highlighting the Stirling re-liquefaction system that will be discarded with the implementation of the open-loop LN<sub>2</sub> delivery system.

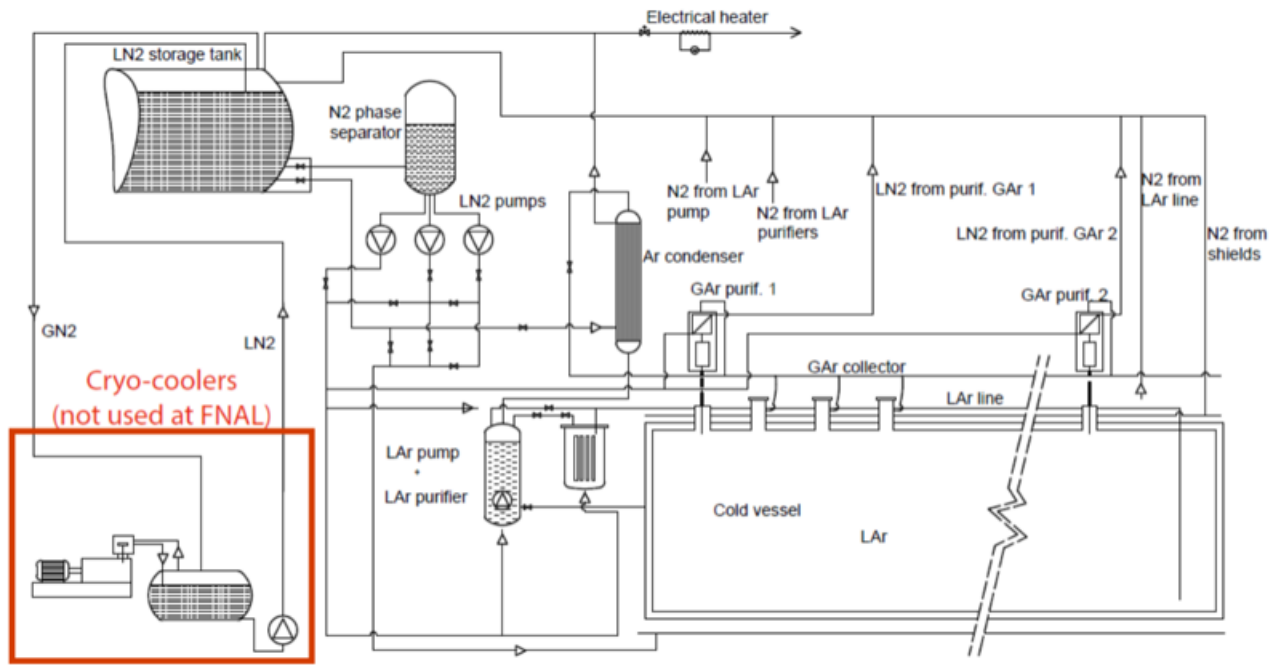


**FIG. 105:** Schematic diagram of the existing T600 cryogenic system, which will be maintained during the FNAL operations as well. The highlighted section in the lower left represents the old Stirling re-liquefaction units, which will be replaced by a new open-loop LN<sub>2</sub> delivery system.

The ICARUS-T600 detector is expected to be delivered to FNAL in the first half of 2017, with about 6 months needed for installation. Commissioning can take place during the second half of 2017. It will require from 3 to 5 months, based on the experience gained at LNGS. In Gran Sasso 5 months were needed, including about 3 of vacuum pumping. The consumption of LN<sub>2</sub> and LAr during this commissioning phase can be estimated, based on the fact that the total expected heat loss through the new insulation, as mentioned above, is of the order of 10 kW, and that larger cold power consumption during the first cooling down can be assumed. Approximately 100,000 liters of LN<sub>2</sub> should be needed for cooling down, along with 273,000 liters of LAr per module of the T600. Assuming present pricing for the cryogenic liquids, Tab. XIX can be constructed, summarizing the estimated costs of LN<sub>2</sub> and LAr for the commissioning phase.

Before closing this section, further drawings of the new cold vessels are reported, referring as an example to one of the endcaps of the vessel, exploded (Fig. 106), and to the whole exploded view (Fig. 107), respectively.



Material	Quantity (l)	Price(US\$)/liter	Total cost (US\$)
Liquid nitrogen	100,000	0.07	7,000
Liquid argon (per module)	273,000	1.5	409,500
<b>Total*</b>			<b>826,000</b>

**TABLE XIX:** Summary of costs of the commissioning phase, for what concerns usage of  $LN_2$  and  $LAr$  during cooling down. \*Note that Liquid argon cost is detailed for one module of the T600, while the grand total accounts for both modules ( $2 \times 409,500\$$ ).

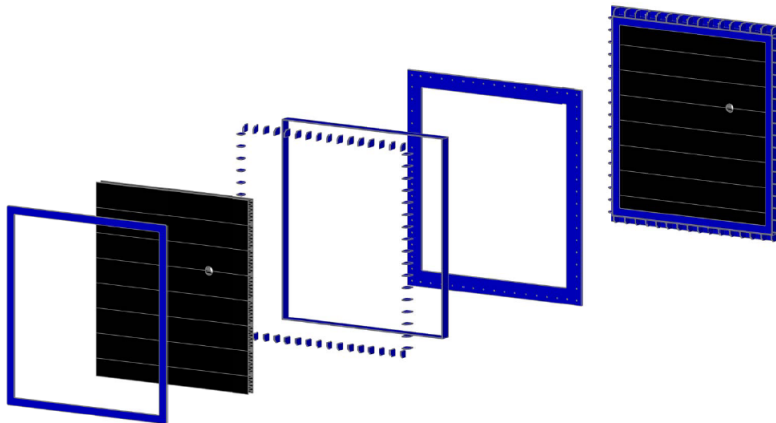


**FIG. 106:** Exploded detail of one of the endcaps of the new aluminum vessel. The hole corresponding to the  $LAr$  extraction line (for liquid recirculation) is visible.

## VI. Cosmic Ray Tagging System

As already mentioned in Sec. III, very effective new methods must be introduced to reduce the cosmic ray related signals [126]. For example, a segmented, fast anti-coincidence with  $4\pi$  coverage detector (Cosmic Ray Tagging System, CRTS), may record each charged particle crossing the outer boundaries of the  $LAr$  containers. At the nominal BNB intensity of  $5 \times 10^{12}$  pot/spill, only 1 neutrino CC interaction every 240 spills is expected to trigger the T600, with vertex in the  $LAr$ -TPCs. This rate has to be compared with the expected cosmic rays rate of 1 every 55 beam spills. The CRTS detector could be used to deplete by a significant factor the spurious cosmic ray induced interactions, by tagging events in the beam spill without any crossing cosmic ray. According to the expected time resolution of the PMT detection system and of the CRTS, a tagging window  $<100$  ns will reduce spurious coincidences generated by CRTS.

The positions and the timings of all random muon tracks crossing the walls of the CRTS during the T600 imaging window will be recorded. Each muon track reconstructed in the TPC may be then correctly determined by associating the charge image with the corresponding absolute drift time  $t_0$  coming both from the CRTS and from the internal light collection system, matching the track geometry with the CRTS recorded positions.

This would be achieved by means of a system which provides signals, independently from the

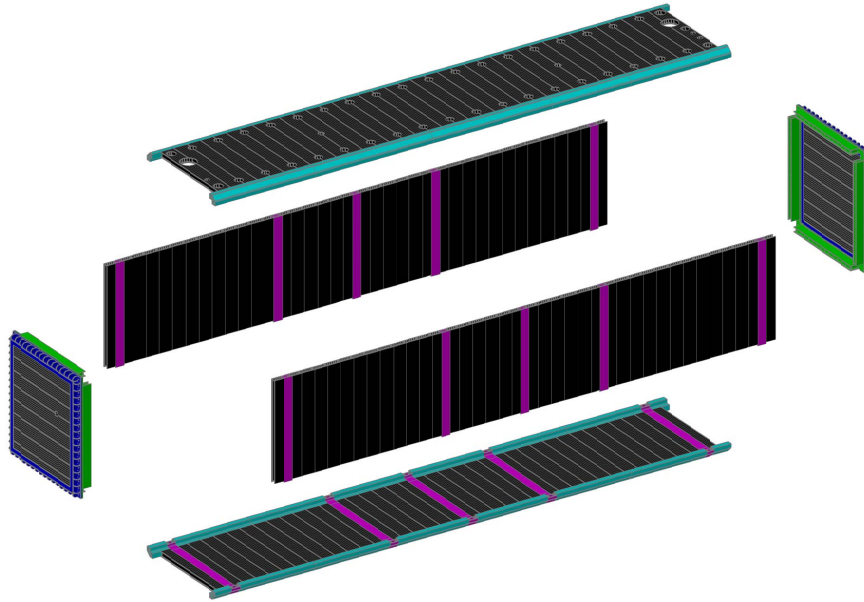


**FIG. 107:** *Exploded view of the whole cold vessel.*

LAr-TPC and the light collection system, that indicate the passage of charged particles through the surface of the LAr sensitive volume. These signals would be used as anti-coincidence to identify and recognize the interactions generated by external particles.

### A. CRTS efficiency

The performance of the CRTS system will depend both on the intrinsic efficiency of each CRTS detector unit and on the coverage of the adopted layout, which must approximate the ideal limit of a complete  $4\pi$  solid angle.

According to the overall size of the T600 cryostat, a shell made of particle detectors with a large surface area (order of  $1,000 \text{ m}^2$ ) will be required. The CRTS spatial granularity has to allow the unambiguous association between the reconstructed tracks in the TPC and the position where the cosmic rays cross the CRTS.

Since the TPC mixes drift time with space coordinates, a relation between the absolute time  $t_{true}$  and position  $y_{true}$  on the CRTS along the drift coordinate  $y$  is determined, as:

$$y_{true} = y_{img} + v_{drift} \cdot (t_{true} - t_0), \quad (11)$$

where  $y_{img}$  is the position on CRTS extrapolated by the recorded image on TPC,  $v_{drift}$  is the drift velocity and  $t_0$  is the absolute trigger time opening the acquisition window. Among all the possible pairs  $(t, y)_{CRTS}$  only the one satisfying Eq. 11 is considered to correctly tag the muon track crossing the CRTS. The other CRTS coordinates  $x$  and  $z$  are instead determined unambiguously.

The absolute time  $t_0$  is expected to be obtained from the PMT system, with resolution of the order of 1 ns, in order to exploit the bunch structure of the beam. Therefore, the time

resolution requested for the detectors comprising the CRTS must be at least of the same order of magnitude. As a consequence, the uncertainty in localizing the track in space, due to the mentioned time resolution, is not less than 30 cm.

These considerations must be taken into account, when choosing the detector technology to be employed for the CRTS and its geometrical segmentation, as discussed in the next section.

## B. CRTS layout

There are few well consolidated technologies to realize large-area detectors with high space and time resolution. Among these, the following may be taken into account: Resistive Plate Chambers (RPC) and plastic scintillator slabs coupled to PMTs or SiPMs. The RPCs allow building large panels (up to 3 m<sup>2</sup> of area) that can be easily arranged in large walls, but their implementation involves the use of gas mixtures and HV operation which may pose special safety issues.

A very promising detector technology, based on the use of LAr readout plates, has been proposed [126]. These plates, deployed directly inside the cryostats few centimeters away from its edges, could detect the presence of the dE/dx signals generated by the cosmic particles in the LAr with a relatively modest electric field ( $\sim 1$  kV/cm) added between the readout plates and the cryostat grounded walls. The performance of these detectors in terms of efficiency, rates, stability and noise must be carefully investigated.

The choice of the adopted detector solution must also take into account the size and shape of the T600 detector and its mechanical structure. As already discussed, the CRTS should completely surround the T600 volume, and for each side it is necessary to evaluate the most suitable technical solution, either internal or external.

The design of the top side of CRTS, which is interested by the largest amount of incoming cosmic particles flow, is certainly the most critical. Due to the presence of many dead spaces inside the TPCs, including flange feed-throughs, signal wire and HV cables, the deployment of such a detector inside the T600 will limit its effective geometrical coverage. It should be rather positioned at a suitable distance (about 3 m) from the T600 upper floor, conveniently above the readout electronics racks and the GAR recirculation units.

Similarly, vertical CRTS side walls could be more easily placed outside, positioned close to the cryostat walls, since the internal space behind the wire chambers is occupied by the PMTs, the slow control sensors and the TPC mechanical supports.

On the contrary, the bottom side CRTS detectors should be more conveniently placed into the LAr cryostat, due to the presence of the external mechanical supporting structure placed below it.

The presence of the electronics racks inside the CRTS envelope could prevent adopting a completely hermetic structure, to allow the necessary access to the TPC upper floor for maintenance and inspection purposes. For this reason, the CRTS top plane has to be kept separated from the CRTS vertical walls surrounding the T600, and the cooling system of the electronics must be carefully designed taking into account a reduced heat dissipation by natural convection.

For what concerns the future steps for a CRTS design finalization, first of all a detailed Monte Carlo simulations have to be carried out to study how to disentangle the genuine neutrino events from cosmogenic-induced backgrounds. The combined action of the CRTS and of the internal PMT system has to be studied in detail to define a possible analysis strategy for the neutrino event selection and reconstruction.

The probability of an autoveto signal by charged particles generated in the neutrino interactions and escaping the LAr-TPCs has to be carefully evaluated. According to results of a preliminary evaluation, considering the CTRS system installed inside the cryostats and surrounding the LAr volume,  $\sim 45\%$  of  $\nu_\mu$  CC and  $\sim 10\%$  of  $\nu_e$  events are expected to provide a signal. Alternatively  $\sim 10\%$  of  $\nu_\mu$  and few percent of  $\nu_e$  events are expected to give a signal in an external muon tagging system.

The T600 CTRS must be realized in a common framework with the LAr1-ND CTRS, being mandatory for the two detectors to adopt the same design of the cosmic ray detection efficiency with identical sensitivities and systematics.

**A Proposal for a Three Detector  
Short-Baseline Neutrino Oscillation Program  
in the Fermilab Booster Neutrino Beam**

---

*Part 4: Infrastructure and Civil Construction*

---

## I. Introduction

The Short Baseline Neutrino program is proposed to include three Liquid Argon Time Projection Chamber detectors (LAr-TPCs) located on-axis in the Booster Neutrino Beam (BNB) as shown in Figure 108. The near detector (LAr1-ND) will be located in a new building directly downstream of the existing SciBooNE enclosure 110 m from the BNB target as also shown in Figure 109 (right). The MicroBooNE detector, which is currently in the final stages of installation, is located in the Liquid Argon Test Facility (LArTF) at 470 m. The far detector (the existing ICARUS-T600) will be located in a new building, 600 m from the target between MiniBooNE and the  $\text{NO}\nu\text{A}$  near detector surface building as shown in Figure 109 (left).

The following sections address the new infrastructure required to support these detectors:

- cryostats for the near and far detectors,
- cryogenic systems for the near and far detectors,
- buildings for the near and far detectors, and
- common computing and software systems.

The infrastructure required for the the MicroBooNE detector is not described here since the detector installation will have been completed by early 2015. However, development of common computing and software systems for the SBN program can benefit significantly by the participation of MicroBooNE in the development and experience from the use of these tools on MicroBooNE data.

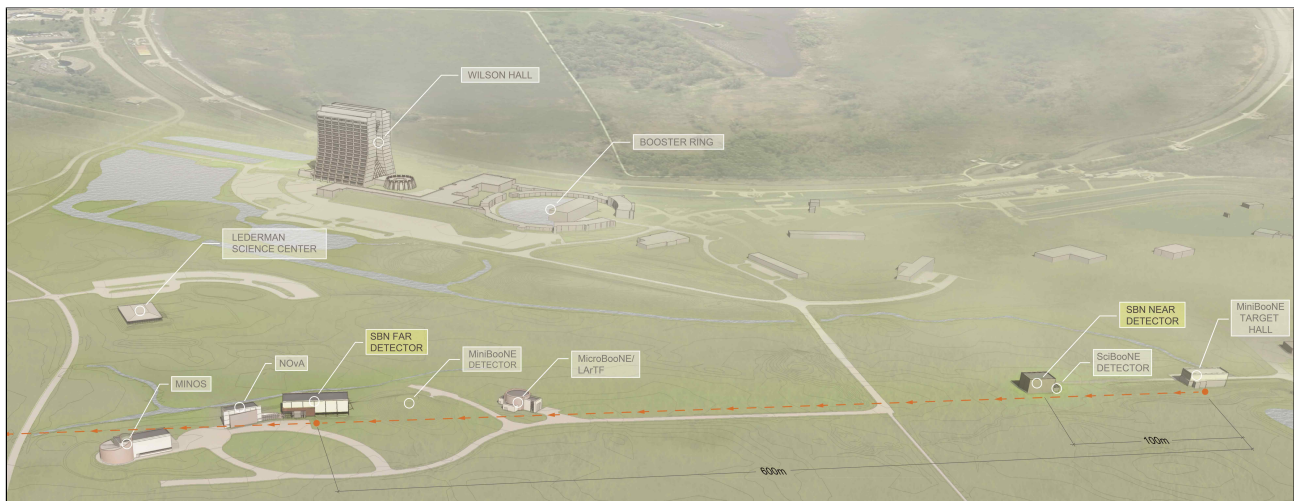


**FIG. 108:** Diagram of the Fermilab neutrino beamline area (looking east) showing the axis of the BNB (red dashed line) and approximate locations of the SBN detectors at 110 m, 470 m, and 600 m.

The detectors of the SBN program will need external detectors for tagging/vetoing cosmic ray muons as explained in Part 1 of this proposal. As described in Parts 2 and 3 the conceptual designs for cosmic taggers the near and far detectors are being developed. While these concepts were developed independently and described separately, it is likely that the realization of these systems will be managed as a joint project with a common underlying design. The Collaborations have made provisions in their funding requests for the necessary resources.

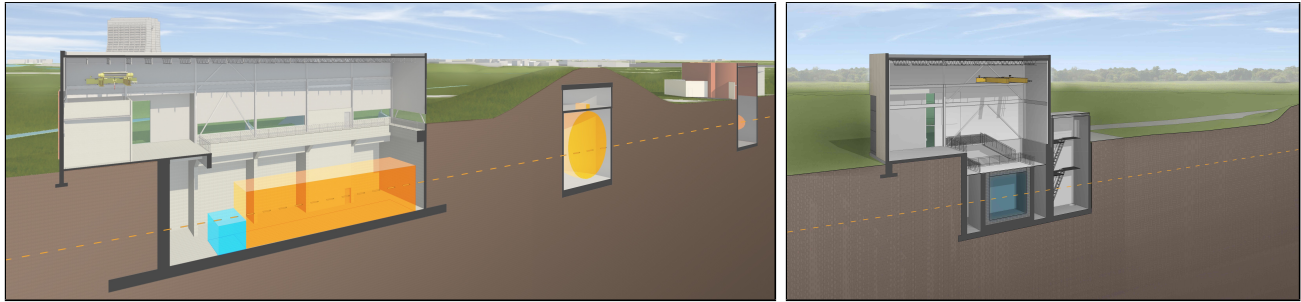


**FIG. 109:** *Cross-sectional views of a design concept for the far detector building (left) and near detector building (right). In the left view the existing enclosures for the MiniBooNE and MicroBooNE detectors are also seen.*

The SBN program provides an excellent opportunity for a collaborative effort on the design of LAr-TPC infrastructure between the recently formed LAr Cryogenic engineering groups at CERN and Fermilab along with engineering resources within INFN. These teams are also collaborating on developments for other short and mid-term projects leading to a long-baseline neutrino facility. The following two sections describe the cryostat and cryogenic needs for the near and far detectors.

## II. Cryostats

### A. Near Detector Cryostat

The near detector will use a membrane tank technology to contain the base design of 220 tons of LAr equivalent to about  $158 \text{ m}^3$ . The design is based on a scaled up version of the LBNE 35 Ton Prototype. The cryostat will be housed in a dedicated building next to the existing SciBooNE hall where the cryogenic system components will be located. The two buildings will be connected with an underground tunnel spanning about 9 feet. The cryostat will use a steel outer supporting structure with a metal liner inside to isolate the insulation volume. An alternative that was considered was a concrete supporting structure with vapor barrier and heating elements embedded in the concrete to control the temperature.

The scope of the Near Detector cryostat subsystem includes the design, procurement, fabrication, testing, delivery and oversight of a cryostat to contain the liquid argon and the TPC. This section describes a reference design, whose scope encompasses the following components:

- steel outer supporting structure,
- main body of the membrane cryostat (sides and floor),
- top cap of the membrane cryostat.

A membrane cryostat design commonly used for liquefied natural gas (LNG) storage and transportation will be used. In this vessel a stainless steel membrane contains the liquid cryogen. The pressure loading of the liquid cryogen is transmitted through rigid foam insulation to the surrounding outer support structure, which provides external support. The membrane is corrugated to provide strain relief resulting from temperature related expansion and contraction. The vessel is completed with a top cap that uses the same technology.

Two membrane cryostat vendors are known: GTT (Gaztransport & Technigaz) from France and IHI (Ishikawajima-Harima Heavy Industries) from Japan. Each one is technically capable of delivering a membrane cryostat that meets the design requirements for the Near Detector. To provide clarity, only one vendor is represented in this document, GTT; this is for informational purposes only. Figure 110 shows a 3D model of the GTT membrane and insulation design.

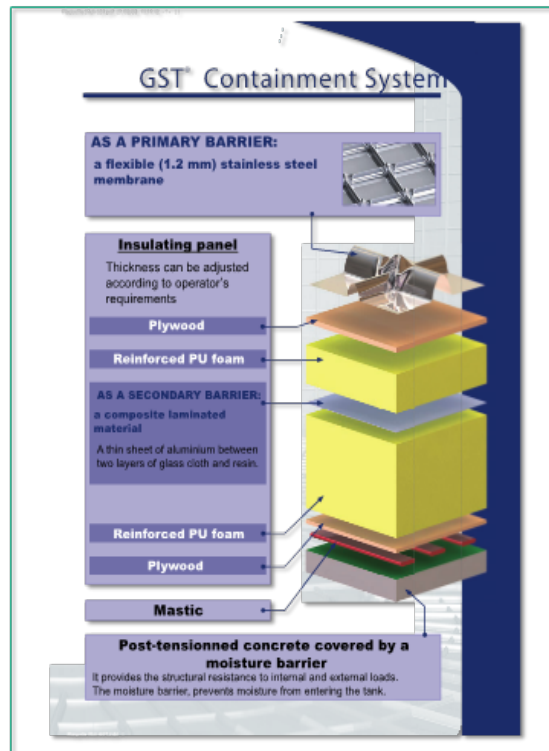


FIG. 110: Exploded view of the membrane cryostat technology.

### *Cryostat Design*

The conceptual reference design for the Near Detector cryostat is a rectangular vessel measuring 6.38 m in length (parallel to the beam direction), 5.17 m in width, and 4.80 m in height; containing a total mass of 220 tons of liquid argon. Figure 111 shows a 3D view of the Near Detector cryostat with a neck and two main plates constituting the top: plate A and plate B. Two cold penetrations are located on plate A; all the other penetrations are located on plate B. To minimize the contamination from warm surfaces, the liquid argon level touches the membrane underneath top plate A. The gas is all contained in the neck region underneath plate B. An alternative design is being considered with a single removable plate for the top. The TPC could be directly hung from underneath this top plate. In this case the gas ullage will all be contained over the liquid argon bath.



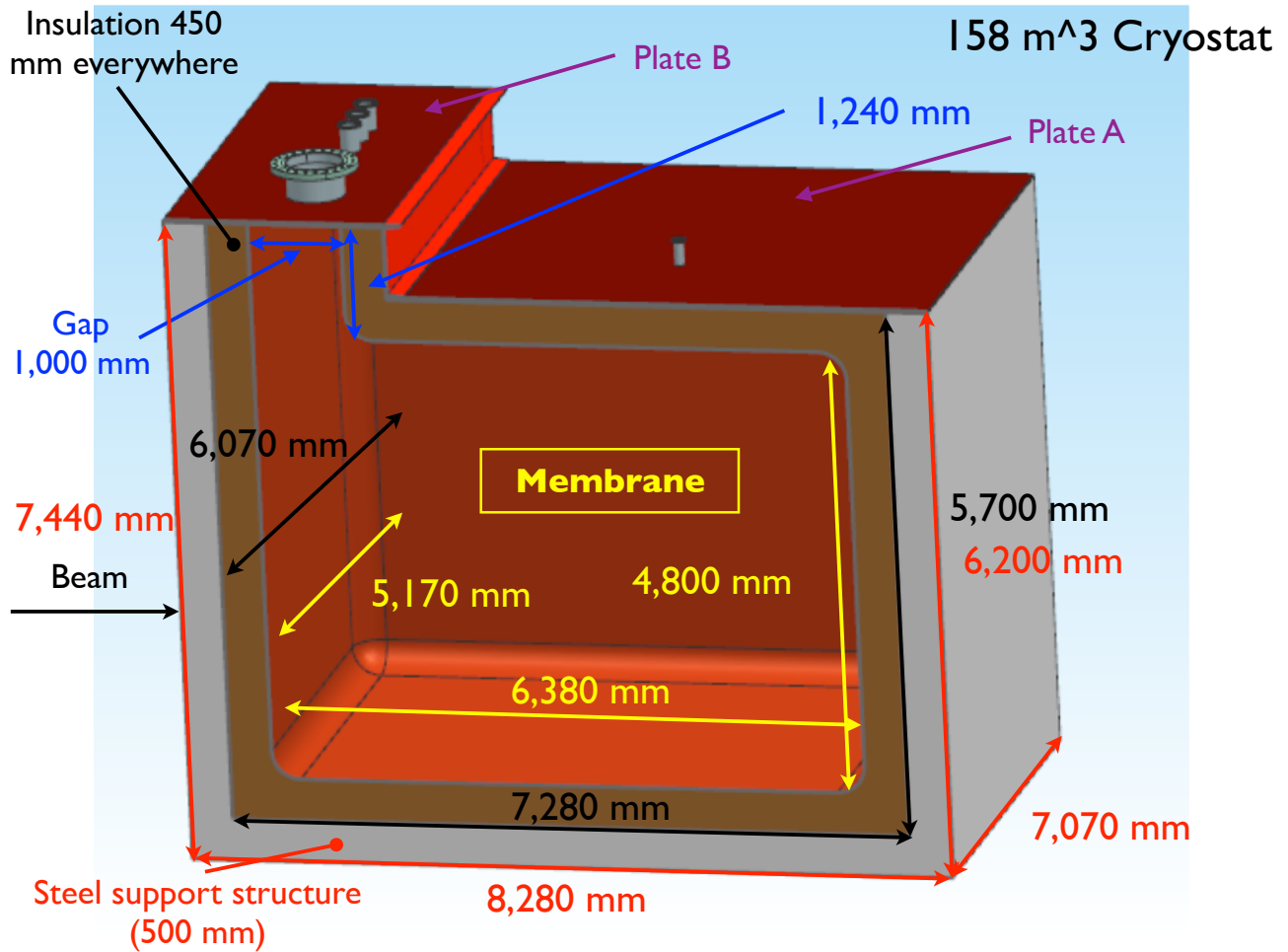


FIG. 111: A 3D view of the LAr1-ND cryostat using membrane technology.

#### Design parameters

This design is meant also to test technical solutions that may be of interest for the Long Baseline Neutrino program as well. The use of a cold ullage ( $< 100$  K) to lower the impurities in the gas region, and of a LAr pump outside the cryostat to minimize the effect of noise, vibration and microphonics to the TPC inside the LAr are Value Engineering studies for the Long Baseline program performed in synergy with the LBNF cryostat and cryogenics team.

The design parameters for the Near Detector cryostat are listed in Table XX.

#### Insulation system and secondary membrane

The membrane cryostat requires insulation applied to all internal surfaces of the outer support structure and roof in order to control the heat ingress and hence required refrigeration heat load. Choosing a reasonable, maximum insulation thickness of 0.45 m and given an average thermal conductivity coefficient for the insulation material of  $0.0283$  W/(m·K), the heat input

Design Parameter	Value
Total Cryostat volume	166 m <sup>3</sup>
Total LAr volume	158 m <sup>3</sup>
Liquid argon total mass	220,000 kg
Inner dimensions of the cryostat	6.38 m (L) x 5.17 m (W) x 4.80 m (H)
Depth of liquid argon	4.80 m (5% ullage all in the neck region)
Insulation	0.45 m Polyurethane foam
Primary membrane	1.2 mm thick SS 304L corrugated stainless steel
Secondary barrier system	0.07 mm thick aluminum between fiberglass cloth. Overall thickness is 1 mm located between insulation layers.
Outer support structure	Steel enclosure with metal liner to isolate the outside from the insulation space
Liquid argon temperature	88 ± 1°K
Operating gas pressure	Positive pressure. Nominally 70 mbar (~1psig)
Vacuum	No vacuum
Design pressure	350 mbar (~5 psig) + LAr head
Design temperature	77°K (liquid nitrogen temperature for flexibility)
Temperature of all surfaces in the ullage during operation	100°K
Minimize noise/vibration/microphonics inside cryostat	LAr pump preferably outside the cryostat
Leak tightness	1 × 10 <sup>-6</sup> mbar ℓ s <sup>-1</sup>
Heat leak	< 15 W/m <sup>2</sup>
Lifetime	10 years (5 years of run + 5 years of potential upgrade)
Thermal cycles	20 complete cycles (cool down and total warm up)

**TABLE XX:** *Design parameters for the Near Detector cryostat.*

from the surrounding steel is expected to be about 3 kW total. It assumes that plates A and B are both foam insulated. This is shown in Table XXI. The overall heat leak is then about 13 W/m<sup>2</sup>.

The insulation material is a solid reinforced polyurethane foam manufactured as composite panels. The panels get laid out in a grid with 3 cm gaps between them (that will be filled with fiberglass) and fixed onto anchor bolts anchored to the support structure. The composite panels contain the two layers of insulation with the secondary barrier in between. After positioning adjacent composite panels and filling the 3 cm gap, the secondary membrane is spliced together by epoxying an additional overlapping layer of secondary membrane over the joint. All seams are covered so that the secondary membrane is a continuous liner.

The secondary membrane is comprised of a thin aluminum sheet and fiberglass cloth. The fiberglass-aluminum-fiberglass composite is very durable and flexible with an overall thickness of about 1 mm. The secondary membrane is placed within the insulation space. It surrounds the bottom and sides. In the unlikely event of an internal leak from the primary membrane of the cryostat into the insulation space, it will prevent the liquid cryogen from migrating all the way through to the steel support structure where it would degrade the insulation thermal

performance and could possibly cause excessive thermal stress in the support structure. The liquid cryogen, in case of leakage through the inner (primary) membrane will escape to the insulation volume, which is purged with GAr at the rate of one volume exchange per day.

Element	Area (m <sup>2</sup> )	k (W/m·K)	$\Delta T$ (K)	Heat Input (W)
Base	38	0.0283	205	495
End Walls	75	0.0283	205	973
Side Walls	77	0.0283	205	987
Roof	38	0.0283	205	495
Total				2,945

**TABLE XXI:** Heat load calculation for the near detector cryostat (insulation thickness = 0.45 m for all)

#### *Cryostat Configuration*

This section describes the configuration of the cryostat only. The TPC is described in Part II, the LAr1-ND CDR. With the intent to minimize the contamination in the gas region, the ullage will be kept cold ( $< 100$  K). A possible way to achieve this requirement is to spray a mist of clean liquid and gaseous argon to the metal surfaces in the ullage and keep them cold, similar to the strategy that was developed for the cool down of the LBNE 35 Ton prototype.

#### *Outer Support Structure*

Two types of outer support structures have been evaluated: steel and concrete. With the current cryostat dimensions, the two are similar in cost, but the steel one presents some advantages. The current reference design is a steel support structure with a metal liner on the inside to isolate the insulation region and keep the moisture out. This choice allows natural and forced ventilation to maintain the temperature of the steel within acceptable limits, without the need of heating elements and temperature sensors, otherwise embedded within the concrete. It reduces the time needed for the construction: the structure will be prefabricated in pieces of dimensions appropriate for transportation, shipped to the destination and only assembled in place. Fabrication will take place at the vendors facility for the most part. This shortens the construction of the outer structure on the detector site, leaving more time for completion of the building infrastructure. If properly designed, a steel structure may allow the cryostat to be moved, should that be desired later in the future.

#### *Main body of the membrane cryostat*

The sides and bottom of the vessel constitute the main body of the membrane cryostat. They consist of several layers. From the inside to the outside the layers are stainless steel primary membrane, insulation, thin aluminum secondary membrane, more insulation, metal vapor barrier, and steel outer support structure. The secondary membrane contains the LAr in case of any primary membrane leaks and the vapor barrier prevents water ingress into the

insulation. The main body does not have side openings for construction. The access is only from the top. There is a side penetration for the liquid argon pump for the purification of the cryogen.

### *Top cap*

In the current reference design two plates constitute the top cap: plate A and plate B. The stainless steel primary membrane, intermediate insulation layers and vapor barrier continue across the top of the detector, providing a leak tight seal. The secondary barrier is not used nor required at the top. The cryostat roof is a removable steel truss structure that bridges the detector. Stiffened steel plates are welded to the underside of the truss to form a flat vapor barrier surface onto which the roof insulation attaches directly. Depending on the number and size of the penetrations, Plate B may be the primary container for the gaseous argon itself. In that case there will be radiation shields only and no membrane underneath instead of the same polyurethane and membrane configuration as plate A. The truss structure rests on the top of the supporting structure where a positive structural connection between the two is made to resist the upward force caused by the slightly pressurized argon in the ullage space. The hydrostatic load of the LAr in the cryostat is carried by the floor and the sidewalls. Everything else within the cryostat (TPC planes, electronics, sensors, cryogenic and gas plumbing connections) is supported by the steel plates under the truss structure. All piping and electrical penetration into the interior of the cryostat are made through this top plate, primarily through Plate B to minimize the potential for leaks. Studs are welded to the underside of plate A to bolt the insulation panels. Insulation plugs are inserted into the bolt-access holes after panels are mounted. The primary membrane panels are first tack-welded then fully welded to complete the inner cryostat volume.

Table [XXII](#) presents the list of the design parameters for the top of the cryostat.

### *Cryostat grounding and isolation requirements*

The cryostat has to be grounded and electrically isolated from the building. Table [XXIII](#) presents the list of the current grounding and isolation requirements for the cryostat. Figure [112](#) shows the layout of the top plate grounding.

### *Leak prevention*

The primary membrane will be subjected to several leak tests and weld remediation, as necessary. All (100%) of the welds will be tested by an Ammonia colorimetric leak test (ASTM E1066-95) in which welds are painted with a reactive yellow paint before injecting a Nitrogen-Ammonia mixture into the insulation space of the tank. Wherever the paint turns purple or blue, a leak is present. The developer is removed, the weld fixed and the test is performed another time. Any and all leaks will be repaired. The test lasts a minimum of 20 hours and is sensitive enough to detect defects down to 0.003 mm in size and to a  $10^{-7}$  std-cm<sup>3</sup>/s leak rate (equivalent leak rate at standard pressure and temperature, 1 bar and 273 K). To prevent infiltration of water vapor or oxygen through microscopic membrane leaks (below detection level) the insulation spaces will be continuously purged with gaseous argon to provide one volume exchange per day. The insulation space will be maintained at 30 mbar, slightly above

Design Parameter	Requirement
Configuration	Removable metal plate reinforced with trusses anchored to the membrane cryostat support structure. Contains multiple penetrations of various sizes and a manhole. Number, location and size of the penetrations TBD. Provisions shall be made to allow for removal and re-welding six (6) times.
Plate/Trusses non-wet material	Steel if room temperature. SS 304/304L or equivalent if at cryogenic temperature.
Wet Material	SS 304/304L, 316/316L or equivalent.
Fluid	Liquid argon (LAr)
Design Pressure	5.0 psig ( $\sim 350$ mbar)
Design Temperature	77 K (liquid nitrogen temperature for flexibility)
Inner Dimensions	To match the cryostat
Maximum allowable roof deflection	0.018 m
Maximum static heat leak	$< 20$ W/m <sup>2</sup>
Temperatures of all surfaces in the ullage during operation	$< 100$ K
Additional design loads	Top self-weight TPC ( $\sim 2,300$ kg total, to be distributed over all anchors) TPC anchors (TBD) Live load (488 kg/m <sup>2</sup> ) Electronics racks (400 kg in the vicinity of the feedthroughs) Services (150 kg on every feed through)
TPC anchors	Capacity: to be determined by the number of anchors (1,000 kg each anchor, if six). Number and location TBD. Minimum 6.
Grounding plate	1.6 mm thick copper sheet brazed to the bottom of the top plate
Lifting fixtures	Appropriate for positioning the top at the different parts that constitute it.
Cold penetrations	Minimum 2. Location and design TBD.
Lifetime	10 years (5 years of run + 5 years of potential upgrade)
Thermal cycles	20 complete cycles (cool down and total warm up)

**TABLE XXII:** *Near detector cryostat top requirements*

atmospheric pressure. This space will be monitored for changes that might indicate a leak from the primary membrane. Pressure control devices and safety relief valves will be installed on the insulation space to ensure that the pressure does not exceed the operating pressure inside the tank. The purge gas will be recirculated by a blower, purified, and reused as purge gas. The purge system is not safety-critical; an outage of the purge blower would have negligible impact on LAr purity.

Parameter	Requirement
Isolation	1) The cryostat membrane and any supporting structure, whether it is a steel structure or a concrete and rebar pour, shall be isolated from any building metal or building rebar with a DC impedance greater than 300 k $\Omega$ . 2) The outer support structure shall be electrically isolated from the building. 3) All conductive piping penetrations through the cryostat shall have dielectric breaks prior to entering the cryostat and the top plate.
Grounding	1) The cryostat, or detector ground, shall be separated from the building ground. 2) A safety ground network consisting of saturated inductors shall be used between detector ground and building ground. 3) Parameters TBD.
Top Plate Grounding	1) The top plate shall be electrically connected to the outer support structure. Parameters TBD. 2) The top grounding plate shall be electrically connected to the cryostat membrane by means of copper braid connections. <ol style="list-style-type: none"> <li>a) Each connection shall be at least 1.6 mm thick and 63.5 mm wide.</li> <li>b) The length of each connection is required to be as short as possible.</li> <li>c) The distance between one connection and the next one shall be no more than 1.25 m.</li> <li>d) The layout can follow the profile of several pieces of insulation, but it shall be continuous.</li> <li>e) The DC impedance of the membrane to the top plate shall be less than 1 <math>\Omega</math>.</li> </ol>

**TABLE XXIII:** *Near detector cryostat grounding and isolation requirements.*

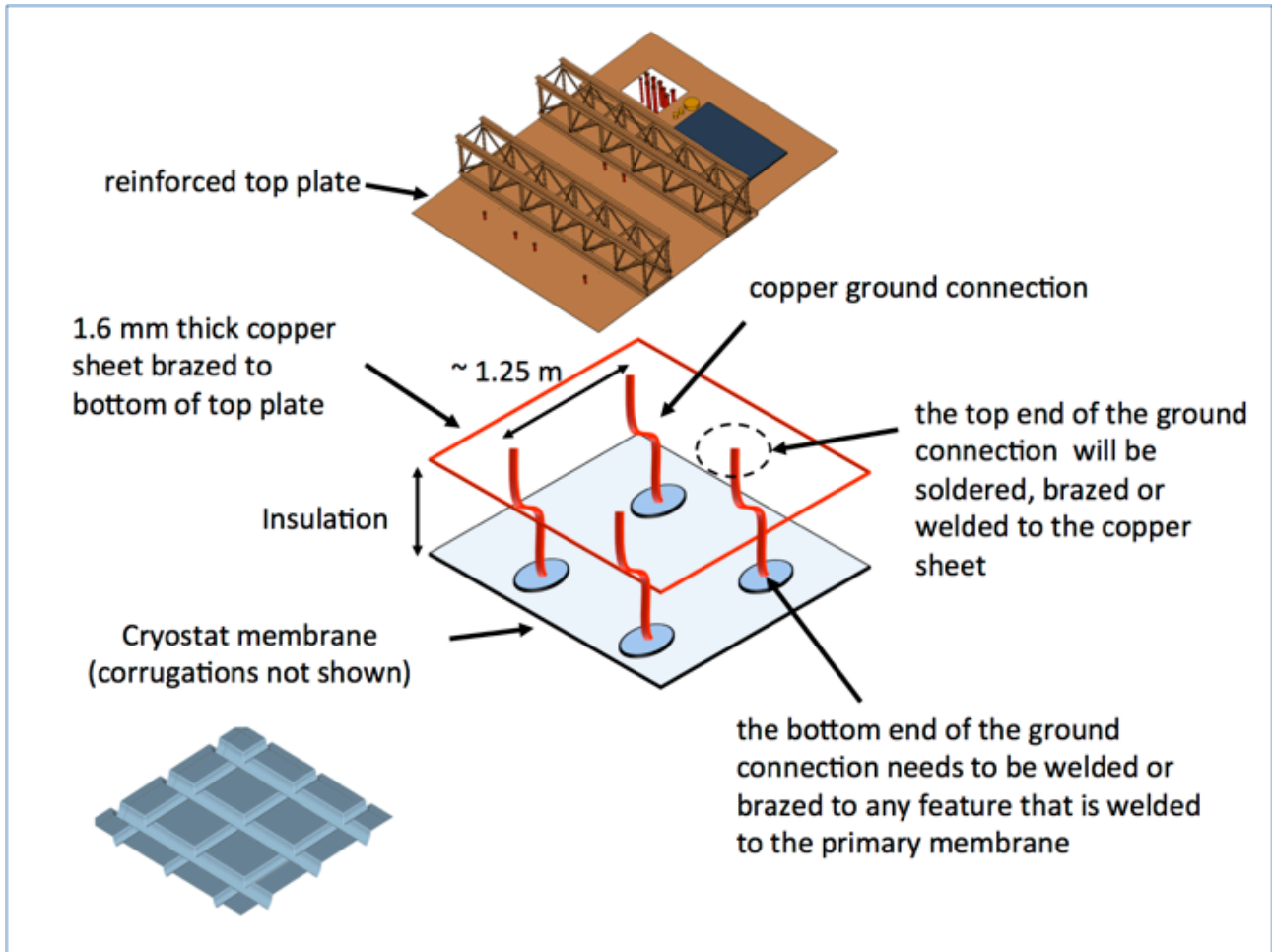
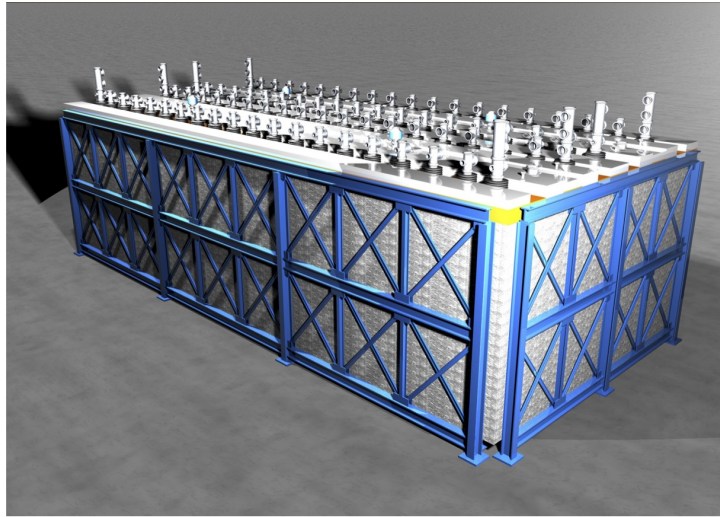


FIG. 112: Top plate grounding layout for the near detector cryostat.

## B. Far Detector Cryostat

The features of the Far Detector new cryostats and insulation were already described in Part III Section V D. In the following, only a brief summary of the specifications is reported.

New cryostats using a passive polyurethane foam insulation, similar to that used for the membrane cryostat of the near detector, have been designed to house the refurbished T600 detector as shown in Figure 113. The inner cryostats will consist of Aluminum vessels constructed from welded extruded profiles designed by a collaboration between industries and Milano Politecnico (Italy). The vessels are required to be super clean, vacuum-tight and to stand a 1.5 bar maximal operating internal over-pressure. Figure 114 shows a 3D model of the vessel assembly.



**FIG. 113:** A 3D model of the T600 detector in new cryostat consisting of new Aluminum inner vessels, polyurethane insulation and outer cryostat.

The inner cryostats will be enclosed in a passive polyurethane foam insulation developed by GTT, similar to that used for the membrane cryostat of the Near Detector, as shown in Figure 115. The foam insulation will be contained in a new outer frame and coupled to boiling-LN<sub>2</sub> cooling shields, used for heat interception. Expected heat loss through the insulation is estimated at approximately 6.6 kW.

Although not described in detail here, the grounding and isolation for the far detector cryostat will need to be handled with the same care as described above for the near detector. The grounding and isolation for the T600 will abide by all Fermilab safety standards.



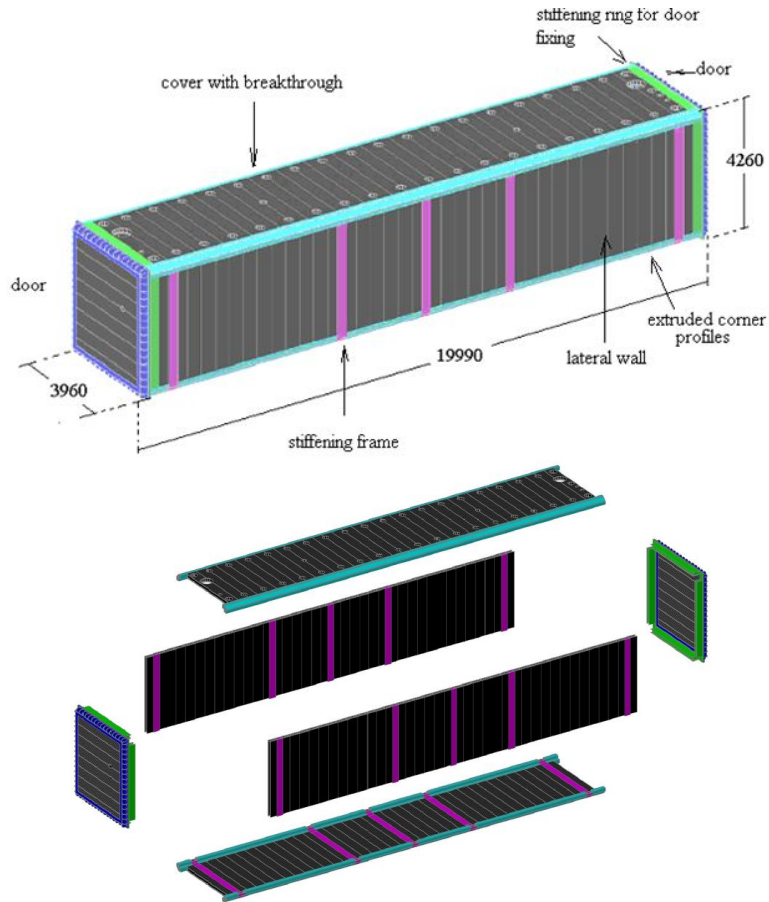


FIG. 114: 3D model of the proposed new Aluminum vessels for the T600 far detector.

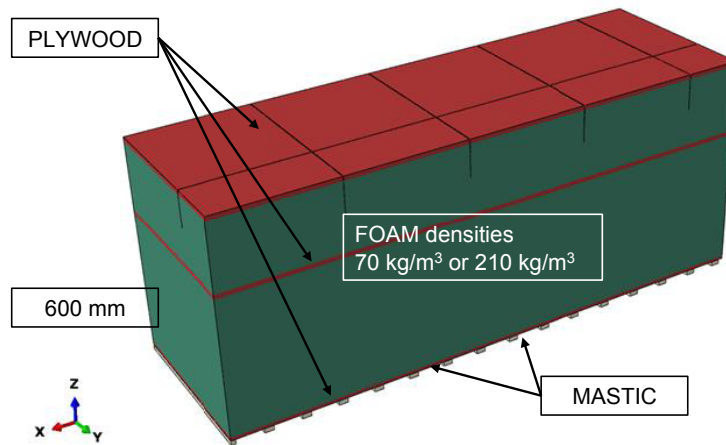


FIG. 115: A 3D model of the insulation for proposed new T600 cryostat. A 600 mm thick element is displayed

### III. Cryogenic Systems

The near and far detector cryogenic designs are being developed with a focus on commonalities which can be used across both detectors and also as a stepping stone for LBNF collaborative efforts. These systems will be modular in design and constructed on skids that can be tested separately prior to delivery to Fermilab for installation. Figure 116 outlines the basic LN<sub>2</sub> supply system which is proposed by CERN and agreed as an appropriate solution for both detectors. Each experiment will rely on LN<sub>2</sub> tankers for regular deliveries to local dewar storage. Storage dewars will be sized to provide several days of cooling capacity in the event of a delivery interruption. Note that for the far detector, the original Stirling machines used at Gran Sasso will not be used in the LN<sub>2</sub> cycle. The lower estimated heat leak of the newly designed vessels allows for use of an open loop system typical of other LAr-TPC vessels operated at Fermilab (LAPD, LBNE 35 Ton proto., and MicroBooNE).

Figure 117 shows a schematic diagram of the proposed LAr1-ND liquid argon system. It is based on experience in the design of the LBNE 35 ton prototype and the MicroBooNE detector systems.

Preliminary discussions on the requirements and development of the T600 cryogenic system are ongoing. These discussions include the purification system, best re-condensation strategy, and ullage conditions. It is not expected that these aspects will change significantly from previous experience, where the systems performed well enabling the experiment to achieve very high levels of Argon purity with electron lifetime exceeding 15 ms. A description of the existing T600 cryogenic and purification systems can be found in [9] and the latest results on Argon purity are detailed in [121].

The existing cryogenic system on the ICARUS-T600 detector is therefore meant to be kept as is, apart from the implementation of the open-loop LN<sub>2</sub> delivery system. Figure 118 shows a schematic diagram of the T600 argon system including the existing LN<sub>2</sub> refrigerators. These refrigerators would be replaced by a system like that shown in Figure 116 (bottom).

The responsibility for the design and construction of the cryogenic systems will be shared between CERN and Fermilab, along with INFN, by Liquid Argon Cryogenics groups that have been formed at each laboratory. A preliminary division of the responsibilities by deliverable is outlined in Table XXIV. The schedule for the development of the ND/FD cryogenic systems, cryostats, and detectors is described in Part VI of the proposal.

LAr/GAr System	Service Type	Responsible
LAr Receiving Facility	Cryo	FNAL
LAr/GAr Transfer Lines	Cryo/Non Cryo	FNAL
GAr/H2 Supply and Transfer Lines	Non Cryo	FNAL
GAr Filtration	Non Cryo	shared
GAr Analyzers	Non Cryo	shared
Condenser	Cryo	shared
LAr handling and purification System	Cryo	shared
Inside piping	Cryo/Non Cryo	shared
GAr handling system	Non Cryo	shared
LN2 System	Service Type	Responsible
LN2 Receiving Facility	Cryo	FNAL
LN2 Transfer Lines	Cryo	FNAL
GN2 returns	Non Cryo	INFN/CERN
LN2/GN2 handling system	Cryo/Non Cryo	INFN/CERN
LN2 Distribution Facility	Cryo	INFN/CERN
LN2 Pumping Station	Cryo	INFN/CERN
Services	Cryo	shared
Ancillary Items	Service Type	Responsible
Process Controls	Non Cryo	FNAL
Design/Drafting	Non Cryo	shared
Smart P&IDs	Cryo/Non Cryo	shared
Safety aspects of cryogenic installation at Fermilab	Cryo	FNAL

**TABLE XXIV:** Draft proposal for CERN, FNAL and INFN responsibilities, for what concerns the management of the cryogenic system maintenance and on-site logistics. The keyword 'shared' refers to tasks to be undertaken jointly by all groups.

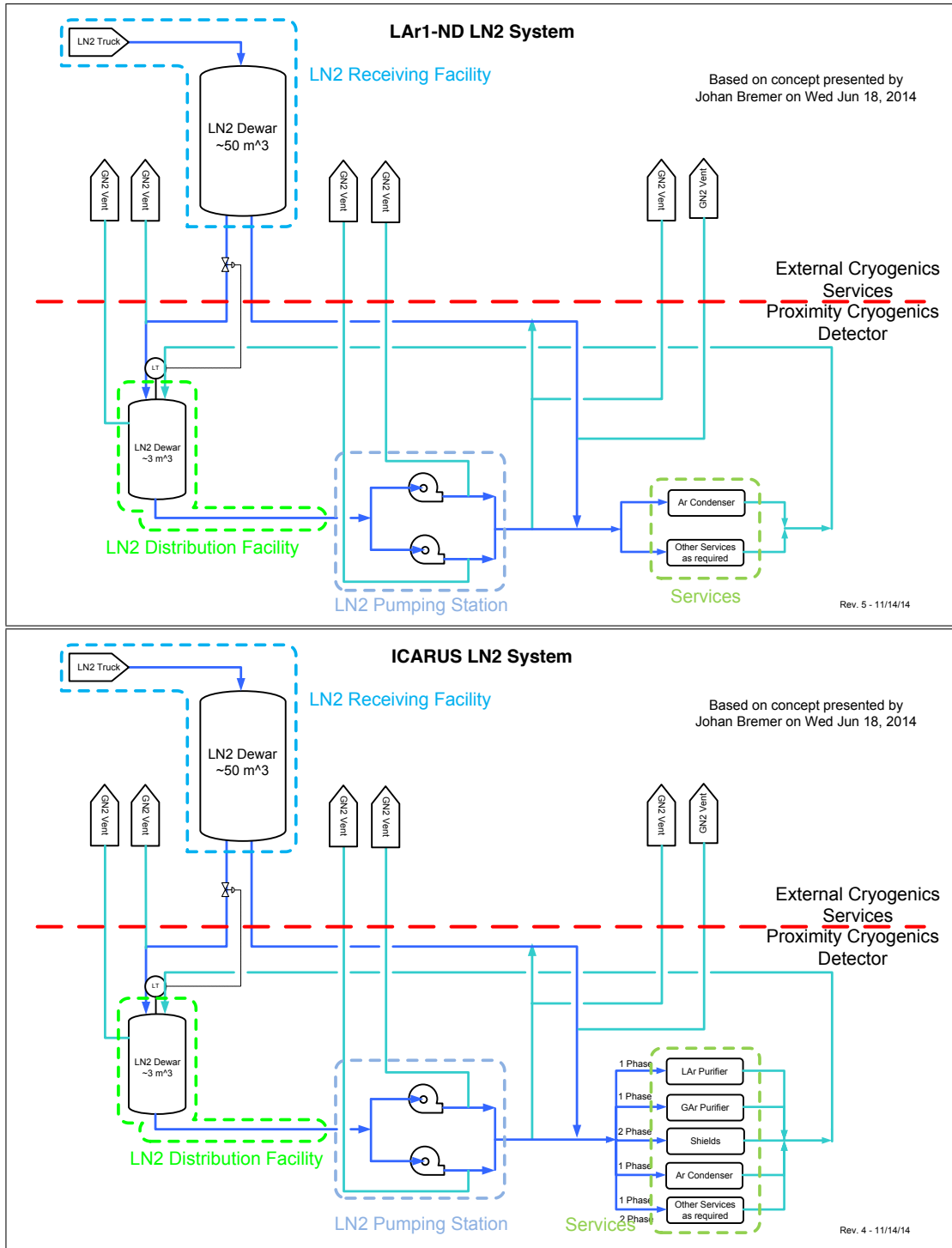


FIG. 116: Schematic diagrams for the proposed  $LN_2$  systems for LAr1-ND (top) and T600 (bottom) detectors.

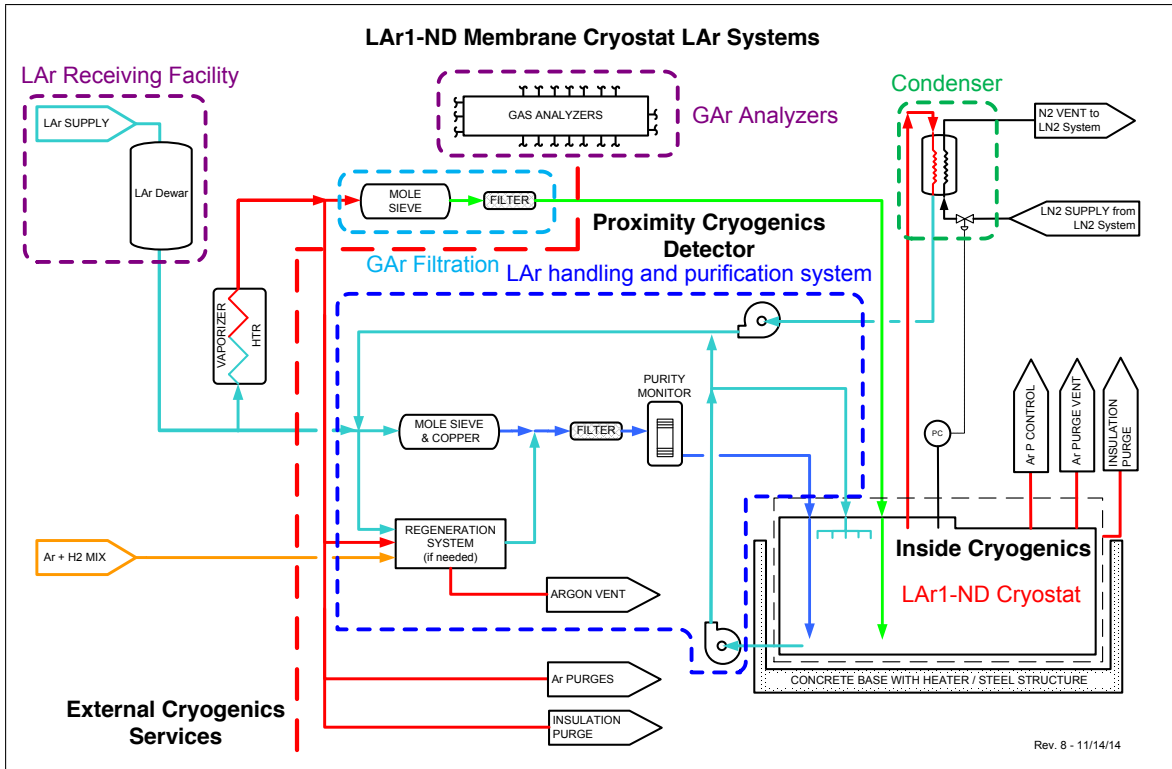


FIG. 117: Schematic diagram for the proposed LAr1-ND liquid argon systems.

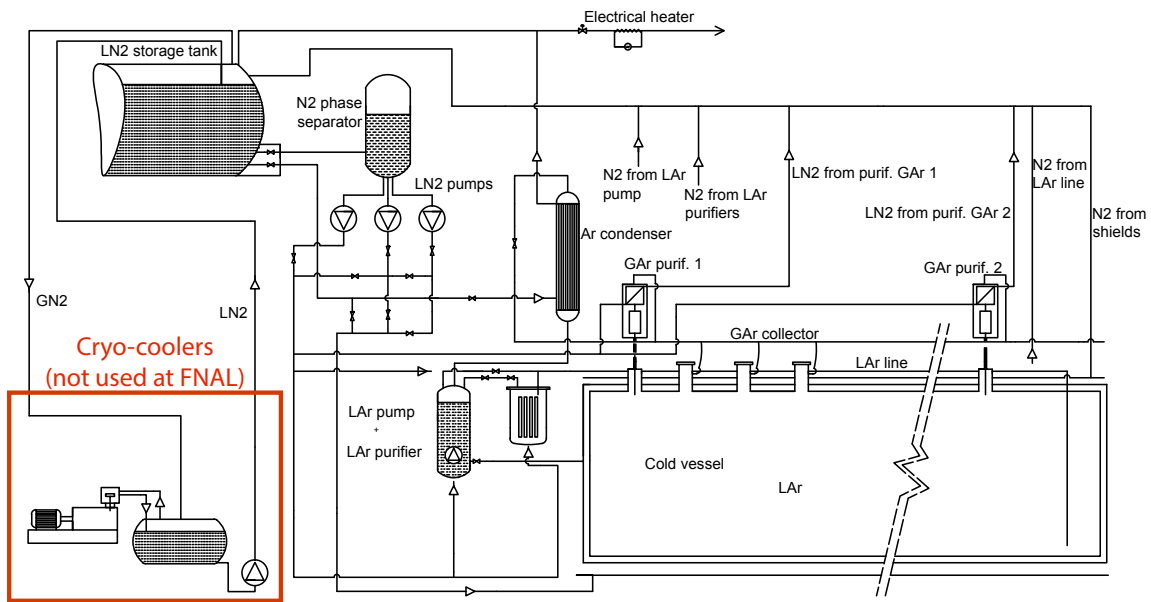


FIG. 118: Schematic diagram of T600 cryogenic system. The section in the lower left would be replaced by the new liquid nitrogen delivery system show in Figure 116.

#### IV. Requirements for Near and Far Detector Buildings

We present preliminary lists of requirements for the far and near detector buildings for support of the cryostats, cryogenics and detector systems. These are shown for example only, the complete list of requirements are contained in separate documents maintained by the Fermilab Engineering Support Services personnel responsible for the building design.

The following is a list of required infrastructure for the cryostat and TPC installation in the near detector building:

- minimum free area around perimeter of cryostat of 0.92 m (per FESHM);
- lay down space equivalent to one cryostat footprint for assembly staging;
- a crane with capacity of 5 ton for cryostat assembly and TPC installation, higher capacity may be needed if TPC is installed with the cryostat top;
- full crane coverage over the cryostat and lay down space;
- minimum hook height above the cryostat 5.75 m (6.0 m if top cap installed with TPC already mounted). Detailed requirements for power and cooling are under development.

The following is a list of key infrastructure requirements to support the installation and operation of the T600 detector in the far detector building:

- a crane with 5/10 ton capacity;
- 300 kW power is needed, to be divided among read-out electronics and cryogenic plant. This evaluation does not include general services as light, ventilation, heating. An UPS will be needed for control and monitoring systems;
- a closed-circuit water cooling system, with flow rate of 5 m<sup>3</sup>/h, and a pressure/temperature drop of 1.5 bar and 10°C, respectively;
- for safety, separation walls to surround the T600 and cryogenic areas (minimum height 3-4 m), safety sensors (oxygen, smoke, temperature), emergency light, audio alarms;
- for other general services, as no specific requests are needed, the FNAL Standards and Rules will apply, as in the case of Safety Ventilation: two flow rates systems are foreseen, one always running, the other to be started in case of emergency (e.g.: low Oxygen).

For both the near and far detector buildings, the requirement to place concrete blocks for the required overburden will most likely set a higher requirement for the crane capacity.

#### V. Near Detector Siting and Construction

The location of the near detector building is approximately 110 meters from the existing BNB target located in the MI-12 Building. The new building incorporates conventional facilities to provide the spatial and infrastructure requirements needed to install and operate the components that comprise the near detector. Figure 119 shows a concept for the near detector building in cross section. In general, the construction will consist of a 1,300 square foot (120 m<sup>2</sup>), below-grade enclosure centered on the existing Booster Neutrino Beam that will house

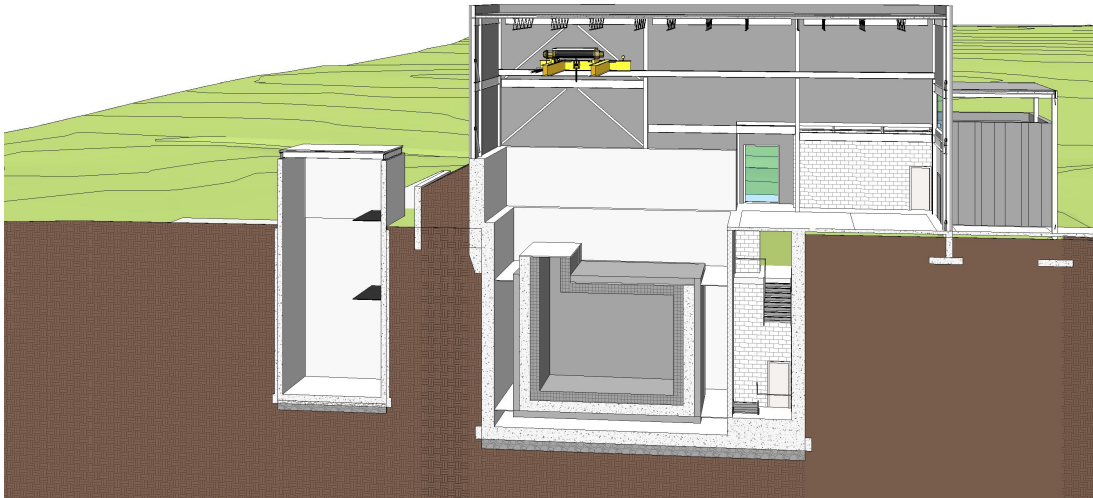


**FIG. 119:** *Cross-sectional view of a design concept for the building that will house the near detector below-grade. The design includes a surface building. The existing SciBooNE enclosure to the left will be used for the cryogenic system. The beam enters from the left in this view.*

the LAr-TPC and related electronics while the 2,300 square foot (215 m<sup>2</sup>) above-grade portion will provide a means for staging and installing the detector components as well as personnel access. The site work will include utility extensions from MI-12, cryogenic storage tanks, gravel staging areas and vehicle access to the near detector building. Figure 120 shows an aerial view of the building with the SciBooNE and MI-12 target buildings to the left.

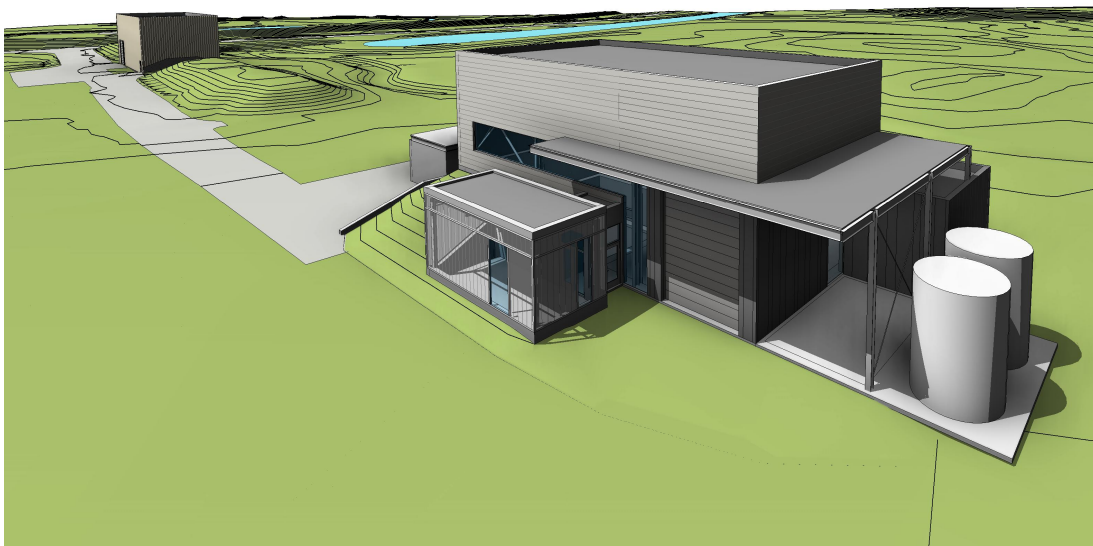


**FIG. 120:** *Aerial view of design concept of the near detector building.*

This near detector location, north of the existing SciBooNE Detector Enclosure allows the existing SciBooNE enclosure to be re-purposed to provide support space for the cryogenic equipment required to operate the detector. The SciBooNE enclosure can be seen on the left in Figure 119. An alternate solution with the cryogenic equipment located on the surface is under study.

The lower level of the near detector building will house the 220 ton near detector. The detector will be located to align slightly off center horizontally (to the east) of the existing Booster Neutrino Beam, placing the floor of the lower level at elevation 713 feet (217.3 m), or approximately 30 feet (9.1 m) below existing grade. The floor plan of the lower level includes access around the near detector and a stairway to grade. The stairs to grade will include a landing at the top of the detector to provide access to the cryostat and supporting equipment. An opening will be cut into the existing SciBooNE Detector Enclosure at the lower level to allow piping and communication access between the two spaces. The below grade walls and floors will be constructed of cast-in-place concrete and will include a groundwater underdrain system connected to the existing SciBooNE Detector Enclosure sump pump.

The upper level of the near detector building will provide unloading/loading, staging and support space for the construction, assembly and operation of the near detector. The structure will be designed to accommodate a 5 ton capacity overhead bridge crane to unload and transport detector components from the grade level loading dock to the below grade detector enclosure. While not installed initially, the structure will be designed to accommodate the installation of up to 9.84 feet (3 meters) of removable precast shield blocks over the detector. This shielding can be added after detector installation if needed to reduce cosmogenic backgrounds. The surface building will be a steel framed, metal sided building with a cast-in-place concrete foundation.

## VI. Far Detector Siting and Construction

The new far detector building incorporates the conventional facilities to provide the spatial and infrastructure required to assemble, install, and operate the physics components that comprise the T600 far detector. The location of the far detector building is approximately 600 meters from the existing BNB target just downstream of the existing MiniBooNE experiment building. In general, the construction will consist of a 7,100 square foot (660 m<sup>2</sup>) below-grade enclosure housing the relocated T600 detector as well as related electronics while the 4,000 square foot (370 m<sup>2</sup>) above-grade portion will provide a means for staging and installing the detector components as well as personnel access. Figure 121 shows a cross-section view the design concept for the far detector building at the early stages of final design. Figure 122 shows an aerial view of the building with the MiniBooNE hill visible to the right.

The site work for the far detector building will include utility extensions from existing utility corridors, storage tanks, gravel staging areas, and vehicle access to the far detector building.

The lower level of the far detector building is sized to house the T600 detector. The detector will be located to align both horizontally and vertically with the existing BNB, placing the floor of the lower level at elevation 713 feet (217.4 m), or 32 feet (9.7 m) below existing grade. The floor plan of the lower level includes code required access space around the detector as well as space to the north end of the detector for detector support equipment. Surrounding the detector enclosure are several alcoves that will house electronics and support equipment required for detector operations.

The structure will be designed to accommodate a 10 ton capacity overhead bridge crane to unload and transport detector components from the grade level loading dock to the below



grade detector enclosure. The lower level of the building will be designed to accommodate up to 9.84 feet (3 meters) of earth equivalent shielding over the below grade detector enclosure if this is found to be needed to reduce cosmogenic backgrounds. Prior to the installation of the concrete shield blocks, the lower level will be open to the crane bay above. Once the shielding blocks are in place and crane access is not available, a 5,000 pound (2,200 kg) capacity material hoist will be used to transport equipment between the upper and lower levels. The lower level will include two (2) code-compliant exit stairs to grade as well as a duplex underdrain system which will collect groundwater.

The upper level of the far detector building will provide unloading/loading, staging and support space for the construction, assembly and operation of the far detector in addition to the mechanical, electrical and toilet facilities required to operate the building. The surface building will be a steel framed, metal sided building with a cast-in-place concrete foundation. The building will have exposed finishes.

The SBN Far Detector Building will be designed to allow the detector to be installed through removable roof sections.

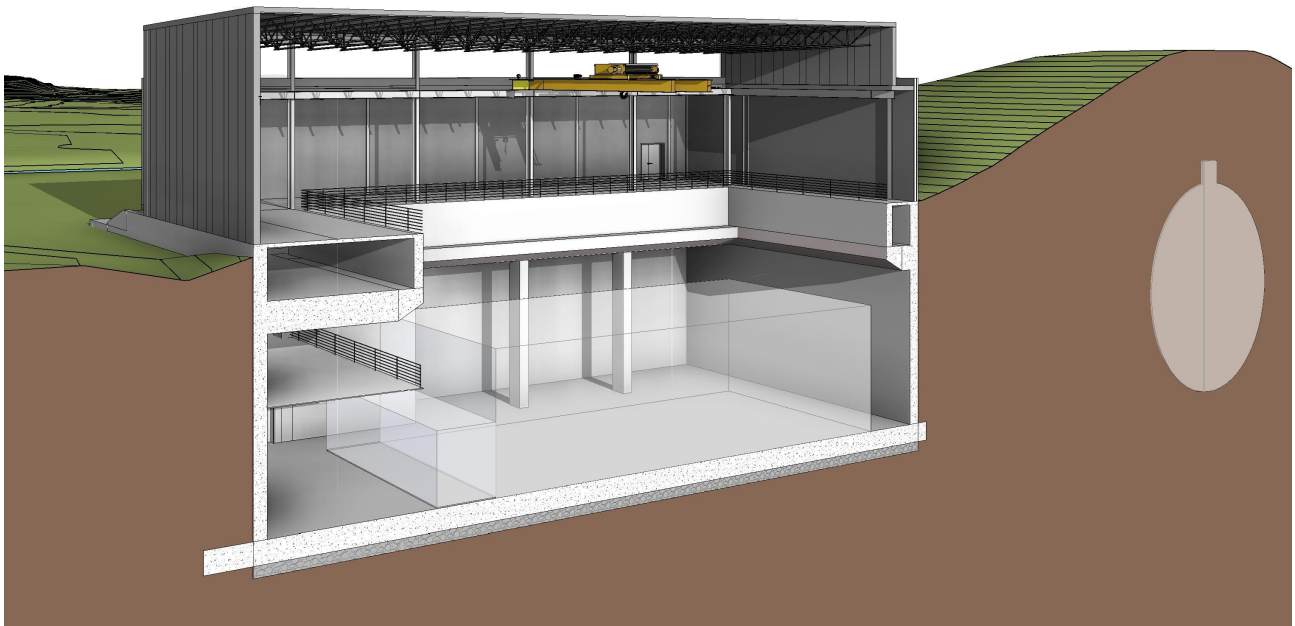


**FIG. 121:** *Cross-sectional view of a design for the far detector building. The T600 cryostat will be housed in the below-grade portion. Equipment can be lowered into the below-grade area from the surface building using the internal overhead crane. The two T300 TPC modules will be installed through a removal roof section. The beam enters from the right in this view. The MiniBooNE hill is to the right.*

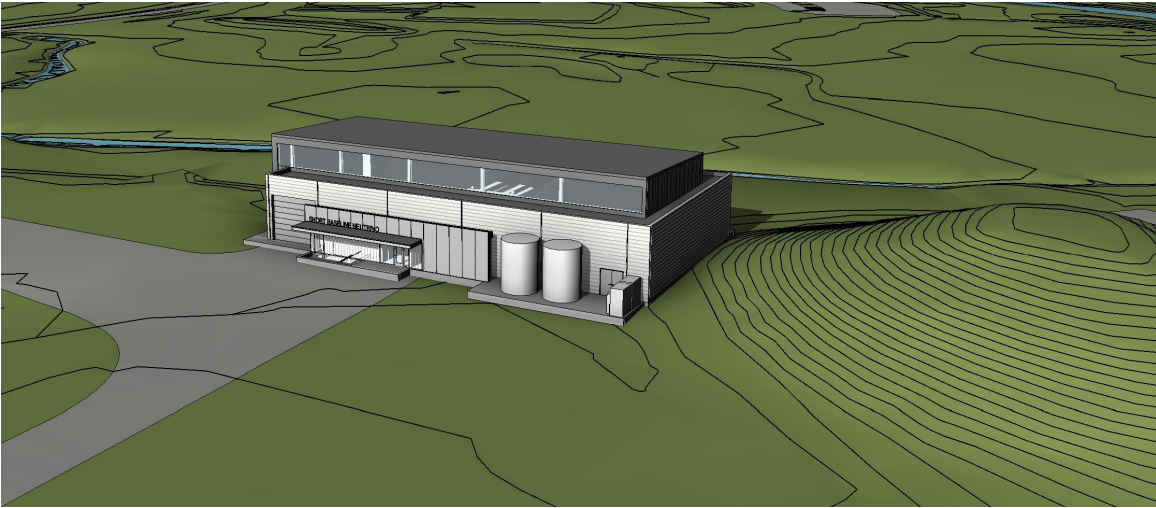


**FIG. 122:** *Aerial view of design for the detector building.*

## VII. Computing Infrastructure and Software

The details of the computing needs for the near and far SBN detectors have not yet been fully specified, but it is recognized that the use of similar or identical applications, software libraries, and user interfaces would simplify development, maintenance, and operation. Developing common solutions will be valuable through the full data processing stream from data acquisition software to event reconstruction and analysis. It will not be possible to have completely identical software due to physical differences in the design of the detectors and electronics. However, common frameworks can be used where differences are handled through geometry databases and detector specific versions of some modules. Not only will common solutions result in a more efficient use of scarce programming resources, in a number of places it will be critical to maximizing the sensitivity of the measurements. For example, common reconstruction tools will be needed to ensure that systematic effects between the different detectors can be carefully studied and minimized.

In this section, we outline where common solutions could most benefit the program: data acquisition, data quality monitoring, analysis framework, and reconstruction tools. The description uses several Fermilab support products as examples: the *art* analysis framework, the *artdaq* data acquisition package, and the LArSoft tools interface. We then discuss the current state of automated event reconstruction within the collaborations and plans to advance this critical area in common.

### A. Data Acquisition and Data Quality Monitoring

Common data acquisition infrastructure would allow developers and shift crews to more easily switch between the DAQ systems on the different detectors. Of course, the DAQ software can not be completely identical because of differences in the detectors, the readout electronics, and any online analysis needs. However, the use of a common DAQ software framework would provide the benefit of common infrastructure and functionality while supporting experiment-specific customizations.

There are several data acquisition frameworks in use in high energy physics today, including *artdaq* which has been developed by the Scientific Computing Division at Fermilab. As an example of what such a framework provides, *artdaq* includes core functionality in the areas of data transfer, event building, process management, system and process state behavior, control messaging, message logging, and configuration of software and hardware. It also provides online processing and data quality monitoring functionality using the *art* framework which is used in the offline environments of many of the current experiments at Fermilab.

With frameworks such as this, experimenters can focus on the development of the software components that are particular to their experiment. In the case of *artdaq*, this includes the modules that read out and configure the electronics that are used by the experiment. It also includes the reconstruction, filtering, and compression modules that are run online, and the software modules that monitor the quality of the data as it is being acquired. The framework model that is implemented in *artdaq* is shown graphically in Figure 123.

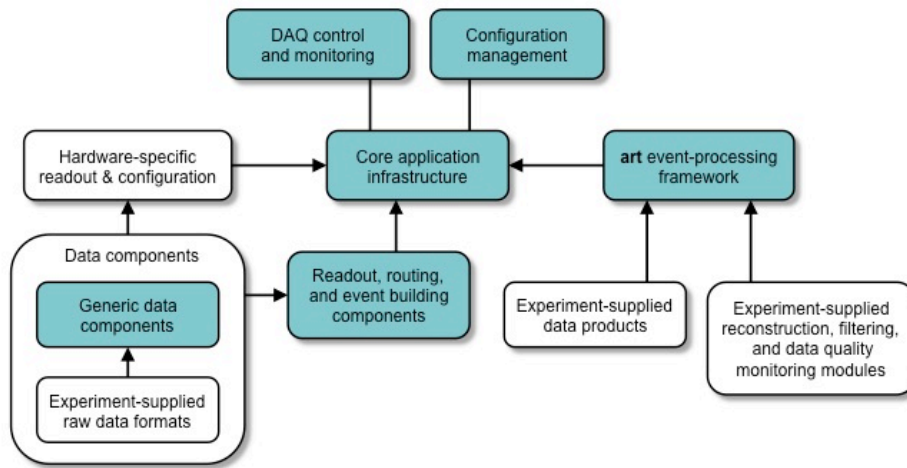


**FIG. 123:** Sample data acquisition framework architecture, as demonstrated by the *artdaq* toolkit. The blue-shaded boxes show functions that are provided by the framework. The white boxes show the components that are developed by each experiment.

The *artdaq* framework is currently used or will be used by several experiments including the DarkSide-50 experiment, the LArIAT testbeam experiment, the LBNE 35-ton prototype detector, and Mu2e. The benefits of using such a framework has been demonstrated in each of these, most notably the LBNE 35t DAQ in which experimenters from the UK developed the software interfaces to the custom DAQ hardware.

In addition to making maintenance and operation easier, the use of a common DAQ system or framework would allow for coordinated operation, if that would be useful. For example, an umbrella run control application could allow shift operators to *start* and *stop* data taking runs for the SBN detectors simultaneously, even if the internal timing structure of the data and the analysis and storage of the data are independent.

Lastly, the use of a common DAQ framework may provide benefits for software organization. If were useful for the software components that provide convenient access to the raw data for each of the three detectors to be grouped into a single software package, that could be facilitated by the use of a single framework.

The implementation of LAr1-ND experiment-specific items in Figure 123, including low-level hardware access for configuration, control and readout, would benefit greatly from experience with MicroBooNE. Although MicroBooNE does not use *artdaq*, as it was designed prior to its existence, many of the design and control features are common. Also, the LAr1-ND front-end electronics are quite similar to that of MicroBooNE, as shown in Part 3 of this proposal. The FEM (Front End Module) readout boards are quite similar (with the exception of cold digitization in the LAr1-ND case). The Nevis PCIe interfaces to the sub-event computers are identical, allowing much of the lowest level Linux software to be recycled. Since the channel counts and expected neutrino rates at both MicroBooNE and LAr1-ND (11,262 channels) are quite similar, the data throughput requirements and the design of the event builder need not be improved or changed. If *artdaq* is chosen, the lower level readout and control code will have to be integrated into that framework; experience with the successful integration in LArIAT will help in this regard. In *artdaq* nomenclature, there would be one BoardReader process per sub-event computer plus FEM crate.

The ICARUS-T600 detector requires readout of significantly more channels (53,248) which makes a common front-end solution more difficult. However, with the downstream solution shown in Figure 36 of Part 3 of this proposal, with a CAEN A3818 PCIe interface, ICARUS will share a common computer-side sub-event readout bus. One *artdaq* BoardReader per A3818 would match with similar function as with LAr1-ND, one in each sub-event computer. With a cluster of identical sub-event Linux computers forming the first stage of ICARUS event building, we can make the data flow elements downstream of the PCIe bus look essentially identical. Any readout control functionalities will of necessity be distinct from LAr1-ND. Extensive experience with the CAEN A3818 PCIe interface on LArIAT, MINER $\nu$ A and CMS experiments would greatly benefit work in this direction. In any choice of framework, whether *artdaq* or other solution, having the frameworks at both ICARUS and LAr1-ND identical will speed development and ease maintenance enormously.

To control all aspects of the items in Figure 123 in a convenient manner for the shift-crew to understand and operate, we will need a Run Control graphical user interfaces (GUI). The MicroBooNE experiment has successfully ported the NO $\nu$ A GUIs based on the QT graphics framework for overall Run Control, application control and resource management. As even porting a GUI is difficult and time consuming, ICARUS and LAr1-ND should come up with a common solution to avoid duplication of effort. Behind the scenes of these applications we need a run configuration database to store configuration options and actual configuration used during run time. The *artdaq* group plans to implement such functionalities, and we tag along or follow the MicroBooNE example. In any case, having a similar DAQ architecture at both far and near detectors will simplify all of these issues.

The final element of online software spans the boundary between online and offline analysis: the online data quality monitor (DQM). The DQM process should have fast access to the data as they arrive, in real-time in order that DQM can find problems with the experiment quickly to avoid beam time loss. Depending on the data rates and the processing speed of the DQM process(es), it may not be possible for the DQM process to analyze all of the data in real-time, so a variable prescaling system is needed to, say, process one out of three events, where three can be adjusted so that DQM in no way impedes the main data flow. The DQM input mechanism can be via data files on disk, via a shared memory or via a network event service. The latter option allows the DQM to run anywhere and to not need to access the disk files or shared memory directly. In any scenario, the DQM must never be allowed to cause the data acquisition to slow or stop, so communications between the DAQ and DQM must be flexible and robust. The DQM process normally produces a set of histograms or other

ROOT objects that let the shift-crew and detector experts see the status quickly. To display the histograms, we envision a light-weight interface to the ROOT objects via a web server like <http://if-wbm.fnal.gov> which hosts histogram displays for MINOS, MINER $\nu$ A and LArIAT.

## B. Data Storage and Processing

At this time, it is difficult to precisely evaluate data sizes for the SBN detectors. We assume that data from the detector will be staged to disk and then to tape for archival storage. New data are assumed to remain on disk until an initial pass of production processing can be performed. Subsequent reprocessing of the data, which can be assumed to occur at least once or twice per year, will draw data from tape with a cache disk front end. Production data will, under ideal circumstances, remain on disk for as long as needed for analysis purposes. At least two complete production passes must be resident on disk at any given time. Additional storage will be needed for testing, staging intermediate results, user analysis and management of production processing.

Monte Carlo data production will consume additional storage. We assume that each pass of data production is accompanied by a complete generation and reconstruction of the production Monte Carlo samples. The statistics in each of the Monte Carlo samples will be approximately ten times that.

The following data model is based upon experience from other neutrino experiments and broad assumptions about data sizes and rates. Given the large uncertainties at this time about the details of the data and the data model required, we attempt to provide an upper bound on the storage that may be required. Even within this estimate, there are large uncertainties that could change the bound by large factors. Nonetheless, it is instructive to work through some reasonable set of assumptions for the data model to see the order of magnitude of the answer. We should also note that storage technologies change. Any reference to a specific technology in the following should be regarded in that light. The important points will be the total data sizes and rates.

Assuming the new DAQ and beamline operates at a maximum rate of 5 Hz with an addition 5 Hz of simultaneous cosmic ray data taking, the expected upper bound of the data rate from ICARUS-T600 is expected to be or order 500 MB/sec. The LAr1-ND detector will contribute an additional 100 MB/sec in this limit. The raw data is assumed to be compressed, but not zero suppressed. The upper bound on the total raw data size over the course of the SBN run would then be about 1 PB.

The signal samples are approximately 10% of the total, so about 100 TB. Since the raw data is compressed, each pass of reconstructed data will be larger than 100 TB. Low level data, however, could be dropped for the production output. Here, we assume that the production data output is 150 TB per full re-processing pass on the final dataset, which is still small on the scale of the total storage needs for the experiment. We assume that the dataset will be re-processed at least twice per year for the three years of data taking, and twice more in the year after data taking, which results in about 6 x 150 TB, or about 1 PB of production output over the course of the experiments.

For Monte Carlo data, we assume that we will require 10 times the signal statistics, and that Monte Carlo data is twice as large as raw data in order to accommodate truth information. This yields a total size of 2 PB for a full pass of Monte Carlo on the final dataset. If we assume the same number of re-processings, we get approximately 10 PB for the full Monte Carlo sample by the end of the experiment, which obviously dominates the estimated data size.

Summing over all of these datasets, we arrive at an upper bound on the total production data size that is on the order of 10 PB.

Additional disk storage or the equivalent will be required for the following uses:

- Staging raw data from the detector before writing the archiving the data to tape. Ideally, this data will remain on disk until the first pass of production processing is completed, and large enough to weather latencies and downtimes in the production and archival apparatus.
- Staging of data from tape for production data re-processing
- Staging production output data. Ideally, production output will remain on disk until it is no longer needed for analysis. We should assume at that at least two full production passes must be on disk at once.
- Storage associated with production processing, which includes both special purpose staging and large scale production testing
- Storage for smaller analysis datasets and user analysis
- Storage associated with a DOE mandated data management plan

It is difficult to estimates the needs for these categories, but the asymptotic bound assuming the data size estimates above put the size in the area of a few PB.

Existing technologies deployed at Fermilab, such as dCache and Enstore, already operate at the capacities and throughput scales implied by the above data estimates, so should not introduce unknown costs.

CPU:

Given that the development of simulation and reconstruction algorithms are at a very early stage with only limited exposure to real data (only that from ArgoNeuT), it is premature to make estimates of the CPU capacity required to process and analyze the SBN data. Suffice it to say that there must be sufficient processing available to perform the first pass of production processing in real time with data taking, while at the same time that a full production pass on the data is being performed. In order to provide rapid turn around for analysis, a full reconstruction re-processing of the data, including the accompanying Monte Carlo production, should be possible on the time scale of one to three months.

Even knowing the production processing requirements, it is often difficult to estimate the analysis CPU in advance of actual analysis. In many experiments, the analysis CPU dominates the total consumed, while in others, it is comparable to or smaller than the production CPU. In order to enable the construction of sensible CPU demand models, it is important that the data processing and job submission infrastructure used by the SBN experiments provides the capability to track the specific use for any given job. Fermilab supports several systems that provide this capability.

### C. Data Analysis Framework and Tools

The *artproduct* supported by Fermilab is a general-purpose data processing framework for offline data production and analysis that is well-suited for use in neutrino and related experiments. A number of experiments have adopted the *artframework*, including NO $\nu$ A,

g-2 and Mu2e, as well as the LAr-based experiments ArgoNeuT, MicroBooNE, the former LBNE, LArIAT, and LAr-1ND. The question of using *art* for ICARUS-T600 will be addressed separately later in this section.

The choice of LAr-TPC technology and the consequent similarities in readout geometries across experiments offers a unique opportunity for developing common solutions for the simulation, reconstruction and analysis of data for the experiments. The LArSoft project, a joint venture between the experiments, software providers and Fermilab, supports the development and maintenance of an integrated, *art*-based, experiment-agnostic software suite for simulation, reconstruction and analysis of LAr-TPC data. All of the current LAr-TPC-based experiments at Fermilab are members of LArSoft; Fermilab manages the project. Participating experiments contribute algorithms to the LArSoft suite. By using generic interfaces to the services that provide otherwise detector-specific information, the algorithms can be decoupled from the details of the experiment for which code was originally written. In participating in LArSoft, the member experiments also gain access to the algorithms and tools contributed by other experiments.

Some elements of the offline software necessarily require specific knowledge of the particular experiment. In some cases, the required functionality can be hidden behind interfaces that are sufficiently general to be used for all experiments. In either case, each experiment must develop and maintain this software, which includes the geometry description for the detector, readout electronics simulation and digitization algorithms, interfaces to calibration data, etc. Some fraction of the photon reconstruction software may also need to be experiment specific.

At the present time, MicroBooNE contributes code more quickly than do the other experiments, due largely to the proximity to data taking. As a result, most of the reconstruction and simulation algorithms were developed either by ArgoNeuT, the original LArSoft user, or MicroBooNE. While MicroBooNE has successfully completed 5 Monte Carlo challenges using the LArSoft suite over the past few years, the remaining active experiments, LBNE, LArIAT and LAr-1ND have successfully used the same simulation and reconstruction code, but with their respective detector geometries. Notably, LBNE found that a track merging algorithm designed to fix certain reconstruction pathologies in MicroBooNE was able to fully reconstruct tracks that crossed TPC boundaries. While it is clear that each experiment may require algorithms that are only used in their respective experiments or for specific analyses (something which may be particularly true for the SBN analyses), it is equally clear that the existing LArSoft software provides a strong foundation from which to begin development.

The case of the ICARUS-T600 detector is special in that it comes with a legacy data processing and analysis framework, plus simulation and reconstruction algorithms. The choices from this point are to either port the ICARUS code into LArSoft, port the LArSoft code into the ICARUS framework, or to allow each set of code to evolve independently. Oscillation experiments will benefit from using the same or very similar algorithms across all detectors by offering better control of systematics. We argue that porting the ICARUS code into LArSoft is preferred because it allows the most direct and complete sharing of the experience gained by ICARUS for the benefit of the other experiments including eventually the long baseline program. Porting LArSoft into the ICARUS framework might increase the cost of sharing from ICARUS back to the other LArSoft participants. Leaving each independent raises the cost of sharing in either direction, so would be preferred only in the case that porting is prohibitively expensive.

The problem of porting code from one framework into another presents a number of issues that need to be addressed. In no particular order, these issues include the compatibility between data structures and their relationships to each other and the framework; the dependence of algorithm code on framework-specific features; the compatibility of the analysis-level plug-ins

between the frameworks; and the feature sets available within each of the frameworks. Issues such as build systems and external dependencies need to be resolved as well, but those typically do not present major impediments.

LArSoft has adopted the strategy of framework independence for all of its algorithms and data structures, although implementation is far from complete. If successful, the task of porting the code into another framework reduces to the relatively simple task of writing an interface layer between the framework and the algorithms and data structures. In LArSoft, this layer does little more than interact with the framework to access data structure and other services managed by the framework and hand them in framework-independent forms to the algorithms.

#### D. Toward an Automated Reconstruction

Reconstruction of events in LAr-TPCs is challenging since the fine-grained tracking and calorimetric aspects of LAr-TPCs provide a large amount of information on each neutrino event. Taking full advantage of this information requires a precise, efficient, and automated event selection and reconstruction package.

Reconstruction algorithms are being developed by all three collaborations. MicroBooNE and LAr1-ND simulation and reconstruction software is in the LArSoft framework, while the ICARUS collaboration has a legacy data analysis and reconstruction framework.

The raw data from LAr TPC detectors consists of signal waveforms from each wire in each of the views (three for all the SBN detectors). The reconstruction of events takes these waveforms as input and proceeds in six steps as outlined below:

1. Hit finding: each of the signal waveforms is analyzed to find pulses that are returned as hits, each representing a time and deposited charge on the analyzed wire. The hits are the basic building blocks for the remaining steps.
2. 2D clustering: a clustering algorithm associates the hits in each view into logical groups called clusters.
3. 3D reconstruction: pattern-recognition algorithms match these two-dimensional (2D) clusters across views to create collections of hits associated with the same three-dimensional (3D) objects. This step can involve splitting or merging 2D clusters to better match candidate 3D groupings.
4. Tracks/showers spatial/calorimetric reconstruction: Candidate 3D objects are passed to track- and shower-reconstruction algorithms to produce collections of tracks and showers.
5. Identification of primary and secondary vertices: vertex reconstruction associates tracks (and showers) to produce the full event. The event is represented as a hierarchical collection of the tracks and showers, starting with the event interaction point, arranged according to the logical structure of the interaction.
6. Particle identification: this is performed via  $dE/dx$  versus residual range measurement or decay/interaction topologies (stopping particles identification, photon/electron discrimination).

Individual pieces of the reconstruction chain are already at a good level of development and have been used in the analysis of ICARUS-T600 data in the CNGS beam at Gran Sasso



laboratory and ArgoNeuT data in the NuMI beam at Fermilab. It should be noted that due to the bubble-chamber like quality of LAr-TPC data, visual scanning is a very powerful tool that provides an understanding of many features of neutrino interactions that was possible with other technologies and existing experiments. As described in the following, some of the analyses of the ArgoNeuT data have taken advantage of visual scanning. The relatively small size of the ArgoNeuT data sample has made this possible.

A big effort is ongoing with the goal of optimizing the most challenging parts of the reconstruction, namely merging two-dimensional (2D) views into a three dimensional (3D) picture and reconstructing the interaction vertex. The full chain of event selection and reconstruction is being automated to be ready for the analysis of much larger data samples from MicroBooNE and future LAr-TPC experiments. Monte Carlo simulated events, with the inclusion of detector effects, are of course an essential tool in order to develop and test the algorithms.

#### *Scale of necessary reconstruction*

The huge number of beam and cosmogenic events that will be recorded in the three SBN detectors (shown in Table XXV) demonstrates the necessity of developing automatic reconstruction tools. It is nonetheless foreseen that subsamples of all event topologies and all electron neutrino candidate events will be visually examined. Table XXV contains the expected trigger rates in the active volume, prior to application of any energy or fiducial volume cut. These triggers together with a significant rate of crossing muons and other particles from neutrino interactions outside the active volume will constitute the initial data sample. Differently from Table VI of Part I, here cosmogenic triggers include all event topologies in coincidence with the beam spill, independently from the presence of photons.

**TABLE XXV:** *Expected trigger rates in the active volume for a  $6.6 \times 10^{20}$  protons on target (POT) exposure, delivered in  $1.32 \times 10^8$  beam spills for LAr1-ND and T600, and for a  $1.32 \times 10^{21}$  POT exposure for MicroBooNE. A significant rate of crossing muons and other particles from neutrino interactions outside the active volume is also expected.*

	LAr1-ND	MicroBooNE	ICARUS
$\nu_\mu$ CC in active volume (AV)	$5.2 \times 10^6$	$3.4 \times 10^5$	$5.6 \times 10^5$
$\nu_e$ CC in AV	$3.7 \times 10^4$	$2.2 \times 10^3$	$3.5 \times 10^3$
$\nu$ NC in AV	$2.0 \times 10^6$	$1.3 \times 10^5$	$2.1 \times 10^5$
Cosmogenic triggers	$3.0 \times 10^6$	$1.8 \times 10^6$	$2.5 \times 10^6$

The aim of the automatic reconstruction algorithms will be:

- rejection of cosmogenic events and “in drift time” cosmogenic tracks,
- identification of the neutrino interaction and its classification (CC, NC..), and
- estimation of the neutrino energy.

For the first item, the coupling with the light detection and muon tagging systems will be certainly beneficial.

Reconstruction that enables  $\nu$  interaction identification involves:

- electron/photon discrimination via initial part of the cascade,

- other discriminating features, e.g. energy in the primary vertex region,
- discrimination between pions and muons.

Identification and reconstruction of the neutrino primary interaction vertex is the first prerequisite for the above tasks. Work in ICARUS software framework has shown that reconstructing the primary vertex requires that the full net of tracks must be reconstructed first (where tracks meet at interaction vertices). From this stage one can search for the primary vertex e.g. by looking for the track directions. Electromagnetic shower reconstruction and identification needs primary vertex reconstruction as well. To identify electron neutrino events it is required to select showers pointing to the primary vertex, validate if the shower is not separated from the vertex and if it is possible to identify the shower as related to single electrons.

*Current reconstruction capabilities and planned near term work*

Reconstruction algorithms of LAr-TPC data have been largely developed on real data from ArgoNeuT and ICARUS-T600 experiments. The MicroBooNE collaboration is giving a very important contribution continuing the development of most of the reconstruction and simulation algorithms in the LArSoft framework.

*ICARUS*

Many pieces of the reconstruction are ready in the ICARUS framework. A novel approach is followed for 3D reconstruction [139], that outclasses the standard approach of hit-by-hit matching through common timing. Hit-by-hit is prone to ambiguities (especially for objects developing in a direction perpendicular to the drift direction), to missing matches (i.e. in case of objects developing in a direction parallel to one of the wire orientation) and to position quantization (wire pitch). The ICARUS approach instead performs a global fit of all the three independent views starting from pre-identified 2D “objects” or “clusters”, allowing to overcome the above difficulties. Particle identification via  $dE/dx$  is also ready, and tested both on Monte Carlo and real events. It is based on a Bayesian neural network algorithm as described in [140].

The automatic identification of 2D “objects” or “clusters” has also been developed and nearly finalized. It is based on a segmentation algorithm that proceeds from the event periphery towards the center, building segments and vertices. The 2D segmentation is fed to the 3D reconstruction to solve ambiguities. Several 2D-3D iteration steps can be envisaged.

Further work is ongoing for the reconstruction of showers and the automatic identification of the primary vertex.

The ICARUS automatic reconstruction has been tested on a large sample of real CNGS events containing muons produced in the materials upstream of the detector. The reconstruction efficiency was checked against visual scanning and found to be about 90% (this sample contains many tracks parallel to the wire planes, thus with almost constant  $t_0$  along the track, which is a very adverse condition for the reconstruction). Tests on low energy real CNGS neutrino events provided encouraging results.

Reconstruction of fully simulated Monte Carlo event samples at the BNB energy has also been performed and shown to give the same identification efficiency as visual scanning. In this case, the position of the primary vertex has been assumed as given from the simulation.

Full automated reconstruction, including the identification of the primary vertex, has been

attempted on a sample of simulated  $\nu_\mu$  CC Quasi-elastic events at 1 GeV. The position of the primary vertex was reconstructed within 3 cm in 92% of the events, out of which 72% resulted to have the correct track multiplicity (zero, one, or more protons depending on final state effects in the interaction). The muon initial direction was reconstructed within  $20^\circ$  in 90% of events, and within  $4^\circ$  in 83% of cases.

The currently available reconstruction algorithms were used to prepare methods for automatic background rejection. Two approaches were studied:

- 3D reconstruction of tracks in order to identify muon tracks crossing the detector. The efficiency was checked on a generation of cosmic muons with the results of 95% tracks correctly reconstructed from the full sample. Improvements are under investigation. Known  $t_0$  was assumed in this study.
- Identification of muon signal and its EM activity in 2D projection of the Collection view. Since the Collection view is the source of the calorimetric and  $dE/dx$  measurements, the region in the close proximity to cosmic muons and induced EM activity should be excluded from the signal analysis. Clustering algorithms were used to study the potential of such an approach, obtaining an almost complete background reduction with an estimated few percent loss in fiducial volume.

### *LArSoft*

ArgoNeuT was the first experiment using the LArSoft package to simulate and reconstruct neutrino events collected during a run in the Fermilab's NuMI LE beam at the MINOS near detector hall in 2009-2010. The ArgoNeuT experiment [141], a 240 kg active volume LAr-TPC, collected several thousand  $\nu$  and anti- $\nu$  interactions. Automated event selection has been used to extract different samples of events: 1) CC (anti-) $\nu_\mu$  events, combining TPC tracking information with the downstream MINOS near detector and 2) events with electromagnetic shower activity in the TPC. Fully automated reconstruction has been used for some analyses, requiring the reconstruction of simple or inclusive topologies, while semi-automated reconstruction procedures, guided by visual scanning have been used for detailed reconstruction of final state event topologies. Individual events have been categorized in terms of exclusive topologies observed in the final state and semi-automated geometrical reconstruction has allowed to reconstruct low energy hadrons (protons with 21 MeV kinetic energy threshold) at the vertex of  $\nu$  events.

Automated geometrical and calorimetric reconstruction of a high statistics sample of minimum ionizing tracks, through-going muons produced by neutrino interactions upstream the detector, has demonstrated the reliability of the geometric and calorimetric reconstruction in the ArgoNeuT detector [142]. Analyses  $\nu_\mu$  and anti- $\nu_\mu$  CC inclusive events [143], [144], coherent charged pion production on argon [145] and highly ionizing tracks [146] have been performed through fully automated geometrical and calorimetric reconstruction and particle identification (PID). Analyses requiring the complete reconstruction of the final state kinematics [147] have been performed through semi-automated geometrical reconstruction of protons at the vertex followed by fully automated calorimetric reconstruction and PID. Analyses of the selected samples of events with electromagnetic shower activity in the TPC using semi-automated reconstruction procedures to study of NC  $\pi_0$  events and electron-gamma separation are expected to be finalized soon.

In LArSoft multiple modules for performing a task using different methods may exist. LArSoft currently contains multiple hit-finding, hit-cluster, and charged-particle-track-finding al-

gorithms. Given the existing common software base, these elements represent a significant reduction in the amount of software that must be developed in order to obtain a full simulation and reconstruction chain. LAr1-ND, for instance, completed the necessary detector-specific elements and ran a complete simulation and analysis chain in significantly less than a month using only two part-time developers. This modularized structure allows for fast, independent development of new algorithms, and seamless incorporation of new and different algorithms into the reconstruction chain. Development and optimization of the different algorithms, test and studies of the performances of automated reconstruction chains are in progress on big samples of MicroBooNE Monte Carlo events.

Because the MicroBooNE TPC is situated near the surface of the earth it experiences significant exposure to cosmic rays, which must be removed during the reconstruction phase. This is facilitated using a two-pass reconstruction. The first pass proceeds through the reconstruction steps 1–3 described above and the results are passed to track reconstruction. The resulting tracks are then analyzed for consistency with the cosmic ray background (aided by the PMT system). Hits associated to tracks identified as coming from cosmic rays are removed from the event. The second pass then runs through all six reconstruction steps using the remaining hits, which are taken to belong to a beam-induced event. Data from MicroBooNE will be very important in order to evaluate the performance of this procedure.

#### *Steps to a joint reconstruction effort*

It is recognized that teams from the different experiments need to collaborate on the development of common solutions for the simulation, reconstruction and analysis of data for the combined analysis of the three detector data. The details of this reconstruction software have not yet been fully specified. A workshop dedicated to LAr-TPC event reconstruction to define a common strategy will be organized. As a first step to test the current performance of the already existing LArSoft and ICARUS tools it is proposed that ICARUS atmospheric neutrino data, which are in the energy region of the BNB events are reconstructed with LArSoft tools and ArgoNeuT data are reconstructed with the ICARUS tools.

There is an ongoing effort to merge ICARUS reconstruction algorithms into the common framework of LArSoft. Currently the ICARUS algorithms for clusters and 3D track reconstruction are being adapted to the structure of LArSoft. The reconstruction in the LArSoft framework is implemented as modules that allow to perform various stages of reconstruction. Such a modular approach would allow to use any configuration of algorithms already available in the LArSoft together with algorithms developed in the ICARUS framework. This would allow to verify and test algorithms on data from different liquid argon detectors, as well as give possibility to compare with each other independently developed algorithms.

The development of common computing and software systems for the SBN program will benefit significantly of the use and development of these tools on the soon to come MicroBooNE data.

It is the natural role of Fermilab as the host laboratory to provide and support software infrastructure such as the art, *artdaq*, and LArSoft. For the SBN program to successfully take advantage of these tools, it will be essential that sufficient resources are available from Fermilab to assist in code development, code porting, and user support. This support will be needed in parallel with the construction and refurbishing of the physical detectors.

**A Proposal for a Three Detector  
Short-Baseline Neutrino Oscillation Program  
in the Fermilab Booster Neutrino Beam**

---

*Part 5: Booster Neutrino Beam*

---

## I. Overview

The short-baseline neutrino program described in this proposal makes use of the existing Booster Neutrino Beamline (BNB). The BNB is a conventional horn focused neutrino beam, fed with 8 GeV protons from Fermilab's Booster accelerator. The beamline was originally optimized for the MiniBooNE detector, the primary user of the beamline over the last decade. One of the considerations when designing the beamline was to have as large a flux as possible at 500 MeV, while keeping the flux at higher energies as low as possible. The higher energy neutrinos produce  $\pi^0$ s in the MiniBooNE detector through Neutral Current interactions and these present significant background for the  $\nu_e$  appearance measurement. The LAr-TPC technology provides much better background rejection and so the constraint of reduced high energy neutrino flux can be relaxed. Maximizing flux at all energies should be generally beneficial.

In the existing beamline configuration the 8 GeV protons from the Booster are guided through the transport line to the target hall as shown in Figure 124. The primary beamline ends with a quadrupole triplet that focuses the beam on the target. The target is embedded within the 1.8 m long horn, and the target horn assembly lies just downstream of the final triplet. A 2.14 m long collimator about 3 m downstream of the target shields the entrance to the decay pipe region.

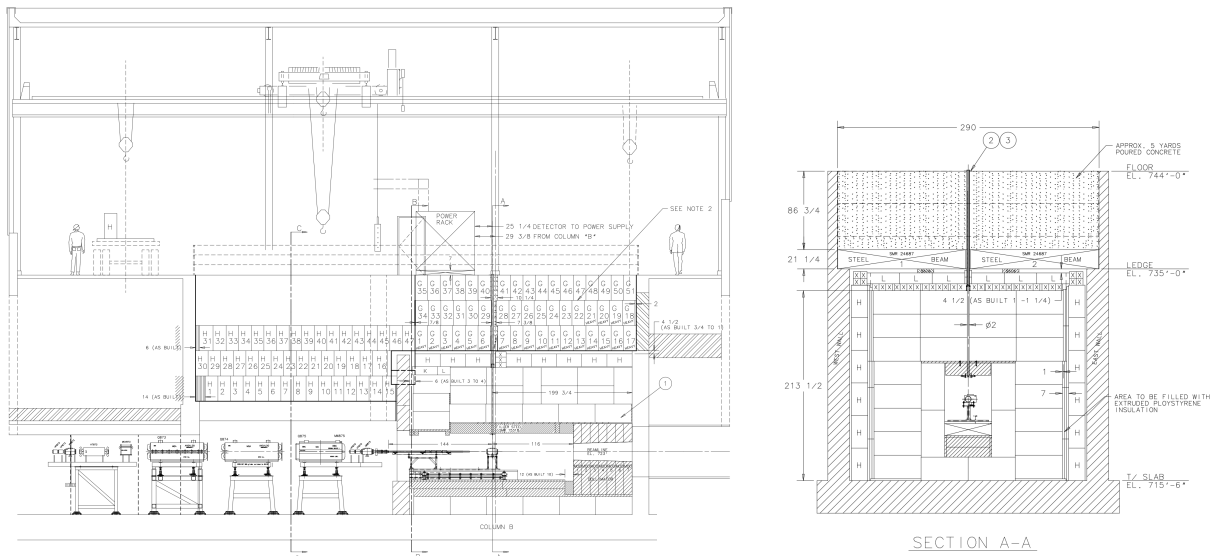


**FIG. 124:** Side (left) and beam (right) view of the target hall region. Final focusing triplet (Q873, Q874 and Q875) can be seen in the side view. The MiniBooNE horn is inserted into the target pile just upstream of the collimator noted as section A in the drawing. This region is 2m high and 1.4m wide. [148]

The Booster operates at the 15 Hz repetition rate with up to 5 Hz average rate delivered to BNB. The intensity per spill is typically about  $4.5 \times 10^{12}$  protons. The time structure of individual beam spills is determined by Booster parameters. The harmonic number for Booster is 84 (81 buckets are filled with beam) and the RF frequency is 53 MHz. This results in  $1.6\mu\text{s}$  long spill comprised of a train of 81, roughly 1 ns wide buckets mutually separated by  $\sim 19$  ns.

The next few sections describe how the neutrino interaction rate in the detectors can be doubled by replacing the existing single horn system with a re-optimized two horn system.

	CC ( <i>Events/t/10<sup>20</sup>POT</i> )		Flux ( $\nu/m^2/10^6$ POT)	
	MiniBooNE Horn	2 Horn	MiniBooNE Horn	2 Horn
$\nu_\mu$	302.0	636.6	7.02	12.6
$\bar{\nu}_\mu$	2.6	2.9	0.44	0.41
$\nu_e$	2	3.8	0.039	0.067
$\bar{\nu}_e$	0.06	0.06	0.004	0.004

**TABLE XXVI:** Predicted neutrino event rates with a two horn system compared to the present BNB configuration with MiniBooNE horn. The rates were calculated using CC inclusive cross section on Ar. Significant increase in the event rate is expected with reoptimized 2 horn system.

The additional space needed for this larger system can be made available in the BNB target building without any need for civil construction by condensing the final components of the proton beamline immediately upstream of the target.

## II. A Re-optimized Horn Configuration

This section discusses the a reoptimization of the target and horn system to better match the capabilities of the LAr-TPC detectors, the future users of the beamline. In addition to the reoptimization motivated by the change in detector technology there is also a push to reoptimize that comes from better knowledge of the system components that is now available. Since the MiniBooNE horn was originally designed, precise measurements of pion production in the beryllium target have been made by the HARP experiment [14] and the kinematic distributions are much better known. These data additionally allow for better optimization of the shape of the inner conductor and the focusing system.

Preliminary studies have been made to estimate possible gains with a reoptimized focusing system. A fast Monte Carlo was developed and used to optimize the horn current, shape of inner conductor of horn 1 (and horn 2), horn position(s), and target position in order to provide focusing of pions that produces the most neutrino events in the on-axis detector(s). The geometry of the optimal design was then simulated using full GEANT4 based Monte Carlo (MC) used by MiniBooNE and other BNB experiments to calculate the neutrino flux. The detailed beam simulation was tuned to match HARP hadron production measurements. Comparing the predicted flux using the full beam MC enables a realistic comparison of the optimized system to the existing MiniBooNE horn focusing.

Figure 125 shows the shapes and locations of the current single horn system and the re-optimized two horn system. Figure 126 shows the fluxes that result from the same proton delivery to the current and re-optimized systems.

Table XXVI shows the expected event rates with two horn system. It is important to note that the intrinsic  $\nu_e$  component which presents irreducible background for  $\nu_e$  appearance measurement remains fractionally the same.

It can also be seen from Table XXVI that the optimized two horn system has a much smaller wrong sign component compared to the original MiniBooNE horn configuration. Both the longer first horn, and the additional second horn further defocus wrong sign (WS) mesons. In neutrino mode this results in a reduction of the WS component by a factor of  $\sim 2$ . While this is not an important feature in the neutrino mode, similar reduction is expected in the antineutrino mode

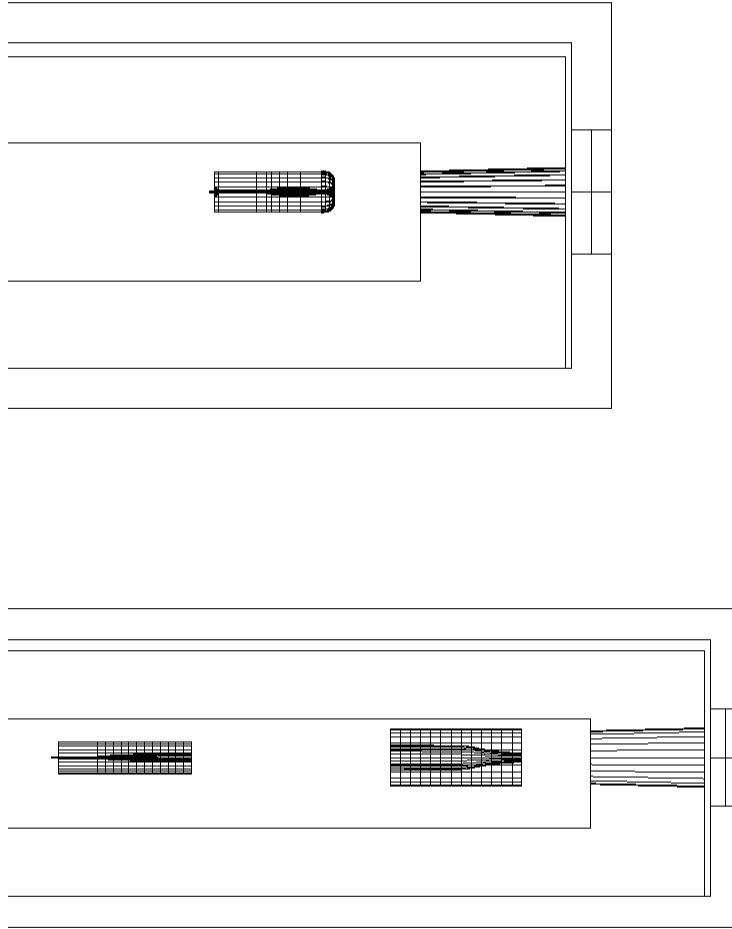


**FIG. 125:** *Two plan views of the target chase showing the shape and location of the current single horn (top) and optimized two horn (bottom) systems.*

where the WS component is significant. Hence, the two horn system would provide a much cleaner measurement of antineutrino oscillations as well as cross sections because the statistical and systematic uncertainties associated with subtracting the wrong sign component would be greatly reduced,

Further optimization of the system is possible. About 20% of the neutrino flux in the MiniBooNE configuration is lost due to pion interactions within the horn conductor. The thickness of conductors in these preliminary studies was taken to be the same as for MiniBooNE horn. Thinner inner and outer conductor could be used, further reducing the losses. The transverse size of the first horn was kept the same as the original MiniBooNE horn. The horn current was limited 250kA, the upper limit of the present MiniBooNE power supply, and both horns were pulsed with same current. All of these parameters could be modified to fine tune the system. The possibility of movable target and horn longitudinal positions will also be explored. This would allow the beam to be tuned to higher or lower energies. Future information from



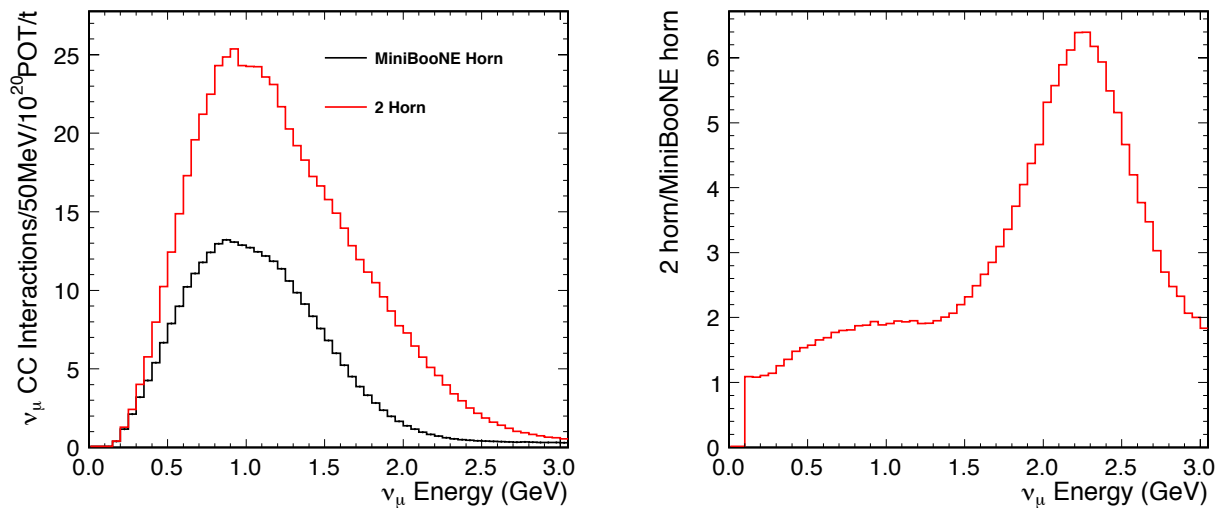


**FIG. 126:** Comparison of the expected neutrino flux with a two horn system to the present MiniBooNE horn focusing. The two horns were optimized to give the most neutrino events, while fitting the constraints of the existing target hall.

running of MicroBooNE or other experiments might make that a useful capability to have, just as it was for the NuMI target and horn system in the pre-NOvA era.

Physical constraints of the existing target hall were taken into account in these preliminary studies. The two horn system requires more room along the beam axis than is presently available (see Figure 124). Some modifications of the primary beamline and shielding within the target hall region would be necessary to accommodate the modified design as discussed in Section III.

The total length of the optimized system was limited to a realistically achievable size. The transverse size of the second horn was limited to the dimensions of the chase. To fully take advantage of the larger second horn, the opening of the collimator at the entrance of the decay pipe was enlarged from 30 to 50cm.

The preliminary studies demonstrate that it is feasible to build a new focusing system that would increase event rate by a factor of 2 or more. This system would provide a huge improvement in the statistics as it doubles the count rate of every detector in the beamline. Further optimizations are possible as well as fine tuning of the horn focusing to shape the spectrum and maximize the physics potential of the experiment.

The new system should be designed to take advantage of present and future accelerator upgrades. The present target/horn system and target hall shielding limits operations to 5 Hz average beam rate with up to  $5 \times 10^{12}$  per spill. The first phase of Proton Improvement Plan (PIP) is presently underway and will allow Booster to deliver beam at a rate of up to 15 Hz starting in FY2016. Future improvements planned for PIP II will allow increasing booster rate to 20 Hz and spill intensity  $6.5 \times 10^{12}$  protons. The design of an upgrade to horn system components should be made capable of handling the higher repetition rate and spill intensity.

### III. Making Space for the New Horn Configuration

In order to accommodate the two-horn system, an additional 5m of space is needed in the Booster Neutrino Beamline.

The Booster Neutrino Beamline (BNB) has three sections. The first section is in the Main Injector tunnel, the second section is a carrier pipe transporting the beam under a road, and the third section points the beam toward the detectors and focuses the beam on the target. This third section is composed of optics to capture the beam from the carrier pipe, a regular lattice to transport the beam through the arc, a vertical dogleg to raise the beam to the height of the target, and a final focusing triplet. The third section is located in the MI12 tunnel and the target hall. The MI12 tunnel is ten feet wide, and the height is eight feet or nine feet, six inches. The tunnel changes height at the approximate center of the first magnet of the dogleg. The target hall, when all shielding is in place, is 23 feet wide, 24 feet deep, and 13 feet high ( $7.0 \times 7.3 \times 4.0$  meters).

In order to gain the additional 5m the dogleg can be moved upstream, beginning in the last cell of the arc and ending at the transition to the higher enclosure. A slight adjustment of position of the quadrupole matching the lattice to the final focusing triplet is also required. A calculation using TRANSPORT [149] shows that a 1mm round beam can be focused at the center of the target with the quadrupole at acceptable currents.

In addition to changes in the beamline, the target pile must also be reconfigured. The present target pile consists of steel blocks filling the downstream half of the target hall. The steel is covered by concrete blocks above. The pile has concrete stacked in front, with an opening large enough to accommodate the horn. Adding an additional 5m of shielding upstream of the existing target pile should be possible.

Figure 127 shows the present and proposed beamline configurations indicating how the space needed for a two horn system can be recovered by adjusting the beamline components.

Figure 128 shows the line 5m upstream of the existing target pile. The new target pile would not occlude the door, although it would cover the sump. Shielding would have to be configured such that the pumps in the sump can be replaced. Existing utilities, such as the cooling skid for the horn, would have to be relocated, perhaps upstream, under the raised beamline.

Another option would be to reconfigure the target pile to allow for more space downstream of the target. This would entail removing all equipment from the MI12 service building, removing the existing shielding blocks, and handling the radioactive steel. However, enough space exists so as not to cover the sump.

#### IV. Secondary Beamline Instrumentation

In this section the current secondary beamline monitoring is described along with some possible upgrades. It should be noted that these monitoring upgrades are completely independent of the horn system upgrades of the previous three sections.

The present secondary beam has minimal instrumentation, consisting of a cross formed by 22 loss monitors located behind the 50m absorber. Twelve loss monitors are placed vertically, approximately six inches apart; and ten loss monitors placed horizontally, five on each side of the vertical column, also spaced approximately six inches apart. The loss monitors are read out through a segmented wire ionization chamber (SWIC) scanner, allowing one to see horizontal and vertical profiles.

The fifty meter absorber consists of 24 blocks of steel stacked roughly into a cube, ten foot on side. The steel is rough cut. This is followed by a ten foot square by three foot deep concrete block. The secondary monitor follows. A stack of steel, eight foot square by two feet deep, ends the absorber. The absorber is buried directly in the ground – no enclosure exists – eliminating the possibility of easily repairing the muon monitor. A steel pipe carries the signal wires to the

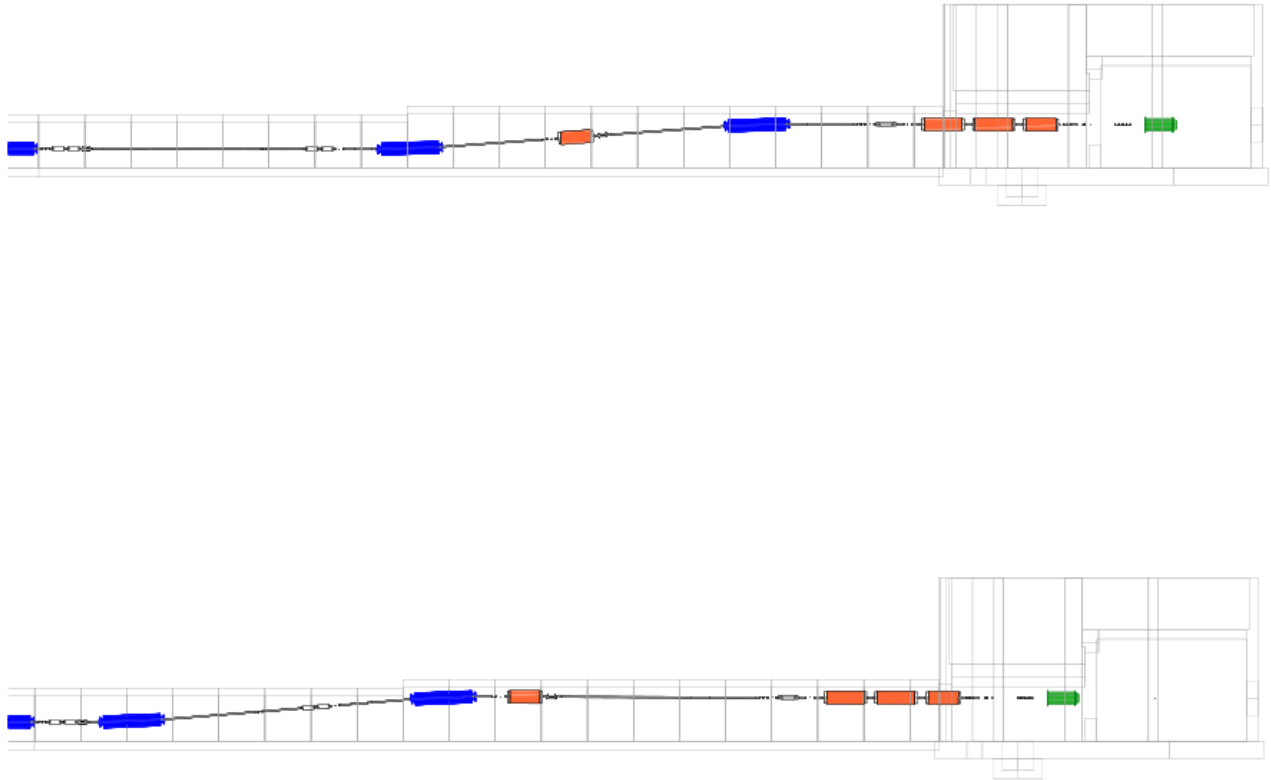


**FIG. 127:** *Side elevations of the Booster Neutrino Beamline (BNB). The present (top) and proposed (bottom) beamline configurations are shown. The dogleg dipoles are shown in blue, the triplet and matching quadrupoles in orange, and the horn in green. The new dogleg is initiated at the beginning of the last cell of the lattice and completed where the enclosure roof rises. The triplet and horn are moved five meters upstream. The location of the matching quadrupole is adjusted slightly.*

surface.

Ideally, one would replace the 50m absorber and provide better instrumentation. A hadron monitor would be placed at the upstream end and a muon monitor at the downstream end. The existing steel would be removed and replaced with more uniform steel plates, eliminating any transverse gaps. An enclosure would be provided to allow for the repair or replacement the hadron or muon monitor.

Constructing such a feature would entail digging into the berm and removing the present 50m absorber. Controls would be in place to manage the irradiated aggregate and steel. The existing water barrier would be breached and resealed around the new enclosure. Power would be run to the new enclosure. Adequate shielding would be placed between the absorber and enclosure, and a means of removing it thought about. Rebuilding the 50m absorber would require significant engineering.

Another option would be a retractable profile monitor at the 25m absorber. This absorber consists of a series of steel and concrete plates that can be lowered into the secondary beamline halfway down the 50m absorber.

In the autumn of 2014, the 25m absorber hatch was opened and the modules adjusted longitudinally to provide a 3/4 inch gap. A profile monitor, 5/8 inch thick, was inserted through this gap to nominal beam center. The monitor consisted of 48 horizontal wires and

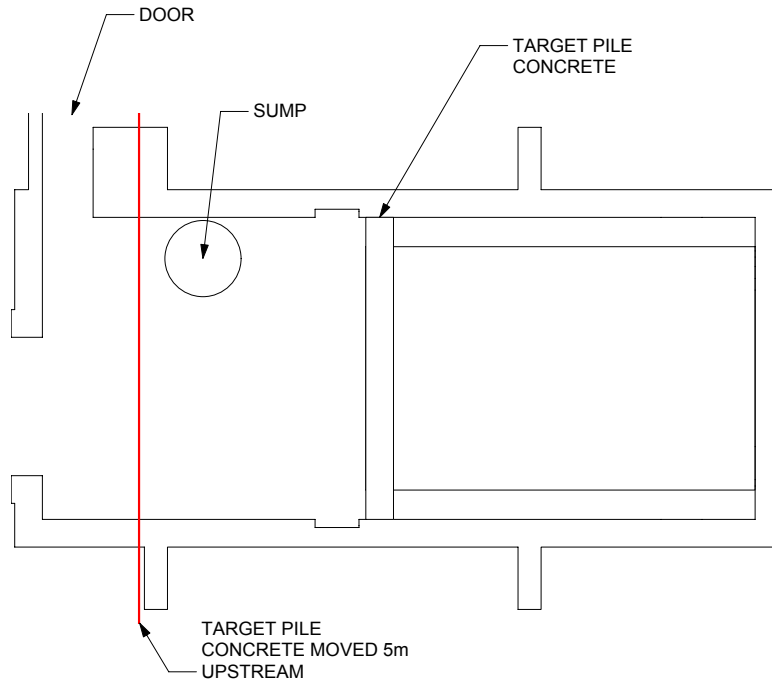


**FIG. 128:** Plan view of target hall showing front face of existing target pile and location 5m upstream. The door is not blocked, but the sump would be covered.

48 vertical wire, each plane having a 2mm pitch. The primary beam was steered around the target and observed on the monitor.

With moderate engineering effort, one could design a profile monitor which would be remotely inserted for alignment runs and retraced for normal runs. The monitor could be of adequate size to see both the primary and secondary beams. By appropriate choice of gain one may be able to distinguish between primary and secondary beam.

## V. Request

Based on the preliminary studies outlined above we make the following requests

- A detailed study of the cost and schedule for conversion to a two horn system should be initiated immediately. This should include the cost of new horns, new or refurbished power supplies, and the necessary work for reconfiguration of the incoming beamline and of the collimator. The system should be capable of (or readily upgradeable to) operation up to 20Hz and of taking the beam intensities anticipated once the PIP II project is complete.
- A detailed study of the cost, schedule, impacts, and benefit of improving the secondary beamline instrumentation of the BNB should be initiated immediately. This should include studies of what instrumentation might be placed near the horn(s), at the 25m absorber, and in the 50m absorber. The instrumentation should be capable of (or readily upgradeable to) operation up to 20Hz and of taking the beam intensities anticipated once the PIP II project is complete.

**A Proposal for a Three Detector  
Short-Baseline Neutrino Oscillation Program  
in the Fermilab Booster Neutrino Beam**

---

*Part 6: Coordination and Schedule*

---

## I. Introduction

This proposal is being submitted jointly by three separate scientific collaborations: ICARUS-WA104, LAr1-ND, and MicroBooNE. Each has an existing organizational structure with an existing scientific mission. The preparation of the proposal is the result of a collaborative effort between the collaborations guided by the SBN task force and the Fermilab SBN coordinator. The mandate of the task force and the five associated working groups ends with the submission of the proposal. In the desired event that this proposal is accepted, a new organizational structure will be necessary to ensure a successful program. The form of the future SBN organization has been the topic of discussions between the leadership of the three collaborations, the management of Fermilab, the management of INFN, and the management of CERN. Since these discussions have not concluded, we only present here some general observations. The new structure will need to ensure the following will happen:

1. the MicroBooNE experiment (E-974) carries out the already approved physics program as an independent collaboration;
2. the ICARUS-T600 detector is refurbished, transported to Fermilab, installed and commissioned;
3. the LAr1-ND detector is designed, constructed, installed and commissioned;
4. the required infrastructure (e.g. buildings, cryogenics, computing) are constructed or purchased and installed;
5. necessary common activities, like cosmic taggers, are designed, constructed and installed;
6. necessary reconstruction and analysis software for a multi-detector oscillation analysis is designed, developed and tested;
7. necessary improvements of the booster neutrino beam for an increased neutrino intensity are studied in detail to provide implementation before the starting of data taking.

All of these activities must take place simultaneously in a very short time-frame.

We expect that the three collaborations will continue to exist in whatever new structure is created for some time to come. The collaborations each have a clear unique role to play in delivering the first three of the above items. The fourth is the responsibility of Fermilab, as host laboratory, in collaboration with international partners such as CERN and INFN. The collaborations have a vested interest in delivery of this infrastructure so the organization must account for that. The last items are clearly of interest to members of all three collaborations.

The three scientific collaborations have worked together through the task force and working groups for the past eight months. As discussed in Part 1 of this proposal, the successful analysis of data from all three detectors for the oscillation analyses will require a coordinated effort on common reconstruction and analysis tools. This effort should start well in advance of start of operations. Joint reconstruction and oscillation analysis group(s) could form the nucleus of the future scientific organization. It will be natural for members of the SBN physics working groups and other relevant people from the collaborations to initiate this effort.

In the following sections we describe the schedule and funding for completion of the components listed above.

## II. Schedule

Initial data-taking with all three detectors operational is foreseen in spring 2018. By this time, the MicroBooNE detector will already have been operational with beam for several years. All steps to prepare the near and far detectors must be accomplished by this time, including design and construction of the near and far buildings, construction of cryostats and cryogenics, preparation of the ICARUS-T600 detector, construction of the near detector, detector installation and commissioning. The proposed schedule is very tight, but with a good level of coordination, it is judged to be feasible. Table [XXVII](#) shows the high level set of milestones.

Milestone	Date
Far Detector building: final CE requirements and start final design	Nov 2014
Far Detector: T600 at CERN and refurbishing starts	Dec 2014
Submit SBN proposal to PAC	Dec 2014
Near Detector: Start preliminary design of TPC and installation	Dec 2014
PAC Review of SBN Proposal	Jan 2015
Near Detector cryostat: Start preliminary design	Jan 2015
Cryogenic plants: Start preliminary design	Jan 2015
Draft MOUs: e.g. Fermilab-INFN, Fermilab-CERN, Fermilab-CH-NSF	Feb 2015
Near Detector building: final CE requirements and start final design	Feb 2015
Independent Review of Near Detector, ND Cryostat and ND Cryogenics (CD-1/2 like)	May 2015
Independent Review of Far Detector refurbishing, cryogenics and installation planning	May 2015
Far Detector building: ground breaking	May 2015
Near Detector building: ground breaking	Aug 2015
Independent review of near detector production readiness	Nov 2015
Independent review of far detector production readiness	Nov 2015
Near Detector building: beneficial Occupancy	Sept 2016
Independent review of installation readiness for near and far detectors	Oct 2016
Far Detector building: beneficial Occupancy	Nov 2016
Near Detector cryostat: start installation	Nov 2016
Far Detector cryostat: start installation	Dec 2016
Far Detector: ICARUS-T600 ready at CERN for transport	Dec 2016
Near and Far Detector Buildings Complete	Jan 2017
Far Detector: start T600 installation	Mar 2017
Near Detector: Start LAr1-ND installation	April 2017
Far Detector: T600 Installed	May 2017
Near Detector: LAr1-ND Installed	July 2017
Far Detector: Cryogenic plant complete	Aug 2017
Near Detector: Cryogenic plant complete	Oct 2017
Start detectors cooling and commissioning	Nov 2017
Start data taking with beam	Apr 2018

**TABLE XXVII:** Overall Milestones for construction, installation and initial commissioning of the Short Baseline Neutrino Program

Figure [129](#) shows the schedule in a summary format for near and far detector, pointing to

the start of data taking with beam to April 2018.

### **A. Near Detector Schedule**

The schedule for design, fabrication, assembly and installation of the components of near detector is shown in Table [XXVIII](#). A detailed resource loaded schedule for these tasks is under development and will be presented at the Independent review in the Spring of 2015.



<b>TPC</b>	Start	End
Requirements Documents		Feb 2015
Preliminary Design	Nov 2014	Jan 2015
Design Review		Mar 2015
Final Design	Jan 2015	Jun 2015
Production Readiness Review		Jul 2015
Fabrication (APAs, CPAs, FCA)	Jul 2015	Apr 2016
QA (Cold Tests)	Apr 2016	Jun 2016
Delivery to Fermilab by		Sep 2016
Assembly	Sep 2016	Feb 2017
Installation	Apr 2017	Jul 2017
<b>Cold Electronics</b>		
Requirements Documents		Mar 2015
Preliminary Design	Jan 2015	Sep 2015
Design Review		Oct 2015
Final Design	Oct 2015	Mar 2016
Production Readiness Review		Mar 2016
Fabrication	Apr 2016	Jun 2016
Assembly	Jul 2016	Sep 2016
Delivery to Fermilab by		Oct 2016
Installation	Nov 2016	Jul 2017
<b>Light Detector</b>		
Preliminary Design	Dec 2014	Mar 2015
Choice of technology		Mar 2015
Final Design	Apr 2015	Sep 2015
Production Readiness Review		Oct 2015
Fabrication	Nov 2015	May 2016
Assembly	Jun 2016	Nov 2016
Delivery to Fermilab by	Dec 2016	Dec 2016
Installation	Jan 2017	Jul 2017
<b>Laser Calibration</b>	Start	End
Requirements Documents		Jan 2015
Preliminary Design		Complete
Final Design	Mar 2015	Jul 2015
Production Readiness Review		Jul 2015
Fabrication	Jul 2015	Jan 2016
Assembly	Jan 2016	Jun 2016
Delivery to Fermilab	Jun 2016	Aug 2016
Installation	Jul 2017	Sep 2017

**TABLE XXVIII:** *Summary of LAr1-ND detector component schedules*

### B. Far Detector Schedule

As for the Near Detector, all steps to prepare ICARUS-T600 must be accomplished by this time, from the submission of the initial design report to start-up of the civil engineering work, construction of cryostats and cryogenics, transportation to site, and overall detector preparation and commissioning.

<b>movement to CERN</b>	Start	End
Laser survey		Complete
Transportation Frames		Complete
Disassembly work		Complete
TPC transport to CERN		Complete
Equipment transport to CERN		Complete
Building 185 preparation		Complete
<b>T600 cryostats</b>		
Engineering cold vessel + production	Jan-13	Sep-16
Engineering cold vessel supports		complete
Engineering warm vessel	Dec14	May15
GTT preliminary study		complete
Procurement extruded Aluminum	Dec14	May15
Assembly cold vessels	Jun15	Dec16
Procurement Warm Vessel + supports	Dec14	Mar16
Procurement Insulation	Jan15	Dec16
Warm vessel assembly	Oct15	Jun16
Insulation installation	Sep16	Dec16
Cold shields	Jan15	Dec16

**TABLE XXIX:** *Summary of ICARUS-WA104 detector overhauling schedules*

The proposed schedule is illustrated in tables [XXIX](#) and [XXX](#). It is a very tight schedule, but with a good level of coordination, it is judged to be feasible, as it is based on the previous experience gained with the Pavia test run in 2001 [\[20\]](#) and the Gran Sasso Physics Run, 2010-2013 [\[9\]](#). Moreover most of the milestones are related to operations at CERN in the frame of the WA104 program, therefore a periodic verification of the project development will be assured. The ICARUS-T600 detector has already be transported to CERN.

### C. Infrastructure Schedule

Table [XXXII](#) shows the schedule for the design, procurement and installation of the cryogenic systems for the near and far detectors. Table [XXXI](#) shows the schedule for the design, procurement and installation of the near detector cryostat. The schedule for the far detector cryostat is included in the schedule for the far detector (Table [XXIX](#)). The schedule for the construction and installation of Cosmic taggers for both near and far detector are presented in Tab. [XXXIV](#).

<b>T600 cryogenics</b>		
Reorganization and packaging	Jan-15	Dec-16
New hardware	May-15	Oct-16
Tests and maintenance	Jan-15	Mar-16
Cryo group at CERN	Mar-15	Oct-16
Vacuum test	Aug-16	Nov-16
Cold gas test (if possible)	Nov-16	Dec-16
<b>T600 refurbishing</b>		
TPC-1 Cabling TPC internal	Dec-14	Aug-15
TPC-1 New PMT procurement	Oct-14	Aug-15
TPC-1 New PMT installation	Mar-15	Sep-15
TPC-1 installation in cold vessel	Nov-15	Jan-16
TPC-2 Cabling TPC internal	Jan-16	Oct-16
TPC-2 New PMT procurement	Oct-15	Jul-16
TPC-2 New PMT installation	Feb-16	Oct-16
TPC-2 installation in cold vessel	Nov-16	Dec-16
New electronics	Mar-14	Dec-16
Final assembly into the warm vessel	Dec-16	Jan-17
<b>T600 controls and tests</b>		
	Start	End
Slow controls hardware	Jan-16	Nov-16
Slow controls software	Jan-16	Nov-16
DAQ system	Jan-16	Nov-16
Tests of Slow controls	Jan-16	Nov-16
Tests of DAQ	Jan-16	Nov-16

**TABLE XXX:** *Summary of ICARUS-WA104 detector overhauling schedules*

Table [XXXIII](#) shows the schedule for design and construction of the far detector and near detector buildings. Also shown is the schedule for the associated site preparation work. The site preparation includes elements that will be completed after construction of the buildings is completed.

<b>Near Detector Cryostat</b>	<b>Start</b>	<b>End</b>
Requirements Documents		Dec 2014
Preliminary Design	Jan 2015	May 2015
Production Readiness Review		Jun 2015
Final Design	Jul 2015	Nov 2015
Procure membrane cryostat materials	Dec 2015	Jun 2016
Procure support structure	Dec 2015	Apr 2016
Procure top plate	Feb 2016	Oct 2016
Delivery to Fermilab (structure)	May 2016	Jun 2016
Delivery to Fermilab (top plate)	Oct 2016	Nov 2016
Assembly	Jul 2016	Nov 2016
Installation	Dec 2016	Jan 2017
Safety Review Complete		Nov 2017

**TABLE XXXI:** *Summary of schedules for design, procurement and installation of the near detector cryostat.*

<b>Near Detector LAr Cryogenics</b>	Start	End
Requirements Documents		Dec 2014
Preliminary Design	Jan 2015	Jun 2015
Production Readiness Review		Aug 2015
Procurement Documents	Sep 2015	Mar 2016
Final Design	Apr 2016	Jun 2016
Fabrication	Jul 2016	Apr 2017
Delivery of skids to Fermilab	Jun 2017	Jul 2017
Installation	May 2017	Oct 2017
Safety Review Complete		Nov 2017
<b>Near Detector LN<sub>2</sub> Cryogenics</b>		
Requirements Documents		Dec 2014
Preliminary Design	Jan 2015	Jun 2015
Production Readiness Review		Aug 2015
Procurement Documents	Sep 2015	Nov 2015
Final Design	Dec 2015	Mar 2016
Fabrication	Apr 2016	Dec 2016
Delivery to Fermilab	Jan 2017	Feb 2017
Installation	Mar 2017	Jul 2017
Safety Review Complete		Nov 2017
<b>Far Detector LAr Cryogenics</b>		
Existing Cryogenics at CERN		Nov 2014
Reorganization and Packaging (Part 1)	Jan 2015	Jun 2015
Production Readiness Review		Aug 2015
Reorganization and Packaging (Part 2)	Sep 2015	Dec 2016
New Hardware	May 2015	Oct 2016
Test and Maintenance	Jan 2015	Mar 2016
Vacuum Test	Aug 2016	Nov 2016
Cold Test	Nov 2016	Dec 2016
Delivery to Fermilab	Jan 2017	Feb 2017
Installation	Mar 2017	Aug 2017
Safety Review Complete		Sep 2017
<b>Far Detector LN<sub>2</sub> Cryogenics</b>		
Requirements Documents		Dec 2014
Preliminary Design	Jan 2015	Jun 2015
Production Readiness Review		Aug 2015
Final Design	Sep 2015	Nov 2015
Procurement Documents	Dec 2015	Mar 2016
Fabrication	Apr 2016	Dec 2016
Delivery to Fermilab	Jan 2017	Feb 2017
Installation	Mar 2017	Jul 2017
Safety Review Complete		Sep 2017

**TABLE XXXII:** Summary of schedules for design, procurement and installation of the cryogenic systems for the near and far detectors.

<b>Site Preparation</b>	Start	End
Preliminary Design	Oct 2014	Nov 2014
Requirements Documents		Nov 2014
Final Design	Jan 2015	Mar 2015
Bidding and Procurement	Apr 2015	May 2015
Construction	May 2015	Jan 2017
<b>Far Detector Building</b>		
Preliminary Design	Jun 2014	Sep 2014
Requirements Documents		Nov 2014
Final Design	Nov 2014	Mar 2015
Final Design Review		Mar 2015
Bidding and Procurement	Apr 2015	May 2015
Construction	May 2015	Jan 2017
Beneficial Occupancy		Nov 2016
<b>Near Detector Building</b>		
Preliminary Design	Jun 2014	Sep 2014
Requirements Documents		Feb 2015
Final Design	Feb 2015	May 2015
Final Design Review		May 2015
Bidding and Procurement	Jun 2015	Aug 2015
Construction	Aug 2015	Nov 2016
Beneficial Occupancy		Sep 2016

**TABLE XXXIII:** *Summary of civil construction schedules for the site preparation, far detector building and near detector building*

<b>Cosmic Tagger</b>		
Requirements Documents		Jan 2015
Preliminary Design	Nov 2014	Mar 2015
Final Design	Mar 2015	Jul 2015
Production Readiness Review		Jul 2015
Fabrication of strips	Jul 2015	Jun 2016
Assembly bottom plane	Mar 2016	Jun 2016
Assembly side planes	Jun 2016	Dec 2016
Assembly top planes	Mar 2016	Apr 2017
Delivery of bottom to Fermilab	Jun 2016	Aug 2016
Delivery of sides to Fermilab	Dec 2016	Feb 2017
Delivery of top to Fermilab	Apr 2017	Jun 2017
Installation bottom	Nov 2016	Nov 2016
Installation sides	Sep 2017	Sep 2017
Installation top	Dec 2017	Dec 2017

**TABLE XXXIV:** *Summary of construction and installation of the Cosmics tagger*

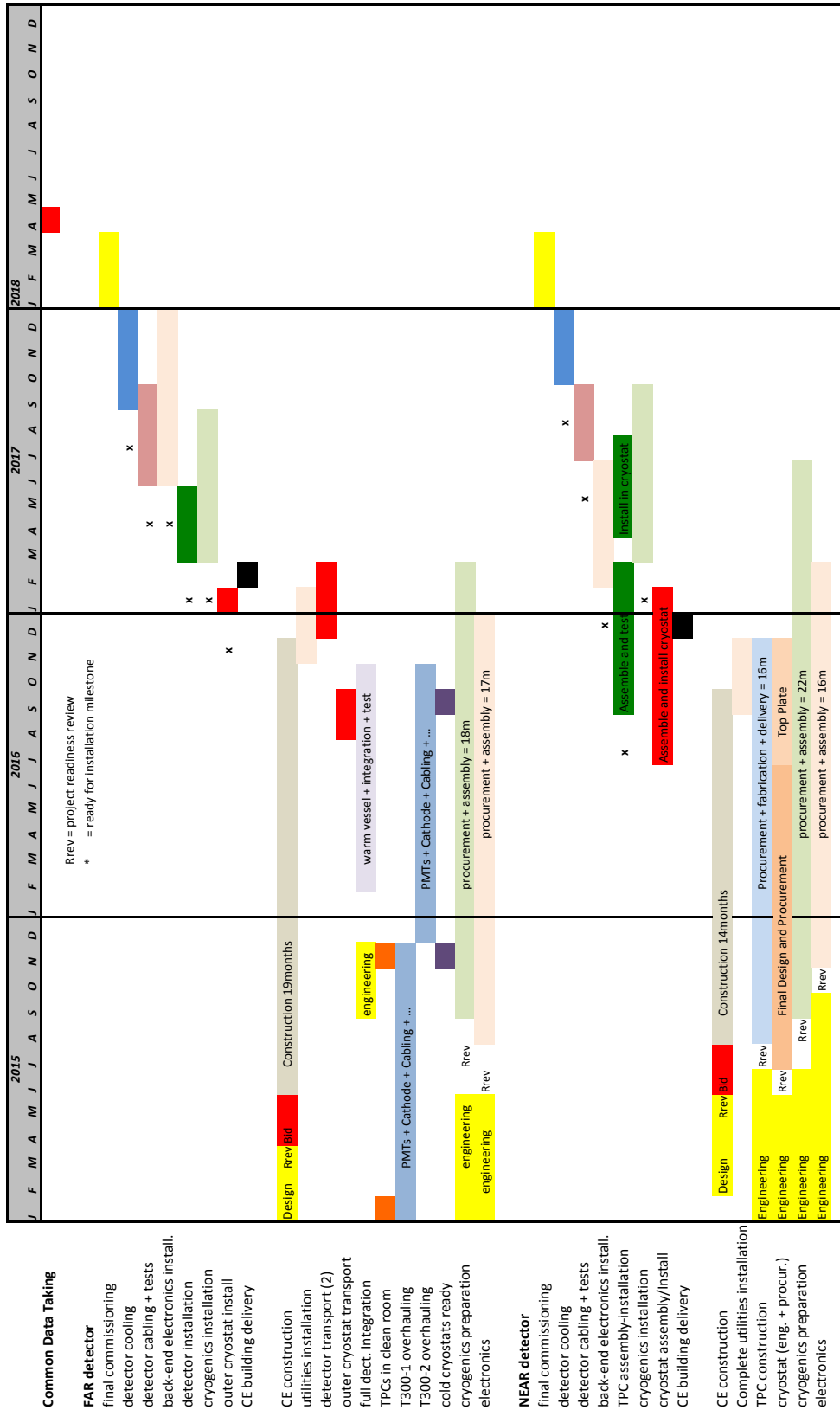


FIG. 129: Overall summary schedule for the far and near detector construction



### A. Detector Volumes and Masses

**TABLE XXXV:** *TPC active and fiducial volumes in each SBN detector used in these analyses.*

Detector volume	W (cm)	H (cm)	L (cm)	volume ( $m^3$ )	argon mass (tons)
LAr1-ND Active	2×200	400	500	80.0	112
LAr1-ND Fiducial ( $\nu_\mu$ analysis)	2×183.5	370	405	55.0	77.0
LAr1-ND Fiducial ( $\nu_e$ analysis)	2×173.5	350	420	51.0	71.4
MicroBooNE Active	256	233	1037	61.9	86.6
MicroBooNE Fiducial ( $\nu_\mu$ analysis)	226	203	942	43.2	60.5
MicroBooNE Fiducial ( $\nu_e$ analysis)	206	183	957	34.2	47.9
ICARUS-T600 Active	4×150	316	1795	340.3	476
ICARUS-T600 Fiducial ( $\nu_\mu$ analysis)	4×133.5	286	1700	259.6	363
ICARUS-T600 Fiducial ( $\nu_e$ analysis)	4×123.5	266	1715	225.4	315

- 
- [1] M. Antonello *et al.*, “ICARUS at FNAL,” (2014), [FERMILAB-PROPOSAL-1052](#).
  - [2] B. Baibussinov, E. Calligarich, S. Centro, D. Gibin, A. Guglielmi, *et al.*, “A New search for anomalous neutrino oscillations at the CERN-PS,” (2009), [arXiv:0909.0355 \[hep-ex\]](#).
  - [3] C. Rubbia *et al.*, “Physics Programme for ICARUS after 2012,” (2011), CERN-SPSC-2011-012, SPSC-M-773.
  - [4] C. Rubbia *et al.*, “A comprehensive search for anomalies from neutrino and anti-neutrino oscillations at large mass differences with two LArTPC imaging detectors at different distances from the CERN-PS,” (2011), CERN-SPSC-P-345.
  - [5] P. Bernardini, A. Bertolin, C. Bozza, R. Brugnera, A. Cecchetti, *et al.*, “Prospect for Charge Current Neutrino Interactions Measurements at the CERN-PS,” (2011), CERN-SPSC-2011-030, SPSC-P-343, [arXiv:1111.2242 \[hep-ex\]](#).
  - [6] M. Antonello, D. Bagliani, B. Baibussinov, H. Bilokon, F. Boffelli, *et al.*, “Search for ‘anomalies’ from neutrino and anti-neutrino oscillations at  $\Delta m^2 \sim 1eV^2$  with muon spectrometers and large LAr-TPC imaging detectors,” (2012), CERN-SPSC-2012-010, SPSC-P-347, [arXiv:1203.3432 \[physics.ins-det\]](#).
  - [7] C. Adams *et al.*, “LAr1-ND: Testing Neutrino Anomalies with Multiple LAr TPC Detectors at Fermilab,” (2014), [FERMILAB-PROPOSAL-1053](#).
  - [8] H. Chen *et al.*, “A letter of Intent for a neutrino oscillation experiment on the Booster Neutrino Beamline: LAr1,” (2012), [FERMILAB-PROPOSAL-1030](#).
  - [9] C. Rubbia, M. Antonello, P. Aprili, B. Baibussinov, M. Baldo Ceolin, *et al.*, “Underground operation of the ICARUS T600 LAr-TPC: first results,” *JINST* **6**, P07011 (2011), [arXiv:1106.0975 \[hep-ex\]](#).
  - [10] P. Wilson *et al.*, “Program Definition Status Report: Short-Baseline Neutrino Oscillation Program on the Fermilab Booster Neutrino Beam,” submitted to the Fermilab PAC in July 2014.
  - [11] I. Stancu *et al.* (BooNE Collaboration), “Technical Design Report for the 8 GeV Beam,” [http://www-boone.fnal.gov/publicpages/8gevtdr\\_2.0.ps.gz](http://www-boone.fnal.gov/publicpages/8gevtdr_2.0.ps.gz) (2001).
  - [12] I. Stancu *et al.* (BooNE Collaboration), “Technical Design Report for the MiniBooNE Neutrino Beam,” [http://www-boone.fnal.gov/publicpages/target\\_tdr.ps.gz](http://www-boone.fnal.gov/publicpages/target_tdr.ps.gz) (2001).
  - [13] A.A. Aguilar-Arevalo *et al.* (MiniBooNE Collaboration), “The Neutrino Flux prediction at Mini-BooNE,” *Phys.Rev.* **D79**, 072002 (2009), [arXiv:0806.1449 \[hep-ex\]](#).
  - [14] M.G. Catanesi *et al.* (HARP Collaboration), “Measurement of the production cross-section of positive pions in the collision of 8.9-GeV/c protons on beryllium,” *Eur.Phys.J.* **C52**, 29–53 (2007), [arXiv:hep-ex/0702024 \[hep-ex\]](#).
  - [15] David W. Schmitz, *A measurement of hadron production cross sections for the simulation of accelerator neutrino beams and a search for  $\nu_\mu$  to  $\nu_e$  oscillations in the  $\Delta m^2 \sim 1 eV^2$  region*, Ph.D. thesis, Columbia University, FERMILAB-THESIS-2008-26 (2008).
  - [16] A. A. Aguilar-Arevalo *et al.* (MiniBooNE Collaboration), “First measurement of the muon neutrino charged current quasielastic double differential cross section,” *Phys. Rev. D* **81**, 092005 (2010).
  - [17] A. Ereditato *et al.*, “A steerable UV laser system for the calibration of liquid argon time projection chambers,” (2014), [arXiv:1406.6400 \[physics.ins-det\]](#).
  - [18] MicroBooNE project, “The MicroBooNE Technical Design Report,” CD3b review (February 2012).
  - [19] T. Briese, L. Bugel, J.M. Conrad, M. Fournier, C. Ignarra, *et al.*, “Testing of Cryogenic Photo-

- multiplier Tubes for the MicroBooNE Experiment,” *JINST* **8**, T07005 (2013), [arXiv:1304.0821 \[physics.ins-det\]](#).
- [20] S. Amerio *et al.* (ICARUS Collaboration), “Design, construction and tests of the ICARUS T600 detector,” *Nucl.Instrum.Meth.* **A527**, 329–410 (2004).
- [21] K.A. Olive *et al.* (Particle Data Group), “Review of particle physics,” *Chin. Phys. C* **38**, 090001 (2014).
- [22] K.N. Abazajian, M.A. Acero, S.K. Agarwalla, A.A. Aguilar-Arevalo, C.H. Albright, *et al.*, “Light Sterile Neutrinos: A White Paper,” (2012), [arXiv:1204.5379 \[hep-ph\]](#).
- [23] G. Mention, M. Fechner, Th. Lasserre, Th.A. Mueller, D. Lhuillier, *et al.*, “The Reactor Antineutrino Anomaly,” *Phys.Rev.* **D83**, 073006 (2011), [arXiv:1101.2755 \[hep-ex\]](#).
- [24] W. Hampel *et al.* (GALLEX Collaboration), “Final results of the Cr-51 neutrino source experiments in GALLEX,” *Phys.Lett.* **B420**, 114–126 (1998).
- [25] J.N. Abdurashitov *et al.* (SAGE Collaboration), “Measurement of the response of the Russian-American gallium experiment to neutrinos from a Cr-51 source,” *Phys.Rev.* **C59**, 2246–2263 (1999), [arXiv:hep-ph/9803418 \[hep-ph\]](#).
- [26] A. Aguilar-Arevalo *et al.* (LSND Collaboration), “Evidence for neutrino oscillations from the observation of anti-neutrino(electron) appearance in a anti-neutrino(muon) beam,” *Phys.Rev.* **D64**, 112007 (2001), [arXiv:hep-ex/0104049 \[hep-ex\]](#).
- [27] A.A. Aguilar-Arevalo *et al.* (MiniBooNE Collaboration), “A Search for electron neutrino appearance at the  $\Delta m^2 \sim 1 \text{ eV}^2$  scale,” *Phys.Rev.Lett.* **98**, 231801 (2007), [arXiv:0704.1500 \[hep-ex\]](#).
- [28] A.A. Aguilar-Arevalo *et al.* (MiniBooNE Collaboration), “Unexplained Excess of Electron-Like Events From a 1-GeV Neutrino Beam,” *Phys.Rev.Lett.* **102**, 101802 (2009), [arXiv:0812.2243 \[hep-ex\]](#).
- [29] A.A. Aguilar-Arevalo *et al.* (MiniBooNE Collaboration), “Improved Search for  $\bar{\nu}_\mu \rightarrow \bar{\nu}_e$  Oscillations in the MiniBooNE Experiment,” *Phys.Rev.Lett.* **110**, 161801 (2013), [arXiv:1207.4809 \[hep-ex\]](#).
- [30] Th.A. Mueller, D. Lhuillier, M. Fallot, A. Letourneau, S. Cormon, *et al.*, “Improved Predictions of Reactor Antineutrino Spectra,” *Phys.Rev.* **C83**, 054615 (2011), [arXiv:1101.2663 \[hep-ex\]](#).
- [31] Patrick Huber, “On the determination of anti-neutrino spectra from nuclear reactors,” *Phys.Rev.* **C84**, 024617 (2011), [arXiv:1106.0687 \[hep-ph\]](#).
- [32] Lasserre T., “(Light) Sterile Neutrinos,” <https://indico.cern.ch/event/303475/contribution/11/material/slides/0.pdf> (2014).
- [33] A.C. Hayes, J.L. Friar, G.T. Garvey, Gerard Jungman, and Guy Jonkmans, “Systematic Uncertainties in the Analysis of the Reactor Neutrino Anomaly,” *Phys.Rev.Lett.* **112**, 202501 (2014), [arXiv:1309.4146 \[nucl-th\]](#).
- [34] A.A. Aguilar-Arevalo *et al.* (MiniBooNE Collaboration), “A Search for Electron Antineutrino Appearance at the  $\Delta m^2 \sim 1 \text{ eV}^2$  Scale,” *Phys.Rev.Lett.* **103**, 111801 (2009), [arXiv:0904.1958 \[hep-ex\]](#).
- [35] B. Armbruster *et al.* (KARMEN Collaboration), “Upper limits for neutrino oscillations  $\bar{\nu}_\mu \rightarrow \bar{\nu}_e$  from muon decay at rest,” *Phys. Rev. D* **65**, 112001 (2002).
- [36] A. Romosan *et al.*, “High Statistics Search for Oscillations in the Small Mixing Angle Regime,” *Phys. Rev. Lett.* **78**, 2912–2915 (1997).
- [37] S. Avvakumov *et al.*, “Search for Oscillations at NuTeV,” *Phys. Rev. Lett.* **89**, 011804 (2002).
- [38] P. Astier *et al.*, “Search for neutrino oscillations in the NOMAD experiment,” *Physics Letters B* **570**, 19 – 31 (2003).
- [39] M Antonello, B Baibussinov, P Benetti, E Calligarich, N Canci, *et al.*, “Search for anomalies in

- the  $\nu_e$  appearance from a  $\nu_\mu$  beam,” *Eur.Phys.J.* **C73**, 2599 (2013), [arXiv:1307.4699 \[hep-ex\]](#).
- [40] C. Giunti, M. Laveder, Y.F. Li, and H.W. Long, “Pragmatic View of Short-Baseline Neutrino Oscillations,” *Phys.Rev.* **D88**, 073008 (2013), [arXiv:1308.5288 \[hep-ph\]](#).
- [41] Joachim Kopp, Pedro A. N. Machado, Michele Maltoni, and Thomas Schwetz, “Sterile Neutrino Oscillations: The Global Picture,” *JHEP* **1305**, 050 (2013), [arXiv:1303.3011 \[hep-ph\]](#).
- [42] K. B. M. Mahn, Y. Nakajima, *et al.* (MiniBooNE and SciBooNE Collaborations), “Dual baseline search for muon neutrino disappearance at  $0.5\text{eV}^2 < \Delta m^2 < 40\text{eV}^2$ ,” *Phys. Rev. D* **85**, 032007 (2012).
- [43] A. Aguilar-Arevalo *et al.* (MiniBooNE Collaboration), “Search for Muon Neutrino and Antineutrino Disappearance in MiniBooNE,” *Phys. Rev. Lett.* **103**, 061802 (2009).
- [44] P. Adamson *et al.* (The MINOS Collaboration), “Search for sterile neutrino mixing in the MINOS long-baseline experiment,” *Phys. Rev. D* **81**, 052004 (2010).
- [45] P. Adamson *et al.* (MINOS Collaboration), “Active to Sterile Neutrino Mixing Limits from Neutral-Current Interactions in MINOS,” *Phys. Rev. Lett.* **107**, 011802 (2011).
- [46] F. Dydak *et al.*, “A search for oscillations in the  $m^2$  range  $0.390\text{ eV}^2$ ,” *Physics Letters B* **134**, 281 – 286 (1984).
- [47] N Agafonova *et al.*, “Search for  $\nu_{\mu} \rightarrow \nu_{\tau}$  oscillations with the OPERA experiment in the CNGS beam,” *J.H.E.Phys.* **1307**, 004 (2013), [arXiv:1303.3953 \[hep-ex\]](#).
- [48] M Antonello, B Baibussinov, P Benetti, E Calligarich, N Canci, *et al.*, “Experimental search for the LSND anomaly with the ICARUS detector in the CNGS neutrino beam,” *Eur.Phys.J.* **C73**, 2345 (2013), [arXiv:1209.0122 \[hep-ex\]](#).
- [49] Lasserre T., “Light Sterile Neutrinos in Particle Physics,” (2014), [arXiv:1404.7352 \[hep-ph\]](#).
- [50] Andi S. Cucoanes (Nucifer Collaboration), “Status of the Nucifer experiment,” *J.Phys.Conf.Ser.* **375**, 042063 (2012).
- [51] K.N. Abazajian, M.A. Acero, S.K. Agarwalla, A.A. Aguilar-Arevalo, C.H. Albright, *et al.*, “Light Sterile Neutrinos: A White Paper,” (2012), [arXiv:1204.5379 \[hep-ph\]](#).
- [52] I. Alekseev, V. Belov, V. Brudanin, M. Danilov, V. Egorov, *et al.*, “DANSSino: a pilot version of the DANSS neutrino detector,” *Phys.Part.Nucl.Lett.* **11**, 473–482 (2014), [arXiv:1305.3350 \[physics.ins-det\]](#).
- [53] A.P. Serebrov, V.G. Zinoviev, A.K. Fomin, U.E. Loginov, M.S. Onegin, *et al.*, “NEUTRINO4 experiment: preparations for search for sterile neutrino at 100 MW Reactor SM-3 at 6-12 Meters,” (2012), [arXiv:1205.2955 \[hep-ph\]](#).
- [54] Gang Guo, Fang Han, Xiangdong Ji, Jianglai Liu, Zhaoxu Xi, *et al.*, “Sterile Neutrino Search Using China Advanced Research Reactor,” (2013), [arXiv:1303.0607 \[physics.ins-det\]](#).
- [55] J. Ashenfelter *et al.* (PROSPECT Collaboration), “PROSPECT - A Precision Reactor Oscillation and Spectrum Experiment at Very Short Baselines,” (2013), [arXiv:1309.7647 \[physics.ins-det\]](#).
- [56] G. Bellini *et al.* (Borexino Collaboration), “SOX: Short distance neutrino Oscillations with BoreXino,” *JHEP* **1308**, 038 (2013), [arXiv:1304.7721 \[physics.ins-det\]](#).
- [57] Michel Cribier, Maximilien Fechner, Thierry Lasserre, Alain Letourneau, David Lhuillier, *et al.*, “A proposed search for a fourth neutrino with a PBq antineutrino source,” *Phys.Rev.Lett.* **107**, 201801 (2011), [arXiv:1107.2335 \[hep-ex\]](#).
- [58] A. Gando, Y. Gando, S. Hayashida, H. Ikeda, K. Inoue, *et al.*, “CeLAND: search for a 4th light neutrino state with a 3 PBq  $^{144}\text{Ce}$ - $^{144}\text{Pr}$  electron antineutrino generator in KamLAND,” (2013), [arXiv:1312.0896 \[physics.ins-det\]](#).
- [59] J. Angrik *et al.* (KATRIN Collaboration), “KATRIN design report 2004,” (2005).

- [60] J.A. Formaggio and J. Barrett, “Resolving the Reactor Neutrino Anomaly with the KATRIN Neutrino Experiment,” *Phys.Lett.* **B706**, 68–71 (2011), [arXiv:1105.1326 \[nucl-ex\]](#).
- [61] Arman Esmaili and Orlando L.G. Peres, “KATRIN Sensitivity to Sterile Neutrino Mass in the Shadow of Lightest Neutrino Mass,” *Phys.Rev.* **D85**, 117301 (2012), [arXiv:1203.2632 \[hep-ph\]](#).
- [62] C. Aberle, A. Adelman, J. Alonso, W.A. Barletta, R. Barlow, *et al.*, “Whitepaper on the DAEdALUS Program,” (2013), [arXiv:1307.2949](#).
- [63] M. Elnimr *et al.* (OscSNS Collaboration), “The OscSNS White Paper,” (2013), [arXiv:1307.7097](#).
- [64] Thierry Lasserre, “Light Sterile Neutrinos in Particle Physics: Experimental Status,” (2014), [arXiv:1404.7352 \[hep-ex\]](#).
- [65] D. Adey, S.K. Agarwalla, C.M. Ankenbrandt, R. Asfandiyarov, J.J. Back, *et al.*, “Neutrinos from Stored Muons nuSTORM: Expression of Interest,” (2013), [arXiv:1305.1419 \[physics.acc-ph\]](#).
- [66] P. Kyberd *et al.* (nuSTORM Collaboration), “nuSTORM - Neutrinos from STORed Muons: Letter of Intent to the Fermilab Physics Advisory Committee,” (2012), [arXiv:1206.0294 \[hep-ex\]](#).
- [67] T.T. Bhlen, F. Cerutti, M.P.W. Chin, A. Fass, A. Ferrari, P.G. Ortega, A. Mairani, P.R. Sala, G. Smirnov, and V. Vlachoudis, “The {FLUKA} Code: Developments and Challenges for High Energy and Medical Applications,” *Nuclear Data Sheets* **120**, 211 – 214 (2014).
- [68] A. Ferrari, P.R. Sala, A. Fassò, and J. Ranft, *FLUKA: a multi-particle transport code*, Tech. Rep. CERN-2005-10, INFN/TC\_05/11, SLAC-R-773 (CERN, 2005).
- [69] G. Battistoni, A. Ferrari, M. Lantz, P. R. Sala, and G. I. Smirnov, “A neutrino-nucleon interaction generator for the FLUKA Monte Carlo code,” in *CERN-Proceedings-2010-001*, pp. 387–394.
- [70] I. Chemakin *et al.* (E910 Collaboration), “Pion production by protons on a thin beryllium target at 6.4-GeV, 12.3-GeV/c, and 17.5-GeV/c incident proton momenta,” *Phys.Rev.* **C77**, 015209 (2008), [arXiv:0707.2375 \[nucl-ex\]](#).
- [71] F. Abe, K. Hara, S. Kim, K. Kondo, S. Miyashita, *et al.*, “Production of Neutral Strange Particles  $K_S^0$  and  $\Lambda^0$  by 12-GeV Protons on Nuclear Targets,” *Phys.Rev.* **D36**, 1302–1319 (1987).
- [72] G. Cheng *et al.* (SciBooNE Collaboration), “Measurement of  $K^+$  production cross section by 8 GeV protons using high energy neutrino interactions in the SciBooNE detector,” *Phys.Rev.* **D84**, 012009 (2011), [arXiv:1105.2871 \[hep-ex\]](#).
- [73] C. Andreopoulos *et al.*, “The GENIE Neutrino Monte Carlo Generator,” *Nucl. Instrum. Meth.* **A614**, 87–104 (2010), [arXiv:0905.2517 \[hep-ph\]](#).
- [74] G.T. Garvey, D.A. Harris, H.A. Tanaka, R. Tayloe, and G.P. Zeller, “Recent Advances and Open Questions in Neutrino-induced Quasi-elastic Scattering and Single Photon Production,” (2014), [arXiv:1412.4294 \[hep-ex\]](#).
- [75] L. Alvarez-Ruso, Y. Hayato, and J. Nieves, “Progress and open questions in the physics of neutrino cross sections at intermediate energies,” *New J.Phys.* **16**, 075015 (2014), [arXiv:1403.2673 \[hep-ph\]](#).
- [76] C. Andreopoulos *et al.* (GENIE Collaboration), “The GENIE Neutrino Monte Carlo Generator: Physics and Users Manual,” [http://genie.hepforge.org/manuals/GENIE\\_PhysicsAndUserManual\\_20130615.pdf](http://genie.hepforge.org/manuals/GENIE_PhysicsAndUserManual_20130615.pdf) (2013).
- [77] G. Battistoni, A. Ferrari, T. Montaruli, and P.R. Sala, “Comparison of the {FLUKA} calculations with {CAPRICE94} data on muons in atmosphere,” *Astroparticle Physics* **17**, 477 – 488 (2002).
- [78] S.Muraro, Ph.D. thesis (2006).
- [79] P Zuccon, B Bertucci, B Alpat, G Ambrosi, R Battiston, G Battistoni, W.J Burger, D Caraf-

- fini, C Cecchi, L Di Masso, N Dinu, G Esposito, A Ferrari, E Fiandrini, M Ionica, R Ionica, G Lamanna, M Menichelli, M Pauluzzi, and P.R Sala, “Atmospheric production of energetic protons, electrons and positrons observed in near Earth orbit,” *Astroparticle Physics* **20**, 221 – 234 (2003).
- [80] C. Hagmann, D. Lange, and D. Wright, “Monte Carlo Simulation of Proton-induced Cosmic-ray Cascades in the Atmosphere,” [http://nuclear.llnl.gov/simulation/doc\\_cry\\_v1.7/cry\\_physics.pdf](http://nuclear.llnl.gov/simulation/doc_cry_v1.7/cry_physics.pdf). (2012).
- [81] T. Gaisser, “Cosmic Rays and Particle Physics,” Cambridge University Press, 1990. isbn: 978-0521339315. (1990).
- [82] C. Rubbia, “Searching for short baseline anomalies with the LAr-TPC detector at shallow depths,” (2014), [arXiv:hep-ex/0702024](https://arxiv.org/abs/hep-ex/0702024) [hep-ex].
- [83] C. Rubbia, “Searching for short baseline anomalies with the LAr-TPC detector at shallow depths,” (2014), SBN docdb 113, internal SBN report.
- [84] P. Adamson *et al.*, “Measurement of  $\nu_\mu$  and  $\nu_e$  Events in an Off-Axis Horn-Focused Neutrino Beam,” *Phys. Rev. Lett.* **102**, 211801 (2009).
- [85] Alexis A. Aguilar-Arevalo *et al.* (MiniBooNE Collaboration), “Measurement of  $\nu(\mu)$  and anti- $\nu(\mu)$  induced neutral current single  $\pi^0$  production cross sections on mineral oil at  $E(\nu) \sim 0(1\text{-GeV})$ ,” *Phys.Rev.* **D81**, 013005 (2010), [arXiv:0911.2063](https://arxiv.org/abs/0911.2063) [hep-ex].
- [86] S. Gninenko, “MiniBooNE Anomaly and Heavy Neutrino Decay,” *Phys. Rev. Lett.* **103**, 241802 (2009).
- [87] S. Gninenko, “Sterile neutrino decay as a common origin for LSND/MiniBooNE and T2K excess events,” *Phys. Rev. D* **85**, 051702 (2012).
- [88] Brian Batell, Maxim Pospelov, and Adam Ritz, “Exploring portals to a hidden sector through fixed targets,” *Phys. Rev. D* **80**, 095024 (2009).
- [89] Patrick deNiverville, Maxim Pospelov, and Adam Ritz, “Observing a light dark matter beam with neutrino experiments,” *Phys. Rev. D* **84**, 075020 (2011).
- [90] Patrick deNiverville, David McKeen, and Adam Ritz, “Signatures of sub-GeV dark matter beams at neutrino experiments,” *Phys. Rev. D* **86**, 035022 (2012).
- [91] A.A. Aguilar-Arevalo *et al.* (MiniBooNE Collaboration), “A Search for Electron Antineutrino Appearance at the  $\Delta m^2 \sim 1 \text{ eV}^2$  Scale,” *Phys.Rev.Lett.* **103**, 111801 (2009), [arXiv:0904.1958](https://arxiv.org/abs/0904.1958) [hep-ex].
- [92] H. Chen *et al.* (MicroBooNE Collaboration), “Proposal for a New Experiment Using the Booster and NuMI Neutrino Beamlines: MicroBooNE,” (2007).
- [93] D. Kaleko, “Low Energy Excess: MiniBooNE to MicroBooNE,” MicroBooNE Document 3862 (2014).
- [94] A.A. Aguilar-Arevalo *et al.* (MiniBooNE Collaboration), “Event Excess in the MiniBooNE Search for  $\bar{\nu}_\mu \rightarrow \bar{\nu}_e$  Oscillations,” *Phys.Rev.Lett.* **105**, 181801 (2010), [arXiv:1007.1150](https://arxiv.org/abs/1007.1150) [hep-ex].
- [95] A. Blatter, A. Ereditato, C C. Hsu, S. Janos, I. Kreslo, M. Luethi, C. Rudolf von Rohr, M. Schenk, T. Strauss, M S. Weber, and M. Zeller, “Experimental study of electric breakdowns in liquid argon at centimeter scale,” *JINST* **9**, P04006 (2014).
- [96] J. Asaadi, J M. Conrad, S. Gollapinni, B J P. Jones, H. Jostlein, J M. St John, T. Strauss, S. Wolbers, and J. Zennamo, “Testing of high voltage surge protection devices for use in liquid argon TPC detectors,” *JINST* **9**, P09002 (2014).
- [97] D. Axen, R. Hackenburg, A. Hoffmann, S. Kane, D. Lissauer, D. Makowiecki, T. Muller, D. Pate, V. Radeka, D. Rahm, M. Rehak, S. Rescia, K. Sexton, J. Sondericker, P. Birney, A. W. Dowling,

- M. Fincke-Keeler, T. Hodges, F. Holness, N. Honkanen, R. Keeler, R. Langstaff, M. Lenckowski, M. Lefebvre, P. Poffenberger, G. Vowles, and C. Oram, “Signal feedthroughs for the atlas barrel and endcap calorimeters,” *Review of Scientific Instruments* **76**, 063306 (2005).
- [98] A. Ereditato, D. Goeldi, S. Janos, I. Kreslo, M. Luethi, *et al.*, “Measurement of the drift field in the ARGONTUBE LAr TPC with 266 nm pulsed laser beams,” (2014), [arXiv:1408.6635 \[physics.ins-det\]](#).
- [99] I. Badhrees, A. Ereditato, S. Janos, S. Haug, I. Kreslo, *et al.*, “Argontube: An & liquid Argon Time Projection Chamber,” *JINST* **7**, C02011 (2012).
- [100] A. Ereditato, C.C. Hsu, S. Janos, I. Kreslo, M. Messina, *et al.*, “Design and operation of ARGONTUBE: a 5 m long drift liquid argon TPC,” *JINST* **8**, P07002 (2013), [arXiv:1304.6961 \[physics.ins-det\]](#).
- [101] M. Zeller, A. Ereditato, S. Haug, C.C. Hsu, S. Janos, *et al.*, “First measurements with ARGONTUBE, a 5m long drift Liquid Argon TPC,” *Nucl.Instrum.Meth.* **A718**, 454–458 (2013).
- [102] I. Badhrees, A. Ereditato, I. Kreslo, M. Messina, U. Moser, *et al.*, “Measurement of the two-photon absorption cross-section of liquid argon with a time projection chamber,” *New J.Phys.* **12**, 113024 (2010), [arXiv:1011.6001 \[physics.ins-det\]](#).
- [103] A. Ereditato, R. Hnni, I. Kreslo, M. Lthi, C. Rudolf von Rohr, *et al.*, “A steerable UV laser system for the calibration of liquid argon time projection chambers,” (2014), [arXiv:1406.6400 \[physics.ins-det\]](#).
- [104] M. Szydagis, “NEST (Noble Element Simulation Technique),” FNAL, Software Workshop, 2013.
- [105] M. Sorel, “Expected performance of an ideal liquid argon neutrino detector with enhanced sensitivity to scintillation light,” *JINST* **9**, P10002 (2014), [arXiv:1405.0848 \[physics.ins-det\]](#).
- [106] J. B. Albert *et al.* ((EXO-200 Collaboration)), “Search for Majoron-emitting modes of double-beta decay of  $^{136}\text{Xe}$  with EXO-200,” *Phys. Rev. D* **90**, 092004 (2014).
- [107] E. Segreto, “An analytic technique for the estimation of the light yield of a scintillation detector,” *JINST* **7**, P05008 (2012), [arXiv:1110.6370 \[physics.ins-det\]](#).
- [108] Kuraray Co, Methacrylic Resin Division, Tokyo, Japan,.
- [109] O. Mineev, Yu. Kudenko, Yu. Musienko, I. Polyansky, and N. Yershov, “Scintillator detectors with long WLS fibers and multi-pixel photodiodes,” *JINST* **6**, P12004 (2011), [arXiv:1110.2651 \[physics.ins-det\]](#).
- [110] Hamamatsu Photonics, “MPPC Technical Information,” [http://www.hamamatsu.com/resources/pdf/ssd/mppc\\_techinfo\\_e.pdf](http://www.hamamatsu.com/resources/pdf/ssd/mppc_techinfo_e.pdf).
- [111] F.J. Hasert *et al.*, “Search for elastic muon-neutrino electron scattering,” *Physics Letters B* **46**, 121 – 124 (1973).
- [112] F.J. Hasert *et al.*, “Observation of neutrino-like interactions without muon or electron in the Gargamelle neutrino experiment,” *Physics Letters B* **46**, 138 – 140 (1973).
- [113] C. Rubbia, “The Liquid Argon Time Projection Chamber: A New Concept for Neutrino Detectors,” (1977).
- [114] P. Benetti *et al.*, “A three-ton liquid argon time projection chamber,” *Nucl.Instrum.Meth.* **A332**, 395 – 412 (1993).
- [115] P. Cennini *et al.*, “Performance of a three-ton liquid argon time projection chamber,” *Nucl.Instrum.Meth.* **A345**, 230 – 243 (1994).
- [116] F. Arneodo *et al.*, “First observation of 140-cm drift ionizing tracks in the ICARUS liquid-argon TPC,” *Nucl.Instrum.Meth.* **A449**, 36 – 41 (2000).
- [117] P Cennini *et al.*, “Detection of scintillation light in coincidence with ionizing tracks in a liquid argon time projection chamber,” *Nucl.Instrum.Meth.* **A432**, 240 – 248 (1999).

- [118] F. Arneodo *et al.*, “Performance of the 10m<sup>3</sup> ICARUS liquid argon prototype,” *Nucl.Instrum.Meth.* **A498**, 292 – 311 (2003).
- [119] M. Antonello *et al.*, “Measurement of the neutrino velocity with the ICARUS detector at the CNGS beam,” *Physics Letters B* **713**, 17 – 22 (2012).
- [120] M. Antonello *et al.*, “Precision measurement of the neutrino velocity with the icarus detector in the cngs beam,” *Journal of High Energy Physics* **2012**, 49 (2012), [10.1007/JHEP11\(2012\)049](https://doi.org/10.1007/JHEP11(2012)049).
- [121] M. Antonello, B. Baibussinov, P. Benetti, F. Boffelli, A. Bubak, *et al.*, “Experimental observation of an extremely high electron lifetime with the ICARUS-T600 LAr-TPC,” (2014), [10.1088/1748-0221/9/12/P12006](https://doi.org/10.1088/1748-0221/9/12/P12006), [arXiv:1409.5592 \[physics.ins-det\]](https://arxiv.org/abs/1409.5592).
- [122] B. Baibussinov *et al.*, “A new, very massive modular Liquid Argon Imaging Chamber to detect low energy off-axis neutrinos from the CNGS beam (Project MODULAR),” *Astroparticle Physics* **29**, 174 – 187 (2008).
- [123] D. Angeli *et al.*, “Towards a new Liquid Argon Imaging Chamber for the MODULAR project,” *Journal of Instrumentation* **4**, P02003 (2009).
- [124] Giuseppe Battistoni, S. Muraro, Paola R. Sala, Fabio Cerutti, A. Ferrari, *et al.*, “The FLUKA code: Description and benchmarking,” *AIP Conf.Proc.* **896**, 31–49 (2007).
- [125] <http://www-numi.fnal.gov>.
- [126] C. Rubbia, “Searching for short baseline anomalies with the LAr-TPC detector at shallow depths,” (2014), [arXiv:1408.6431 \[physics.ins-det\]](https://arxiv.org/abs/1408.6431).
- [127] for the ICARUS Collaboration C. Rubbia, “Using the beam bunch-structure with the T600 detector,” internal SBN report (2014).
- [128] S. Amoruso *et al.*, “Study of electron recombination in liquid argon with the ICARUS TPC,” *Nucl.Instrum.Meth.* **A523**, 275 – 286 (2004).
- [129] A. Ankowski *et al.*, “Characterization of ETL 9357FLA photomultiplier tubes for cryogenic temperature applications,” *Nucl.Instrum.Meth.* **A556**, 146 – 157 (2006).
- [130] P. Benetti, C. Montanari, G.L. Raselli, M. Rossella, and C. Vignoli, “Detection of the VUV liquid argon scintillation light by means of glass-window photomultiplier tubes,” *Nucl.Instrum.Meth.* **A505**, 89 – 92 (2003), proceedings of the tenth Symposium on Radiation Measurements and Applications.
- [131] M. Antonello *et al.*, “The trigger system of the ICARUS experiment for the CNGS beam,” *Journal of Instrumentation* **9**, P08003 (2014).
- [132] <http://www.airliquide.it/>.
- [133] <http://www.stirlingcryogenics.com/>.
- [134] A. Falcone *et al.*, “Comparison between large area photo-multiplier tubes at cryogenic temperature for neutrino and rare event physics experiments,” *Nucl.Instrum.Meth.* , – (2014).
- [135] B. Baibussinov *et al.*, “The ICARUS Front-end Preamplifier Working at Liquid Argon Temperature,” ArXiv e-prints (2011), [arXiv:1108.3825 \[physics.ins-det\]](https://arxiv.org/abs/1108.3825).
- [136] M. Lipinski *et al.*, “Performance results of the first white rabbit installation for cngs time transfer,” in *Precision Clock Synchronization for Measurement Control and Communication (ISPCS), 2012 International IEEE Symposium on* (2012) pp. 1–6.
- [137] <http://www.gtt.fr>.
- [138] <http://www.ihl.co.jp/en>.
- [139] M. Antonello *et al.*, “Precise 3D track reconstruction algorithm for the ICARUS T600 liquid argon time projection chamber detector,” ArXiv e-prints (2012), [arXiv:1210.5089 \[physics.ins-det\]](https://arxiv.org/abs/1210.5089).
- [140] K. M. Graczyk, P. Plonski, and R. Sulej, “Neural Network Parameterizations of Electromagnetic



- Nucleon Form Factors,” *JHEP* **1009**, 053 (2010), [arXiv:1006.0342 \[hep-ph\]](#).
- [141] C. Anderson *et al.* (ArgoNeuT Collaboration), “The ArgoNeuT detector in the NuMI low-energy beam line at Fermilab,” *Journal of Instrumentation* **7**, P10019 (2012).
- [142] C. Anderson *et al.* (ArgoNeuT Collaboration), “Analysis of a Large Sample of Neutrino-Induced Muons with the ArgoNeuT Detector,” *JINST* **7**, P10020 (2012), [arXiv:1205.6702 \[physics.ins-det\]](#).
- [143] C. Anderson *et al.* (ArgoNeuT Collaboration), “First Measurements of Inclusive Muon Neutrino Charged Current Differential Cross Sections on Argon,” *Phys. Rev. Lett.* **108**, 161802 (2012).
- [144] R. Acciarri *et al.* (ArgoNeuT Collaboration), “Measurements of Inclusive Muon Neutrino and Antineutrino Charged Current Differential Cross Sections on Argon in the NuMI Antineutrino Beam,” *Phys.Rev.* **D89**, 112003 (2014), [arXiv:1404.4809 \[hep-ex\]](#).
- [145] R. Acciarri *et al.* (ArgoNeuT Collaboration), “First Measurement of Neutrino and Antineutrino Coherent Charged Pion Production on Argon,” *Phys. Rev. Lett.* **113**, 261801 (2014).
- [146] R. Acciarri *et al.* (ArgoNeuT Collaboration), “A study of electron recombination using highly ionizing particles in the ArgoNeuT Liquid Argon TPC,” *JINST* **8**, P08005 (2013), [arXiv:1306.1712 \[physics.ins-det\]](#).
- [147] R. Acciarri *et al.* (ArgoNeuT Collaboration), “Detection of back-to-back proton pairs in charged-current neutrino interactions with the ArgoNeuT detector in the NuMI low energy beam line,” *Phys. Rev. D* **90**, 012008 (2014).
- [148] , “,” Fermilab drawing number 6755. 160-ME-416180.
- [149] David C. Carey, K.L. Brown, and F. Rothacker, “Third order TRANSPORT with MAD input: A Computer program for designing charged particle beam transport systems,” (1998).